UiT The Arctic University of Norway

Faculty of Science and Technology

Understanding Inner Solar System Dust Environment Through In-Situ Measurements

Samuel Kočiščák

A dissertation for the degree of Philosophiae Doctor – August 2024

Abstract

The inner solar system dust cloud is a dynamic environment, located between the inner planets and the Sun. Some of the open questions about the dust cloud are difficult to address with remote sensing instruments, so in-situ detection, that is the local detection from within the dust cloud, is essential. Two recent and unique missions, Solar Orbiter (SolO) and Parker Solar Probe (PSP) venture as close to the Sun as 0.28 AU and 0.06 AU respectively, and both are suited for the detection of dust impact induced charge cloud with their electrical antennas.

Since electrical antennas are not purpose-built dust detectors, identifying dust impacts and interpreting the signals is ambiguous and a great deal of attention is paid to these tasks. To address the identification issue, we developed a machine learning, convolutional neural network (CNN) detection routine, which is superior to the previously used identification algorithms with its 96 % accuracy and 94 % precision. This routine is applied on several years of SolO's Radio and Plasma Waves (RPW) time domain sampled (TDS) electrical waveforms, providing the highest quality dust data product available for SolO. To address the signal interpretation issue, we present a study of thousands of SolO/RPW/TDS waveforms, which were inspected in detail, to understand the non-conventional double-peaked signature. The signature is at least partially explained with an interaction between the impact generated charge and photoelectron sheath of the electrical antennas. This explanation provides a sharper measure for the total amount of impact generated charge, and for the post-impact speed of the charge cloud. On top of that, the impact location on the SolO's body is studied and the data is consistent with most impacts happening on the heat shield and on the ram side of the spacecraft.

The dust grain motion depends on the grains' properties. When the motion of the grains is understood, properties of the grains are constrained. This is made more difficult if several dust populations are present simultaneously, which differ by their size, origin, speed, and lifetime. The modelling approach must take the populations into account, and we demonstrate a tool suitable for this task. By assuming a two-component dust cloud observed by SolO and with Bayesian fitting of the Poisson-distributed detection counts, we confirmed that the data is indeed consistent with most of the detections being due to β-meteoroids with $\beta \gtrsim 0.5$, as the data is only consistent with decelerating β-meteoroids. Unlike SolO, PSP experiences mostly bound dust impacts in a portion of its orbit. This allows for a study of a single component dust flux. We developed a model for bound dust impact counts using the formalism of the phase space distribution function, known from kinetic theory. The model considers several important dust cloud parameters which were not used pre-

viously. Using the model, we found that the observed flux is only compatible with a differential mass distribution slope δ between 0.14 and 0.49, shallower than previously reported for bound dust. We therefore question the validity of the assumption of power-law distributed masses of the μm-sized bound dust grains near the Sun. We found that the flux minimum observed in each perihelion is too prominent to be explained by the alignment between the velocity of bound dust and the spacecraft, especially when the eccentricities, inclinations and other poorly constrained parameters of the dust grains are considered. Although PSP and SolO have different orbits, we were able to see indication that the PSP's heat shield is less sensitive to dust impacts, by comparing the PSP and SolO data close to 1 AU. With Bayesian modelling of dust impacts on SolO and on PSP together, we were able to estimate that the PSP's heat shield is by a factor of four less sensitive to the dust impacts, compared to the rest of PSP and SolO.

The tools presented in this thesis, specifically the CNN dust identification algorithm, and the phase space distribution function dust model are suitable for future application with other spacecraft. Together with the Bayesian flux fitting approach, these tools allow for more precise modelling and therefore deeper understanding of in-situ dust detection.

Acknowledgements

Man is condemned to be free; because once thrown into the world, he is responsible for everything he does (Sartre, 1956).

The names of people, without whom I could not have done this, do not fit on one page. First and foremost, I would like to express my deepest appreciation to you, Audun. It was your calming and guiding presence, that always made me confident that this project would get to a successful end, and I wish every student had a supervisor like you. Ingrid, I cannot convey how thankful I am that you always pushed me towards improvement and never left me to face it alone. Thank you, Arnaud, for filling the role of mentor perfectly, and for making the time spent in Paris as enjoyable as it was enriching. It was a great pleasure working with you, Sigrunn, who kept patiently helping, regardless of how many times I have asked the same questions. Jakub, thank you for your selfless effort, compassion, and for helping me feel at home V Holešovičkách. More people deserve a mention, besides my supervisors. Special thanks go to Andreas, for your open door and your can-do approach. Many thanks also go to my collaborators, namely Libor, David and Jan, Kristina, Nicole, Amalie, and Alen. Thanks should also go to my office colleagues, the great folks of Forskningsparken and Bâtiment 14; the journey would not have been the same without you.

Having money is a way of being free of money (Camus, 1972).

I am thankful to the funding organizations, and the project managers, who enabled me to study and to pay the mortgage while doing so. This includes the funding from Tromsø forskningsstiftelse, Norges forskningsråd, Grantová agentura České republiky, and UiT Norges artiske universitet. I would like to extend my thanks to all the employees at UiT. You did excellent work in keeping me on track with my study plan. It would be a great negligence not to mention the open-source community. You are the giant whose shoulders we all stand on.

Active love is labor and fortitude, and for some people too, perhaps, complete science (Dostoevsky, 1880).

My utmost thankfulness is for my friends and my loving family. To my dearest wife Veronika, as you make the grim days easier, and the easy days awesome. To my great little sister, Neli, for you never fail to show me a new perspective. To my grandmother, Ria, for encouraging the independence in me. Last but certainly not least, to my parents, Adrián and Marína. The older I grow the more I see how much you sacrificed in providing me with all I always took for granted. I will not forget that.

Contents

List of abbreviations

aph aphelion
AU astronomical unit
CDA Cosmic Dust Analyzer (on Cassini SC)
CME coronal mass ejection
CNN convolutional neural network
CoSMo Complex Systems Modelling group
DS Deep Space (SC family)
EM electromagnetic
EQN equinox
FIELDS instrument, not an abbreviation (on PSP SC)
FNR false negative ratio
FPR false positive ratio
HAE Heliocentric Aries Ecliptic (coordinate system)
HCS heliocentric current sheet
INLA Integrated Nested Laplace Approximation
ISD interstellar dust
ISM interstellar matter
L1 the first Lagrange point
LDEF Long Duration Exposure Facility (experiment)
LIC local interstellar cloud
LOS line of sight
LSE least squares estimatate
MAP maximum a posteriori
MAVEN Mars Atmosphere and Volatile Evolution (SC)
MCMC Markov Chain Monte Carlo
M-H Metropolis-Hastings (algorithm)
ML machine learning
MLE maximum likelihood estimation
MLI multilayer insulation
MMS Magnetospheric Multiscale (SC)
N-S north – south
Norm normal (distribution)
OGO Orbiting Geophysical Observatory (SC family)
peri perihelion
PIA Particulate Impact Analyser (on Giotto SC)
Pois Poisson (distribution)
PPP Poisson point process
PR Poynting-Robertson
PSP Parker Solar Probe (SC)

PVDF polyvinylidene fluoride
R-INLA not an abbreviation (R package)
RDA Radio Dust Analyzer (method)
rp radiation pressure
RPW Radio and Plasma Waves (on SolO SC)
RPSW Radio and Plasma Wave Science (on Cassini SC)
SC spacecraft
SEM scanning electron microscopy
S-N south – north
SNR signal to noise ratio
SOL solstice
SolO Solar Orbiter (SC)
SVM support vector machine
sw solar wind
STEREO Solar Terestrial Relations Observatory (SC family)
TBD to be done
TDS time domain sampling / sampler
ToF time of flight (spectroscopy)
tot total
UiT University of Tromsø
UV ultraviolet
VBSDC Venetia Burney Student Dust Counter (on New Horizons SC)
WISPR Wide-field Imager for Solar Probe (on PSP SC)
WLSE weighted least squares estimate
yr year

Chemical elements

Ag silver
Au gold
Al aluminum
C carbon
Fe iron
H hydrogen
Mg magnesium
O oxygen
Si silicon
S sulphur
Ti titanium
W tungsten

1 Introduction

Rocky, icy, and metallic objects in space, smaller than asteroids, are called cosmic dust. Cosmic dust is created as debris of collisions of larger objects, but also by condensation of gases, or by being expelled from a larger body, such as a comet or a moon with active volcanism. Cosmic dust which originates in the solar system is called interplanetary dust, as opposed to cosmic dust which occupies the interstellar or intergalactic space. The circumsolar interplanetary dust is responsible for zodiacal light, which is the diffuse glow observed in post-sunset and pre-sunrise night sky near the ecliptic plane, shown in Fig. 1.1.

The interplanetary dust cloud is an integral part of the solar system, and its dynamics contains information about the past and the present of other bodies. In the inner solar system, micron-sized dust is a probe into the vicinity of the Sun. When it gets too close to the Sun, it is destroyed by the extreme near-solar conditions, which forms a dust-free zone around the Sun. By understanding how the circumsolar dust moves, where the collisions happen, where it is destroyed, and how its characteristics depend on its composition, we find more about the conditions around the Sun, which influence the rest of the solar system. For example, when a dust grain is sputtered or evaporated by the Sun, its material enters the solar wind and is carried out of the inner solar system. With understanding of the dust dynamics in the solar system, the study of other stars' circumstellar dust clouds and planetary disks is also enabled.

The atmosphere of the Earth offers a great target for cosmic dust, and the cosmic dust of more than 100 μm entering the atmosphere is observable in the form of meteors. The vapors ablated from dust influence the mesosphere and the troposphere. Most meteors are of interplanetary origin. The amount of dust entering the atmosphere was estimated decades ago and remains fairly uncertain. One of the reasons for this is the vast range of the mass of grains which contribute to the influx.

When spacecraft move through a dusty environment, such as the inner solar system, they randomly collide with dust grains of the dust cloud. Most of the collisions in the inner solar system are with sub-micron sized dust. Little

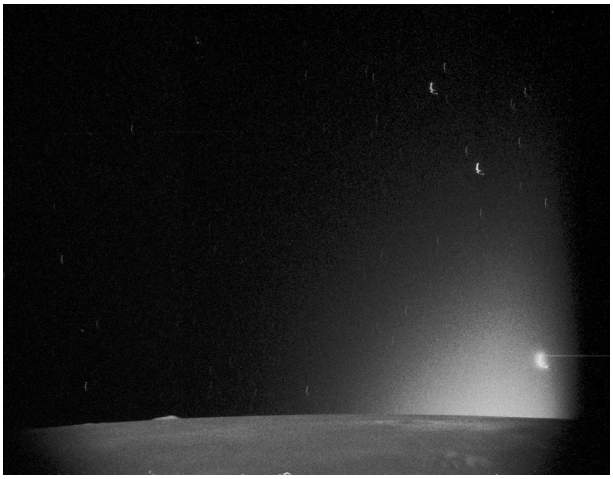

Figure 1.1: A long-exposure photo from the orbit of the Moon, taken shortly after sunset on July 31st, 1971. By NASA - Magazine 98, Apollo 15, March to the Moon.

can be told about the dust cloud based on a single collision, but based on many collisions, generalizations can be made about the size and speed distribution within the cloud.

This thesis is mostly concerned with measurements done by two spacecraft: Solar Orbiter (SolO) and Parker Solar Probe (PSP). Both are Sun-orbiting spacecraft, and are the two human made objects which venture the closest to the Sun. Using their electrical antennas to register collisions with dust grains, they provide dust measurements from the region where no other spacecraft have measured before. This alone makes their measurements valuable, and the fact that they operate simultaneously and over several years only more so.

To understand the dynamics in the interplanetary dust cloud, we make use of the similarities and differences between the two spacecraft. Different statistical modeling approaches must be taken to yield the maximum information in different regions. In the region further away from the Sun, collisions with dust grains are rare. Here, reliable and consistent detection in combination with counting statistics reveals the spatial distribution. In the close vicinity of the Sun, several processes occur at the same time. Here, we identify the most important dust properties by comparing measurements to models. By applying the appropriate tools, we extend the current understanding of the dust grains' speed, masses, collisions, and location in different regions in the inner solar system.

The aim of this thesis is to extend the understanding of the interplanetary

dust inside Earth's orbit from electrical antenna measurements performed by two unique spacecraft, SolO and PSP. We achieve this by taking a more mathematically precise approach than what was used previously. Single-grain dust properties, as well as forces acting on individual dust grains are introduced in Ch. 2. Dust grains in the Solar system compose the interplanetary dust cloud, in which grains of similar properties follow similar trajectories. These form individual dust populations, which are introduced in Ch. 3. To yield the most information possible, sharp statistical tools are needed, some of which are introduced in Ch. 4. The dust detection principles are described in Ch. 5, where emphasis is put on antenna measurements. The articles, which make up a part of this thesis, are described in Ch. 6. Finally, Ch. 7 concludes and offers an outlook.

2 | Dust grain properties and interactions

A dust grain in the solar system is subjected to many interactions. Grains of different sizes and in different locations are naturally susceptible to be influenced by different forces. In this chapter, we describe the dust grains, as well as the most important forces and interactions, with their causes and effects, and their relevance for dust grains of different characteristics. We will later use this to discuss the properties and dynamics of dust populations in the solar system.

2.1 Characterizing a single grain

Newton's second law of motion has it, that

$$\vec{a} = \frac{\vec{F}}{m}, \tag{2.1}$$

where $\vec{a}$ is the acceleration of the object with the constant mass m, induced by the net force $\vec{F}$. Mass of a dust grain is related to its volume V and the mean density ρ as

$$m = V\rho. \tag{2.2}$$

The mean density depends on the composition and the structure of the grain.

Dust composition

There is little direct information on dust composition. Dust grains are relatively hard to collect, and they are mostly collected in the atmosphere of or in the near vicinity of the Earth. Some collection methods, such as collection in the Antarctic ice or from the deep see sediments (Brownlee, 1985) and the near ground collection (Pettersson, 1958) or the collection in the high atmosphere (Fechtig et al., 1968) provided useful data, but are limited to specific dust

grains, ones which were small and slow enough not to completely ablate in the atmosphere (Vondrak et al., 2008). These measurements are also challenging to be performed reliably, as they are very prone to contamination with terrestrial dust (Taylor et al., 2016).

Among the few data points available to this date are the ones provided by the Space Shuttles (McDonnell et al., 1984) and the Stardust mission (Brownlee, 2014), both collected in aerogel (Tsou, 1995). The Stardust samples returned from the vicinity of the Wild 2 comet were found to contain mostly silicon (Si), magnesium (Mg), iron (Fe), and sulfur (S) (Keller et al., 2006). Another proxy for dust composition with much better data availability is the composition of meteorites. Among minerals typically found in meteorites are *olivine*, *quartz*, and *pyroxenes*. Therefore, the most abundant elements in meteorites are again: Si, Mg, Fe, and S, but meteorites also show a vast variety and richness of composition (Anders, 1964) and there is therefore little doubt, that so does the interplanetary dust.

The dust grains do not need to be collected intact for the element composition analysis. A time of flight (ToF) spectroscopy of dust was performed in the vicinity of the comet Halley several times (Jessberger et al., 1988), which besides hydrogen (H) and oxygen (O) revealed mostly carbon (C), Si, Mg, and Fe.

Optical measurements of the elemental abundance in the local interstellar cloud (LIC) probes the composition of dust outside the solar system. It shows a relative depletion of Fe, Mg, and Si which implies these are bound in the dust grains present in the LIC (Sofia et al., 1994).

Based on several pieces of observational evidence, it is reasonable to assume that among the dominant constituents of the dust are H, O, Si, Mg, Fe, C, and S. These are elements which form some of the most abundant minerals on Earth.

Dust shape

The shape of the grains is difficult to establish, since even the grains collected in aerogel are partially damaged during the collection (Burchell et al., 2006). The grains collected in the upper atmosphere, on the sea floor and in deep ice were studied for their shape (Jessberger et al., 2001), but the aforementioned difficulties with the selection bias prevail. A grain recovered from high atmosphere is shown in Fig. 2.1. Information on the dust shape is also yielded from the comparison of remote measurement of scattering properties with the models (Min et al., 2005). A lot was successfully achieved with modelling the dust grains are spheres or ellipsoids, possibly porous and heterogeneous (Mann, 2010), and for many modelling applications, the shape is not crucial.

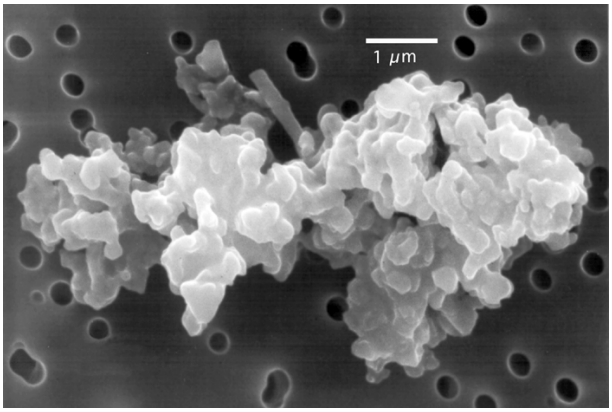

Figure 2.1: A scanning electron microscopy (SEM) image of a porous chondrite dust grain recovered from high atmosphere. The authors of this figure are Donald E. Brownlee, University of Washington, Seattle, and Elmar Jessberger, Institut für Planetologie, Münster, Germany. This file is licensed under CC-BY 2.5 license.

Dust density

Bulk density of the common minerals containing the usual meteorite component elements, such as olivine, quartz or pyroxenes is between $2.6\,\mathrm{gcm}^{-3}$ and $3.8\,\mathrm{gcm}^{-3}$ (Duda and Rejl, 1986). A lot of interplanetary dust, especially in the outer solar system, contains ice. Ice has a bulk density close to $1\,\mathrm{gcm}^{-3}$.

The density is often assumed between $2.5\,\mathrm{gcm}^{-3}$ (Mann et al., 2014) and $3\,\mathrm{gcm}^{-3}$ (McDonnell et al., 1984). Dust grains are often, due to photometric and historical reasons, described in terms of their linear dimension $d = 2r$, which often means the diameter of the sphere with the volume V equivalent to the dust grain's, hence

$$\frac{d}{2} = r = \left(\frac{3V}{4\pi}\right)^{\frac{1}{3}} \approx 0.62\sqrt[3]{V}. \tag{2.3}$$

As a general rule, we will use the radius r as the reference to the grain's size rather than the diameter d throughout this work. Since we meet both mass-based notation and size-based notation, it is useful to keep the conversion in mind, which stands

$$m = \rho\frac{4\pi}{3}r^3 \Leftrightarrow r = \sqrt[3]{\frac{3m}{4\rho\pi}}, \tag{2.4}$$

and assuming $2.5\,\mathrm{gcm}^{-3}$ gives

$$\frac{m}{\mathrm{kg}} \approx 10.4 \cdot 10^3 \left(\frac{r}{\mathrm{m}}\right)^3 \Leftrightarrow \frac{r}{\mathrm{m}} = 4.6 \cdot 10^{-2} \sqrt[3]{\frac{m}{\mathrm{kg}}}, \tag{2.5}$$

which is shown in Fig. 2.2.

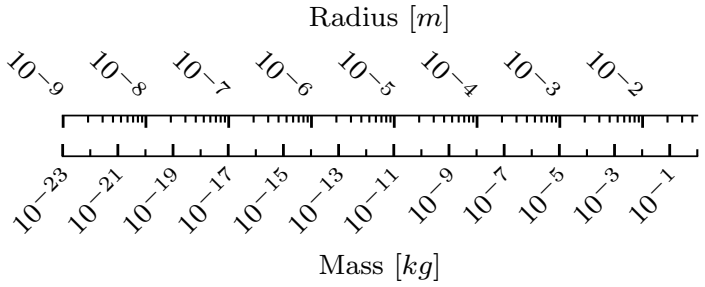

Figure 2.2: A conversion between the mass and the radius of a spherical dust grain, assuming the density of $2.5\,\mathrm{gcm}^{-3}$.

2.2 Forces

2.2.1 Gravity

Gravity is an attractive pair force between two massive objects of the magnitude

$$F_g = G\frac{Mm}{R^2} = \mu\frac{m}{R^2}, \tag{2.6}$$

where $G \approx 6.67 \cdot 10^{-11}\, m^3 kg^{-1} s^{-2}$ is the *gravitational constant*, R is the distance between the objects' centers of mass, and masses M and m belong, by convention, to the more massive object and to the less massive object, respectively. Alternatively, $\mu = GM$ is known as the *gravitational parameter*, which provides a convenient form for the force, especially if $m \ll M$, as is certainly the case of dust grains, with respect to planets and the Sun. In case of the Sun, $\mu \approx 1.3 \cdot 10^{20}\,\mathrm{m}^3\mathrm{s}^{-2}$.

Due to the steep dependence of the force on the distance $F_g \propto R^{-2}$, it is often the case that a single central body suffices to describe the net gravity force affecting a smaller body. This concept is known as the *Hill sphere*, which is the sphere of influence around every massive body in the solar system, within which the body's gravity is the most relevant contributor to the net gravity,

compared against the gravity of the Sun. The approximate planet's Hill radius is equal to the distance to the L_1 or the L_2 Lagrange point, therefore

$$R_H \approx a \sqrt[3]{\frac{m}{3M}}, \tag{2.7}$$

where a is the planet's semimajor axis, m is the mass of the planet, and M is the mass of the Sun (Sheppard et al., 2023). For example, Saturn's Hill sphere with the Hill radius of $R_{H;Saturn} \approx 0.4\,\mathrm{AU}$ is necessary for Saturn to retain is 146 confirmed moons (Sheppard et al., 2023), as well as its far-reaching rings. The rings are an example of a dust system bound to a planet. The Sun is however by far the dominant object in most of the solar system, especially within 1 AU, and its gravity is usually the only one that is relevant for the dust grain in question, unless it is within another body's Hill sphere.

An object orbits the Sun on a circular orbit if the magnitude of centrifugal force F_c is equal to the magnitude of gravity F_g. This condition gives the *circular speed* v_c needed for the equality:

$$\frac{mv_c^2}{R} = \mu\frac{m}{R^2} \Leftrightarrow v_c = \sqrt{\frac{\mu}{R}} \Leftrightarrow R = \frac{\mu}{v_c^2}. \tag{2.8}$$

The circular speed v_c at $R = 1\,\mathrm{AU}$ is $v \approx 29.8\,\mathrm{kms}^{-1}$. Since gravity ceases with $R \to \infty$ as $F_g \propto R^{-2}$, the amount of work required to escape a gravity well is finite. The minimum energy sufficient for the escape is provided by the *escape speed* v_e:

$$\frac{mv_e^2}{2} = \frac{\mu m}{R} \Leftrightarrow v_e = \sqrt{\frac{2\mu}{R}} = \sqrt{2}v_c. \tag{2.9}$$

2.2.2 Radiation pressure

The power density of solar radiation at 1AU is (Kopp and Lean, 2011)

$$G_{SC} \approx 1361\,\mathrm{Wm}^{-2} \tag{2.10}$$

and corresponds to the radiative power of the Sun

$$P_{Sun} \approx 3.9 \cdot 10^{26}\,\mathrm{W}. \tag{2.11}$$

Dividing G_{SC} by the speed of light

$$c \approx 3 \cdot 10^8\,\mathrm{m/s} \tag{2.12}$$

gives the radiation pressure

$$p_{rp}(1\mathrm{AU}) = \frac{G_{SC}}{c} \approx 4.5 \cdot 10^{-6}\,\mathrm{Pa}, \tag{2.13}$$

and the resulting radiation pressure force F_{rp} is readily obtained as

$$F_{rp} = p_{rp}S = \frac{P_{Sun}}{4c\pi R^2}S = \frac{P_{Sun}}{cR^2}r^2, \tag{2.14}$$

where S is the Sun-facing cross section of the body of interest, r is the body's radius, and R is the distance of the body from the Sun, whereas in the second equation we also assumed the body to be spherical and the Sun to be a point source: $r \ll R$. A dimensionless parameter β is used to describe the relative importance of the two forces:

$$\beta = \frac{F_{rp}}{F_g}. \tag{2.15}$$

Since F_{rp} directly opposes F_g, the net force, denoted *effective gravity*, or F_{eg} is obtained as

$$F_{eg} = F_g - F_{rp}, \tag{2.16}$$

and using β, we get

$$F_{eg} = (1 - \beta)F_g. \tag{2.17}$$

In the case of the Earth, the radiation pressure force is $F_{rp;Earth} \approx 5.8 \cdot 10^8\,\mathrm{N}$, which might be compared to the gravity between the Earth and the Sun $F_{g;Earth} \approx 5.2 \cdot 10^{33}\mathrm{N}$, resulting in $\beta_{Earth} \approx 10^{-25}$.

Interestingly, both F_g and F_{rp} scale with the distance from the Sun as $F \propto R^{-2}$. Therefore, β is not a function of the distance from the Sun R, and we are permitted to express the effective gravity as

$$F_{eg} = (1 - \beta)G\frac{Mm}{R^2} = (1 - \beta)\mu\frac{m}{R^2} = \mu_e\frac{m}{R^2}, \tag{2.18}$$

where μ_e is the body-specific effective gravitational parameter, taking radiation pressure into account. We see that the laws of orbital motion (for example Eqs. 2.8 and 2.9) of radiation pressure affected bodies are going to be the same, albeit with a different gravitational parameter μ_e.

We found that β only depends on the properties of the Sun and the body in question, and is therefore body specific. Let us study the dependence of β on the size of the body in question r. It follows that as long as the aforementioned equations for F_g and F_{rp} hold, β depends on r as

$$\beta = \frac{\frac{P_{Sun}}{cR^2}r^2}{\mu\frac{m}{R^2}} = \frac{P_{Sun}}{\mu c}\frac{r^2}{\rho V} = \frac{P_{Sun}}{\mu c\rho}\frac{3r^2}{4\pi r^3} = \frac{3P_{Sun}}{4\pi\mu c\rho}r^{-1}, \tag{2.19}$$

therefore $\beta \propto r^{-1}$, which is not surprising, given $F_g \propto m \propto r^3$ and $F_{rp} \propto S \propto r^2$. Assuming the density of $\rho \approx 2.5\,\mathrm{gcm}^{-3}$ as in Sec. 2.1, we find that

$$\beta \approx 9.6 \cdot 10^{-7}r^{-1}\,\mathrm{m}, \tag{2.20}$$

which gives that for $\beta = 1$, that is the radiation pressure force offsetting the gravity fully, the dust grain must have the radius of $r \approx 960\,\mathrm{nm}$. However, Eq. (2.14) assumes the solar photons are either absorbed or scattered fully as a spherical wave with their momentum transferred to the body. This holds for absorbing materials if $r \gg \lambda$, where λ is the wavelength of the radiation. However, $r \approx 960\,\mathrm{nm}$ is comparable to the typical wavelengths of a sunlight photon and the assumption does not hold fully. A proper calculation of light scattering is necessary and it depends on the material and shape of the grain. This was done previously by other authors (Kimura et al., 2003) for reasonable materials, see Fig. 2.3. It was found that the maximum of β is reached between $10^{-17} - 10^{-16}\,\mathrm{kg}$, which corresponds to the radius of $100 - 200\,\mathrm{nm}$. In any case, the maximum value of β is on the order of unity and β is lower than unity for much smaller or larger grains. Radiation pressure is crucial for the dynamics of the sub-μm grains, which most of this thesis is concerned with.

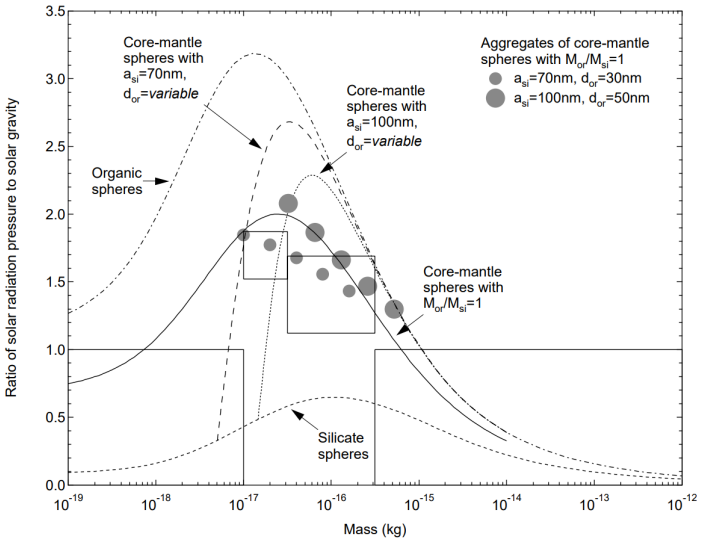

Figure 2.3: The light scattering calculation result for the β value (y-axis) as a function of mass of spherical grains of various composition, adapted from Kimura et al. (2003).

2.2.3 Lorentz force

Grain's electric potential

The grains in the solar system are immersed in the ambient plasma and subjected to the solar UV irradiation, both causing charging of the grains.

Should the ambient conditions remain stable, the grain's electric charge reaches equilibrium. The main charging currents are *electron collection current* and the *photoemission current*. They act to charge the grain to a negative and positive potential, respectively. Should the plasma be dense or should the grain be in shadow, the former prevails, and the grain's potential becomes negative. Should the plasma be sparse and the UV irradiation intense, the latter prevails and the grain becomes positively charged. We will now examine the two extreme cases.

An object immersed in plasma charges to so-called *floating potential* ϕ_f. This potential is typically negative, which is a result of the electron mobility being much higher, compared to the ion mobility. The charging current ceases if the potential of the grain poses a significant barrier to the electrons, therefore the maximum potential is on the order of electron temperature T_e, which is approximately $8\,\mathrm{eVk_B^{-1}}$ near 1 AU and $20\,\mathrm{eVk_B^{-1}}$ near 0.25 AU in the typical solar wind (Guillemant et al., 2013).

Electrons are released from an illuminated neutral grain, in case the incident photon's energy $h\nu$ is above the photoelectric work function W_p of the grain's material. This typically requires UV photons and leaves the grain more positively charged, which adds an additional barrier for the next photoelectron to surpass. The established positive potential ϕ_p is such that no more electrons can escape, therefore it is $\phi_p \approx h\nu - W_p$. While W_p for common materials is between $2 - 5\,\mathrm{eV}$, the last strong spectral line of she sunlight is *Ly-*α at $h\nu \approx 10.2\,\mathrm{eV}$, resulting in the maximum potential of ϕ_p between $5 - 8\,\mathrm{V}$.

The equilibrium potential ϕ of the grain depends on the ambient plasma conditions and the properties of the grain, but typically settles on a value between $-20\,\mathrm{V}$ and $+8\,\mathrm{V}$. A more comprehensive study is out of scope of this work, but is found in literature (Meyer-Vernet, 1982; Horányi, 1996; Krivov et al., 1998; Dzhanoev et al., 2016; Vaverka et al., 2016).

Grain's charge

An isolated grain's charge q is related to its potential ϕ as

$$q = C\phi, \tag{2.21}$$

where C is the grain's capacitance. The capacitance of a solitary sphere in vacuum with the radius of r is

$$C_{sphere} = 4\pi\epsilon_0 r, \tag{2.22}$$

which translates using Eq. 2.21 to

$$\frac{q}{r\phi} = 4\pi\epsilon_0 \approx 1.1 \cdot 10^{-10}\,\mathrm{CV^{-1}m^{-1}}, \tag{2.23}$$

where $\epsilon_0 \approx 8.9 \cdot 10^{-12}\,\mathrm{CV^{-1}m^{-1}}$ is the free space permittivity. This simplistic model predicts the charge of $\pm 10^{-15}\,\mathrm{C}$ for a spherical grain with the radius of $r = 1\,\mu\mathrm{m}$ at the potential of $\phi = \pm 9\,\mathrm{V}$. We note that this value is order of magnitude correct for a grain of any common shape with the greatest linear extent of $\approx 2r$ (Maxwell, 1877). The ratio of mass m to charge q is relevant for the dynamics of dust grains. Given the charge as in Eq. 2.23, and the mass as in Eq. 2.4, we get

$$\frac{q}{m} = \frac{3\epsilon_0\phi}{\rho r^2} \approx 10^{-13} r^{-2}\,\mathrm{m}^2, \tag{2.24}$$

where we assumed $\phi \approx 9\,\mathrm{V}$ and the bulk density $\rho \approx 2.5\,\mathrm{gcm^{-3}}$ as before. Eq. 2.24 is visualized in Fig. 2.4.

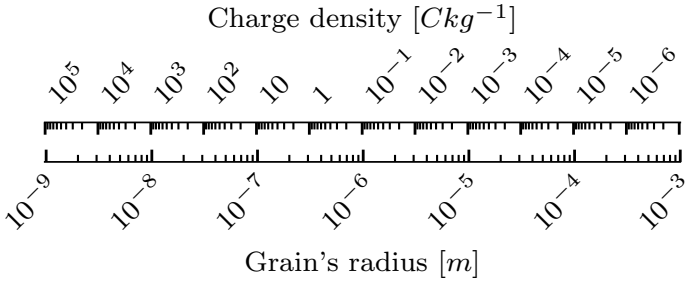

Figure 2.4: A conversion between the radius r and the charge density q/m of a dust grain as in Eq. 2.24, assuming the surface potential $\phi \approx 9\,\mathrm{V}$ and the bulk density $\rho \approx 2.5\,\mathrm{gcm^{-3}}$.

Dynamics

A point charge is usually a very suitable model for a charged dust grain. The Lorentz force acting on a point charge q is

$$\vec{F}_{EM} = q\left(\vec{E} + \vec{v} \times \vec{B}\right), \tag{2.25}$$

where $\vec{E}$ and $\vec{B}$ are the ambient electric and magnetic fields, respectively, and $\vec{v}$ is the velocity of the point charge. If the charge q is sufficiently large, F_{EM} might be more important than effective gravity:

$$F_{eg} < F_{EM} \Rightarrow \frac{q}{m} > \frac{(1-\beta)\mu}{R^2\left|\vec{E} + \vec{v} \times \vec{B}\right|}. \tag{2.26}$$

As an order of magnitude estimate for a grain in the solar wind, assume

$$F_{EM} \approx q v_{sw} B_{IMF}, \tag{2.27}$$

in addition to $\beta = 0$ and $B_{IMF} = 4\,\mathrm{nT}$, which is a reasonable magnetic field strength near $R = 1\,\mathrm{AU}$ (Mann et al., 2007). Thus, the condition from Eq. 2.26 becomes

$$\frac{q}{m} > 5\,\mathrm{Ckg}^{-1}, \tag{2.28}$$

which is equivalent to $r < 0.14\,\mu\mathrm{m}$ (Eq. 2.24), and is not very sensitive to R, provided that $B \propto R^{-2}$, which can often be assumed if $R \gg R_{Sun}$ (Parker, 1958).

This condition describes the state in which Lorentz force is grater in amplitude than gravity. If these two forces are comparably strong, the accelerations they induce are comparable. By extension, the curvature of the trajectory due to gravity and the curvature of the trajectory due to Lorentz force are comparable. The radius of curvature of the trajectory of a grain in orbit due to gravity is on the order of the heliocentric distance of the grain. We therefore must consider the temporal aspect: given enough time, that is over many orbits, even $F_{EM} \ll F_g$ might be consequential for the motion of the dust grain. Vice-versa, $F_{EM} \approx F_g$ does not imply that the grain does not orbit the Sun.

Eq. 2.26 has many degrees of freedom. In this context, the ratio of q/m is the most important of the grain's properties and the grain's motion is often studied with respect to its q/m. Czechowski and Mann (2010) studied the motion of charged grains released in the vicinity of the Sun with the circular speed and charge density of about $10^3\,\mathrm{Ckg}^{-1}$, which corresponds to the radius of $r \approx 10\,\mathrm{nm}$. They assumed the magnetic field $\vec{B}_{IMF}$ as described by the Parker spiral (Parker, 1958) with a tilted heliospheric current sheet (HCS). They found that if the grains are produced within 0.15 AU, they remain trapped near the Sun, on complicated orbits with very low perihelia, and therefore are likely destroyed. If the grains are produced outside of 0.2 AU, they are expelled outward, and their velocity at 1 AU depends on their q/m, and is close to $200\,\mathrm{kms}^{-1}$ if $q/m \gtrsim 10^3\,\mathrm{Ckg}^{-1}$, and lower for grains with lower q/m. The motion of dust near the Sun was studied theoretically by other authors, and many effects were described, such as inclination increase and ejection (Krivov et al., 1998), and gradual shift of the dust cloud symmetry plane (Morfill and Grün, 1979).

Poppe and Lee (2020) studied variability of the flux of dynamically charging nm-sized grains. They made use of electromagnetic field given by a time variable, semi-empirical, corona-solar wind coupled model and found strong variability in the distribution of grains arriving at 1 AU within one Carrington rotation. Especially grains with the radius $r < 10\,\mathrm{nm}$ were found to arrive at 1 AU with the speed well correlated with the local solar wind speed v_{sw}. The influence of the heliospheric magnetic field orientation and solar cycle on the presence of nm-sized dust in the inner heliosphere was studied by Poppe

and Lee (2022). The magnetic field orientation was found to be most consequential for the presence of 10 nm and 20 nm dust at 1 AU, with the grains only reaching 1 AU in case of the focusing configuration of the field, which repeats every other solar cycle and will occur again the late 2020's.

2.2.4 Poynting-Robertson drag

Since an object orbiting the Sun is moving with respect to the source of radiation, the position of the Sun as seen from the object is apparently different, *aberrated*, by an angle of the order of v/c, where v is the orbital speed of the object, and c is the speed of light. Therefore, the light does not arrive from purely radial direction, but partially from the *ram direction*, as observed from the orbiting object. The scattering and absorption of the light then leads to a negative change in the momentum, and therefore in the orbital speed (Poynting, 1903). The magnitude of Poynting-Robertson effect is (Robertson, 1937):

$$F_{PR} = \frac{v}{c^2} P_r, \tag{2.29}$$

where P_r is the power of incoming solar radiation assuming the object's cross section S:

$$P_r = \frac{P_{Sun} S}{4\pi R^2}. \tag{2.30}$$

Assuming the object is on a circular orbit, we make use of Eqs. 2.29, 2.8, and 2.30 to get

$$F_{PR} = \sqrt{\frac{\mu}{R}} \frac{P_r}{c^2} = \frac{P_{Sun} S}{4\pi c^2} \sqrt{\frac{\mu}{R^5}}. \tag{2.31}$$

As an estimate of magnitude of F_{PR}, we evaluate the effective pressure p_{PR}:

$$p_{PR} = \frac{F_{PR}}{S} = \frac{P_{Sun}}{4\pi c^2} \sqrt{\frac{\mu}{R^5}} \approx 4.5 \cdot 10^{-10}\,\mathrm{Pa}, \tag{2.32}$$

where we assumed $R \approx 1\,\mathrm{AU}$, and c, P_{Sun}, and μ as before.

As an estimate of relevance of F_{PR}, we may study the dynamic evolution of the orbital speed, and, by extension, orbital radius. Although F_{PR} acts against the speed v, the speed will actually be rising, as lower energy implies higher orbital speed. Eq. 2.29 gives for the acceleration a in time

$$a_{PR}(t) = \frac{dv}{dt}(t) = \frac{P_r(t) v(t)}{mc^2} = \frac{P_{Sun} v(t)}{4\pi R^2(t) c^2} \frac{S}{m}, \tag{2.33}$$

where we use the assumption of circularity (Eq. 2.8) once again to get

$$a_{PR}(t) = \frac{P_{Sun}}{4\pi \mu^2 c^2} \frac{S}{m} v^5(t), \tag{2.34}$$

which is separable with a single positive real solution for $v(t)$:

$$v(t) = \left(v(0)^{-4} - \frac{P_{Sun}}{\pi \mu^2 c^2} \frac{S}{m} t \right)^{-\frac{1}{4}}, \tag{2.35}$$

which translates to R:

$$\begin{aligned} R(t) &= \mu \sqrt{\left(\frac{R_0}{\mu} \right)^2 - \frac{P_{Sun}}{\pi \mu^2 c^2} \frac{S}{m} t} \\ &= \sqrt{R_0^2 - \frac{P_{Sun}}{\pi c^2} \frac{S}{m} t}. \end{aligned} \tag{2.36}$$

Assuming a spherical dust grain (Eq. 2.4), we get

$$R(t) = \sqrt{R_0^2 - \frac{P_{Sun}}{\pi c^2} \frac{\pi r^2}{\rho \frac{4\pi}{3} r^3} t} = \sqrt{R_0^2 - \frac{3 P_{Sun}}{4 \pi \rho c^2} \frac{t}{r}}, \tag{2.37}$$

where the factor of t/r, the time-scale of the orbital evolution, is proportional to the grain's linear size. Assuming P_{Sun}, ρ as before, $r = 1\,\mu\text{m}$ grain will spiral from $R_0 = 1\,\text{AU}$ down to $R = 0.1\,\text{AU}$ in $t = 1.7 \cdot 10^3\,\text{yr}$. This time becomes $10^6\,\text{yr}$ if we assume an object with the radius of $r \approx 0.6\,\text{m}$, therefore F_{PR} is irrelevant for the dynamics of macroscopic objects, but relevant for the dynamics of the solar system's dust cloud.

We note that the orbital eccentricity of grains subjected to F_{PR} gradually decreases. Briefly, and without mathematical rigor, deceleration in the perihelion does not change the perihelion distance r_{peri}, but lowers the aphelion distance r_{aph}. This decreases eccentricity e. Correspondingly, deceleration in the aphelion lowers r_{peri}, doesn't change r_{aph} and therefore increases eccentricity. We note that $F_{PR} \propto v P_r$, and both these factors reach their maximum in the perihelion of an eccentric orbit, and their minimum in the aphelion, therefore eccentricity is gradually reduced and circular orbit's $e = 0$ is stable. Rigorous results for non-circular orbits are available in literature (Wyatt and Whipple, 1950).

2.2.5 Solar wind pressure

Interplanetary dust grains are in interaction with the solar wind plasma. The solar wind particles are in predominantly radial motion and they therefore project radial pressure p_{sw} on the dust grains, which is in case of a stationary dust grain easily estimated (Shue et al., 1998) as

$$p_{sw} = n m_p v_{sw}^2, \tag{2.38}$$

where n is the number density of solar wind protons with mass m_p, v_{sw} is the solar wind bulk speed, if only solar wind protons are considered and all the protons are assumed to fully pass ther momentum to the grain. Assuming typical 1 AU values of $v_{sw} \approx 300\,\mathrm{kms}^{-1}$, $n \approx 10^7\,\mathrm{m}^{-3}$, and $m_p \approx 1.67 \cdot 10^{-27}\,\mathrm{kg}$, we get $p_{sw} \approx 1.5 \cdot 10^{-9}\,\mathrm{Pa}$. We note that $p_{sw} \ll p_{rp}$ (see Eq. 2.13). Since both pressures scale as $p \propto R^{-2}$ with the heliocentric distance R, solar wind pressure in radial direction p_{sw} is typically negligible compared to the radiation pressure p_{rp}.

Even though radial effect of solar wind pressure is negligible compared to the radiation pressure, its azimuthal component is not, since the orbital speed of a dust grain v is much closer to the solar wind speed v_{sw} than to the speed of light c. Considering a dust grain with speed $\vec{v} = \vec{e_r} v_r + \vec{e_\phi} v_\phi$, the force $\vec{F}_{sw} = \vec{e_r} F_{sw,r} + \vec{e_\phi} F_{sw,\phi}$ on the dust grain is (Burns et al., 1979)

$$\begin{aligned} F_{sw,r} &= S p_{sw} \left(1 - \frac{2 v_r}{v_{sw}}\right), \\ F_{sw,\phi} &= S p_{sw} \left(\frac{v_\phi}{v_{sw}}\right). \end{aligned} \tag{2.39}$$

The force $F_{sw,\phi}$ is often called pseudo-Poynting-Robertson drag, since it acts similarly to F_{PR} discussed in Sec. 2.2.4. Assuming orbital speed of the Earth $v_\phi \approx 30\,\mathrm{kms}^{-1}$ and $v_{sw} \approx 300\,\mathrm{kms}^{-1}$, we find

$$p_{sw,\phi} = \frac{F_{sw,\phi}}{S} \approx 1.5 \cdot 10^{-10}\,\mathrm{Pa}, \tag{2.40}$$

which is comparable to $p_{PR} \approx 4.5 \cdot 10^{-10}\,\mathrm{Pa}$ at the same heliocentric distance $R = 1\,\mathrm{AU}$. With more careful treatment, it was estimated that $p_{sw,\phi} \approx 0.22\, p_{PR}$ for typical dust grains (Whipple, 1967), and more recently it was found that $p_{sw,\phi} > p_{PR}$ for certain grains with radii $r < 0.1\,\mu\mathrm{m}$, and even radial $p_{sw} \approx p_{rp}$ for silicate grains with radii $r < 10\,\mathrm{nm}$, since the cross section with ions is much better than the cross section with sunlight photons for small particles (Mukai and Yamamoto, 1982).

2.3 Erosion

The mass of a grain evolves abruptly at *collisions* and gradually due to the solar radiation and the ambient plasma. The solar radiation causes heating and *sublimation*, while the plasma environment, namely incident solar wind causes erosion by *sputtering*.

2.3.1 Sublimation

To find under what conditions sublimation is important, we will examine the *black body temperature*, that is the equilibrium temperature of a fully absorbing object in sunlight. We note that the temperature of a dust grain may, depending on the size and composition, differ from the black-body temperature by a factor of 3, where the deviation is most prominent for grains with the radius $r \ll 1\,\mu$m (Myrvang, 2018), where scattering effect must be treated carefully. However, for larger grains of common material, the black body temperature is a useful approximation.

The black body temperature in the vicinity of a star is obtained by comparing the incoming solar radiation P_r (Eq. 2.30) and the output power P_{out} of the body:

$$P_{out} = S_{tot}\sigma T^4, \tag{2.41}$$

where S_{tot} is the emitting surface of the body, σ is the Stefan-Boltzmann constant, and T is the temperature of the black body. Eq. 2.41 is the Stefan-Boltzmann law (Stefan, 1879; Boltzmann, 1884). Comparing this to Eq. 2.30, we get the condition for the power equality:

$$\frac{P_{Sun}S}{4\pi R^2} = S_{tot}\sigma T^4 \Leftrightarrow T = \frac{1}{2}\sqrt[4]{\frac{P_{Sun}}{\sigma\pi}}\frac{1}{\sqrt{R}} \approx 279\,\mathrm{K}\left(\frac{R}{\mathrm{AU}}\right)^{-\frac{1}{2}}, \tag{2.42}$$

where we note S is the cross section of the grain, whereas S_{tot} is the irradiating surface of the grain, and for a sphere $S_{tot} = 4S$. For reference, the melting point of iron is approxiamtely 1800 K and the melting point of olivine is between 1500 K and 2200 K, depending on the exact composition (L.-G. Liu and Bassett, 1975; Pinti et al., 2015). The relation as in the equation is shown in Fig. 2.5, along with the melting point of water and the highest melting point of olivine.

The *rate of sublimation* of droplets is described by Langmuir's evaporation equation (Langmuir, 1918):

$$\frac{dm}{dt}(t) = -p_v\sqrt{\frac{M_e}{2\pi RT}}S_{tot}(t) = -2p_v\sqrt{\frac{2\pi M_e}{RT}}r^2(t), \tag{2.43}$$

where p_v is the vapor pressure of the droplet fumes at the temperature of the droplets T, S_{tot} is the surface of the droplet, M_e is the molar mass of the fumes, R is the gas constant, and the second equality assumes a spherical droplet of radius r. This is applicable on dust grains composed of a sublimating material. The parameters p_v and M_e are material-dependent, and the former is also a steeply increasing function of T. We note the proportionality

$$\frac{dm}{dt}(t) \propto S_{tot}(t) \propto r^2(t), \tag{2.44}$$

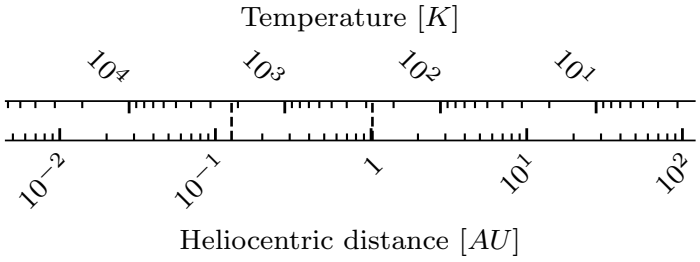

Figure 2.5: The equilibrium black body temperature as a function of heliocentric distance, assuming spherical body. The temperatures of 273 K and 2200 K are shown for reference.

which implies that the radius decreases linearly and, therefore, the sublimation lifetime is proportional to the original radius of the spherical grain. The differential equation can be solved for initial dust composition and temperature.

2.3.2 Sputtering

Sputtering is a non-thermal process of erosion of an object due to collisions between the object and energetic particles. Unlike sublimation, sputtering depends on the properties of the plasma environment in addition to the properties of the bombarded object. In the interplanetary space, the energetic particles are provided by the Sun, in the form of solar wind and occasional mass ejections. *Sputtering mass loss rate* is measured in laboratory as

$$\frac{dm}{dt}(t) = -\frac{M_e \lambda_i Y}{N_A} S(t), \tag{2.45}$$

where M_e is the molar mass of the grain's atoms, S is the grain's cross section, λ_i is the flux of incident particles, N_A is Avogadro's constant and finally Y is the dimensionless *sputtering yield*, which is modelled as a function of the state of the grain, and energy and mass of the incident particles (Vyšinka, 2018). Many assumptions must be done in order to solve Eq. 2.45.

2.3.3 Collisions

High-speed collisions between dust grains are inelastic and the mass distribution is changed as the parent grains produce smaller offspring grains. Assume the parent grains have masses M_1 and M_2, where $M_1 < M_2$. Modelling success was previously achieved (Gault et al., 1963; Dohnanyi, 1969) by assuming

so-called *crushing law* to be of the form

$$g(m) = C(M_1, M_2)m^{-\eta}, \tag{2.46}$$

where $g(m)$ is a probability density function for the offspring mass m, η is the power-law exponent, and the factor C is a function of the parent objects' masses. Since the power-law distribution is constrained by the total amount of collisionally ground material M_Σ and is right-bound due to the upper limit of the offspring grain mass M_{max} (that is the largest offspring grain), the normalization is

$$C(M_1, M_2) = (2 - \eta)M_\Sigma M_{max}^{\eta-2}. \tag{2.47}$$

The parameter of η was experimentally established (Gault et al., 1963) to be $\eta \approx 1.8$, in case $M_2 \to \infty$ which implies that most of the offspring mass is retained in the small offspring grains. A related modelling concept is that of *catastrophic collisions* (Dohnanyi, 1969; Grün et al., 1985). These are collisions which completely shatter both parent grains: $M_\Sigma = M_1 + M_2$. If the smaller of the grains is too small $M_1 \ll M_2$, the bigger grain is not shattered completely. Laboratory experiments have repeatedly shown linearity of the process with mass (Gault et al., 1963; Dietzel et al., 1973; Grün, 1984; McBride and McDonnell, 1999; Collette et al., 2014; Shen, 2021). In that case, the condition for a catastrophic collision can be written as

$$M_2 < \Gamma M_1, \tag{2.48}$$

where the threshold ratio Γ is a theoretical concept only, and is a decreasing function of the impact speed and a function of the material properties. It is also difficult to establish experimentally (Grün et al., 1985), and different values are found in the literature. For the impact speed of 10 km/s, the values on the order of $5 \cdot 10^4$ were reported (Gault and Wedekind, 1969; Fujiwara et al., 1977), but they range from 10^2 to $5 \cdot 10^5$ for broader speed interval (Whipple, 1967; Zook and Berg, 1975; Dohnanyi, 1978). Collisional lifetime of a dust grain is the time it takes for the grain to catastrophically collide with another grain. The other grain is likely to be smaller than the test grain, since there are many more (by count) small dust grains than large dust grains. Collisional lifetime greatly depends on the mass and speed distribution and to some extent also on the material properties of the dust grains, and is therefore dependent on the heliospheric region.

2.3.4 Lifetimes

All three erosion processes presented in this section (sublimation, sputtering, and collisions) depend, beyond other assumptions, on the size, the material,

and on the location in the solar system. All three are major factors in shaping the solar system dust cloud's dynamics and are important in different heliocentric regions.

Since sublimation rate depends on the grain's temperature, it prevails in the near vicinity of the Sun. It was evaluated to be dominant within $R < 0.1\,\mathrm{AU}$, where the sublimation lifetime of $\approx 10^{-1}\,\mathrm{yr}$ is implied for $r \approx 1\,\mu\mathrm{m}$ silicate dust (Baumann et al., 2020). Sublimation lifetime for carbon dust at the same heliocentric distance is however $\approx 10^{4}\,\mathrm{yr}$, since carbon has 10^5-times lower vapor pressure at 2300 K. Silicate and metal oxide grains sublimate quickly within $R < 0.1\,\mathrm{AU}$, but for carbon dust grains, sputtering and collisions are important even at $R = 0.1\,\mathrm{AU}$. Let us note that these general results do not cover the instances of high density solar wind, such as during the coronal mass ejections (CMEs), which might shorten the lifetime of certain dust grains by a great deal (Baumann et al., 2020). High mass loss due to sublimation is the most important process behind the formation of the near-solar dust free zone (H. N. Russell, 1929).

Poynting-Robertson drag is not an erosion process on its own, but since it acts to decrease the orbital distance of the grains in orbit around the Sun, it gradually increases the mass loss due to the true erosion processes. As evaluated in Sec. 2.2.4, the time for $1\,\mu\mathrm{m}$ particle to spiral down from $R_0 = 1\,\mathrm{AU}$ to $R = 0.1\,\mathrm{AU}$ is on the order of $10^3\,\mathrm{yr}$. It was in fact concluded that while collisions limit the lifetime of grains $r \geq 10^{-4}\,\mathrm{m}$, Poynting-Robertson drag limits the lifetime of the smaller ones (Grün et al., 1985).

For the dust of radius $r \approx 1\,\mu\mathrm{m}$, the collisional lifetime at 1 AU is on the order of $10^6\,\mathrm{yr}$, whereas at 0.1 AU it is on the order of $10^3\,\mathrm{yr}$ (Grün et al., 1985). We can compare this to the sputtering lifetime of silicate grains of the same size, which is $\approx 10^4\,\mathrm{yr}$ at 1 AU, and $\approx 10^2\,\mathrm{yr}$ at 0.1 AU even in slow solar wind conditions (Klepper, 2021). It was in fact calculated by Klepper (2021) that the sputtering lifetime is shorter than the collisional lifetime between 0.1 AU and 1 AU for silicate and metal oxide dust grains with $r < 20\,\mu\mathrm{m}$. We note that the orbital period at 0.1 AU is 12 days, therefore, the erosion processes take many orbits to erode a grain, even at 0.1 AU.

To sum up, sublimation limits the lifetime of most grains in the near vicinity of the Sun ($R < 0.1\,\mathrm{AU}$). In most of the inner solar system, Poynting-Robertson drag limits the life-time of small grains with $r < 10^{-4}\,\mathrm{m}$, while collisions limit the life time of larger grains with $r > 10^{-4}\,\mathrm{m}$. Sputtering lifetime is comparable, but somewhat longer than Poynting-Robertson and collisional lifetimes, except for extreme plasma environments, such as CMEs. A more nuanced discussion is found in literature (Klepper, 2021; Baumann et al., 2020; Grün et al., 1985; Whipple, 1967; Myrvang, 2018).

3 | Dust populations

Different sources of dust, along with different forces acting on dust grains as a result of their location and size, allow us to distinguish populations of dust. For the context, in which the presented research is set, we are going to introduce and characterize several important dust populations in the solar system.

3.1 Bound dust

Among the forces discussed in Ch. 2, the force with the steepest proportion to the grain's radius r is gravity: $F_g \propto r^3$. Gravity therefore determines the motion of large bodies in the solar system. The dust particles that are dominantly influenced by gravity and are in bound orbits, are denoted *bound dust*. The term *zodiacal dust* is sometimes used since this dust contributes to the zodiacal light the most. The term *F-corona* is used for the zodiacal light observed close to the Sun. We may encounter the term *alpha* (abv. α) meteoroids, sometimes used interchangeably with bound dust, but appropriateness of the term as a synonym to bound dust was debated (Sommer, 2023), since the term was originally coined to describe highly eccentric bound grains only (Zook and Berg, 1975) and, therefore, we will not use the term.

Size range

The lower size threshold for a dust grain to be bound may be estimated by comparison with the forces dependent $\propto r^2$, namely radiation pressure force F_{RP} and Poynting-Robertson drag F_{PR}. If we set the criterion for $F_{RP} \ll F_g$ to $\beta < 0.1$, then using Eq. 2.20 we find $r > 10\,\mu$m. The Poynting-Robertson lifetime of $r = 10\,\mu$m dust (Eq. 2.37) is approximately 13 kyr, which allows for many orbits. For completeness, using Eqs. 2.24 and 2.27 we find that for $r = 10\,\mu$m dust, the electromagnetic force $F_{EM} < 2 \cdot 10^{-4} F_g$. Therefore, the motion of $r > 10\,\mu$m dust is dominated by gravity.

Leinert et al. (1981) found that the range of $10\,\mu\text{m} < r < 100\,\mu$m contributes to the intensity of Zodiacal light the most. The reason for this is that

much larger dust has a low ratio of surface to mass, and much smaller dust neither lasts long in orbit, nor scatters light very effectively.

Dynamics

The number density n of $10 - 100\,\mu$m dust near the ecliptic plane was established based on remote observations of the zodiacal light to follow

$$n(R) \propto R^{-1.3} \tag{3.1}$$

in the range of $0.3\,\mathrm{AU} < R < 1\,\mathrm{AU}$ (Leinert et al., 1981), and since the zodiacal light seems to be constant in time (Buffington et al., 2016), it is believed to be constantly replenished by fragments of colliding, larger, $r \geq 1\,$mm dust with the number density $n \propto R^{-\nu}$, where $1 < \nu < 1.1$ (Leinert et al., 1983).

Bound dust grains are gradually losing mass due to erosion. The erosion is faster if the grains are closer to the Sun. This process is therefore accelerated by shrinking the orbital distance due to Poynting-Robertson drag. The grains also lose mass abruptly, in collisions, as we discussed in Sec. 2.3.3. It was found that collisions are the reason for the greatest proportion of the mass loss from the bound dust population (Grün et al., 1985). On the other hand, the population is refilled by dust newly released from larger bodies. Although debris of asteroidal collisions contribute to the population of bound dust, the majority of bound dust is likely created in fragmentation of comets. This is supported by numerical modelling of the motion and the collisional cascade of dust grains ejected by different orbital group bodies (Nesvorný et al., 2010), and by the comparison of the reflective properties of bound dust to those of comets and various asteroidal groups (Yang and Ishiguro, 2015).

It was found (Dohnanyi, 1969) that erosive and catastrophic collisions between asteroids (Sec. 2.3.3) lead to a steady-state mass distribution of the asteroids in the power-law form:

$$f(m) \propto m^{-\delta}, \tag{3.2}$$

where $\delta = 11/6 \approx 1.83$, provided that the crushing-law (Eq. 2.46) slope $\eta < 2$, that is, there are not too many large objects left after the collision. It is important to note that under the assumption that $\eta < 2$ and that the catastrophic collisions dominate the mass loss, the slope $\delta = 11/6$ is not a function of η at all and is only a very shallow function of η if the erosive collisions are relevant. It was also shown that the solution of $\delta = 11/6$ is stable if perturbed by an additional inflow of low or high m into the distribution (Dohnanyi, 1969). This does not hold fully for the dust grains with $r < \mu$m, since more loss processes are relevant in this region (Grün et al., 1985), most notably, β-meteoroid production.

Open questions

Remote observations provide information about the spatial distribution of dust, while in-situ detections and modelling provide information about its mass distribution. Both are however fairly insensitive to dust eccentricities and inclinations, therefore to the velocity distribution and the spatial distribution out of the ecliptic plane. Bound dust is an important contributor to the counts observed by PSP, and the compatibility of the observed counts with eccentric and inclined dust was studied in Paper IV. While it is clear that the dust is concentrated around the ecliptic plane, it is not straightforward to deduce the off-ecliptic density dependence from remote observations and several models were proposed and debated (Giese et al., 1986). Future measurements of SolO might shed some light on this, as the orbit of the spacecraft, which performs dust measurements, will get gradually inclined between 2025 and 2029.

Since the lifetime of dust grains in near vicinity of the Sun is short due to intense erosion processes (Sec. 2.3), a dust-free zone (DFZ) was hypothesized (H. N. Russell, 1929). DFZ might be enveloped by a transition region, so called dust-depletion zone (DDZ). Due to the limitations of the experimental techniques and the difficulties with decomposing the brightness measurements to dust and other light-producing phenomena, the DFZ was not convincingly observed to this date, although DDZ was observed remotely from onboard PSP (Stenborg et al., 2018). It was thus estimated, that the DDZ lies between $5\,R_{Sun}$ and $19\,R_{Sun}$, while the DFZ is expected inward of $5\,R_{Sun}$ (Stenborg et al., 2022). This implies that PSP has already travelled well into the DDZ with its perihelia of $\approx 12\,R_{Sun}$. An investigation of the DDZ was one of the objectives of Paper IV, results of which suggest that the DDZ explains the observed dust detection counts near the perihelia of PSP.

3.2 Beta meteoroids

Pioneer 8 and 9 spacecraft discovered a previously unobserved population of dust grains, when it was apparent that most of the grains of the size $r < 10^{-6}$ m were coming from the direction of the Sun (Berg and Grün, 1973). This phenomenon is explained as a population of dust leaving the Sun's gravity well on a hyperbolic trajectory due to the solar radiation pressure successfully competing with solar gravity, and the term *beta meteoroids* (*β-meteoroids*) was coined for the population (Zook and Berg, 1975). Many other space missions observed the population since, for example Solar Terrestrial Relations Observatory (STEREO) (Zaslavsky et al., 2012), Wind (Malaspina et al., 2014), and SolO (Zaslavsky et al., 2021).

Size range

As we showed previously (Eq. 2.18), the laws of motion do not change even if the radiation pressure is significant, it is the effective gravitational parameter $\mu_e = (1-\beta)\mu$, which changes with β. Since the escape speed v_e and the circular speed v_c differ by a factor of $\sqrt{2}$ and both depend on μ (Eqs. 2.8, 2.9), in terms of effective gravity:

$$v_c(\beta = 0) = v_e(\beta = 1/2). \tag{3.3}$$

This implies that if a dust grain on a circular orbit with $\beta = 0$ suddenly changes its β value to $\beta = 1/2$, it becomes critically unbound, that is on a parabolic trajectory. A change to a higher β would then naturally lead to a hyperbolic trajectory. Since dust grains change their β value suddenly at collisions, and since the post-collision fragment speed is not going to be very different from the pre-collision parent object speed, the value of $\beta = 1/2$ is often considered the minimum β required for the dust grain to be on an unbound trajectory pointed away from the Sun.

Using our estimate with simplistic assumptions (Eq. 2.20), $\beta > 0.5$ for $r < 1.9\,\mu$m. More refined estimates (Kimura et al., 2003) point to the region of $100\,\text{nm} < r < 1\,\mu$m and are material dependent. We note that if the parent grains are on eccentric orbits, the requirement of $\beta > 0.5$ is not exact, but this does not influence the size estimate greatly. We also note that beta meteoroids are smaller than bound grains with $r > 1\,\mu$m, which seem to contribute to the brightness of the Zodiacal light the most (Leinert et al., 1981). This makes remote observation difficult, and they are therefore, in practice, only reliably detected in-situ.

Dynamics

The beta meteoroids are believed to be created in collisions between bound grains, which naturally happens where the bound dust spatial density and the relative velocities between the grains are high. It was recently reported that the dust detections of PSP are compatible with the beta meteoroid creation region at around $10 - 20\,R_{Sun}$ (Szalay et al., 2021). Since beta meteoroids are unbound, they leave the inner solar system shortly after their creation, and other forces have limited time to act. For example, even relatively short Poynting-Robertson lifetime of $\approx$ *kyr* is unimportant compared to the timescale of $< 1\,$yr, in which a grain created in the vicinity of the Sun passes beyond 1 AU. On their way out, beta meteoroids follow the conservation of angular momentum and the conservation of energy. The former implies that sufficiently far from the region of their creation, their velocity is nearly radial. The latter implies they accelerate if $\beta > 1$, since they feel net solar repulsion,

and they decelerate if $\beta < 1$, since they feel net solar attraction. In the special case of $\beta = 1$, the grains neither accelerate nor decelerate, and their number density sufficiently far from the Sun depends on the heliocentric distance R as

$$n(R) \propto R^{-2}. \tag{3.4}$$

Open questions

One of the open questions related to beta meteoroids is to what extent their flux is constant in time and rotationally symmetric. Answering this question is complicated, since beta meteoroids are only detected in-situ, and there is always a bond between the time and location of the detecting spacecraft. Beta meteoroids were claimed to be produced in collisions between the main, rotationally symmetric bound dust population and the Geminids meteoric stream (Szalay et al., 2021), as a means to explain excess detections with PSP. Further investigation of this phenomenon is desirable.

The dynamics of β-meteoroids is understood theoretically, but there is little experimental evidence about where they are created, their speed, mass distribution, and other parameters, which influence their dynamics. β-meteoroids are important for both PSP and SolO observations. In Paper II of this thesis and using the measurements of SolO, we estimated the speed of β-meteoroids. We found that they decelerate significantly on their way out of the inner solar system, which implies effective mean β near the liberation threshold, that is $\beta \approx 0.5$. We studied the features of individual impacts in Paper III, proposing a better measure for impact-generated charge, enabling a more precise study of the mass distribution of the grains.

3.3 Interstellar dust

We know that dust of various sizes is present in the interstellar medium of our galaxy since it is needed to explain the interstellar extinction measurements (Desert et al., 1990). The heliosphere moves with respect to the local interstellar medium. The relative speed and the direction are known, since the velocity distribution of interstellar neutral gas was measured, for example onboard Ulysses spacecraft (Witte, 2004). It was also with the Ulysses spacecraft, that a population of dust, coming from the direction of the interstellar neutral gas was detected (Grün et al., 1993). Since then, other spacecraft reported interstellar dust (ISD) detections in-situ, such as Galileo (M. Baguhl et al., 1995), Cassini (Altobelli et al., 2003), STEREO (Zaslavsky et al., 2012), and Wind (Malaspina et al., 2014).

Size range and dynamics

ISD is created by condensation and aggregation, and destroyed by sputtering, sublimation, and collisions (Mann, 2010). Only the ISD grains with masses higher than $3 \cdot 10^{-16}$ kg (that is $r \approx 0.3\,\mu$m) are believed to be able to enter the heliosphere (Kimura and Mann, 1998). Upon entry, the grains move according to the laws of gravity and under the influence of Lorentz force. The effective gravitational parameter $\mu_e(\beta)$ (see Eq. 2.18) depends on the amount of radiation pressure compared to gravity. Should $\beta > 1$, the grains are deflected and do not reach close vicinity of the Sun (Henriksen, 2022). If $\beta \approx 1$, they do not feel the influence of the Sun and move with nearly constant speed. The motion of the dust grains is also influenced by the Lorentz force, and this effect is also size dependent (Morfill and Grün, 1979).

Open questions

The exact dynamics of ISD grains in the solar system is an object of study, especially the possible effect of dust *focusing* and *defocusing* to and from the plane of ecliptic due to the polarity of the interplanetary magnetic field, which switches between N-S and S-N configurations with the period of 22 years, that is two solar cycles (Morfill and Grün, 1979). This long period, longer than the duration of many experiments, makes the effect difficult to study. It is however the case that most of the in-situ ISD detections happened around the year 2009, during the solar minimum between solar cycles 23 and 24, when the interplanetary magnetic field was in the focusing configuration (Racković Babić, 2022) and the observed ISD flux decreased significantly, although not disappear completely, since then. Although instrumental explanations remain possible, it was hypothesized that the change in observed flux is physical and that the flux should rise again during the minimum between solar cycles 25 and 26, which is expected in late 2020's (Mann, 2010).

Gravitational focusing of the ISD grains with $\beta < 1$ and an increased spatial density in the inner heliosphere and especially behind the Sun is a logical consequence of their trajectories (Mann, 2010), yet experimental evidence of this is scarce (Altobelli et al., 2006). The low density, the temporal variability, and the difficulty of distinguishing this population from other dust complicates the detection. Neither SolO nor PSP observed clear evidence of ISD.

3.4 Nanodust

Small dust grains are produced in collisions of larger dust. If the created dust grains are so small that $\beta \ll 1$, the radiation pressure does not liberate

them from the gravity well of the Sun. Small grains have, however, a high capacitance to mass ratio C/m, and by extension, high charge to mass ratio q/m. For example, $r = 10\,\mathrm{nm}$ spherical grain at the potential of $\phi = 1\,\mathrm{V}$ has the charge density $q/m \approx 71\,\mathrm{Ckg}^{-1}$ (Eq. 2.24). The defining feature of *nanodust* grains is that they are therefore highly susceptible to be influenced by Lorentz force (Czechowski and Mann, 2010).

As we discussed in Sec. 2.2.5, solar wind pressure provides an additional pseudo-Poynting-Robertson drag, which is usually smaller than radiational Poynting-Robertson drag for larger dust, but is likely very relevant for small dust with $r < 10\,\mathrm{nm}$ (Mukai and Yamamoto, 1982), when even radial solar wind pressure might contest gravity.

Planetary nanodust was also identified in Cassini's Radio and Plasma Wave Science (RPWS) spectra at 1 AU (Schippers et al., 2014), and between 1 AU and 5 AU, and it was concluded, that the asteroid belt's contribution to the nanodust flux is negligible (Schippers et al., 2015). It was also identified in the Jovian system (Meyer-Vernet et al., 2009a), and in the Saturnian system (Kempf et al., 2005). It was in fact concluded that nanodust is so ubiquitous, that some was detected whenever the RPWS instrument was on (Schippers et al., 2015). Cometary nanodust was detected by Giotto/PIA and Vega/PUMA mass spectrometers near the comet Halley, although limited information about their composition was yielded, due to low signal (Utterback and J. Kissel, 1990).

Open questions

Since nanodust grains are highly susceptible to the influence of Lorentz force, a strong temporal variation is naturally expected, as the interplanetary magnetic field is not constant (Poppe and Lee, 2020). The complications are that nanodust is not observed remotely, and observation in-situ is problematic (Pantellini et al., 2012; Kellogg et al., 2016; Kellogg, 2017).

Nanodust was reportedly detected on STEREO spacecraft (Meyer-Vernet et al., 2009b) and mostly disappeared after solar cycle 24 started after 2010 (Zaslavsky et al., 2012). It was argued that this might be due to an unfavorable interplanetary magnetic field orientation during solar cycle 24, and that the nanodust flux will reappear in the STEREO measurements later during solar cycle 25, at some time before 2028 (Poppe and Lee, 2022). The presence of nanodust in the SolO and PSP data remains a possibility. However, the counts can be explained with models without nanodust, therefore, it is a minor contributor for now. This might change later during solar cycle 25.

3.5 Localized dust

Planetary dust

The dust linked to a planet, is called *planetary dust*. The passage of Pioneers 10 and 11 through the Jovian system discovered flux of dust several orders of magnitude higher than the flux commonly observed elsewhere at the same heliocentric distance (Humes et al., 1974). The subsequent study by Ulysses, which measured intermittent dust streams originating in the Jovian system (Grün et al., 1993), and Voyager, which revealed the active volcanism at Io (Krüger et al., 2004), confirmed the Jovian system as a locally important source of dust. Cassini's Cosmic Dust Analyzer (CDA) and RPWS detected nanodust near Jupiter, which was also confirmed to be originating at the moon Io (Meyer-Vernet et al., 2009a). Similarly, in the Saturnian system, Enceladus was linked to the tenuous E-ring of Saturn (Baum et al., 1981). Cassini/CDA data also showed nanodust detections (Kempf et al., 2005) and later confirmed the volcanic activity on Enceladus (Spahn et al., 2006), which feeds the E-ring of Saturn (Kempf et al., 2010).

Inhomogeneity

Unlike the omnipresent gradual erosion, the inflow of new dust into the system is very stochastic and non-constant, as for example comets, which are believed to be an important source of the dust cloud, are not uniformly distributed in time and space. More than half of all the catalogued comets are *sungrazers*, which are comets which have the perihelion in a close vicinity of the Sun (G. H. Jones et al., 2018), at the heliocentric distance of a few solar radii R_{Sun}. These are typically small objects ($r < 100\,\mathrm{m}$) which do not survive the passage but are destroyed near the perihelion by the combination of heat and tidal stress. Their material is then partially transferred to the dust cloud. In general, such highly eccentric comets might arrive from any direction, but a few massive bodies were identified to have been destroyed in the past, which are responsible for most of the identified near-sun comets (G. H. Jones et al., 2018). Among these, the most prominent cometary group is the Kreutz group (Kreutz, 1888), members of which are believed to be descended from a single body, which got fractured into thousands of smaller bodies over several perihelia. The evidence for this is the strong similarity in the orbital elements between the individual Kreutz group comets (G. H. Jones et al., 2018), but the exact origin story of the group is not easily established (Kalinicheva, 2017; Fernández et al., 2021). What is certain is that dust is released from the comets of the group in a spatially highly non-uniform way.

Meteor is a visual phenomenon accompanying the entry of a sufficiently massive dust grain in the Earth's atmosphere. Over a 100 distinct meteor showers were identified and confirmed to this day (Jenniskens et al., 2020), which well document the spatial inhomogeneity of the dust in the solar system. The number of observed meteors, which belong to shower, is comparable to the number of meteors which do not (Jenniskens et al., 2016).

Meteors are caused by comparably large grains of $r \gtrsim$ mm and these are very rare among in situ detections, which are dominated by $r \lesssim \mu$m grains. These massive and sparse grains however produce smaller grains at collisions, which may be much more frequent where the meteor stream crosses a dense solar system dust cloud, and this may cause inhomogeneity even in the flux of smaller dust. This effect was proposed as an explanation for the post-perihelion enhancement of flux detected by PSP (Szalay et al., 2021).

Open questions

The model, which we used to explain the dust flux measured with SolO (Paper II), assumed a symmetric and homogeneous dust cloud. This assumption might be checked statistically, for example by looking for unexplained variance in the dust counts. One uncomplicated way of doing such analysis is comparing the posterior predictive distribution to the data, as we briefly did in Paper II, finding that the used model was appropriate, and that no major contributor to the flux was overlooked.

4 | Poisson rates

Dust impacts happen randomly, and are uncorrelated with each other, fulfilling the definition of Poisson point process (PPP). Since detections might be relatively rare, the fitting routine must be chosen and carried out carefully to yield the available information. Several approaches are commonly taken and in this chapter, the most important and commonly used ones are introduced, demonstrated and practically compared. As we will see, not all of the common algorithms are always appropriate. Notably, the least squares fitting is problematic for Poisson process, and more appropriate algorithms are introduced in this chapter.

4.1 Poisson point process

The defining feature of PPP is that it consists of points $\vec{\omega}$ located randomly and independently of each other in the mathematical space of interest Ω. This space might be the physical space Ω_{3D} with the process modelling locations of events, or Ω might be the timeline Ω_{time}, and then PPP models *when* events happen. In the case of in-situ detection of cosmic dust, the space is the physical space Ω_{3D}, but since the location of the spacecraft is implicitly bound with time through its trajectory, the problem is usually solved on the timeline Ω_{time}.

Let A be a subset of Ω. A feature of PPP is that the number of points N within A is a random variable, which follows the *Poisson distribution* with the probability mass function:

$$P(N = n) = \mathrm{Pois}(n, \Lambda) \equiv \frac{\Lambda^n e^{-\Lambda}}{n!}, \tag{4.1}$$

where $\Lambda = \mathbb{E}(N)$ is the expected value of N. In the special case of *homogeneous* PPP, Λ is proportional to the *measure* μ of A in Ω with the scaling factor of λ:

$$\Lambda = \lambda\mu(A), \tag{4.2}$$

where λ is called the *rate*. In the general case of PPP, λ is a non-negative function of the location ω in Ω:

$$\lambda = \lambda(\omega) \geq 0;\ \omega \in \Omega, \tag{4.3}$$

and then

$$\Lambda = \int_A \lambda(\omega)\, d\mu. \tag{4.4}$$

In the special case of Ω being the timeline Ω_{time}, and A being the interval of observation between the times t_{start} and t_{stop}, we have

$$\Lambda = \int_{t_{start}}^{t_{stop}} \lambda(t)\, dt. \tag{4.5}$$

This is an appropriate model for the number of dust detections N detected over a temporal interval (t_{start}, t_{stop}).

4.2 Maximum likelihood estimation

Assume the following experimental scheme: let *data* $\vec{x} = (x_1, x_2, \ldots, x_k)$ be the *realizations* of a random variable X, and let the parametric probability density function (also called the *family*) of the process f_X be known, with the *parameters* $\vec{\theta}$ being unknown:

$$f_X = f_X(x_i|\vec{\theta}). \tag{4.6}$$

This means that in a repeated experiment, and given the parameters $\vec{\theta}$, a value x_i is acquired with the frequency proportional to $f_X(x_i|\vec{\theta})$. The usual goal is to find the underlying $\vec{\theta}$, which is the most compatible with the experiment results $\vec{x}$. *Likelihood* $\mathcal{L} = \mathcal{L}(\vec{\theta})$ is a function of $\vec{\theta}$ defined as

$$\mathcal{L}(\vec{\theta}|x_i) = f_X(x_i|\vec{\theta}) \tag{4.7}$$

in the case of a single data point x_i, where $|x_i$ means the single data point x_i is used to evaluate the likelihood. The intuitive meaning of likelihood is how well the $\vec{\theta}$ corresponds to the observed data point x_i. Since observing x_i is more probable for $\vec{\theta}_1$ with high $\mathcal{L}(\vec{\theta}_1|x_i)$ than for $\vec{\theta}_2$ with low $\mathcal{L}(\vec{\theta}_2|x_i)$, one might say that $\vec{\theta}_1$ is more likely than $\vec{\theta}_2$, given x_i was observed. We note that $\mathcal{L}$ is not a probability distribution, since it is a function of $\vec{\theta}$ rather than $\vec{x}$. Furthermore, it is generally not normalized, or even integrable. Should the random vector $\vec{x}$ contain k realizations of an independent random variable, the likelihood of $\vec{\theta}$ given $\vec{x}$ is

$$\mathcal{L}(\vec{\theta}|\vec{x}) = \prod_{i=1}^{k} f_X(x_i|\vec{\theta}), \tag{4.8}$$

where $\mathcal{L}$ retains all the properties discussed earlier. Then maximum likelihood estimation is the method of finding $\vec{\theta}_{max}$, which maximizes $\mathcal{L}$ in the space Θ of possible $\vec{\theta}$. Such a $\vec{\theta}_{max}$ is called the *maximum likelihood estimate* (MLE). We note that the same $\vec{\theta}_{max}$ maximizes $\mathcal{L}(\vec{\theta}|\vec{x})$ and $l(\vec{\theta}|\vec{x}) = \log\Big(\mathcal{L}(\vec{\theta}|\vec{x})\Big)$. Since

$$l(\vec{\theta}|\vec{x}) = \log\Big(\mathcal{L}(\vec{\theta}|\vec{x})\Big) = \log\left(\prod_{i=1}^{k} f_X(x_i|\vec{\theta})\right) = \sum_{i=1}^{k} \log\Big(f_X(x_i|\vec{\theta})\Big), \tag{4.9}$$

the MLE is also found by maximizing l, so called *log-likelihood*, which is often computationally much cheaper.

In the special case of f_X being the Poisson probability mass function (Eq. 4.1), there is a single parameter Λ to maximize $\mathcal{L}$ with. Having observed k realizations (data points) $\vec{n} = (n_1, n_2, \ldots, n_k)$, the log-likelihood of Λ is

$$l(\Lambda|\vec{n}) = \sum_{i=1}^{k} \log\left(\frac{\Lambda^{n_k} e^{-\Lambda}}{n_k!}\right) = \log(\Lambda)\sum_{i=1}^{k} n_k - k\Lambda - \sum_{i=1}^{k} \log(n_k!), \tag{4.10}$$

where $\log(n!)$ is easily evaluated for small n and can be cost-effectively very closely approximated for large n, using for example Ramanujan's approximation (Ramanujan, 1920).

It is also possible that the rate Λ was not constant during the data acquisition, but changed with time t as

$$\Lambda = \Lambda(t, \vec{\xi}), \tag{4.11}$$

that is Λ was a parametric function of time t with unknown parameters $\vec{\xi}$. If the family f_X is known, as is the parametric function Λ, but not the parameters $\vec{\xi}$, this might be solved the same way, that is with maximizing (now more complicated) likelihood $\mathcal{L}$, or log-likelihood $l = \log(\mathcal{L})$.

4.3 Least squares estimation

Assume experimental data $\vec{x}$ and unknown parameters vector $\vec{\theta}$. In addition, let us assume that x_i of $\vec{x}$ are not independently distributed, but each x_i has its own distribution function family f_{X_i}, which might for example represent a time dependent experiment, such as the one in Eq. 4.11. Assuming a value for the parameters vector $\vec{\theta}$, a vector of expected values of $\vec{\tilde{x}}(\vec{\theta}) = (\mathbb{E}(X_1|\vec{\theta}), \mathbb{E}(X_2|\vec{\theta}), \ldots, \mathbb{E}(X_k|\vec{\theta}))$ is calculated. We evaluate S:

$$S(\vec{\theta}) = ||\vec{x} - \vec{\tilde{x}}(\vec{\theta})||_2 = \sum_{i=1}^{k} \Big(x_i - \mathbb{E}(X_i|\vec{\theta})\Big)^2. \tag{4.12}$$

If the parameter vector $\vec{\theta}$ minimizes S in the space of possible parameter vectors Θ, then $\vec{\theta}$ is called the *least squares estimate* (LSE). Weighted least squares estimate (WLSE) is a modification of LSE, in which the weights w_i are introduced in Eq. 4.12:

$$S_w(\vec{\theta}) = \sum_{i=1}^{k} \left(w_i \left(x_i - \mathbb{E}(X_i|\vec{\theta}) \right) \right)^2, \tag{4.13}$$

where the estimate is improved if the weights are the reciprocal standard deviations for each of the data points $w_i = \sigma^{-1}$. Finding the LSE is often computationally much cheaper than finding the MLE as described in Sec. 4.2, and in some special cases, they are equivalent. However, LSE is just a mathematical optimization algorithm, which disregards the distribution of the data, and in general is not equivalent to MLE.

4.3.1 Maximum likelihood equivalence

Assume:

$$f_{X_i}(x_i|\vec{\theta}) = \mathcal{N}(\mathbb{E}(X_i|\vec{\theta}), \sigma) = \frac{1}{\sqrt{2\pi}\sigma} e^{-\left(\frac{x_i - \mathbb{E}(X_i|\vec{\theta})}{\sqrt{2}\sigma}\right)^2}, \tag{4.14}$$

that is, the value observed in a repeated experiment is *normally distributed* around its expected value, or in other words, the errors $\epsilon_i = x_i - \mathbb{E}(X_i|\vec{\theta})$ are *Gaussian*. If independence of ϵ_i is assumed, then we get for log-likelihood:

$$\begin{aligned} l(\vec{\theta}|\vec{x}) &= \sum_{i=1}^{k} \log \left(f_{X_i}(x_i|\vec{\theta}) \right) \\ &= \sum_{i=1}^{k} \log \left(\frac{1}{\sqrt{2\pi}\sigma} e^{-\left(\frac{x_i - \mathbb{E}(X_i|\vec{\theta})}{\sqrt{2}\sigma}\right)^2} \right) \\ &= k \log \left(\frac{1}{\sqrt{2\pi}\sigma} \right) - \frac{1}{2\sigma^2} \sum_{i=1}^{k} \left(x_i - \mathbb{E}(X_i|\vec{\theta}) \right)^2 \\ &= k \log \left(\frac{1}{\sqrt{2\pi}\sigma} \right) - \frac{S}{2\sigma^2}, \end{aligned} \tag{4.15}$$

therefore by minimizing S, we maximized l (compare Eqs. 4.12 and 4.15). We note we assumed a single standard deviation σ for all the x_i, which might be generalized to individual σ_i by weighting in the sum (Eq. 4.13). This can further be generalized for the case of regular exponential family distributions (Charnes et al., 1976), therefore also for Poisson distribution. In any case, we either evaluate or approximate MLE with LSE, which offers no advantages over the straight evaluation of MLE beyond the computational cost.

4.3.2 Linear combination fitting

A common experimental task is to explain an observed variable count as an unknown combination of known effects, which combine into a rate. Let us have data $\vec{n} = (n_1, n_2, \ldots, n_k)$, and assume

$$f_{N_i}(n_i) = \mathrm{Pois}(n_i, \Lambda_i) = \mathrm{Pois}(n_i, \beta_1\lambda_{1,i} + \beta_2\lambda_{2,i} + \cdots + \beta_m\lambda_{m,i}), \tag{4.16}$$

where unknown Λ_i was not a constant for all i, but was a single unknown linear combination $\vec{\beta} = (\beta_1, \beta_2, \ldots, \beta_m)$; $\beta_i \geq 0\ \forall i$ of known non-constant effects $\lambda_{1,i}, \lambda_{2,i}, \ldots, \lambda_{m,i}$. This task is best approached keeping Poisson family in mind, which is not the case when a simple LSE of $\vec{\beta}$ is evaluated, which we show on an example.

Comparing MLE and LSE for real experimental data is not very instructive, since the true process is never really known. For this reason, we use a toy model. Let us examine a fit of such a toy model, which retains the most important characteristics of dust detection rate fitting. Assume we have observations $\vec{n}$ of a Poisson-distributed random variable defined as

$$f_{N_i}(n_i) = \mathrm{Pois}(n_i, \Lambda_i) = \mathrm{Pois}(n_i, \beta_1 y_i + \beta_2 y_i^5), \tag{4.17}$$

where y_i are the values of the independent variable, so called *covariate*, which produced the actual rates Λ_i according to

$$\Lambda_i = \beta_1 y_i + \beta_2 y_i^5, \tag{4.18}$$

which is a linear combination of two polynomial terms. Let's further assume the actual values of $\vec{\beta} = (\beta_1, \beta_2)$ are

$$\begin{aligned} \beta_1 &= 1 \\ \beta_2 &= 3, \end{aligned} \tag{4.19}$$

and that we have a set $\vec{n}$ of 150 observations of n_i, which were drawn according to Eq. 4.17 with different covariates $y_i \in (0, 2)$. One such a draw is shown in Fig. 4.1.

Having run the experiment, one might attempt to estimate the underlying parameters $\vec{\beta}$, knowing the model family (Eq. 4.17), but not the true values of the parameters (Eq. 4.19). In this case, both MLE and LSE estimate the values reasonably, and both are even (as empirically observed) asymptotically unbiased, but they are not equivalent and show a very different accuracy, as a repeated experiment shows. Averaging 500 independent runs, the mean L^2 distance between the estimate of $\vec{\beta}$ and the correct $\vec{\beta}$ is ≈ 0.48 in case of LSE and ≈ 0.22 in case of the proper MLE, which is shown in Fig. 4.2. We

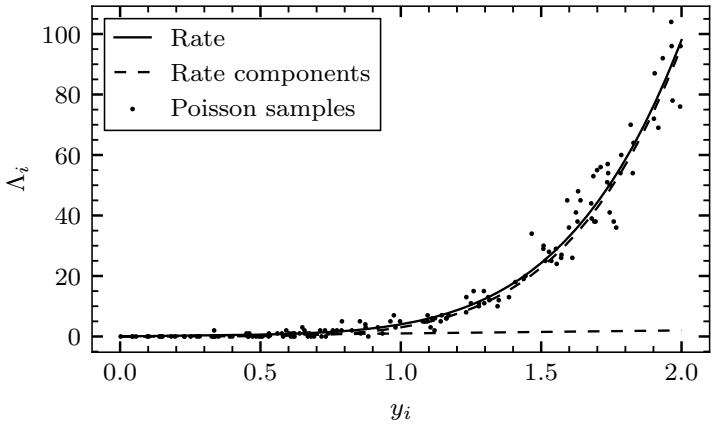

Figure 4.1: A possible realization of the experiment defined by Eqs. 4.17 - 4.19.

clearly observe a higher negative correlation for LSE (≈ -0.78) than for MLE (≈ -0.46). A correlated estimates might indicate an inappropriate model, but in this case rather indicate a difficult model and (in case of LSE) an inappropriate fitting procedure.

We note that the presented fitting task is really relatively difficult, since majority of detections come from high y_i, where the component $\propto y_i^5$ is very dominant compared to the component $\propto y_i$, and it is easily seen in Fig. 4.2 that it is the β_1, which is estimated by LSE much more poorly than by MLE. The information is however still there, since for low y_i, it is β_1, which is important. It turns out that LSE is too crude to yield the information fully. We note that it is often the case in practice, that Poisson distributed data is fitted WLSE, assuming $\sigma_i = \sqrt{n_i}$ weights. This places more emphasis on the lower values, but is only appropriate for the values of n_i high enough, so that $\sqrt{n_i} \ll n_i$, since $\sigma = \sqrt{\mu}$ for Poisson distribution, see Fig. 4.3. This is quite incorrect for low values, and not viable at all for $n_i = 0$, as such a weighting would incorrectly assume that all zeroes must have come out as a result of the rate $\Lambda = 0$, which is clearly not true, as seen in Fig. 4.3. Sometimes weighting with $\sqrt{n_i + 1}$ is used, in which $+1$ is a rather arbitrary constant, and which is still not correct, and in our specific case is not even an unbiased estimate, as is demonstrated in Fig. 4.4.

Lastly, we note that the presented toy model shares some characteristics with dust flux fitting. The linear combination of several components as in Eq. 4.16 is often assumed (Szalay et al., 2021; Zaslavsky et al., 2012), as we also did in Paper II. The dust detection rate with spacecraft also often changes

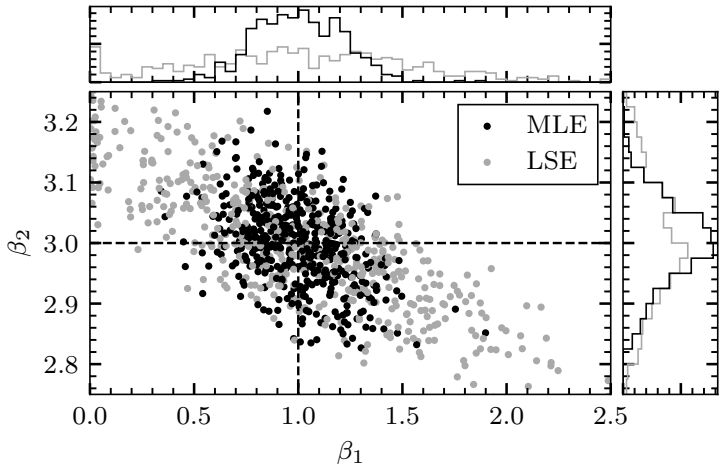

Figure 4.2: A repeated experiment followed by MLE and LSE estimation of the parameters $\beta_1; \beta_2$, the experiment as defined by Eqs. 4.17 - 4.19. The dashed lines show the true value of $\vec{\beta}$. The histograms of estimated β_1 and β_2 are shown in the x-axis and y-axis histograms respectively.

over several orders of magnitude, and is much lower if certain components are dominant, which might, similar to the presented example, lead to a bias, if not treated carefully.

4.4 Bayesian statistics

Probability is a complicated epistemological concept. Intuitively understood, probability becomes difficult, if confronted with other related concepts, such as causality, knowledge, or choice. In Bayesian statistics, unknown parameters are regarded as random variables, with their probability distribution representing the state of knowledge or belief about them, and with data being used to improve the level of this knowledge. An event A is regarded as having high probability, if it is reasonable to expect that the event A happens. This is put in contrast with so-called frequentist interpretation of probability, in which probability is regarded as the long-term average frequency of the event A happening under the same circumstances, as the unknown parameters are treated as free, but not random variables. This doesn't make a difference in many practical applications, but the formulation of statistical task might be different. A typical frequentist task is to assess the most likely value (MLE) of an unknown (but certain) parameter, given what evidence was observed.

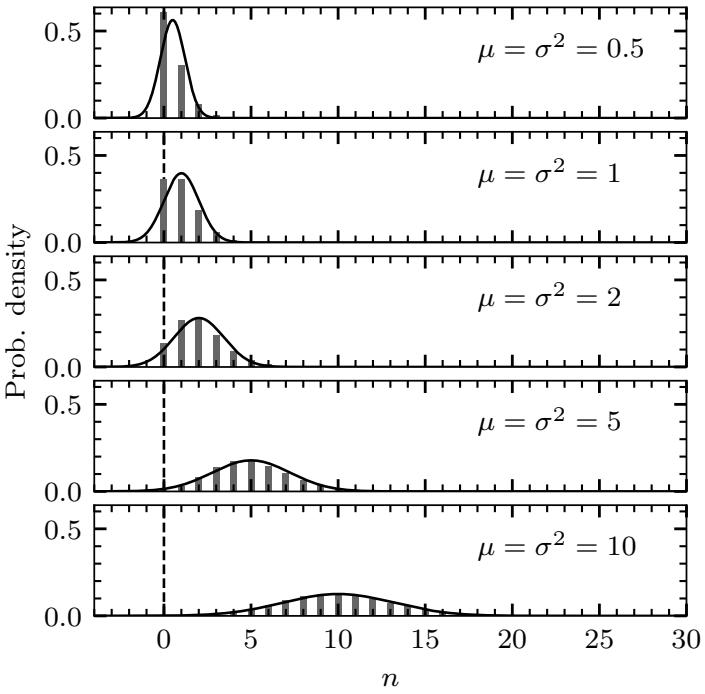

Figure 4.3: A comparison of Poisson (bars) and normal (solid line) distributions with identical mean μ and standard deviation σ.

If more data is considered, the most likely value might change. In a typical Bayesian task, a probability density of the value of the unknown parameter is inferred, approaching the unknown parameter as a random variable. If more data is added, knowledge gets better, and the probability distribution becomes narrower.

4.4.1 Bayes theorem

Bayes theorem stems from the axiom of probability:

$$P(A \cap B) = P(A|B)P(B) = P(B|A)P(A), \tag{4.20}$$

which states that the probability of events A and B occurring together is the same as the product of probabilities of one of them occurring, given the other one does times the other one occurring.

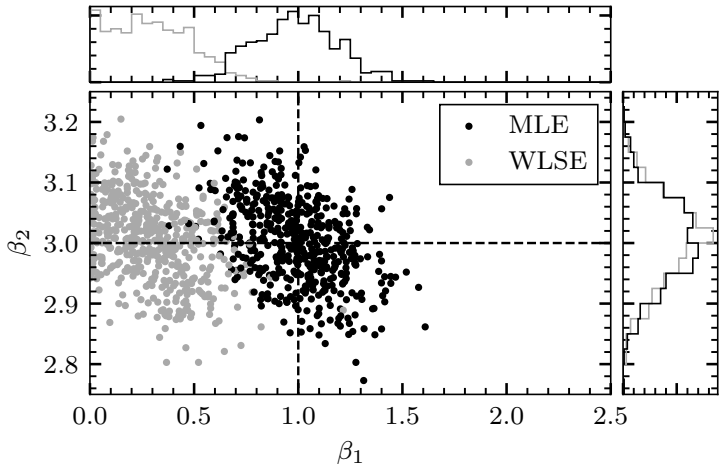

Figure 4.4: A repeated experiment followed by MLE and WLSE estimation of the parameters $\beta_1; \beta_2$, the experiment as defined by Eqs. 4.17 - 4.19. The weights in WLSE are $w_i = (1+n)^{-0.5}$, and the WLSE is in this case not an unbiased estimate, since too much weight is put on the $n_i = 0$ data points. However, we observe that the estimation of β_2 is not burdened by this, as the WLSE points show even less variance in β_2, compared to LSE estimates in Fig. 4.2.

The Bayes theorem (Bayes, 1763) in its modern form states:

$$P(A|B) = \frac{P(B|A)P(A)}{P(B)}, \tag{4.21}$$

whenever $P(B) \neq 0$. This equation is instrumental to many statistical problems, such as evaluating blinded experiments, commonly used in medicine and other sciences. It also builds the basis for Bayesian inference.

4.4.2 Bayesian inference

Assume a model family f_X is known, as well as the data $\vec{x}$, which are realizations of the random variable X. Similarly to Sec. 4.2, we are interested in the parameters $\vec{\theta}$. With MLE in Sec. 4.2, the goal was to find the *single value* $\vec{\theta}$, which fits the data best, that is $\vec{\theta}$ with the highest likelihood. However, MLE does not by itself provide any measure of uncertainty.

Bayesian estimation needs a *prior distribution* of $\vec{\theta}$, denoted $\pi(\vec{\theta})$ to be defined in addition to the model family f_X and the data $\vec{x}$. This distribution

represents our *prior belief* in the value of $\vec{\theta}$ before the data $\vec{x}$ are examined. Described mathematically, we assume that $\vec{\theta}$ is a random variable with the value in the space Θ coming from the prior distribution $\pi(\vec{\theta})$; $\vec{\theta} \in \Theta$. Without the actual realization of $\vec{\theta}$ being known, this $\vec{\theta}$ plays the role of a parameter in $f_X(x|\vec{\theta})$, which generates the sample of data $\vec{x}$, which is observed. Based on the value of $\vec{x}$, which was observed, the belief in $\vec{\theta}$, represented by π, changes. The goal is to obtain $\pi(\vec{\theta}|\vec{x})$, which not only provides the most compatible value of $\vec{\theta}$, but also a measure of uncertainty.

The desired posterior distribution $\pi(\vec{\theta}|\vec{x})$ is evaluated using the Bayes theorem (Eq. 4.21):

$$\pi(\vec{\theta}|\vec{x}) = \frac{p(\vec{x}|\vec{\theta})\pi(\vec{\theta})}{p(\vec{x})} = \frac{\mathcal{L}(\vec{\theta}|\vec{x})\pi(\vec{\theta})}{p(\vec{x})} \propto \mathcal{L}(\vec{\theta}|\vec{x})\pi(\vec{\theta}), \tag{4.22}$$

where the equality becomes proportionality for practical reasons: it is often difficult to evaluate the normalization factor $p(\vec{x})$, and if, for example, a sampling procedure is used to evaluate the right hand side, the result is automatically normalized.

For demonstration purposes, we apply Bayesian inference on the problem defined by Eqs. 4.17 – 4.19. We use identical and independent priors for β_1 and β_2:

$$\pi(\beta_i) = \sqrt{\frac{2}{\pi}} e^{\left(-\frac{\beta_i^2}{2}\right)} \mathbb{1}_{\mathbb{R}^+}, \tag{4.23}$$

that is standard normal distribution for positive numbers, and zero elsewhere. We draw 150 numbers y_i from uniform distribution between zero and two, as before. For each y_i we draw n_i according to Eq. 4.17. In Fig. 4.5 we show the MLE, LSE, and Bayesian results compared. Unlike in Fig. 4.2, the experiment is done only once, therefore yielding only one MLE and one LSE estimate. In principle, Bayesian inference solves a different task, compared to MLE. The Bayesian posterior is not a point, but a multivariate distribution function, which, unlike the other two estimates, shows a measure of uncertainty. The prior is consequential for Bayesian inference. However, the prior becomes less important as the number of data points increases. If data is plentiful and the support of the prior covers the MLE estimate, the maximum of Bayesian posterior (called *maximum a posteriori*, or MAP) is in practice equivalent to the MLE estimate, as is demonstrated in Fig. 4.5, where the relatively broad prior does not influence the posterior much, compared to the 150 data points. We showed the result of a repeated experiment in Fig. 4.2. The Bayesian posterior changes in a repeated experiment, with the actual values of $(\beta_1, \beta_2) = (1, 3)$ likely being covered by the posterior. Increasing the number of data points beyond 150 will then make the posterior more localized with the MAP closer to

the point $(1, 3)$. To demonstrate this, we use the same procedure to obtain the posterior distribution for β_1 and β_2, but using a gradually increasing number of points y_i and corresponding n_i. We show the maxima of the posterior marginal distributions and symmetric 90 % credible intervals as functions of the number of drawn data points n_i. This is shown in Fig. 4.6.

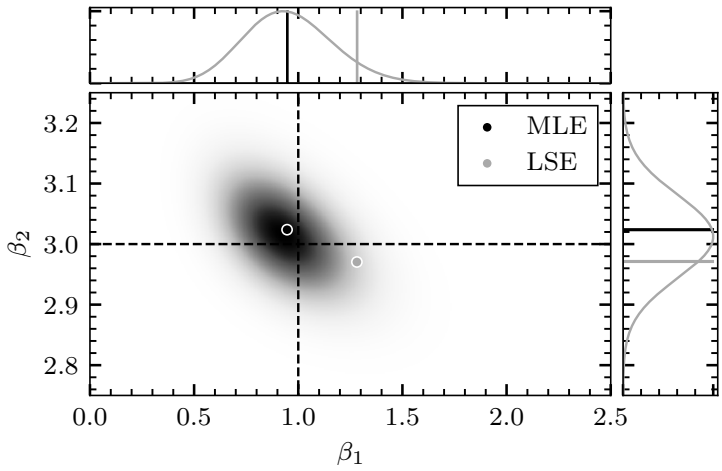

Figure 4.5: A comparison of the Bayesian estimate and the points estimates MLE and LSE, including 150 data points. β_1 and β_2 marginal posteriors are shown in the top and in the right panel, with the lines showing the MLE and LSE estimates.

4.4.3 Computational methods

Conjugate priors In special cases, the task of inferring the posterior distributions of the unknown parameters might be approachable analytically, through so-called *conjugate priors*. The strongest requirement is that the prior and the likelihood are of certain families, for which analytical solutions were found. Many useful family combinations were described (Fink, 1997), as before the boom in computational power, this was the most practical way of doing Bayesian inference. All other methods described in further paragraphs of this section are numerical, that is, approximate.

Grid evaluation The most straight-forward way of finding the approximate posterior $\pi(\vec{\theta}|\vec{x})$ is to define a grid in Θ and to evaluate the product of the likelihood and the prior (Eq. 4.22) in all the grid points. To maintain a good resolution, the number of grid points scales with the power equal to the dimension,

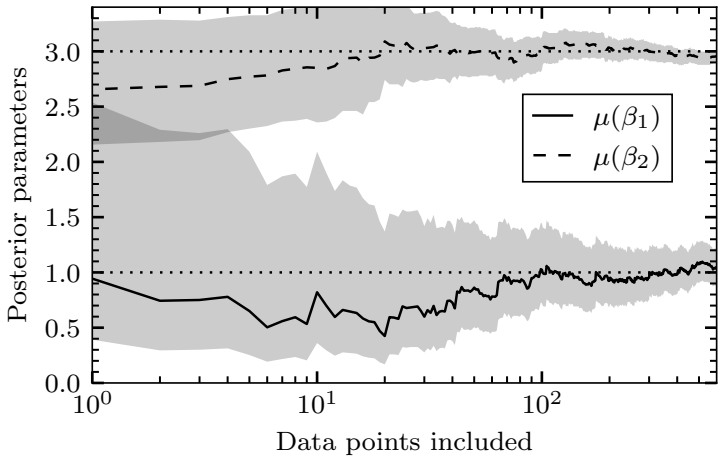

Figure 4.6: A repeated experiment followed by Bayesian inference of the parameters $\beta_1; \beta_2$, the experiment as defined by Eqs. 4.17 - 4.19. $\mu(\cdot)$ denotes the posterior mean. The shaded regions show symmetric 90 % credible intervals. The priors prefer values lower than the actual $\beta_1 = 1$; $\beta_2 = 3$ but are broad and play a small role once many data points are included. We note that β_2 is much better constrained, compared to β_1.

hence, this approach easily becomes memory and time intensive. Furthermore, normalization might be difficult, and the choice of grid points can be non-trivial. Many of these disadvantages are abated if a sampling method is used instead.

Markov chain Monte Carlo The posterior $\pi(\vec{\theta}|\vec{x})$ can be approximately reconstructed and many of its features are available easily, if a sample of values θ drawn from $\pi(\vec{\theta}|\vec{x})$ is available. This is the idea of Markov chain Monte Carlo (MCMC) Bayesian inference. The discrete Markov chain is a stochastic process, in which the current state is a random value, probability of which is governed by the preceding value (Markov, 1906), forming a random walk. If the conditions of the Markov chain central limit theorem are met (G. L. Jones, 2004), this walk reaches a stationary state, in which the elements are distributed as if they were coming from a distribution. Using the right Markov chain, it is possible to draw a sample from any probability density function. The common methods of constructing the appropriate Markov chain include *Metropolis-Hastings* (M-H) algorithm, (Metropolis et al., 1953; Hastings, 1970), *Gibbs sampling* (S. Geman and D. Geman, 1984), and *slice sampling* (Damlen et al., 1999). These all have different strengths, and their computa-

tional efficiency varies based on the problem at hand, but in higher dimensions, with a more complicated model, or a big data set, they are computationally expensive. Their common disadvantage is that, since the samples form a Markov chain, the subsequent values are correlated. This usually does not pose an issue but must be kept in mind and handled carefully. MCMC remains popular, since it is very versatile and allows for evaluating virtually any Bayesian inference problem. Further introduction into MCMC is available in literature (Brooks et al., 2011).

Integrated nested Laplace approximation Since MCMC is very versatile, but computationally expensive, and conjugate priors can only be used on a narrow class of problems, a method is needed which would be fairly generally useful, but computationally efficient. Integrated nested Laplace approximation (INLA) is one such method (Rue et al., 2009; Martins et al., 2013), as it avoids sampling the posterior distribution, and rather approximates the posterior distributions analytically. It allows for fitting two-level, hierarchical models. On the lower-level, the parameters for the higher-level distributions are contained. These lower-level parameters are called *hyperparameters*, and they are random variables with priors called *hyperpriors*, which are defined explicitly. On this lower-level, the hyperparameters are used to construct the higher-level parameters, called *latent parameters*, which are used in the higher-level distribution functions of the observed data. This hierarchical setup is very convenient in spatio-temporal modelling, where the data is often grouped in some way, as some of the data points are close to each other, either in location or in time. It poses some limitations:

- hyperparameters are assumed independent,
- the number of hyper-parameters n needs to be relatively low, that is $n \lesssim 10$,
- due to the use of Laplace approximations, the model must be *latent Gaussian*, which means that the latent parameter vector is assumed to come from a multivariate Gaussian distribution.

Considering the hierarchical form of INLA with observations $\vec{x}$, latent effects $\vec{z}$ and hyperparameters $\vec{\theta}$, and sticking with the notations of probability rather than likelihood, Eq. 4.22 has the form (Gómez-Rubio, 2020):

$$\pi(\vec{z}, \vec{\theta}|\vec{x}) \propto p(\vec{x}|\vec{z}, \vec{\theta}) p(\vec{z}|\vec{\theta}) \pi(\vec{\theta}). \tag{4.24}$$

Assuming the independence of data $\vec{x}$ given $\vec{z}$ and $\vec{\theta}$, we get

$$p(\vec{x}|\vec{z},\vec{\theta}) \propto \prod_{i=1}^{k} p(x_i|y_i,\vec{\theta}), \tag{4.25}$$

and since the latent parameter vector $\vec{z}$ comes from the multivariate Gaussian distribution, we have

$$p(\vec{z}|\vec{\theta}) = |\overleftrightarrow{Q}(\vec{\theta})|^{\frac{1}{2}} e^{-\frac{1}{2}\vec{z}^T \overleftrightarrow{Q}(\vec{\theta})\vec{z}}, \tag{4.26}$$

where $\overleftrightarrow{Q}(\vec{\theta})$ is the precision matrix of the latent multivariate Gaussian distribution. Now by moving the product to the exponent, we get

$$\pi(\vec{z},\vec{\theta}|\vec{x}) \propto |\overleftrightarrow{Q}(\vec{\theta})|^{\frac{1}{2}} e^{\left(-\frac{1}{2}\vec{z}^T \overleftrightarrow{Q}(\vec{\theta})\vec{z} + \sum_{i=1}^{k} \ln p(x_i|y_i,\vec{\theta})\right)} \pi(\vec{\theta}). \tag{4.27}$$

The goal of INLA is to obtain the posterior marginals of the unknown hyperparameters and the latent parameters. For the marginal of each of the hyperparameters in $\vec{\theta}$ we get by definition

$$\pi(\theta_j|\vec{x}) = \int_{\mathbb{R}^{n-1}} \pi(\vec{\theta}|\vec{x})\, d\vec{\theta}_{-j}, \tag{4.28}$$

where $\vec{\theta}_{-j}$ stands for the vector of all hyperparameters except for θ_j. Similarly for the latent parameters $\vec{z}$ we have

$$\pi(z_i|\vec{x}) = \int_{\mathbb{R}^n} \pi(z_i|\vec{\theta},\vec{x})\pi(\vec{\theta}|\vec{x})\, d\vec{\theta}. \tag{4.29}$$

The previous equation is solved approximately on a finite grid of M hyperparameter values $\vec{\theta}_m$:

$$\tilde{\pi}(z_i|\vec{x}) = \sum_{m=1}^{M} \tilde{\pi}(z_i|\vec{\theta}_m,\vec{x})\tilde{\pi}(\vec{\theta}_m|\vec{x})\Delta_m, \tag{4.30}$$

where $\tilde{\pi}$ is an approximation of the probability function π and $\tilde{\pi}(z_i|\vec{\theta}_m,\vec{x})$ is approximated, for example with Laplace approximation. To evaluate both integrals, an approximation $\tilde{\pi}(\vec{\theta}|\vec{x})$ is needed. This is done as

$$\tilde{\pi}(\vec{\theta}|\vec{x}) \propto \frac{\pi(\vec{x}|\vec{z},\vec{\theta})\pi(\vec{z}|\vec{\theta})\pi(\vec{\theta})}{\tilde{\pi}_G(\vec{z}|\vec{\theta},\vec{x})}\Big|_{x=x^*}, \tag{4.31}$$

where $\tilde{\pi}_G(\vec{z}|\vec{\theta},\vec{x})$ is a Gaussian approximation, which is justified, since the latent effects $\vec{z}$ are Gaussian. The INLA toolbox is available as a library R-INLA (R-INLA, n.d.) and allows for convenient use via a function call, including options for many popular hyperpriors, latent random effects, different approximations of $\tilde{\pi}(z_i|\vec{\theta},\vec{x})$, and a lot of freedom for special purposes. Both the background and a practical user guide for R-INLA is offered in the book by Gómez-Rubio (2020). To use R-INLA in a simple Poisson case, such as in the toy model defined by Eqs. 4.17 – 4.19, a vector of measured counts is needed, in addition to a vector of covariates of the same length, which would be the y_i and y_i^5 values in this specific case. In Paper II. of this thesis, we used INLA to fit dust rates observed by SolO in a similar setup, where the higher-level was degenerate, and only the hyperparameters were used in a nonlinear rate-defining model, making use of INLA's speed, although not utilizing its spatial modelling potential.

4.4.4 The importance of prior

The prior distribution $\pi(\vec{\theta})$ represents the prior belief about the value of $\vec{\theta}$ and it might be based for example on previous estimations, personal preference, community consensus, or computational convenience, and each of these choices might lead to a different result and implies a different meaning of the result. This is why the necessity of prior is often regarded as a disadvantage of the Bayesian approach. On the other hand, inclusion of the prior makes the process more transparent. A non-Bayesian parameter estimation is often followed by a discussion comparing the result with previous estimates and discussing the limits of applicability. Alternatively, the result might not get published, if it doesn't match the expectations. The expectations and other constraints could be transparently included in the form of a prior.

Non-informative prior A flat prior ($\pi = const.$) is often used and assumed to be a neutral starting point. In such a case, the likelihood is effectively treated as being the posterior distribution, except for the normalization prefactor. Although the flat prior can be a legitimate choice, it is important to appreciate that any prior choice is a choice, and there is no prior without assumptions. Flat prior implies that all the possible values of the inferred parameter are equally possible and expected, which is untruth more often than not. Furthermore, depending on the model, domain, data, coordinates, and the transformation used, flat prior might not be the least informative (Lemoine, 2019).

Another aspect of flat priors is that a flat prior over $\mathbb{R}$ is not a valid probability density function. Therefore, a flat prior over a great finite range is often

used, with zero probability elsewhere. Depending on the numerical method, an *improper prior* might be used, which is a non-integrable prior, provided that the likelihood factor $\mathcal{L}(\vec{\theta}|\vec{x})$ ensures the integrability of the results. The interpretation of such a result is complicated, as the assumptions of the Bayes theorem are not met.

Conversely, the likelihood factor might be non-integrable, which is not an issue, if both the prior and the posterior are. This is often the case when a single data point is used to get the posterior. In such a case, the choice of prior is very consequential. Generally speaking, the importance of prior is the lower, the more data points are used to construct the likelihood.

Informative prior Using a non-flat, *weakly informative* prior might be numerically beneficial by ensuring integrability of the posterior. Also, extrema are relatively rare in higher dimension. For a stationary point to be an extremum rather than a saddle point, the sign of the second derivative must be the same in all the dimensions, which is automatically satisfied in one dimension, but rarely satisfied in high dimensions. Multiplying the likelihood with an appropriate (weakly informative) prior might make this problem numerically a lot easier.

Existing knowledge might be leveraged, when constructing a prior. We then speak of *informative* prior, as it holds a non-trivial information. Such a prior must be backed by theory rather than to be constructed based on the inspection of the available data, otherwise the same information is harnessed twice. These are especially useful if only a few data points are available. In Paper II, we used moderately informative priors. We could do so, since the unknown parameters were constrained by previous results of other authors and by physics, as not all the values were physically meaningful.

5 | Dust detection

The presence of dust in space was hypothesized long ago by Cassini (1685) as an explanation for the faint light on the night sky near the plane of ecliptic, the zodiacal light. Dust was also observed locally, that is *in-situ*, by its interaction with spacecraft since the dawn of the space age, when the concern about the risk it posed to the spacecraft was present (Whipple, 1958). This chapter provides an introduction into dust detection methods in general, and into antenna detected impact ionization in particular, since it is vital for the rest of the present work.

5.1 Remote observations

Since dust grains in space absorb light, they are observed by extinction of light, (Desert et al., 1990) allowing for transmission spectroscopy, which is useful on the galactic scale (Mann, 2010). In terms of the solar system, refraction, reflection, and thermal emission by dust is important, since it shows the spatial distribution and size distribution of dust in the zodiacal cloud (Allen, 1946; Van de Hulst, 1947; Leinert et al., 1981; Stenborg et al., 2018; Stenborg et al., 2021). Measurements of luminance in principle integrate the luminosity on a line of sight (LOS) between the observer and infinity. Most of the luminosity originates near the Sun, where both the dust density and the sunlight are the strongest. However, as the existence of Gegenschein shows (Roosen, 1971), scattering is very angle dependent. It favors smaller angles and, therefore, the sources closer to the observer, and makes the inversion of LOS luminance into dust density more model dependent and ambiguous (Mann et al., 2004; Kneißel and Mann, 1991). Observations from 1 AU are therefore limited, especially a few angular degrees from the Sun. The best results are achieved with measurements closer to the Sun, such as those of the two Helios spacecraft (Leinert et al., 1981), which, as we mentioned previously (Eq. 3.1), found the number density of bound dust between 0.3 AU and 1 AU scaling as $n(R) \propto R^{-1.3}$. More recently, measurements of the Wide-field Imager for

Solar Probe (WISPR) confirmed this trend (Stenborg et al., 2021), and even observed a dust depletion zone within $19\,R_{Sun} \approx 0.09\,\mathrm{AU}$ (Stenborg et al., 2022). The measurements are difficult to interpret because the luminance of dust-caused F-corona and dust-independent K-corona are hard to distinguish.

WISPR observed many phenomena, one of them being the clouds of spacecraft debris liberated by impacts of hypervelocity dust on the insulating carbon foam (Malaspina et al., 2022). The carbon thermal insulation is fragile, and the debris moves slowly enough that the light they scatter is captured in individual shots, allowing for the estimation of their speed, which was found to be about of 1 m/s. Trajectories of the debris were also found to be curved around biased electrical antennas, which is a motion similar to the motion of electrons in Pantellini et al. process (Pantellini et al., 2012), which we hypothesize might be responsible for the double-peak signals reported on SolO in Paper III.

5.2 Impact ionization

5.2.1 Charge generation process

A very fast impact of a dust grain onto a solid target, such as spacecraft body, releases free charges. This is because of the great energy density at the impact site (Shen, 2021). At moderate relative speeds of $v \lesssim 10\,\mathrm{kms}^{-1}$, the ionization is mostly due to surface effects on the grain and on the target (J. Kissel and Krueger, 1987). At much higher speeds $v \gtrsim 20\,\mathrm{kms}^{-1}$, the grain is destroyed completely, and the ionization is due to the effects in the bulk of the target (Hornung and J. Kissel, 1994). For this, shock wave formation in the target at supersonic speed is important (Drapatz and Michel, 1974), which concentrates the available energy into the shock front, which makes up a small volume of the target, resulting in high volumetric energy density.

The first reported observation (Friichtenicht, 1964) of impact ionization followed shortly after the development of the first MV dust accelerator (Friichtenicht, 1962). The charge leaving the impact site after the impact of carbon and iron dust grains was measured with a preamplifier connected to a metallic target. The charge was observed to be quasi neutral, and the amount of generated charge q was found consistent with the relation

$$q \propto mv^3, \tag{5.1}$$

for the velocities $2\,\mathrm{kms}^{-1} < v < 15\,\mathrm{kms}^{-1}$, where m is the mass of the grain and v is the impact speed. Later measurements (A. Auer and Sitte, 1968; McBride and McDonnell, 1999; Grün, 1984; Collette et al., 2014; Shen, 2021)

worked with a more general empirical equation of

$$q \propto m^{\alpha} v^{\gamma}, \tag{5.2}$$

and mostly found $\alpha \approx 1$ and $3 < \gamma < 5$, depending on the speed interval and the combination of the grain material and the target material.

We note that the amount of generated charge is random, even if m, v, α, γ are known, and Eq. 5.2 is the model for the average amount of the generated charge. The difference between this average and the individual data points is often significant, with a spread of a factor of two or more (Collette et al., 2014; Shen, 2021). Due to the randomness involved, and due to the steep dependence on the impact speed v, little information about mass m is usually recovered from the measurement of charge q, unless the measurement happened in a well controlled environment of a laboratory.

5.2.2 Laboratory simulation

The most successful dust accelerators are based on electrostatic acceleration principle, not dissimilar to the ion gun. The latest such device offers the acceleration voltage of up to 3 MV (Shu et al., 2012), allowing for speeds up to $v \gtrsim 50\,\mathrm{kms}^{-1}$ for $r \lesssim 1\,\mu$m grains, measuring both the mass and the charge state of the grain right before it hits the target. It not only allows for study of the impact ionization process (Collette et al., 2014; Nouzák et al., 2018; Kočiščák et al., 2020; Nouzák et al., 2021; Shen et al., 2021a; Shen et al., 2021b; Shen et al., 2023), but also for the study of atmospheric ablation (Thomas et al., 2017; DeLuca et al., 2018; DeLuca et al., 2022; Tarnecki et al., 2023). Many aspects of each impact can be measured at the same time, as there is no limitation on the payload nor on the transmission capacity, such as in the case of spacecraft experiments. Although versatile, accelerator measurements bear disadvantages: the experiment happens in a confined chamber in finite vacuum, the accelerated dust grain is selected randomly from a reservoir, and there is an intrinsic correlation between the speed and the mass of a grain, given the charge and the accelerating voltage are constant (Shelton et al., 1960). As far as the replication of space environment goes, the plasma conditions (solar wind, UV illumination) can be partially replicated in laboratory (Shu et al., 2012; Horányi et al., 2008), but the noise level in laboratory is never achieved as low as in space.

5.2.3 Dedicated ionization detectors

The mechanism of impact ionization is used to detect dust impacts on spacecraft. In principle, a surface is in a chamber, where the entry of charged particles is blocked by a filter, which is however not capable of blocking the entry of

dust grains. The surface is therefore exposed to potential dust impacts, which are the only thinkable source of charge in the chamber. Charge is monitored with a bias collector in the chamber, and whenever it appears, it is due to a dust impact. The first such detector was used on the Orbiting Geophysical Observatory (OGO) 3 mission (Alexander and Bohn, 1968), and was used many times in forms of variable complexity, some of them resolving the charge and directionality (Grün et al., 1992a; Grün et al., 1992b; Berg and Richardson, 1969) of the incident grains, or even allowing for spectroscopy of the impact plasma (R. Srama et al., 2004; Sommer et al., 2023). Impact ionization detectors are sensitive and versatile, and they are used not only in orbit, but also on sounding rockets (Gunnarsdottir, 2019; Trollvik et al., 2019) to study smoke particles in the mesosphere.

5.2.4 Non-ionization dust detectors

Mechanical methods

A penetration method was employed on Pioneer 10 and 11 (Humes, 1980). A $25\,\mu$m and a $50\,\mu$m pressurized steel cells were mounted on Pioneer 10 and 11 respectively, 234 cells on each, counting the impacts of dust grains fast and big enough to penetrate them, which showed by the pressure loss in the cell. Together, these detectors counted 182 dust impacts, showing clearly higher abundance of dust near Jupiter and Saturn, and concluding that the $\approx 10\,\mu$m grains observed between the asteroid belt and Jupiter were not circular and in the ecliptic plane, but rather eccentric or inclined.

An integration experiment was conducted on the Long Duration Exposure Facility (LDEF) satellite (Love and Brownlee, 1993), which consisted of a study of $5.6\,\mathrm{m}^2$ aluminium plate exposed to the near-Earth environment for nearly six years. In total 761 craters were found on a microscope scan, allowing for the estimate of the total meteoric mass accretion rate by the Earth to $40 \pm 20\,\mathrm{kgy}^{-1}$.

Aerogel, an extremely low-density silica material, was shown to provide gentle enough dissipation of kinetic energy to capture hypervelocity cosmic dust grains intact (Tsou, 1995). The same material was used to recover a dust sample from the Wild 2 comet, which was achieved by the Stardust mission (Brownlee, 2014).

Piezoelectric

At the early age of in-situ dust science, dust was detected with so-called microphone detectors (Alexander et al., 1963). The principle is quite simple, as such a device consists of a hard target connected to a piezoelectric element, which

acoustically registers each strong enough impact. The detectors were however often sensitive to other effects, which led to vastly imprecise expectations of dust-induced erosion of spacecraft (Whipple, 1958).

PVDF

Polyvinylidene fluoride (PVDF) is a ferroelectric polymer, hence, a polymer capable of holding a permanent electric dipole. When a thin PVDF foil is perturbed by a dust impact, the dipoles are locally perturbed and the material gets locally depolarized, creating a current spike between the surfaces of the foil. Such detector is sensitive to $r \lesssim \mu$m hypervelocity grains and can be made with a relatively large detection area and a very low dead time (Tuzzolino, 1996). The latter was used in Vega 1 and Vega 2 missions in the proximity of the comet Halley (Simpson et al., 1988). If calibrated, such detector provides information about the magnitude of the impact, as the amount of released charge depends on the mass and the speed of the incident grain. The Venetia Burney Student Dust Counter (VBSDC) (James et al., 2010), a device of the New Horizons mission based on this principle has reported the dust flux between 1 AU and 50 AU (Bernardoni et al., 2022) and has already been functioning for over 18 years, since 2006.

5.2.5 Antennas

Many spacecraft carry electrical antennas, which are, not necessarily by design, sensitive to changes in the potential of the spacecraft body (Meyer-Vernet et al., 2017). The term *antenna detection* is misleading, since it is the whole spacecraft surface, which acts as a dust detector. It is then the antennas, which register the free charge created upon impact. The spacecraft body is typically positively charged whenever the spacecraft is in sunlight, due to the current of photoelectrons escaping from the spacecraft body (Guillemant et al., 2013). Since the resulting electric field around the spacecraft acts to separate the impact-created charge, attracting negative and repulsing positive charge, the positive potential of the spacecraft is transiently lowered. If the time before the equilibrium is restored is long enough, the impact is registered (Mann et al., 2019). The first spacecraft to measure these transient signals attributable to dust was Voyager 1 in 1980 (Scarf et al., 1982; Aubier et al., 1983; Gurnett et al., 1997), and numerous spacecraft, such as Voyager 2 (Gurnett et al., 1983), Vega (Laakso et al., 1989), Deep Space (DS) 1 (Tsurutani et al., 2003), Cassini (Kurth et al., 2006), Wind (Malaspina et al., 2014), Mars Atmosphere and Volatile Evolution (MAVEN) (Andersson et al., 2015), STEREO (Zaslavsky et al., 2012), Cluster (Vaverka et al., 2017), and Magnetospheric

multiscale (MMS) mission (Vaverka et al., 2018) were shown to be suitable for this analysis, adding a new purpose to their electric antenna measurements.

Recently, this method was acknowledged during the design phase of the electrical antenna suite of PSP's FIELDS (Bale et al., 2016), and of SolO's Radio and Plasma Waves (RPW) (Maksimovic et al., 2020), making the data a lot more usable for dust identification by design choice (Mann et al., 2019). Even still, the process is dependent on the impact site, spacecraft's state, the ambient conditions, and the parameters of the grain. The time-domain sampled waveforms carry non-trivial information on these. The interpretation of the waveforms' fine structure in terms of the charge generation and collection process was attempted in Paper III.

Another method of antenna dust detection was proposed, called Radio Dust Analyzer (RDA) (Lesceux et al., 1989), which is not to be confused with antenna detection as commonly referred. RDA is based on remote sensing of the grain's own electric field, as it (narrowly) misses an electrical antenna, and, therefore, antennas detect dust more directly than by merely being sensitive to impacts on the body. The method offers a great detection area, but is susceptible to noise (Meuris et al., 1996; Meyer-Vernet, 2001).

5.3 Dust detection in antenna measurements

Many electrical phenomena happen in the inner solar system, which can be found in the electrical antenna data. Some of them are short in time, such as encounters of electron holes and related solitary waves (Malaspina et al., 2013; Steinvall et al., 2019). These produce various signals (Pickett et al., 2004), and are often difficult to distinguish from dust impacts (Malaspina and Wilson, 2016; Vaverka et al., 2018). Besides, reliably identifying a dust impact with a low signal to noise ratio (SNR) is complicated in itself. In this section, we first introduce several metrics, which are useful for comparing the performance of different identification procedures, and then we introduce several detection approaches.

5.3.1 Performance metrics

For all the detection methods described in this section, time is discretized to temporal intervals, each of which is studied for the presence of dust independently of the other intervals. During each interval, a dust impact either truly happened, or truly did not. We denote the former case I and the latter case O. Typically, O intervals are much more numerous than I intervals. Many of the O intervals are however very easily ruled out as impacts, as for example, the maximum electrical amplitude within the interval is within the noise level

(nothing happens). For the performance testing purposes, a *balanced* test sample containing $\approx 50\,\%$ of either of the two categories I/O is commonly used. Therefore, the performance on the actual experimental data set might differ from the test performance.

A detection method assigns either a *positive* — P or a *negative* — N label to each of the temporal intervals of the test sample of length Σ. Given two options for the dust presence, and the two options for the label, four options are possible for each of the test sample intervals. Ideally, each of the I intervals is assigned the P label. We call these *true positives* and the number of these in the sample is denoted TP. In the ideal case, each of the O intervals is assigned the N label, becoming *true negative*, count of which is denoted TN. It is rarely the case that $TP + TN = \Sigma$. A fraction of O intervals will likely be labeled P, which are called *false positive errors* or *type I errors*, number of which we denote FP. Vice-versa, each of the T intervals labeled N is called a *false negative error* or *type II error* and their number FN. By definition,

$$\Sigma = TP + TN + FP + FN. \tag{5.3}$$

One of the relevant measures is called *false positive rate* — FPR, and is evaluated as

$$FPR = \frac{FP}{FP + TN} \approx 2\frac{FP}{\Sigma}, \tag{5.4}$$

where the denominator is the total number of O intervals in the test sample, and $FP + TN \approx \Sigma/2$ for a balanced test sample. Similarly to FPR, the *false negative rate* — FNR is defined as

$$FNR = \frac{FN}{FN + TP} \approx 2\frac{FN}{\Sigma}, \tag{5.5}$$

where the denominator is the total number of I intervals in the test set, and $FN + TP \approx \Sigma/2$ for a balanced test sample. The term *accuracy* commonly evaluates the proportion of correctly labeled intervals, therefore

$$accuracy = \frac{TP + TN}{TP + TN + FP + FN} = \frac{TP + TN}{\Sigma}, \tag{5.6}$$

and *precision* is defined as

$$precision = \frac{TP}{TP + FP}, \tag{5.7}$$

so, it evaluates the proportion of correctly labeled intervals among all the intervals labeled as P. Sometimes the term *specificity* is used, which commonly

means $1 - FPR$. Similarly, the terms *recall* and *sensitivity* are used and both commonly mean $1 - FNR$. In addition, the F_1 *score* is defined as

$$F_1 = 2\frac{precision \cdot recall}{precision + recall} = \frac{2\,TP}{2\,TP + FP + FN}. \tag{5.8}$$

In Paper I, we used the metrics: accuracy, precision, recall, and F_1, but all the other metrics may be evaluated easily, since the TP, TN, FP, FN are all listed in Paper I.

We note that the information whether the impact truly happened or not (I/O) is usually not available unless the experiment takes place in a controlled environment. Therefore, this information is substituted with approximate information, which needs to be provided by a method, which is a lot more reliable than the tested method. Such a more reliable, yet approximate method then serves the function of a *benchmark*.

5.3.2 Power spectra

The typical main purpose of an in-situ electric antenna measurement device is detection and analysis of plasma waves. Such measurements are typically shown in frequency space, such as in a spectrogram or a scalogram. This is often the main, or even the only data product of the measurement, due to physical limitations of the device or due to a limitation in data transmission capacity, especially for non-Earth orbiting spacecraft. This is why the first antenna detection of dust relied on a multi-channel spectrum analyzer (Scarf et al., 1982). Since dust signatures are very short-lived, they are visible as short-lasting broad-band signals, and therefore they interfere with measurements in many frequency bands.

The upper limit of frequency f_{hi} generated by the impact is due to the fastest process, that is the rise of the signal. The rise-time is very variable due to several processes responsible, but usually happens in $\tau_{rise} \approx \mu$s (Meyer-Vernet et al., 2017; Shen et al., 2023), which implies the frequency of $f_{hi} \approx$ MHz. The slope of the high-frequency tail in the power spectrum is related to the rise-time (Meyer-Vernet et al., 2017).

The lowest frequency f_{lo} is limited by the slowest related process, that is the relaxation to the equilibrium potential (Zaslavsky, 2015). The characteristic time τ_{decay} of the exponentially decaying signal returning to the equilibrium depends on the spacecraft's capacitance C_{SC} and the ambient plasma as

$$\tau_{decay} \approx \frac{C_{SC} k_B T_{ph}}{e|I_e|} \approx \frac{C_{sc} k_B T_{ph}}{e^2 n_e v_e S_{SC}}, \tag{5.9}$$

where $k_B T_{ph}$ is the photoelectron temperature, I_e is the ambient electron current on the body of the spacecraft, n_e is the ambient electron number density,

v_e is the ambient electron mean speed, S_{SC} is the spacecraft's effective surface, and e is the elementary charge (Henri et al., 2011). The typical 1 AU solar wind conditions yield $\tau_{decay} \approx 1\,\mathrm{ms}$, which corresponds to $f_{lo} \gtrsim 1\,\mathrm{kHz}$, but can be longer in sparse plasma, and shorter in dense plasma (Zaslavsky, 2015; Vaverka et al., 2017; Meyer-Vernet et al., 2017).

Although useful, spectral signatures of dust are always ambiguous, as the short and broad band dust impact signal is not very different from other short signals, such as solitary waves, or even electrical interference. These are however more confidently distinguished in the time domain signal, which is the topic of Paper I. In Paper III, we found the rise and decay time theory, recently developed for the purpose of dust identification in spectra (Meyer-Vernet et al., 2017), capable of explaining many of the characteristic times derived from the time domain waveforms.

5.3.3 Time domain identification

If the spacecraft's electrical measurements are recorded in the time domain with high enough sampling rate, the dust impacts are more recognizable, compared to the frequency domain measurements. The typical features were described previously in laboratory measurements (A. Auer and Sitte, 1968; Nouzák et al., 2018; Shen et al., 2021b; Shen et al., 2023), in spacecraft data (Zaslavsky et al., 2012; Kellogg et al., 2016; Vaverka et al., 2021), and explained theoretically (Zaslavsky, 2015; Meyer-Vernet et al., 2017; Shen et al., 2021a; Racković Babić et al., 2022). The response depends on the antenna configuration (Shen et al., 2023; Vaverka et al., 2021), especially on whether the antennas are configured in a dipole, when the voltage between two antennas is measured, or in a monopole, when the voltage between one of the antennas and the spacecraft body is measured. Since the spacecraft body usually offers a much bigger target, compared to the antennas, most impacts happen on the body. Although both monopole and dipole measurements were shown to be sensitive to dust impacts on the spacecraft body, the monopole configuration is favorable (Meyer-Vernet et al., 2014; Mann et al., 2019), since in this mode, the potential of the body is directly measured against an antenna.

Visual identification

A simplified signature of an impact on a positively charged spacecraft body in the case of monopole measurement is shown in Fig. 5.1 and is briefly described as follows: upon impact, quasi-neutral charge is released near the spacecraft. Due to their lower mass, the electrons in the cloud have much higher speed than the ions, and the most energetic of them escape the potential well of

the spacecraft, leaving the spacecraft more positive than before. Ions follow, and more of them escape, since they are repulsed by the positive potential of the spacecraft, leaving the spacecraft less positive than it was before the impact. The net potential has changed, and this change as a function of the equilibrium spacecraft potential was studied in laboratory (Collette et al., 2016; Kočiščák et al., 2020). The new potential of the spacecraft exponentially decays to the original equilibrium. A more elaborate description, directly applied to SolO's RPW measurements, is offered in Paper III.

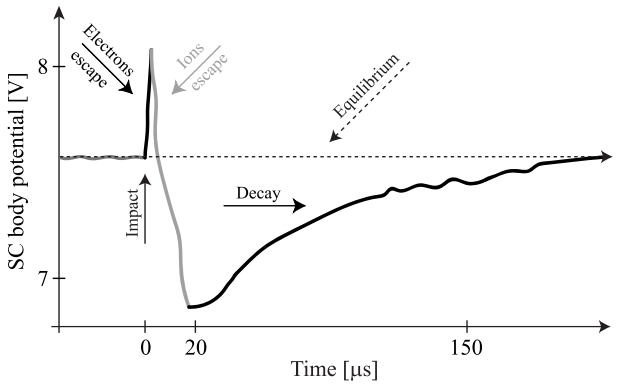

Figure 5.1: A simplified dust impact monopole electrical signature after an impact onto a positively charged spacecraft body.

Therefore, there are several features to look for in the time-domain measurements, such as the quick rise of the signal, and the exponential decay of the maximum. Visual identification is robust to the extent to which experts' opinions on the impact shape agree. Such identification is however very time consuming, and for a big data set, it is clearly not feasible to use this method alone.

This method is often regarded as the standard (benchmark) for any other electrical antenna dust identification method since for spacecraft data, the true information whether an impact happened, is not available. We also used this approximation in Paper I. The expert visual classification, albeit imperfect, is by definition the most reliable approximation of the truth.

Hard-coded identification

The features of dust impact signatures can be translated into algorithmic criteria, which are then efficiently applied to a big data set. While these identification criteria work well for textbook examples of dust impacts, the actual impacts in space may be quite different from the canonical example, as they

might contain a lot of noise, saturated data, solitary waves, or a superposition of a dust impact and a wave, and other non-standard signals (Vaverka et al., 2018; Ye et al., 2019; Malaspina et al., 2023). One such algorithm is used for on-board identification of dust impacts on SolO (Maksimovic et al., 2020), and in Paper I, we found this algorithm to be 85 % accurate and 75 % precise. The test was performed on a sample containing 50 % dust and 50 % non-dust recordings, as assigned by the tested algorithm. Classification performance improvement was the main motivation for the development of a more reliable automatic identification procedure presented in Paper I.

Machine learning

Supervised machine learning has established itself as a method of time-series classification, particularly in cases, when the exact classification criteria are hard to formulate, but labelled data are abundant (Wickstrøm et al., 2022). This makes it suitable for the problem of dust identification. Methods are available, such as support vector machine (SVM), which evaluates a set of pre-defined quantitative features on labelled data and creates a decision algorithm based on them (Vapnik, 1997). Convolutional neural network (CNN) is a type of a neural network particularly useful for the classification of grid-like objects, such as images or time-series (Gu et al., 2018). Unlike SVMs, CNNs yield the features vector by convolution operations, and therefore, they do not require a pre-defined feature extracting routine. One common disadvantage of neural networks (NNs), including CNNs, is that their decision making might be difficult to explain, as NNs generally are black boxes, with their internal working hard to interpret. However, great progress in NN explainability was achieved, at least for a limited class of CNNs, in the recent past (Samek et al., 2021). If designed to be so, CNN can be explainable to the extent that even features with non-linear effects are interpretable. This not only mitigates the black box trust issue but provides more insight into the problem. In Paper I, both an SVM and an explainable CNN were successfully used to meaningfully improve the performance of the dust identification algorithm, compared to the on-board hard-coded algorithm. The best performing CNN model showed 96 % accuracy and 94 % precision on a balance sample.

5.4 Dust detection flux modelling

With antenna detection of dust impacts, the whole body of the spacecraft acts as a detection surface for collisions between dust grains and the spacecraft. Assuming a 6D phase space probability density function $f(\vec{r}, \vec{v})$ for the dust cloud composed of grains of identical mass, where $\vec{r}$ is the location and $\vec{v}$ is

the velocity of the dust, and normalized to dust number density n as

$$n(\vec{r}) = \iiint_{\mathbb{R}^3} f(\vec{r}, \vec{v})\, dv_x\, dv_y\, dv_z, \tag{5.10}$$

and a spherical spacecraft with the cross section of S, the detection rate λ is

$$\lambda(\vec{r}) = S \iiint_{\mathbb{R}^3} |\vec{v} - \vec{v}_{sc}| f(\vec{r}, \vec{v})\, dv_x\, dv_y\, dv_z, \tag{5.11}$$

assuming the spacecraft speed $\vec{v}_{sc}$. If the spacecraft moves through a dust cloud with a sharp relative speed between the spacecraft and the dust $v_{imp} = |\vec{v}_{sc} - \vec{v}|$, which is provided by the dust grains having the same velocity $\vec{v}$:

$$\iiint_{\mathbb{R}^3} f(\vec{r}, \vec{v})\, dx\, dy\, dz = \delta(\vec{v}), \tag{5.12}$$

the detection rate simplifies to

$$\lambda = S n v_{imp}, \tag{5.13}$$

assuming that the local number density of dust is n and that all the grains are detected, if collided with. In reality, the dust cloud is not composed of grains of identical mass. Therefore, all the collisions are never registered, and the higher relative speed v_{imp} implies a higher charge produced on impact (Eq. 5.2), and in turn higher probability of detection, therefore the rate is sometimes modelled as

$$\lambda = S n v_{imp}^{1+\alpha\delta}, \tag{5.14}$$

where α is the parameter in charge generation (Eq. 5.2), and δ is the mass distribution slope (Eq. 3.2).

Eq. 5.14 can be simplified for different dust populations. For example, for bound dust, there is a bond between the dust speed $\vec{v}$ and the heliocentric distance r (Szalay et al., 2020). For β-meteoroids sufficiently far from the Sun, $\vec{v}$ can be reasonably assumed radial and with a speed v, which does not depend on $\vec{r}$ (Zaslavsky et al., 2021). For both bound dust and β-meteoroids, n depends only depends on the heliocentric distance r (Eqs. 3.1 and 3.4). For interstellar dust, n and $\vec{v}$ are sometimes assumed constant and homogeneous, which is often compatible with the data (Racković Babić, 2022). In principle, the cross section S in Eq. 5.14 is orientation dependent for non-spherical spacecraft. The total model rate Λ in a multi-component model is a superposition of the detection rates λ_i for each of the modelled populations as

$$\Lambda = \sum_{\forall i} \lambda_i, \tag{5.15}$$

where each individual λ_i is reasonably approximated.

In Paper II, we decided to explain the flux observed on SolO with a two-component, semi-empirical model (as in Eq. 5.15). This way, we were able to constrain some of the parameters of the β-meteoroids, such as their speed and acceleration. In Paper IV, we built a physics based model for bound dust detections on PSP, using the phase space distribution approach (Eq. 5.11) and we were able to constrain some of the orbital parameters of the near-solar dust.

5.4.1 Orbital parameters and the data set

Depending on the orbit of a spacecraft, the observed dust flux is dependent on, and therefore holds the information about different dust populations, while being unable to resolve other populations. We discussed the defining properties of common dust populations in Ch. 3. The orbits of selected spacecraft are shown in Fig. 5.2. In this section, we present different spacecraft, and we explain why their measurements complement each other.

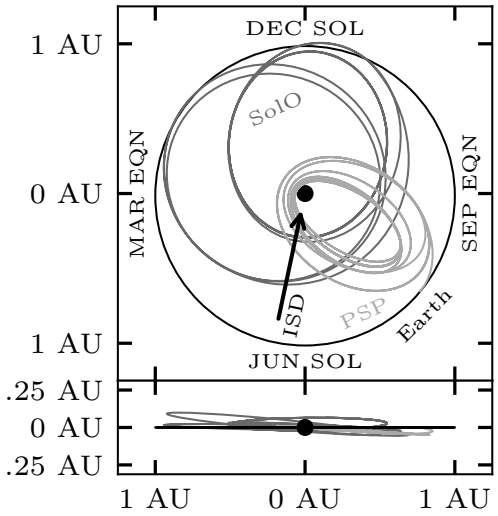

Figure 5.2: The orbit of SolO and PSP in heliocentric (HAE) coordinates between their respective launch date and the summer of 2024, shown in XY (top) and XZ (bottom) planes. The orbit of the Earth is shown for reference, which is very similar to the orbits of the two STEREO spacecraft. The direction of ISD flow is shown with an arrow.

Solar Terrestrial Relations Observatory

The two STEREO spacecraft orbit the Sun on a nearly circular orbits close to 1 AU. Their electrical antenna measurements allow for dust identification (Meyer-Vernet et al., 2009b). Beyond the intermittent and hard to explain nanodust (Meyer-Vernet et al., 2009b), the flux was found to be dominated by β-meteoroids (Zaslavsky et al., 2012). However, distinguishing β-meteoroids from bound dust is virtually impossible, since, owing to the circular orbit, the flux of both is expected to be constant throughout the orbit and the years. This is also an advantage for the detection of interstellar dust (ISD), which is directional, and even though its flux is relatively low, compared to β-meteoroids, it causes most of the observed variance (Zaslavsky et al., 2012; Malaspina et al., 2015; Racković Babić, 2022), with the flux maxima coinciding with the anti-parallel velocity between STEREO and ISD, and minima coinciding with the parallel configuration. Like STEREO, the spacecraft located in Earth's L1 point also exhibit a nearly-constant β-meteoroid and bound dust fluxes and are in a good position to investigate ISD (Malaspina et al., 2014; Malaspina and Wilson, 2016).

Solar Orbiter

SolO orbits the Sun on an elliptical orbit between 0.3 AU and 1 AU (eccentricity $e \approx 0.52$ in 2024), which means that neither its exposure to bound dust, nor β-meteoroids is constant. This makes identification of ISD difficult, as it is no longer responsible for an important part of the observed variance. However, the β-meteoroids are clearly apparent, since the spacecraft's radial speed alternates between negative (pre-perihelia) and positive (post-perihelia), which changes the incidence between the spacecraft and the outgoing β-meteoroids. Asymmetry in the flux between the inbound and the outbound leg allowed for some of the β-meteoroid parameters to be constrained by Zaslavsky et al. (2021) and in Paper II. The β-meteoroids are dominant in the SolO data to the extent that it is not even clear from SolO data alone that bound dust is needed to explain the observed flux.

Parker Solar Probe

The orbit of PSP is even more eccentric ($e \approx 0.86$ in 2024), compared to SolO, but even more importantly, PSP gets as close as 0.052 AU from the Sun. The relative speed between PSP and the dust components was evaluated by Szalay et al. (2020), and all suggests that unlike for any other spacecraft, the near-solar dust flux is dominated by bound dust impacts, especially in the post-perihelia. While ISD is difficult to distinguish in SolO data, it is very

unlikely to be confidently identified in PSP data, since the variation of the flux on PSP is even much higher, and the alignment is even more unfortunate, with the likely peak of ISD impacts being nearly aligned with the perihelia (see Fig. 5.2). The bound dust component, crucial for the flux modelling on PSP, was modelled and constrained in Paper IV. In the paper, we also discuss the different material of the heat shield, and how it likely causes the heat shield to be less sensitive to the impacts. The great variability of the ambient conditions poses additional challenges, as the electric potential, and even conductivity of the spacecraft changes throughout each orbit significantly, which we also investigated and discussed in Paper IV.

5.4.2 Compatibility of Solar Orbiter and Parker Solar Probe dust data

In Paper II, we presented a Bayesian fit of a semi empirical dust flux model to the SolO data from between 6/2020 and 12/2021. As a natural continuation of that effort, in this section we build on that model, and adjust the procedure from Paper II. We perform a similar fit but done using the aggregated SolO data from between 6/2020 and 6/2023 and PSP data from between 10/2018 and 7/2023. As we will see, a good fit is possible, but it does not yield much new information about the dust cloud.

Since the goal of this section is to incorporate measurements from PSP, the model needs to change with respect to the model used in Paper II, as there are physical differences between the spacecraft. Having more data, however, we can afford to fit a somewhat more complicated model, working with six unknowns (hyperparameters). The changes with respect to Paper II are:

- a two-component model assuming β-meteoroids and bound dust is used, as opposed to the two-component model assuming β-meteoroids and a constant background rate used in Paper II,
- a cuboid shape is assumed for both spacecraft with a different cross section from the front, from the side, and from the back, assuming a motion in the plane of ecliptic,
- while in the case of SolO, the cross sections from the front and from the back are assumed equal, in the case of PSP, the front side is assumed to have a smaller cross section, due to a different material of the heat shield, as discussed in Paper IV.

We model the detection count per day in the case of SolO and per eight hours in the case of PSP. This choice is not very consequential, if it is reasonable to assume the detection rate constant within one detection interval, and if an

Table 5.1: The cuboid-approximation cross section for SolO and PSP. Front side means the sunward side, back is the opposing side. α_{shield} is the PSP heat shield miss rate parameter.

	$S_{front}\,[m^2]$	$S_{side}\,[m^2]$	$S_{back}\,[m^2]$
SolO	10.34	8.24	10.34
PSP	$6.11 \cdot (1 - \alpha_{shield})$	4.62	6.11

appropriate procedure is used. The SolO/RPW data is a product of the CNN procedure presented in Paper I and the PSP/FIELDS data is the data product by Malaspina et al. (2023), which is the same data product as used in Paper IV. The detection count is assumed to come from a Poisson distribution (as in Eq. 4.1) and the six-parameter model for the rate, with the free parameters $\lambda_a, \lambda_b, v_{b,r}, \epsilon_v, \epsilon_{b,r}, \alpha_{shield}$ is

$$\Lambda = E(\lambda_{bound} + \lambda_\beta), \tag{5.16}$$

where E is the exposure time, and the components $\lambda_{bound}, \lambda_\beta$ are

$$\begin{aligned} \lambda_{bound} &= \lambda_a S(sc, \phi a) \left(\frac{|\vec{v}_a - \vec{v}_{sc}|}{v_{a,norm}} \right)^{\epsilon_v} \left(\frac{R}{1\,\mathrm{AU}} \right)^{-1.3} \\ \lambda_\beta &= \lambda_b S(sc, \phi b) \left(\frac{|\vec{v}_b - \vec{v}_{sc}|}{v_{b,norm}} \right)^{\epsilon_v} \left(\frac{R}{1\,\mathrm{AU}} \right)^{\epsilon_{b,r}}, \end{aligned} \tag{5.17}$$

where R is the heliocentric distance, and $S(sc, \alpha)$ is the effective cross section, dependent on the spacecraft and the incident angle ϕ, which in turn depends on the velocity of the dust cloud $\vec{v}_a, \vec{v}_b$ and of the spacecraft $\vec{v}_{sc}$. For compactness, the subscripts a and b correspond to bound dust and β-meteoroids, respectively. The bound dust velocity $\vec{v}_a$ is assumed to be purely azimuthal with the speed

$$|\vec{v}_a| = \left(\frac{R}{1\,\mathrm{AU}} \right)^{\frac{1}{2}} \cdot 29.8\,\mathrm{kms}^{-1}, \tag{5.18}$$

while the velocity of β has two components

$$\begin{aligned} \vec{v}_b &= \vec{e}_{rad} v_{b,rad} + \vec{e}_{azim} v_{b,azim} \\ v_{b,rad} &= \left(\frac{R}{1\,\mathrm{AU}} \right)^{-2-\epsilon_{b,r}} v_{b,r} \\ v_{b,azim} &= \frac{R}{1\,\mathrm{AU}} \cdot 9\,\mathrm{kms}^{-1}. \end{aligned} \tag{5.19}$$

Finally, the speed normalization is done with respect to a stationary (non-orbiting) object at 1 AU, therefore

$$\begin{aligned} v_{a,norm} &= 29.8\,\mathrm{kms}^{-1} \\ v_{b,norm} &= \left(v_{b,r}^2 + \left(9\,\mathrm{kms}^{-1}\right)^2\right)^{\frac{1}{2}}, \end{aligned} \tag{5.20}$$

where the speed of β-meteoroids at 1 AU of $9\,\mathrm{kms}^{-1}$ is based on a discussion in Paper II. In this case, the fit was performed by M-H MCMC sampling. The assumed cross sections are based on the projections of the 3D models (Garcia, 2018; ESA, 2023) of the two spacecraft and are summarized in Tab. 5.1.

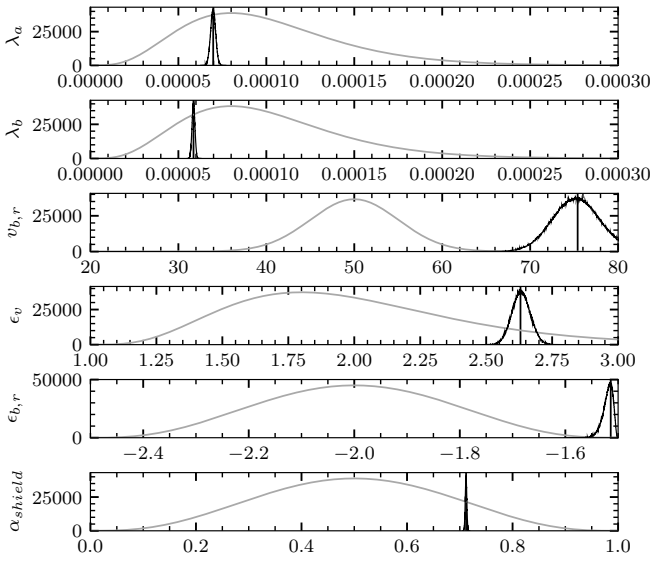

Figure 5.3: The marginals of the prior (gray) and the posterior (black) of the fit. The posterior is based on a sample of 10^7 points and the MAP values are indicated with vertical lines. Neither prior nor the posterior are normalized. The summary of both is shown in Tab. 5.2.

The main shortcomings of the model are the single dust speed assumed, the cuboid approximation, and the approximation of $\lambda_\beta \propto R^{\epsilon_{b,r}}$. The dimension of the model, six, is quite high. Therefore, we constrained the support of the hyperparameters wherever reasonable. This is done with the transformations used for the prior, indicated in Tab. 5.2. This constraint is most apparent

Table 5.2: The summary of the prior and the posterior marginals, the same as shown in Fig. 5.3.

	prior		posterior	
	distribution	support	mean	st. dev.
λ_a	$\Gamma(k=5, \theta=2\cdot10^{-5})$	$\mathbb{R}^+$	$6.97\cdot10^{-5}$	$1.4\cdot10^{-6}$
λ_b	$\Gamma(k=5, \theta=2\cdot10^{-5})$	$\mathbb{R}^+$	$5.85\cdot10^{-5}$	$8.2\cdot10^{-7}$
$v_{b,r}$	$Norm(\mu=50, \sigma=5)$	$\mathbb{R}$	75.3	2.7
ϵ_v	$1+\Gamma(k=5, \theta=2\cdot10^{-1})$	$(1,\infty)$	1.63	$3.5\cdot10^{-2}$
$\epsilon_{b,r}$	$-1.5-B(\alpha=4, \beta=4)$	$(-2.5,-1.5)$	-1.52	$9.6\cdot10^{-3}$
α_{shield}	$B(\alpha=4, \beta=4)$	$(0,1)$	0.71	$1.4\cdot10^{-3}$

in the value of $\epsilon_{b,r}$ being close to the support boundary, which indicates a deficient model, perhaps on the assumption of a single β-meteoroid speed at each heliocentric distance. However, we note that in Paper II, the posterior mean of the corresponding parameter ϵ_r was found to be -1.61 with the standard deviation of 0.16, hence, compatible with the present result, even as the prior support spanned $\mathbb{R}$.

The priors and posteriors are shown in Fig. 5.3 and summarized in Tab. 5.2. They are somewhat different from the results of Paper II, but this is to be expected, since the data is different, as is the model. Therefore, the unknown parameters do not have the exact same meaning as they had in Paper II. The conclusions drawn from the fit in Paper II would not be substantially different if they were to be drawn from this fit. Interestingly, the PSP heat shield miss rate parameter α_{shield} implies that the sensitivity of the PSP's front side is by a factor of nearly four lower than the sensitivity of its other sides, and that of SolO. Two things are apparent from Fig. 5.4. First, the model predicts that there is a period present in each post perihelion of PSP, when bound dust dominates the flux, consistently with the predictions made by (Szalay et al., 2020; Szalay et al., 2021). This supports the validity of the analysis done in Paper IV. This is not observed for SolO, for which β-meteoroids are always dominant. Second, the model is deficient, as it fails to represent the aphelia fluxes of later PSP orbits, where the model flux is higher than observed. This might be an instrumental effect, if the change of the spacecraft's sensitivity introduces variance beyond what is a part of the model, but it might be a sign that the model does not sufficiently capture the dynamics of the dust cloud. We however see that both spacecraft do fit well in the same framework of a two-component, β and bound dust model.

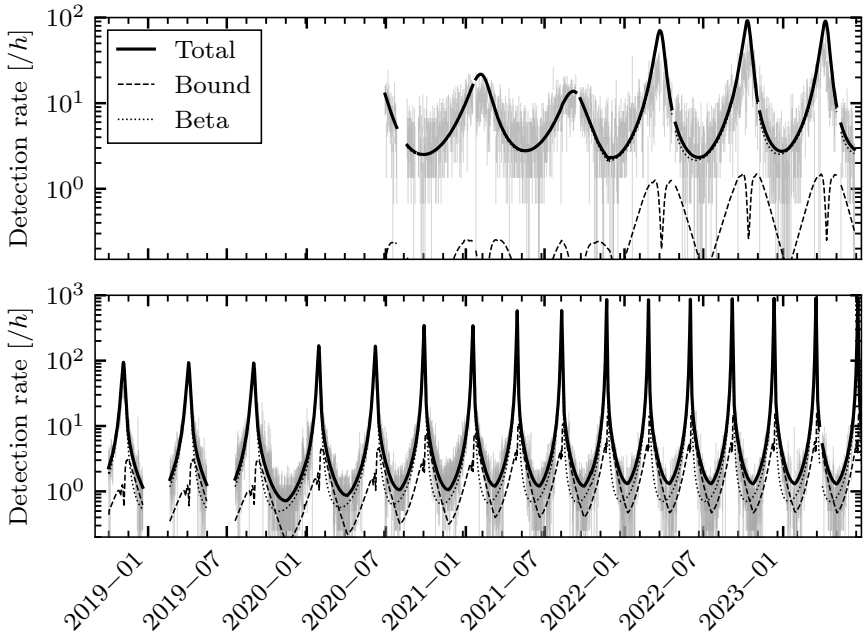

Figure 5.4: The measured impact rate for SolO (top) and PSP (bottom), where the error bars correspond, for visualization purposes, to 90 % confidence intervals, assuming the rate was identical to the observed count per exposure time. The lines correspond to the MAP result of the two-component fit.

6 | Summary of Papers

The thesis aims to infer physical properties of the interplanetary dust in terms of dust populations by analyzing experimental data. We use the electrical antenna measurements of two spacecraft: SolO and PSP. To yield the most information, the data had to be treated carefully, keeping the limited confidence of dust identification in mind. The dust cloud analysis is indirect, as the antenna measurements yield little information about each individual impact. Therefore, the physical properties of the dust populations only emerge in statistics.

The main body of this work is the four papers presented below. Each of the papers has several co-authors, and the thesis author's particular contribution is explicitly described in the acknowledgments in each of the papers.

Paper I

SolO's antennas record electrical time-domain waveforms when the electric field shows signs of potentially interesting activity, not necessarily of dust origin. It is a long-standing issue to convincingly classify electrical signatures by means other than visual event-by-event human labelling. In Paper I, we report on the development of a machine learning tool, which provides this functionality. We tried two machine learning approaches and improvement was attained with a purpose-developed convolutional neural network, which achieved 96 % classification accuracy and 94 % precision, compared to 85 % accuracy and 75 % precision of the previously used algorithm. Developing this tool was instrumental for the subsequent work on SolO dust counts, as a solid data product is key for any more refined analysis, such as that done in Papers II and III.

Paper II

There are many degrees of freedom in dust flux models. To constrain them as much as possible, we employed a Bayesian approach to analyze the antenna dust counts for the first time in Paper II. We constructed a semi-empirical two-

component model, inspired by previous works of other authors, and applied it to SolO data, specifically the data product of Paper I, from between 07/2020 and 12/2021, all recorded between 0.5 AU and 1 AU. We estimated the speed of outgoing β-meteoroids to $63 \pm 7\,\mathrm{kms}^{-1}$. We found with confidence that the β-meteoroid population is decelerating on its way out of the inner solar system, which clearly implies that the radiation pressure is lower than gravity for these grains, that is $\beta < 1$.

Paper III

In Paper II, we only used the impact counts, that is the binary information, whether an impact happened, for each of the many temporal intervals. Electrical antenna measurements also provide information about the amplitude and shape of each of the impacts, which was disregarded in Paper II. This was the motivation for Paper III, where we report on the finding that the signals recorded with SolO/RPW are typically double peaked. In fact, we found that the chronologically first peak, denoted *primary*, is explainable by the current theory of the dust impact signal formation. The *secondary* peak, which was found to be much more variable, was found to appear on a significantly longer time scale explained by the ion motion. This is possibly explained by the escaping ions having influence on the individual antennas. We found this secondary peak to be too strong to be caused by direct ion detection. A possible explanation was found in the application of the Pantellini et al. (2012) process, which predicts a strong response of cylindrical antennas to the vicinity of ions, which prevents the photoelectron recollection for a short time. With our adaptation of the Pantellini process, we partially explained the relation between the primary and the secondary peak's amplitude. Based on the findings of Paper III, we suggest that the maximum amplitude of a signal is not a good proxy for the impact-generated charge, and the amplitude of the primary peak is to be studied instead.

Paper IV

PSP detects most of the dust impacts in the near vicinity of the Sun, where an important, or even dominant, portion of the impacts is attributable to bound dust. This makes the measurements unique with respect to other instruments, and this motivated Paper IV, in which we: first compared the measurements of PSP and SolO near 1 AU and, second developed a phase-space distribution function based model for the impact counts, which takes into account orbital parameters of the bound dust cloud and semi-empirical parameters of the experiment. We did not fit the PSP data with the model directly, as the model

is clearly too crude to replicate the experiment, but two general features were studied. We compared the heliocentric dependence of the dust count predicted by the model with the dependence observed in the data. We found that the dependence of the observed count on the relative speed between dust and PSP is lower than previously assumed, implying a comparatively flat mass distribution of dust inside 0.5 AU. By studying the predicted and the observed dust count near perihelia, we found that the flux minimum observed near the perihelia is too prominent to be explained by the alignment between the spacecraft velocity and the dust velocity. We offered alternative explanations for the flux minimum, including the presence of a dust depletion zone.

7 | Conclusions and future work

This thesis has shown that by statistical analysis, physically meaningful parameters of the interplanetary dust cloud can be yielded from the dust impact counts recorded with spacecraft, which improves our understanding of the inner solar system dust cloud. We showed that a convolutional neural network is a viable tool for dust identification in antenna measurements, which we used for SolO data, and which has the potential to improve the quality of data products of other spacecraft. We presented a Bayesian approach to modelling the dust counts recorded with spacecraft, which can fit more sophisticated models. We also presented and demonstrated a statistical toolbox for this task, and we used it to characterize the dynamics of β-meteoroids, and to describe their deceleration. As a part of this thesis, the method of dust detection with antennas was studied, and we have shown the importance of photoelectrons for the detection. Understanding of the data relies on robust knowledge of the impact process, which we also contributed to as a part of this thesis, by pointing out and the presence of a two-peak structure in the impact records. Using the formalism of kinetic theory, we explained several features of the dust flux observed with PSP and we showed that such modelling effort is fruitful and potentially practical for other spacecraft and other dust environments. In particular, we showed that the available data are compatible with a near-solar dust depletion zone and that the spacecraft properties are consequential for the interpretation of the data. To understand the inner solar system dust environment more deeply, and to make the most of the presented methods, several tasks remain for future inquiry.

The dust identification method presented in Paper I is significantly more reliable than the methods used before, but it is limited to certain measurement regimes of the specific device used on SolO. The development of a routine for automatic classification of waveform signals is challenging, as the compatibility between different measurements is limited, due to differences in physical

design, and in the data products. Since human experts can classify waveforms from different devices without technical knowledge of the device, it is feasible. Having such a routine would be useful, as it would provide another layer of harmonization of data between different spacecraft. The application of such routine onboard spacecraft would save the data transfer, and therefore, potentially allow for better data coverage.

The statistical analysis presented in the thesis and used in Paper II is superior to the often used least squares fitting, since it treats the counting error correctly. This is especially important if the number of detections within a temporal interval is a small number, which it often is. It is strongly suggested that such a method is used for future analysis of dust counts of not only SolO and PSP.

The assumption of a dust flux proportional to the impact speed to a power higher than one was used in several works, including Paper IV of this thesis. The reason is that since higher impact speed generates more charge, small grains are detected at a high impact speed, but not at a low impact speed. The flux therefore depends on the mass distribution of the grains, and on the charge production as a function of the impact speed. As a simplification, it was assumed that the produced charge depends on the power of the impact speed, and that the mass distribution is a power-law. Both are arguable. The charge production was never experimentally measured at a speed as high as is the typical impact speed on PSP, or even SolO, so we are limited to a reasonable extrapolation. More questionable is the assumption of a power-law distribution of masses. While it might be true for large masses, when grain to grain collisions shape the cloud, the dynamics of sub-micron dust depends on the size in a different way. This is clearly demonstrated with β-meteoroids, which move differently from bound dust, but they occupy only an order of magnitude or two on the mass scale. Since nearly all grains within the mass range of β-meteoroids are β-meteoroids, these are missing in the mass distribution of bound dust. Therefore, the mass distribution of micron and sub-micron sized bound dust grains cannot be a power-law. A further investigation of their distribution would prove instrumental for modelling efforts.

Interstellar dust (ISD) was barely addressed in the thesis, since neither SolO nor PSP are very well suited for its detection. The situation might change when SolO's orbit becomes more inclined, and gets to the region, where bound dust and β-meteoroids are less plentiful. This is coincidentally planned for the late 2020's, when the ISD flux will likely have recovered, due to the orientation of the solar magnetic field. Understanding the flux observed out of the plane of ecliptic would require generalization of the models for the flux but will place further constraints on the dust parameters. We offered tools which are suitable

for the forward modelling of ISD in Paper IV and for statistical analysis of ISD in Paper II.

Several spacecraft have reported nanodust observations and since nanodust dynamics are strongly influenced by the electromagnetic field, its flux is likely to depend on the solar cycle. We did not observe nanodust with SolO nor with PSP, but this might be due to solar cycle. As was shown in Paper III, antenna dust detection is specific for each spacecraft, and the understanding of the antenna detection process is still limited. However, SolO's electrical suite is similar to that of STEREO, which detected nanodust, so nanodust detection remains an option for SolO in the future.

Each spacecraft's in-situ detections happen along its orbit. An intrinsic bond exists between the velocity and the location, and, therefore, between the amount of detected bound dust and β-meteoroids. Spacecraft, which change their orbital elements due to gravity assists, such as SolO and PSP, change this bond in discrete steps, allowing for a decoupling the two components of the flux from each other. Multi-spacecraft analysis allows for even more, as time and location are not bonded together, allowing for the estimates of time-evolution of the dust cloud. As demonstrated in Paper IV, multi-spacecraft analysis is complicated, but feasible. It is therefore worthy of future pursuit, as SolO will get inclined, and more dust-detecting spacecraft will operate in the solar system simultaneously.

Bibliography

Alexander, W. M. and J. L. Bohn (1968). "Zodiacal dust measurements in cislunar and interplanetary space from OGO III and Mariner IV experiments between June and December 1966." In: *Cospar Plenary Meeting*. North-Holland Publishing CO.

Alexander, W. M., C. W. McCracken, L. Secretan, et al. (1963). "Review of direct measurements of interplanetary dust from satellites and probes". In: p. 39.

Allen, C. W. (1946). "The spectrum of the corona at the eclipse of 1940 October 1". In: *Monthly Notices of the Royal Astronomical Society* 106.2, pp. 137–150.

Altobelli, N., E. Grün, and M. Landgraf (2006). "A new look into the Helios dust experiment data: presence of interstellar dust inside the Earth's orbit". In: *Astronomy & Astrophysics* 448.1, pp. 243–252.

Altobelli, N., S. Kempf, M. Landgraf, et al. (2003). "Cassini between Venus and Earth: Detection of interstellar dust". In: *Journal of Geophysical Research: Space Physics* 108.A10.

Anders, E. (1964). "Origin, age, and composition of meteorites". In: *Space Science Reviews* 3, pp. 583–714.

Andersson, L., T. D. Weber, D. M. Malaspina, et al. (2015). "Dust observations at orbital altitudes surrounding Mars". In: *Science* 350.6261, aad0398.

Aubier, M. G., N. Meyer-Vernet, and B. M. Pedersen (1983). "Shot noise from grain and particle impacts in Saturn's ring plane". In: *Geophysical Research Letters* 10.1, pp. 5–8.

Auer, A. and K. Sitte (1968). "Detection technique for micrometeoroids using impact ionization". In: *Earth and Planetary Science Letters* 4.2, pp. 178–183.

Baguhl, M., E. Grün, D. P. Hamilton, et al. (1995). "The flux of interstellar dust observed by Ulysses and Galileo". In: *The High Latitude Heliosphere: Proceedings of the 28th ESLAB Symposium, 19–21 April 1994, Friedrichshafen, Germany*. Springer, pp. 471–476.

Bale, S. D., K. Goetz, P. R. Harvey, et al. (2016). "The FIELDS instrument suite for Solar Probe Plus: measuring the coronal plasma and magnetic field, plasma waves and turbulence, and radio signatures of solar transients". In: *Space science reviews* 204, pp. 49–82.

Baum, W. A., T. Kreidl, J. A. Westphal, et al. (1981). "Saturn's E ring: I. CCD observations of March 1980". In: *Icarus* 47.1, pp. 84–96.

Baumann, C., M. Myrvang, and I. Mann (2020). "Dust sputtering within the inner heliosphere: a modelling study". In: *Annales Geophysicae* 38.4, pp. 919–930.

Bayes, T. (1763). "An essay towards solving a problem in the doctrine of chances." In: *Philosophical transactions of the Royal Society of London* 53. By the late Rev. Mr. Bayes, FRS communicated by Mr. Price, in a letter to John Canton, AMFR S, pp. 370–418.

Berg, O. E. and E. Grün (1973). "Evidence of hyperbolic cosmic dust particles." In: *Plenary Meeting on Space research XIII*.

Berg, O. E. and F. F. Richardson (1969). "The Pioneer 8 cosmic dust experiment". In: *Review of Scientific Instruments* 40.10, pp. 1333–1337.

Bernardoni, Edwin., M. Horányi, A. Doner, et al. (Mar. 2022). "Student Dust Counter Status Report: The First 50 au". In: *The Planetary Science Journal* 3.3, p. 69.

Boltzmann, L. (1884). "Ableitung des Stefanschen Gesetzes, betreffend die Abhängigkeit der Wärmestrahlung von der Temperatur aus der electromagnetischen Lichttheorie". In: *Annalen der Physik* 258.6, pp. 291–294.

Brooks, S., A. Gelman, G. Jones, et al. (2011). *Handbook of markov chain monte carlo*. CRC press.

Brownlee, D. E. (1985). "Cosmic dust: Collection and research". In: *Annual Review of Earth and Planetary Sciences* 13.1, pp. 147–173.

Brownlee, D. E. (2014). "The Stardust mission: analyzing samples from the edge of the solar system". In: *Annual Review of Earth and Planetary Sciences* 42, pp. 179–205.

Buffington, A., M. M. Bisi, J. M. Clover, et al. (2016). "Measurements and an empirical model of the Zodiacal brightness as observed by the Solar Mass Ejection Imager (SMEI)". In: *Icarus* 272, pp. 88–101.

Burchell, M. J., G. Graham, and A. Kearsley (2006). "Cosmic dust collection in aerogel". In: *Annu. Rev. Earth Planet. Sci.* 34, pp. 385–418.

Burns, J. A., P. L. Lamy, and S. Soter (1979). "Radiation forces on small particles in the solar system". In: *Icarus* 40.1, pp. 1–48.

Camus, A. (1972). *A Happy Death*. Alfred A. Knopf.

Cassini, G.-D. (1685). *Découverte de la lumière céleste qui paroist dans le zodiaque*. Paris: Imprimerie Royale.

Charnes, A., E. L. Frome, and P. L. Yu (1976). "The Equivalence of Generalized Least Squares and Maximum Likelihood Estimates in the Exponential Family". In: *Journal of the American Statistical Association* 71.353, pp. 169–171.

Collette, A., E. Grün, D. M. Malaspina, et al. (2014). "Micrometeoroid impact charge yield for common spacecraft materials". In: *Journal of Geophysical Research: Space Physics* 119.8, pp. 6019–6026.

Collette, A., D. M. Malaspina, and Z. Sternovsky (2016). "Characteristic temperatures of hypervelocity dust impact plasmas". In: *Journal of Geophysical Research: Space Physics* 121.9, pp. 8182–8187.

Czechowski, A. and I. Mann (2010). "Formation and acceleration of nano dust in the inner heliosphere". In: *The Astrophysical Journal* 714.1, p. 89.

Damlen, P., J. Wakefield, and S. Walker (1999). "Gibbs sampling for Bayesian non-conjugate and hierarchical models by using auxiliary variables". In: *Journal of the Royal Statistical Society: Series B (Statistical Methodology)* 61.2, pp. 331–344.

DeLuca, M., T. Munsat, E. Thomas, et al. (2018). "The ionization efficiency of aluminum and iron at meteoric velocities". In: *Planetary and Space Science* 156, pp. 111–116.

DeLuca, M., Z. Sternovsky, S. P. Armes, et al. (2022). "Differential ablation of organic coatings from micrometeoroids simulated in the laboratory". In: *Journal of Geophysical Research: Planets* 127.4.

Desert, F.-X., F. Boulanger, and J. L. Puget (1990). "Interstellar dust models for extinction and emission". In: *Astronomy and Astrophysics* 237, pp. 215–236.

Dietzel, H., G. Eichhorn, H. Fechtig, et al. (1973). "The HEOS 2 and HELIOS micrometeoroid experiments". In: *Journal of Physics E: Scientific Instruments* 6.3, p. 209.

Dohnanyi, J. S. (1969). "Collisional model of asteroids and their debris". In: *Journal of Geophysical Research* 74.10, pp. 2531–2554.

Dohnanyi, J. S. (1978). "Particle dynamics." In: *Cosmic dust*. Wiley, pp. 527–605.

Dostoevsky, F. (1880). *The Brothers Karamazov*. translated by Constance Garnett.

Drapatz, S. and K. W. Michel (1974). "Theory of shock-wave ionization upon high-velocity impact of micrometeorites". In: *Zeitschrift für Naturforschung A* 29.6, pp. 870–879.

Duda, R. and L. Rejl (1986). *Minerals of the World*. Spring books. Spring. ISBN: 9780600333753.

Dzhanoev, A. R., J. Schmidt, X. Liu, et al. (2016). "Charging of small grains in a space plasma: Application to Jovian stream particles". In: *Astronomy & Astrophysics* 591, A147.

ESA (2023). *ESA Science Satellite Fleet — Solar Orbiter 3D model*. Version 2.0.0. Accessed: 19.3.2023. URL: `https://scifleet.esa.int/model/solar_orbiter`.

Fechtig, H., U. Gerloff, and J. H. Weihrauch (1968). "Results of cosmic-dust collection on Luster 1965". In: *Journal of Geophysical Research* 73.16, pp. 5029–5037.

Fernández, J. A., P. Lemos, and T. Gallardo (2021). "On the origin of the Kreutz family of sungrazing comets". In: *Monthly Notices of the Royal Astronomical Society* 508.1, pp. 789–802.

Fink, D. (1997). *A compendium of conjugate priors*. Accessed: 1.7.2024". URL: `johndcook.com/CompendiumOfConjugatePriors.pdf`.

Friichtenicht, J. F. (1962). "Two-million-volt electrostatic accelerator for hypervelocity research". In: *Review of Scientific Instruments* 33.2, pp. 209–212.

Friichtenicht, J. F. (1964). "Micrometeroid simulation using nuclear accelerator techniques". In: *Nuclear Instruments and Methods* 28.1, pp. 70–78.

Fujiwara, A., G. Kamimoto, and A. Tsukamoto (1977). "Destruction of basaltic bodies by high-velocity impact". In: *Icarus* 31.2, pp. 277–288.

Garcia, M. (2018). *NASA-3D-Resources/3D Models/Parker Solar Probe*. Commit: 39dc094. URL: `https://https://github.com/nasa/NASA-3D-Resources`.

Gault, D. E., E. M. Shoemaker, and H. J. Moore (1963). *Spray ejected from the lunar surface by meteoroid impact*. National Aeronautics and Space Administration.

Gault, D. E. and J. A. Wedekind (1969). "The destruction of tektites by micrometeoroid impact". In: *Journal of Geophysical Research* 74.27, pp. 6780–6794.

Geman, S. and D. Geman (1984). "Stochastic relaxation, Gibbs distributions, and the Bayesian restoration of images". In: *IEEE Transactions on pattern analysis and machine intelligence* 6, pp. 721–741.

Giese, R. H., B. Kneissel, and U. Rittich (1986). "Three-dimensional models of the zodiacal dust cloud: a comparative study". In: *Icarus* 68.3, pp. 395–411.

Gómez-Rubio, V. (2020). *Bayesian inference with INLA*. Chapman and Hall/CRC.

Grün, E. (1984). "Impact ionization from gold, aluminum and PCB-Z". In: *The Giotto Spacecraft Impact-induced Plasma Environment*, pp. 39–41.

Grün, E., H. Fechtig, M. S. Hanner, et al. (1992a). "The Galileo dust detector". In: *Space Science Reviews* 60, pp. 317–340.

Grün, E., H. Fechtig, J. Kissel, et al. (1992b). "The Ulysses dust experiment". In: *Astronomy and Astrophysics Supplement Series (ISSN 0365-0138), vol. 92, no. 2, Jan. 1992, p. 411-423.* 92, pp. 411–423.

Grün, E., H. A. Zook, M Baguhl, et al. (1993). "Discovery of Jovian dust streams and interstellar grains by the Ulysses spacecraft". In: *Nature* 362.6419, pp. 428–430.

Grün, E., H. A. Zook, H. Fechtig, et al. (1985). "Collisional balance of the meteoritic complex". In: *Icarus* 62.2, pp. 244–272.

Gu, J., Z. Wang, J. Kuen, et al. (2018). "Recent advances in convolutional neural networks". In: *Pattern recognition* 77, pp. 354–377.

Guillemant, S., V. Génot, J.-C. M. Velez, et al. (2013). "Simulation study of spacecraft electrostatic sheath changes with the heliocentric distances from 0.044 to 1 AU". In: *IEEE Transactions on Plasma Science* 41.12, pp. 3338–3348.

Gunnarsdottir, T. (2019). "Charging effects and detection of mesospheric dust with the instrument spid on the g-chaser rocket". MA thesis. UiT Norges arktiske universitet.

Gurnett, D. A., J. A. Ansher, W. S. Kurth, et al. (1997). "Micron-sized dust particles detected in the outer solar system by the Voyager 1 and 2 plasma wave instruments". In: *Geophysical research letters* 24.24, pp. 3125–3128.

Gurnett, D. A., E. Grün, D. Gallagher, et al. (1983). "Micron-sized particles detected near Saturn by the Voyager plasma wave instrument". In: *Icarus* 53.2, pp. 236–254.

Hastings, W. K. (1970). "Monte Carlo sampling methods using Markov chains and their applications". In.

Henri, P., N. Meyer-Vernet, C. Briand, et al. (2011). "Observations of Langmuir ponderomotive effects using the Solar TErrestrial RElations Observatory spacecraft as a density probe". In: *Physics of Plasmas* 18.8.

Henriksen, A. J. (2022). "Interstellar Dust in the Inner Heliosphere and Impact Detection Capabilities with ESA's Solar Orbiter Spacecraft". MA thesis. UiT Norges arktiske universitet.

Horányi, M. (1996). "Charged dust dynamics in the solar system". In: *Annual review of astronomy and astrophysics* 34.1, pp. 383–418.

Horányi, M., X. Wang, S. Robertson, et al. (2008). "Surface—Plasma Interaction on the Moon". In: *AIP Conference Proceedings*. Vol. 1041. American Institute of Physics, pp. 113–116.

Hornung, K. and J. Kissel (1994). "On shock wave impact ionization of dust particles". In: *Astronomy and Astrophysics* 291, pp. 324–336.

Humes, D. H. (1980). "Results of Pioneer 10 and 11 Meteoroid Experiments: Interplanetary and near-Saturn". In: *Journal of Geophysical Research: Space Physics* 85.A11, pp. 5841–5852.

Humes, D. H., J. M. Alvarez, R. L. O'Neal, et al. (1974). "The interplanetary and near-Jupiter meteoroid environments". In: *Journal of Geophysical Research* 79.25, pp. 3677–3684.

James, D., V. Hoxie, and M. Horanyi (Mar. 2010). "Polyvinylidene fluoride dust detector response to particle impacts". In: *Review of Scientific Instruments* 81.3, p. 034501.

Jenniskens, P., T. J. Jopek, D. Janches, et al. (2020). "On removing showers from the IAU Working List of Meteor Showers". In: *Planetary and Space Science* 182, p. 104821.

Jenniskens, P., Q. Nénon, P. S. Gural, et al. (2016). "CAMS newly detected meteor showers and the sporadic background". In: *Icarus* 266, pp. 384–409.

Jessberger, E. K., A. Christoforidis, and J. Kissel (1988). "Aspects of the major element composition of Halley's dust". In: *Nature* 332.6166, pp. 691–695.

Jessberger, E. K., S. Thomas, R. Detlef, et al. (2001). "Properties of Interplanetary Dust: Information from Collected Samples". In: *Interplanetary Dust*. Berlin, Heidelberg: Springer Berlin Heidelberg, pp. 253–294. ISBN: 978-3-642-56428-4.

Jones, G. H., M. M. Knight, K. Battams, et al. (2018). "The science of sungrazers, sunskirters, and other near-sun comets". In: *Space Science Reviews* 214, pp. 1–86.

Jones, G. L. (2004). "On the Markov chain central limit theorem". In: *Probability Surveys* 1.none, pp. 299–320.

Kalinicheva, O. V. (2017). "Specific features of orbits of Kreutz dwarf comets". In: *Solar System Research* 51, pp. 221–232.

Keller, L. P., S. Bajt, G. A. Baratta, et al. (2006). "Infrared Spectroscopy of Comet 81P/Wild 2 Samples Returned by Stardust". In: *Science* 314.5806, pp. 1728–1731.

Kellogg, P. J. (2017). "Note on the Pantellini et al. process for dust impact signals on spacecraft". In: *Journal of Geophysical Research: Space Physics* 122.1, pp. 63–70.

Kellogg, P. J., K. Goetz, and S. J. Monson (2016). "Dust impact signals on the wind spacecraft". In: *Journal of Geophysical Research: Space Physics* 121.2, pp. 966–991.

Kempf, S., U. Beckmann, and J. Schmidt (2010). "How the Enceladus dust plume feeds Saturn's E ring". In: *Icarus* 206.2, pp. 446–457.

Kempf, S., R. Srama, M. Horányi, et al. (2005). "High-velocity streams of dust originating from Saturn". In: *Nature* 433.7023, pp. 289–291.

Kimura, H. and I. Mann (1998). "The electric charging of interstellar dust in the solar system and consequences for its dynamics". In: *The Astrophysical Journal* 499.1, p. 454.

Kimura, H., I. Mann, and E. K. Jessberger (2003). "Composition, structure, and size distribution of dust in the local interstellar cloud". In: *The Astrophysical Journal* 583.1, p. 314.

Kissel, J. and F. R. Krueger (1987). "Ion formation by impact of fast dust particles and comparison with related techniques". In: *Applied Physics A* 42, pp. 69–85.

Klepper, K. (2021). "The influence of mass loss on the dynamics of dust near the Sun". MA thesis. UiT Norges arktiske universitet.

Kneißel, B. and I. Mann (1991). "Spatial distribution and orbital properties of zodiacal dust". In: *International Astronomical Union Colloquium*. Vol. 126. Cambridge University Press, pp. 139–146.

Kočiščák, S., Å. Fredriksen, M. DeLuca, et al. (2020). "Effective temperatures of olivine dust impact plasmas". In: *IEEE Transactions on Plasma Science* 48.12, pp. 4298–4304.

Kopp, G. and J. L. Lean (2011). "A new, lower value of total solar irradiance: Evidence and climate significance". In: *Geophysical Research Letters* 38.1.

Kreutz, H. (1888). *Untersuchungen über das Cometensystem 1843 I, 1880 I und 1882 II.* 3. Druck von C. Schaidt, CF Mohr nachfl.

Krivov, A., H. Kimura, and I. Mann (1998). "Dynamics of dust near the Sun". In: *Icarus* 134.2, pp. 311–327.

Krüger, H., M. Horányi, A. V. Krivov, et al. (2004). "Jovian dust: streams, clouds and rings". In: *Jupiter: The Planet, Satellites and Magnetosphere*, pp. 219–240.

Kurth, W. S., T. F. Averkamp, D. A. Gurnett, et al. (2006). "Cassini RPWS observations of dust in Saturn's E ring". In: *Planetary and Space Science* 54.9-10, pp. 988–998.

Laakso, H., R. Grard, A. Pedersen, et al. (1989). "Impacts of large dust particles on the VEGA spacecraft". In: *Advances in Space Research* 9.3, pp. 269–272.

Langmuir, I. (1918). "The evaporation of small spheres". In: *Physical review* 12.5, p. 368.

Leinert, C. H., I. Richter, E. Pitz, et al. (1981). "The zodiacal light from 1.0 to 0.3 AU as observed by the Helios space probes". In: *Astronomy and Astrophysics, vol. 103, no. 1, Nov. 1981, p. 177-188. Bundesministerium für Forschung und Technologie* 103, pp. 177–188.

Leinert, C. H., S. Roser, and J. Buitrago (1983). "How to maintain the spatial distribution of interplanetary dust". In: *Astronomy and Astrophysics, vol. 118, no. 2, Feb. 1983, p. 345-357.* 118, pp. 345–357.

Lemoine, N. P. (2019). "Moving beyond noninformative priors: why and how to choose weakly informative priors in Bayesian analyses". In: *Oikos* 128.7, pp. 912–928.

Lesceux, J. M., J. Lemaire, and N. Meyer-Vernet (1989). "Electric dipole antennae used as micrometeoroid detectors". In: *Planetary and space science* 37.10, pp. 1291–1302.

Liu, L.-G. and W. A. Bassett (1975). "The melting of iron up to 200 kbar". In: *Journal of Geophysical Research (1896-1977)* 80.26, pp. 3777–3782.

Love, S. G. and D. E. Brownlee (1993). "A Direct Measurement of the Terrestrial Mass Accretion Rate of Cosmic Dust". In: *Science* 262.5133, pp. 550–553.

Maksimovic, M., S. D. Bale, T. Chust, et al. (2020). "The Solar Orbiter Radio and Plasma Waves (RPW) instrument". In: *Astronomy & Astrophysics* 642, A12.

Malaspina, D. M., M. Horányi, A. Zaslavsky, et al. (2014). "Interplanetary and interstellar dust observed by the Wind/WAVES electric field instrument". In: *Geophysical Research Letters* 41.2, pp. 266–272.

Malaspina, D. M., D. L. Newman, L. B. Willson III, et al. (2013). "Electrostatic solitary waves in the solar wind: Evidence for instability at solar wind current sheets". In: *Journal of Geophysical Research: Space Physics* 118.2, pp. 591–599.

Malaspina, D. M., L. E. O'Brien, F. Thayer, et al. (2015). "Revisiting STEREO interplanetary and interstellar dust flux and mass estimates". In: *Journal of Geophysical Research: Space Physics* 120.8, pp. 6085–6100.

Malaspina, D. M., G. Stenborg, D. Mehoke, et al. (2022). "Clouds of spacecraft debris liberated by hypervelocity dust impacts on parker solar probe". In: *The Astrophysical Journal* 925.1, p. 27.

Malaspina, D. M., A. Toma, J. R. Szalay, et al. (2023). "A Dust Detection Database for the Inner Heliosphere Using the Parker Solar Probe Spacecraft". In: *The Astrophysical Journal Supplement Series* 266.2, p. 21.

Malaspina, D. M. and L. B. Wilson (2016). "A database of interplanetary and interstellar dust detected by the Wind spacecraft". In: *Journal of Geophysical Research: Space Physics* 121.10, pp. 9369–9377.

Mann, I. (2010). "Interstellar dust in the solar system". In: *Annual Review of Astronomy and Astrophysics* 48, pp. 173–203.

Mann, I., H. Kimura, D. A. Biesecker, et al. (2004). "Dust near the Sun". In: *Space science reviews* 110, pp. 269–305.

Mann, I., N. Meyer-Vernet, and A. Czechowski (2014). "Dust in the planetary system: Dust interactions in space plasmas of the solar system". In: *Physics reports* 536.1, pp. 1–39.

Mann, I., E. Murad, and A. Czechowski (2007). "Nanoparticles in the inner solar system". In: *Planetary and Space Science* 55.9, pp. 1000–1009.

Mann, I., L. Nouzák, J. Vaverka, et al. (2019). "Dust observations with antenna measurements and its prospects for observations with Parker Solar Probe and Solar Orbiter". In: *Annales Geophysicae*. Vol. 37. 6. Copernicus GmbH, pp. 1121–1140.

Markov, A. A. (1906). "Extension of the law of large numbers to quantities, depending on each other. Reprint 2006." In: *Journal Électronique d'Histoire des Probabilités et de la Statistique* 2.1b, Article 10, 12 p.

Martins, T. G., D. Simpson, F. Lindgren, et al. (2013). "Bayesian computing with INLA: new features". In: *Computational Statistics & Data Analysis* 67, pp. 68–83.

Maxwell, J. C. (1877). "On the Electrical Capacity of a long narrow Cylinder, and of a Disk of sensible Thickness". In: *Proceedings of the London mathematical society* 1.1, pp. 94–102.

McBride, N. and J. A. M. McDonnell (1999). "Meteoroid impacts on spacecraft: sporadics, streams, and the 1999 Leonids". In: *Planetary and Space Science* 47.8-9, pp. 1005–1013.

McDonnell, J. A. M., W. C. Carey, and D. G. Dixon (1984). "Cosmic dust collection by the capture cell technique on the Space Shuttle". In: *Nature* 309.5965, pp. 237–240.

Metropolis, N., A. W. Rosenbluth, M. N. Rosenbluth, et al. (1953). "Equation of state calculations by fast computing machines". In: *The journal of chemical physics* 21.6, pp. 1087–1092.

Meuris, P., N. Meyer-Vernet, and J. F. Lemaire (1996). "The detection of dust grains by a wire dipole antenna: The radio dust analyzer". In: *Journal of Geophysical Research: Space Physics* 101.A11, pp. 24471–24477.

Meyer-Vernet, N. (1982). "Flip-flop of electric potential of dust grains in space". In: *Astronomy and Astrophysics, vol. 105, no. 1, Jan. 1982, p. 98-106.* 105, pp. 98–106.

Meyer-Vernet, N. (2001). "Detecting dust with electric sensors in planetary rings, comets and interplanetary space". In: *Spacecraft Charging Technology*. Vol. 476, p. 635.

Meyer-Vernet, N., A. Lecacheux, M. L. Kaiser, et al. (2009a). "Detecting nanoparticles at radio frequencies: Jovian dust stream impacts on Cassini/RPWS". In: *Geophysical Research Letters* 36.3.

Meyer-Vernet, N., M. Maksimovic, A. Czechowski, et al. (2009b). "Dust detection by the wave instrument on STEREO: nanoparticles picked up by the solar wind?" In: *Solar Physics* 256, pp. 463–474.

Meyer-Vernet, N., M. Moncuquet, K. Issautier, et al. (2014). "The importance of monopole antennas for dust observations: Why Wind/WAVES does not detect nanodust". In: *Geophysical Research Letters* 41.8, pp. 2716–2720.

Meyer-Vernet, N., M. Moncuquet, K. Issautier, et al. (2017). "Frequency range of dust detection in space with radio and plasma wave receivers: Theory and application to interplanetary nanodust impacts on Cassini". In: *Journal of Geophysical Research: Space Physics* 122.1, pp. 8–22.

Min, M., J. W. Hovenier, and A. de Koter (2005). "Modeling optical properties of cosmic dust grains using a distribution of hollow spheres". In: *Astronomy & Astrophysics* 432.3, pp. 909–920.

Morfill, G. E. and E. Grün (1979). "The motion of charged dust particles in interplanetary space—II. Interstellar grains". In: *Planetary and Space Science* 27.10, pp. 1283–1292.

Mukai, T. and T. Yamamoto (1982). "Solar wind pressure on interplanetary dust". In: *Astronomy and Astrophysics, vol. 107, no. 1, Mar. 1982, p. 97-100.* 107, pp. 97–100.

Myrvang, M. (2018). "Temperature and thermal emission of cosmic dust around the Sun, Vega and Fomalhaut". MA thesis. UiT Norges arktiske universitet.

Nesvorný, D., P. Jenniskens, H. F. Levison, et al. (2010). "Cometary origin of the zodiacal cloud and carbonaceous micrometeorites. Implications for hot debris disks". In: *The Astrophysical Journal* 713.2, p. 816.

Nouzák, L., S. Hsu, D. M. Malaspina, et al. (2018). "Laboratory modeling of dust impact detection by the Cassini spacecraft". In: *Planetary and Space Science* 156, pp. 85–91.

Nouzák, L., D. James, Z. Němeček, et al. (2021). "Detection of Dust Particles Using Faraday Cup Instruments". In: *The Astrophysical Journal* 909.2, p. 132.

Pantellini, F., S. Belheouane, N. Meyer-Vernet, et al. (2012). "Nano dust impacts on spacecraft and boom antenna charging". In: *Astrophysics and Space Science* 341, pp. 309–314.

Parker, E. N. (1958). "Dynamics of the interplanetary gas and magnetic fields." In: *Astrophysical Journal, vol. 128, p. 664* 128, p. 664.

Pettersson, H. (1958). "Rate of accretion of cosmic dust on the earth". In: *Nature* 181.4605, pp. 330–330.

Pickett, J. S., S. W. Kahler, L.-J. Chen, et al. (2004). "Solitary waves observed in the auroral zone: the Cluster multi-spacecraft perspective". In: *Nonlinear Processes in Geophysics* 11.2, pp. 183–196.

Pinti, D. L., M. Gargaud, W. M. Irvine, et al. (2015). "Olivine". In: *Encyclopedia of Astrobiology*. Berlin, Heidelberg: Springer Berlin Heidelberg, pp. 1769–1770. ISBN: 978-3-662-44185-5.

Poppe, A. R. and C. O. Lee (2020). "The effects of solar wind structure on nanodust dynamics in the inner heliosphere". In: *Journal of Geophysical Research: Space Physics* 125.10.

Poppe, A. R. and C. O. Lee (2022). "The effects of solar cycle variability on nanodust dynamics in the inner heliosphere: Predictions for future STEREO A/WAVES measurements". In: *Journal of Geophysical Research: Space Physics* 127.5.

Poynting, J. H. (1903). "Radiation in the solar system: its effect on temperature and its pressure on small bodies". In: *Monthly Notices of the Royal Astronomical Society, Vol. 64, Appendix, p. 1* 64, p. 1.

R-INLA (n.d.). *R-INLA Project*. Accessed: 18.6.2024. URL: `https://www.r-inla.org/`.

Racković Babić, K. (2022). "In-situ dust detection using radio antennas of different spacecraft: space observations and modeling". PhD thesis. Université Paris sciences et lettres; Univerzitet u Beogradu.

Racković Babić, K., A. Zaslavsky, K. Issautier, et al. (2022). "An analytical model for dust impact voltage signals and its application to STEREO/WAVES data". In: *Astronomy & Astrophysics* 659, A15.

Ramanujan, A. S. (1920). *Lost notebook and other unpublished papers*. Accessed: 19.6.2024. URL: `https://archive.org/details/lost-notebook/page/n337`.

Robertson, H. P. (1937). "Dynamical effects of radiation in the solar system". In: *Monthly Notices of the Royal Astronomical Society, Vol. 97, p. 423* 97, p. 423.

Roosen, R. G. (1971). "The gegenschein". In: *Reviews of Geophysics* 9.2, pp. 275–304.

Rue, H., S. Martino, and N. Chopin (2009). "Approximate Bayesian inference for latent Gaussian models by using integrated nested Laplace approximations". In: *Journal of the Royal Statistical Society Series B: Statistical Methodology* 71.2, pp. 319–392.

Russell, H. N. (1929). "On meteoric matter near the stars". In: *Astrophysical Journal, vol. 69, p. 49* 69, p. 49.

Samek, W., G. Montavon, S. Lapuschkin, et al. (2021). "Explaining deep neural networks and beyond: A review of methods and applications". In: *Proceedings of the IEEE* 109.3, pp. 247–278.

Sartre, J. P. (1956). *Being and Nothingness*. Philosophical Library.

Scarf, F. L., D. A. Gurnett, W. S. Kurth, et al. (1982). "Voyager 2 plasma wave observations at Saturn". In: *Science* 215.4532, pp. 587–594.

Schippers, P., N. Meyer-Vernet, A. Lecacheux, et al. (2014). "Nanodust detection near 1 AU from spectral analysis of Cassini/Radio and Plasma Wave Science data". In: *Geophysical Research Letters* 41.15, pp. 5382–5388.

Schippers, P., N. Meyer-Vernet, A. Lecacheux, et al. (2015). "Nanodust detection between 1 and 5 AU using Cassini wave measurements". In: *The Astrophysical Journal* 806.1, p. 77.

Shelton, H., C. D. Hendricks Jr., and R. F. Wuerker (1960). "Electrostatic acceleration of microparticles to hypervelocities". In: *Journal of Applied Physics* 31.7, pp. 1243–1246.

Shen, M. M. (2021). "Cosmic Dust Detection by Antenna Instruments — Modeling and Laboratory Measurements". PhD thesis. University of Colorado at Boulder.

Shen, M. M., Z. Sternovsky, A. Garzelli, et al. (2021a). "Electrostatic model for antenna signal generation from dust impacts". In: *Journal of Geophysical Research: Space Physics* 126.9.

Shen, M. M., Z. Sternovsky, M. Horányi, et al. (2021b). "Laboratory study of antenna signals generated by dust impacts on spacecraft". In: *Journal of Geophysical Research: Space Physics* 126.4, e2020JA028965.

Shen, M. M., Z. Sternovsky, and D. M. Malaspina (2023). "Variability of Antenna Signals From Dust Impacts". In: *Journal of Geophysical Research: Space Physics* 128.4.

Sheppard, S. S., D. J. Tholen, M. Alexandersen, et al. (2023). "New Jupiter and Saturn Satellites Reveal New Moon Dynamical Families". In: *Research Notes of the AAS* 7.5, p. 100.

Shu, A., A. Collette, K. Drake, et al. (2012). "3 MV hypervelocity dust accelerator at the Colorado Center for Lunar Dust and Atmospheric Studies". In: *Review of Scientific Instruments* 83.7.

Shue, J.-H., P. Song, C. T. Russell, et al. (1998). "Magnetopause location under extreme solar wind conditions". In: *Journal of Geophysical Research: Space Physics* 103.A8, pp. 17691–17700.

Simpson, J. A., D. Rabinowitz, A. J. Tuzzolino, et al. (1988). "The dust coma of comet P/Halley: Measurements on the Vega-1 and Vega-2 spacecraft". In: *Exploration of Halley's Comet*. Springer, pp. 742–752.

Sofia, U. J., J. A. Cardelli, and B. D. Savage (1994). "The abundant elements in interstellar dust". In: *The Astrophysical Journal, vol. 430, no. 2, pt. 1, p. 650-666* 430, pp. 650–666.

Sommer, M. (2023). "Alpha-Meteoroids then and now: Unearthing an overlooked micrometeoroid population". In: *Planetary and Space Science* 236, p. 105751.

Sommer, M., Y. Li, R. Srama, et al. (2023). "Measuring Micro-Debris In-Situ with the DESTINY+ Dust Analyzer". In: *2nd NEO and Debris Detection Conference*, p. 37.

Spahn, F., J. Schmidt, N. Albers, et al. (2006). "Cassini dust measurements at Enceladus and implications for the origin of the E ring". In: *Science* 311.5766, pp. 1416–1418.

Srama, R., T. J. Ahrens, N. Altobelli, et al. (2004). "The Cassini cosmic dust analyzer". In: *Space Science Reviews* 114, pp. 465–518.

Stefan, J. (1879). "Uber die beziehung zwischen der warmestrahlung und der temperatur, sitzungsberichte der mathematisch-naturwissenschaftlichen classe der kaiserlichen". In: *Akademie der Wissenschaften* 79, S–391.

Steinvall, K., Y. V. Khotyaintsev, D. B. Graham, et al. (2019). "Multispacecraft analysis of electron holes". In: *Geophysical Research Letters* 46.1, pp. 55–63.

Stenborg, G., R. A Howard, A. Vourlidas, et al. (2022). "PSP/WISPR observations of dust density depletion near the Sun. II. New insights from within the depletion zone". In: *The Astrophysical Journal* 932.2, p. 75.

Stenborg, G., R. A. Howard, P. Hess, et al. (2021). "PSP/WISPR observations of dust density depletion near the Sun-I. Remote observations to $8R\odot$ from an observer between 0.13 and 0.35 AU". In: *Astronomy & Astrophysics* 650, A28.

Stenborg, G., R. A. Howard, and J. R. Stauffer (2018). "Characterization of the white-light brightness of the F-corona between 5 and 24 elongation". In: *The Astrophysical Journal* 862.2, p. 168.

Szalay, J. R., P. Pokornỳ, S. D. Bale, et al. (2020). "The near-sun dust environment: initial observations from parker solar probe". In: *The Astrophysical Journal Supplement Series* 246.2, p. 27.

Szalay, J. R., P. Pokornỳ, D. M. Malaspina, et al. (2021). "Collisional evolution of the inner zodiacal cloud". In: *The Planetary Science Journal* 2.5, p. 185.

Tarnecki, L. K., R. A. Marshall, J. Fontanese, et al. (2023). "Experimentally derived luminous efficiencies for aluminum and iron at meteoric speeds". In: *Geophysical Research Letters* 50.7.

Taylor, S., S. Messenger, and L. Folco (2016). "Cosmic dust: finding a needle in a haystack". In: *Elements* 12.3, pp. 171–176.

Thomas, E., J. Simolka, M. DeLuca, et al. (2017). "Experimental setup for the laboratory investigation of micrometeoroid ablation using a dust accelerator". In: *Review of Scientific Instruments* 88.3.

Trollvik, H. M. T., T. Gunnarsdottir, I. Mann, et al. (2019). "Observation of mesospheric dust and ionospheric conditions during the G-chaser rocket campaign". In.

Tsou, P. (1995). "Silica aerogel captures cosmic dust intact". In: *Journal of Non-Crystalline Solids* 186, pp. 415–427.

Tsurutani, B. T., D. R. Clay, L. D. Zhang, et al. (2003). "Dust impacts at comet P/Borrelly". In: *Geophysical research letters* 30.22.

Tuzzolino, A. J. (1996). "Applications of PVDF dust sensor systems in space". In: *Advances in Space Research* 17.12, pp. 123–132.

Utterback, N. G. and J. Kissel (1990). "Attogram dust cloud a million kilometers from comet Halley". In: *Astronomical Journal* 100, pp. 1315–1322.

Van de Hulst, H. C. (1947). "Zodiacal Light in the Solar Corona." In: *Astrophysical Journal, vol. 105, p. 471* 105, p. 471.

Vapnik, V. N. (1997). "The support vector method". In: *International conference on artificial neural networks*. Springer, pp. 261–271.

Vaverka, J., Takuji Nakamura, Johan Kero, et al. (2018). "Comparison of dust impact and solitary wave signatures detected by multiple electric field antennas onboard the MMS spacecraft". In: *Journal of Geophysical Research: Space Physics* 123.8, pp. 6119–6129.

Vaverka, J., J. Pavlů, L. Nouzák, et al. (2021). "Ion Cloud Expansion after Hyper-velocity Dust Impacts Detected by the Magnetospheric Multiscale Mission Electric Probes in the Dipole Configuration". In: *The Astrophysical Journal* 921.2, p. 127.

Vaverka, J., Asta Pellinen-Wannberg, Johan Kero, et al. (2017). "Detection of meteoroid hypervelocity impacts on the Cluster spacecraft: First results". In: *Journal of Geophysical Research: Space Physics* 122.6, pp. 6485–6494.

Vaverka, J., I. Richterová, J. Pavlů, et al. (2016). "Lunar surface and dust grain potentials during the earth's magnetosphere crossing". In: *The Astrophysical Journal* 825.2, p. 133.

Vondrak, T., J. M. C. Plane, S. Broadley, et al. (2008). "A chemical model of meteoric ablation". In: *Atmospheric Chemistry and Physics* 8.23, pp. 7015–7031.

Vyšinka, M. (2018). "Odprašování prachových zrn a jeho vazba na procesy v kosmickém prostoru." PhD thesis. Univerzita Karlova, Matematicko-fyzikální fakulta.

Whipple, F. L. (1958). "The meteoritic risk to space vehicles". In: *VIII th International Astronautical Congress Barcelona 1957*. Springer, pp. 418–428.

Whipple, F. L. (1967). "On maintaining the meteoritic complex". In: *SAO Special Report* 239, p. 1.

Wickstrøm, K., M. Kampffmeyer, K. Ø. Mikalsen, et al. (2022). "Mixing up contrastive learning: Self-supervised representation learning for time series". In: *Pattern Recognition Letters* 155, pp. 54–61.

Witte, M. (2004). "Kinetic parameters of interstellar neutral helium-Review of results obtained during one solar cycle with the Ulysses/GAS-instrument". In: *Astronomy & Astrophysics* 426.3, pp. 835–844.

Wyatt, S. P. and F. L. Whipple (1950). "The Poynting-Robertson effect on meteor orbits". In: *Astrophysical Journal, vol. 111, p. 134-141 (1950).* 111, pp. 134–141.

Yang, H. and M. Ishiguro (2015). "Origin of interplanetary dust through optical properties of zodiacal light". In: *The Astrophysical Journal* 813.2, p. 87.

Ye, S.-Y., J. Vaverka, L. Nouzak, et al. (2019). "Understanding Cassini RPWS antenna signals triggered by dust impacts". In: *Geophysical Research Letters* 46.20, pp. 10941–10950.

Zaslavsky, A. (2015). "Floating potential perturbations due to micrometeoroid impacts: Theory and application to S/WAVES data". In: *Journal of Geophysical Research: Space Physics* 120.2, pp. 855–867.

Zaslavsky, A., I. Mann, J. Soucek, et al. (2021). "First dust measurements with the Solar Orbiter Radio and Plasma Wave instrument". In: *Astronomy & Astrophysics* 656, A30.

Zaslavsky, A., N. Meyer-Vernet, I. Mann, et al. (2012). "Interplanetary dust detection by radio antennas: Mass calibration and fluxes measured by STEREO/WAVES". In: *Journal of Geophysical Research: Space Physics* 117.A5.

Zook, H. A. and O. E. Berg (1975). "A source for hyperbolic cosmic dust particles". In: *Planetary and Space Science* 23.1, pp. 183–203.

Paper I:
Machine learning detection of dust impact signals observed by the Solar Orbiter

A. Kvammen, K. Wickstrøm, S. Kočiščák, J. Vaverka, L. Nouzák, A. Zaslavsky, K. Racković Babić, A. Gjelsvik, D. Píša, J. Souček, and I. Mann
Annales Geophysicae 41, No. 1 (2023)
doi: 10.5194/angeo-41-69-2023
GitHub: AndreasKvammen/ML_dust_detection

Ann. Geophys., 41, 69–86, 2023
https://doi.org/10.5194/angeo-41-69-2023

Annales Geophysicae
Open Access
EGU

Machine learning detection of dust impact signals observed by the Solar Orbiter

Andreas Kvammen[1], Kristoffer Wickstrøm[1], Samuel Kociscak[1], Jakub Vaverka[2], Libor Nouzak[2], Arnaud Zaslavsky[3], Kristina Rackovic Babic[3,4], Amalie Gjelsvik[1], David Pisa[5], Jan Soucek[5], and Ingrid Mann[1]

[1]Department of Physics and Technology, UiT The Arctic University of Norway, 9037 Tromsø, Norway
[2]Department of Surface and Plasma Science, Charles University Prague, 18000 Prague, Czech Republic
[3]LESIA – Observatoire de Paris, Université PSL, CNRS, Sorbonne Université, Université de Paris,
5 place Jules Janssen, 92195 Meudon, France
[4]Department of Astronomy, Faculty of Mathematics, University of Belgrade, Studentski trg 16, 11000 Belgrade, Serbia
[5]Department of Space Physics, Institute of Atmospheric Physics, Czech Academy of Sciences,
Bocni II/1401, 14100 Prague, Czech Republic

Correspondence: Andreas Kvammen (andreas.kvammen@uit.no)

Received: 31 July 2022 – Discussion started: 11 August 2022
Revised: 22 November 2022 – Accepted: 5 December 2022 – Published: 24 January 2023

Abstract. This article presents the results of automatic detection of dust impact signals observed by the Solar Orbiter – Radio and Plasma Waves instrument.

A sharp and characteristic electric field signal is observed by the Radio and Plasma Waves instrument when a dust particle impacts the spacecraft at high velocity. In this way, $\sim$5–20 dust impacts are daily detected as the Solar Orbiter travels through the interplanetary medium. The dust distribution in the inner solar system is largely uncharted and statistical studies of the detected dust impacts will enhance our understanding of the role of dust in the solar system.

It is however challenging to automatically detect and separate dust signals from the plural of other signal shapes for two main reasons. Firstly, since the spacecraft charging causes variable shapes of the impact signals, and secondly because electromagnetic waves (such as solitary waves) may induce resembling electric field signals.

In this article, we propose a novel machine learning-based framework for detection of dust impacts. We consider two different supervised machine learning approaches: the support vector machine classifier and the convolutional neural network classifier. Furthermore, we compare the performance of the machine learning classifiers to the currently used on-board classification algorithm and analyze 2 years of Radio and Plasma Waves instrument data.

Overall, we conclude that detection of dust impact signals is a suitable task for supervised machine learning techniques. The convolutional neural network achieves the highest performance with $96\,\% \pm 1\,\%$ overall classification accuracy and $94\,\% \pm 2\,\%$ dust detection precision, a significant improvement to the currently used on-board classifier with 85 % overall classification accuracy and 75 % dust detection precision. In addition, both the support vector machine and the convolutional neural network classifiers detect more dust particles (on average) than the on-board classification algorithm, with $16\,\% \pm 1\,\%$ and $18\,\% \pm 8\,\%$ detection enhancement, respectively.

The proposed convolutional neural network classifier (or similar tools) should therefore be considered for post-processing of the electric field signals observed by the Solar Orbiter.

1 Introduction

1.1 The dust population in the inner solar system

The interplanetary dust population in the inner solar system (≤ 1 AU) is formed by collisional fragmentation of asteroids, comets and meteoroids. The meteoroids and the larger dust particles are in bound orbits around the Sun and their life-

time is limited by collisions, while the smaller particles that form through collisional fragmentation are repelled from the Sun by the radiation pressure force (Mann et al., 2004). The sources and sinks of the interplanetary dust particles are well studied at the orbit of Earth (Grün et al., 1985), while there have been few observations inside 1 AU until recent years.

Model calculations show that the number density of dust within 1 AU is diminished by collisional destruction (Ishimoto, 2000). However, there are a number of uncertainties that enter the model calculations since the dust collision rates depend both on the dust number density distribution and on the relative velocities between the dust particles. These parameters are generally unknown inside the orbit of the Earth and the estimated sizes of the fragmented dust particles are currently based on empirical relations, inferred from laboratory measurements of accelerated dust particles (Mann and Czechowski, 2005). Furthermore, there is an additional dust population with an interstellar origin that streams through the solar system. The interstellar dust distribution is largely unknown and thus complicates the analysis of the interplanetary dust population. Remote observations of the zodiacal light and the Fraunhofer corona (F-corona) provide some information of the dust population within 1 AU, but mainly of the larger ($>\mu$m) dust particles (Mann et al., 2004). For all these reasons, in situ measurements are needed in order to better understand the role of dust in the inner solar system.

1.2 Exploration of the inner solar system

At present, the inner solar system is explored by the Parker Solar Probe (Szalay et al., 2020), launched 12 August 2018, and the Solar Orbiter (Müller et al., 2020), launched 10 February 2020. Systematic studies of the dust flux near 1 AU are conducted with the Solar Terrestrial Relations Observatory (STEREO) (Zaslavsky et al., 2012) and Wind (Malaspina et al., 2014). The first analyses show that a large fraction of the observed dust particles are repelled from the Sun, i.e., the dust particles are in unbound orbits (Zaslavsky et al., 2021; Szalay et al., 2020; Malaspina et al., 2020). Mann and Czechowski (2021) used model calculations to explain the impact rates observed by the Parker Solar Probe. The dust production was modeled by collisional fragmentation near the Sun and the dust trajectories were calculated with included radiation pressure and Lorentz force terms. Mann and Czechowski (2021) showed that the observed impact rates largely agree with the model calculations for dust >100 nm and proposed that the differences may be explained by the influence of smaller particles and of other dust components, such as dust in bound orbits and interstellar dust.

In this work, we analyze data acquired by the Solar Orbiter. The spacecraft orbits the Sun in an elliptic orbit with a period of approximately 6 months. At perihelion, the Solar Orbiter reaches a minimum solar distance of 0.28 AU, just within the perihelion of the Mercury orbit. The expected mission duration is 7 years, with a possible 3-year extension. The Solar Orbiter will thus provide long-term, in situ observations of the environment in the inner solar system with multiple instruments. One of these instruments is the Radio and Plasma Waves instrument, allowing observations of the cosmic dust flux with typical diameters ranging from ~ 100 to ~ 500 nm (Zaslavsky et al., 2021).

1.3 Radio and plasma waves instruments for dust detection

Radio and plasma waves instruments (i.e., antennas) have been used for studying dust in the solar system since the Voyager mission (Gurnett et al., 1983; Aubier et al., 1983). A dust impact is observed by the spacecraft antennas as a sharp and characteristic electric field signal, produced by the impact ionization process.

The impact ionization process occurs when dust particles hit a target in space with impact speeds on the order of $\sim \mathrm{km\,s^{-1}}$ or larger, impact speeds which are typical for space missions in the interplanetary medium. The kinetic energy of the impact is transferred into deformation, shattering, melting and vaporization of the dust projectile – and target material, producing a cloud of free electrons and ions on the surface of the spacecraft. Laboratory measurements (Collette et al., 2014) and model calculations (Hornung et al., 2000) indicate that the free-charge yield depends on multiple parameters, where the most important are the dust impact velocity, the dust mass, and the material of both the dust projectile and the target (the spacecraft surface) (Mann et al., 2019). The forming cloud of charged particles is partly expanding into the ambient solar wind and is partly recollected by the spacecraft. This induces the characteristic electric field signal, hereafter referred to as the dust impact signal/waveform.

Radio and plasma waves instruments allow for the entire spacecraft body to serve as a dust detector, providing a large collection area in comparison to dedicated dust detection instruments. Thus, radio and plasma waves instruments can provide dust distribution estimates based on thousands of dust impacts each year, statistical products that are difficult to acquire by dedicated dust instruments. Still, radio and plasma waves instruments have lower sensitivities than dedicated dust detectors (Zaslavsky, 2015) and the shape of the dust impact waveform is highly dependent on the potential difference between the spacecraft and the ambient plasma (Vaverka et al., 2017). This complicates the analysis of the dust distribution in the solar system since statistical studies rely on automatic dust detection with high accuracy, which is difficult to attain with the software currently in use.

1.4 Machine learning classification of time series data

In this article, we present a machine learning-based framework as a novel method for detecting dust impact signals in radio and plasma waves instrument data. Machine learning

methods, in particular neural networks in the recent decade, have been extensively used for challenging time series classification problems, such as: speech recognition (Trosten et al., 2019), heart rate monitoring (Wickstrøm et al., 2022) and human activity classification (Villar et al., 2016).

A neural network has previously been used for selecting the signals of interest observed by the WAVES instrument on board the Wind spacecraft (Bougeret et al., 1995). An unsupervised method (self-organizing maps) was used for identifying and categorizing plasma waves in the magnetic field data observed by the MMS_1 spacecraft (Vech and Malaspina, 2021). Still, no machine learning tools have been developed for classifying dust impacts in radio and plasma waves instrument data, although the characteristic signal produced by the impact ionization process is distinctive and could therefore be suitable for machine learning detection.

1.5 Motivation and article structure

The main motivation for this work was to develop a dedicated dust detection tool that can be used to automatically process the large amount of data acquired by the Radio and Plasma Waves instrument on board the Solar Orbiter. The aim was to develop a classifier with a high overall classification accuracy on a balanced data set that can make statistical studies more reliable and easier to conduct. For this project, we defined high accuracy to be ($\gtrsim 95\,\%$) after some initial testing. We considered ($\gtrsim 95\,\%$) accuracy to be satisfactory for meaningful statistical studies and a significant improvement to the currently used classification system. In order to achieve this objective, we used supervised machine learning techniques to develop the dust classifiers, trained and tested on a set of 3000 manually labeled observations.

The remaining of this article is structured as follows. Section 2 explains the Solar Orbiter – Radio and Plasma Waves observations and the on-board algorithm that is currently used for dust impact detection. Section 3 describes the procedure that was used for developing the machine learning classifiers, from the downloaded data to the training and testing of the classifiers. Section 4 investigates the performance of the classifiers and includes the resulting dust impact rates, calculated by analyzing 2 years of automatically classified Solar Orbiter data. Finally, Sect. 5 presents the overall conclusions of this project.

2 Observations and data acquisition

2.1 The Radio and Plasma Waves (RPW) Instrument and the Time Domain Sampler (TDS) receiver

This work focuses on electric field signals (i.e., waveforms) observed by the Radio and Plasma Waves (RPW) instrument on board the Solar Orbiter (Maksimovic et al., 2020). The RPW instrument consists of three antennas operating synchronously and the measured electric potential is recorded by the Time Domain Sampler (TDS) receiver unit (Soucek et al., 2021).

The TDS receiver is designed to capture plasma waves (such as ion acoustic and Langmuir waves) in the frequency range 200 Hz–100 kHz, in addition to the dust impact signals (Soucek et al., 2021). The antenna voltages are converted to electric field values using the antenna effective lengths but are otherwise uncalibrated. We consider only signals sampled with a sampling rate of 262.1 kHz in snapshots of 16 384 time steps, acquired when the TDS receiver was operating in the XLD1 mode.

The XLD1 mode is the most commonly used observational mode of the RPW–TDS system (Soucek et al., 2021). XLD1 is a hybrid mode, where channel 3 ($\boldsymbol{CH}_3$) is operating in monopole mode, while channel 1 ($\boldsymbol{CH}_1$) and channel 2 ($\boldsymbol{CH}_2$) are operating in dipole mode:

$$\boldsymbol{CH}_1 = \left(\frac{V_1 - V_{\mathrm{SC}}}{L_1}\right)\hat{\boldsymbol{L}}_1 - \left(\frac{V_3 - V_{\mathrm{SC}}}{L_3}\right)\hat{\boldsymbol{L}}_3 \tag{1}$$

$$\boldsymbol{CH}_2 = \left(\frac{V_2 - V_{\mathrm{SC}}}{L_2}\right)\hat{\boldsymbol{L}}_2 - \left(\frac{V_1 - V_{\mathrm{SC}}}{L_1}\right)\hat{\boldsymbol{L}}_1 \tag{2}$$

$$\boldsymbol{CH}_3 = \left(\frac{V_2 - V_{\mathrm{SC}}}{L_2}\right)\hat{\boldsymbol{L}}_2, \tag{3}$$

where $V_i - V_{\mathrm{SC}}$ denotes the potential difference between antenna i and the spacecraft body along the antenna boom with unit vector $\hat{\boldsymbol{L}}_i$ and effective length L_i. For this work however, the three RPW antenna signals are all converted to monopole electric field signals ($\boldsymbol{E}_1$, $\boldsymbol{E}_2$, $\boldsymbol{E}_3$) by the following conversion:

$$\begin{aligned}\boldsymbol{E}_1 &= \boldsymbol{CH}_3 - \boldsymbol{CH}_2 = \left(\frac{V_2 - V_{\mathrm{SC}}}{L_2}\right)\hat{\boldsymbol{L}}_2 \\ &\quad - \left(\left(\frac{V_2 - V_{\mathrm{SC}}}{L_2}\right)\hat{\boldsymbol{L}}_2 - \left(\frac{V_1 - V_{\mathrm{SC}}}{L_1}\right)\hat{\boldsymbol{L}}_1\right) \\ &= \left(\frac{V_1 - V_{\mathrm{SC}}}{L_1}\right)\hat{\boldsymbol{L}}_1\end{aligned} \tag{4}$$

$$\boldsymbol{E}_2 = \boldsymbol{CH}_3 = \left(\frac{V_2 - V_{\mathrm{SC}}}{L_2}\right)\hat{\boldsymbol{L}}_2 \tag{5}$$

$$\begin{aligned}\boldsymbol{E}_3 &= \boldsymbol{CH}_3 - \boldsymbol{CH}_2 - \boldsymbol{CH}_1 = \boldsymbol{E}_1 - \boldsymbol{CH}_1 \\ &= \left(\frac{V_1 - V_{\mathrm{SC}}}{L_1}\right)\hat{\boldsymbol{L}}_1 - \left(\left(\frac{V_1 - V_{\mathrm{SC}}}{L_1}\right)\hat{\boldsymbol{L}}_1\right. \\ &\quad \left. - \left(\frac{V_3 - V_{\mathrm{SC}}}{L_3}\right)\hat{\boldsymbol{L}}_3\right) = \left(\frac{V_3 - V_{\mathrm{SC}}}{L_3}\right)\hat{\boldsymbol{L}}_3.\end{aligned} \tag{6}$$

The Solar Orbiter RPW–TDS detection threshold is ~ 5 mV, allowing dust impact identification of the cosmic dust flux with typical diameters ranging from ~ 100 to ~ 500 nm (Zaslavsky et al., 2021).

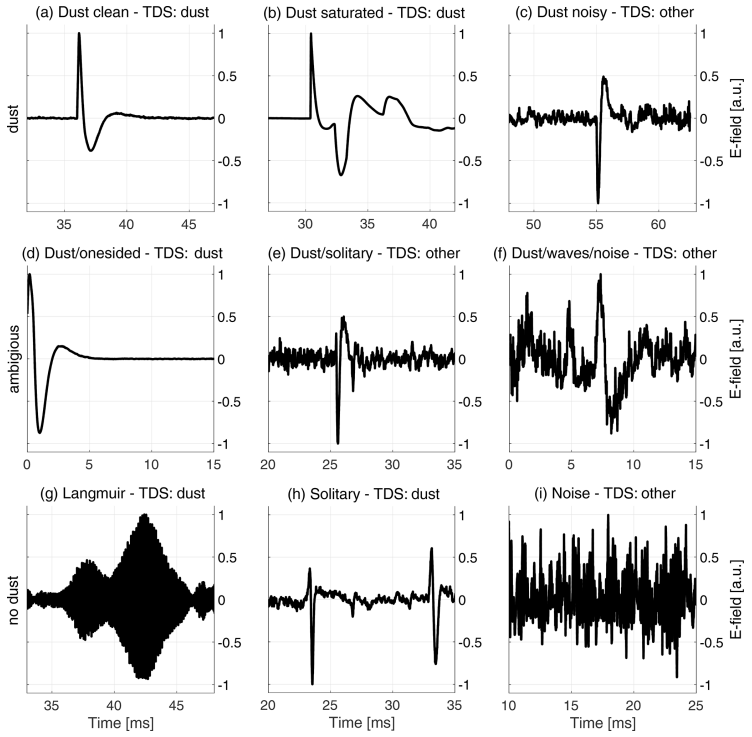

Figure 1. Waveforms recorded by the TDS receiver and measured by one of the RPW antennas. The signal label, classified by the TDS classification algorithm, is included for each snapshot in the subplot titles. The top row presents dust waveforms: **(a)** is a clean dust impact waveform; **(b)** shows a dust impact that saturates the receiver unit (or reaches the non-linearity limit); and **(c)** presents a weak dust impact signal that is strongly affected by noise. The middle row presents ambiguous waveforms: **(d)** might be a dust impact, but information is limited by the signal framing; **(e)** is likely a dust impact, but the signal shape resembles solitary waves and is strongly affected by noise; and **(f)** might be a dust impact, but noise and possible electromagnetic waves make the signal difficult to interpret. The bottom row presents waveforms without dust: **(g)** shows Langmuir waves, characterized by the high-frequency E-field oscillations with a lower-frequency amplitude modulation; **(h)** presents solitary waves, which sometimes resemble dust impact waveforms; and **(i)** shows a signal dominated by noise, without any clear features. Note that the full (63 ms) snapshots are zoomed to 15 ms intervals around the interesting features and that the signal amplitudes are normalized to ± 1 and centered around zero for illustrative purposes.

2.2 The Triggered Snapshot WaveForms (TSWF) data product and the TDS classifier

For this project, we use the Triggered Snapshot WaveForms (TSWF) data product, processed with software version 2.1.1 and acquired over a 25-month period, spanning between 15 June 2020 to 14 July 2022. The TSWF data product consists of signal packets (63 ms snapshots) that are down-linked only if the classification algorithm on board the Solar Orbiter is triggered. The accuracy of the on-board classification algorithm is therefore important in order to optimize the data transfer and provide reliable data products for statistical analysis.

The input to the on-board classification algorithm, hereafter named the TDS classifier or the TDS classification algorithm, is the 63 ms signal packet, while the output is categorized into one out of three labels: *dust*, *wave* or *other*. Figure 1 presents a few examples of recorded snapshots with included labels, as classified by the TDS classification algorithm. The TDS classifier assigns the label based on three extracted features as follows:

1. The snapshot peak amplitude ($V_{\max}$)

2. The ratio of the peak amplitude to the median absolute value of the signal ($V_{\max}/V_{\mathrm{med}}$)

3. The full width half maximum (BW) of the main spectral peak, identified by analyzing the discrete Fourier transform of the signal.

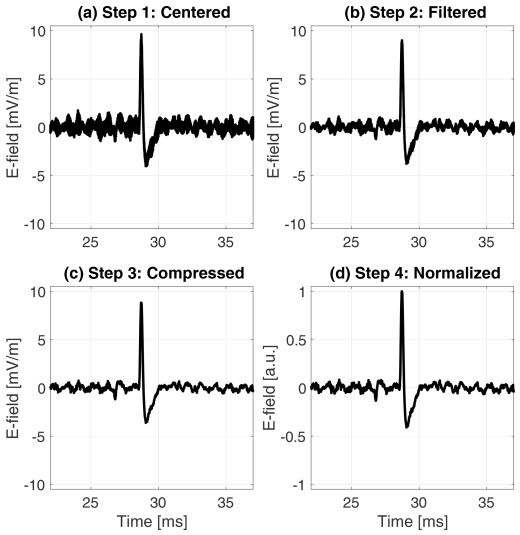

Figure 2. A dust waveform observed by antenna 2 on 8 September 2021. The panels illustrate the different stages of the pre-processing procedure. **(a)** The electric field offset is removed and the signal is centered around $0\,\mathrm{mV\,m^{-1}}$. **(b)** The signal is filtered by a median filter over seven time steps to reduce the high-frequency noise. **(c)** The signal is compressed by a factor of 4 to reduce the data size. **(d)** The waveform is normalized by the maximum absolute value of the signal in order to ease the parameter optimization of the machine learning classifier. Note the waveform is zoomed to a 15 ms time period around the dust impact in order to better visualize the impact shape modification by the pre-processing procedure.

The signal label is then determined by comparing the extracted feature values against configurable thresholds. The threshold criterion reflects that observations of waves are typically narrow band (low BW) and the peak of the signal is not much larger than the median value (low $V_{\max}/V_{\mathrm{med}}$). In contrast, dust observations are sharp non-periodic signals (high BW) that generally have a high maximum to median amplitude ratio (high $V_{\max}/V_{\mathrm{med}}$). For more detailed descriptions of the TDS classifier, see Soucek et al. (2021).

Figure 1 illustrates that it is challenging to detect and separate dust signals from the plural of other signal shapes. In particular, the dust waveform in panel (c) is classified as *other*, while the Langmuir wave and solitary wave snapshots in panels (g) and (h) are erroneously classified as *dust* by the TDS classification algorithm. For more information on observations of Langmuir and ion acoustic waves in the Solar Orbiter data, see e.g., Soucek et al. (2021), and for an analysis of Wind observations of electrostatic solitary waves, see Malaspina et al. (2013).

3 Machine learning-based framework for automatic dust impact detection

The goal of the machine learning classifier is to take a monopole RPW snapshot as an input and automatically output if the signal contains a dust impact or not. For this purpose, we use a supervised classifier. A supervised classifier relies on manually labeled data to learn (i.e., train) the function that maps the input observation (the electric field signal) to the output label. For this work, we focus exclusively on detecting dust impact signals, we therefore use the binary labels: *dust* or *no dust*. Additional labels, such as: *ion-acoustic waves*, *Langmuir waves* and *solitary waves*, could however be implemented in a similar machine learning-based framework.

3.1 Data pre-processing for machine learning classification

In order to construct a balanced data set, we selected ~ 1500 waveforms classified as *dust* and ~ 1500 waveforms classified as *wave/other* by the TDS classification algorithm. The signals were randomly drawn from the TDS data archive and acquired between 15 June 2020 to 16 December 2021. The TDS signals were then pre-processed to standardize the input to the classifier and speed up the training. Standardized data further reduces bias effects and makes the manual labeling of the signals easier to conduct. For this work, a four-step pre-processing procedure was used independently on each antenna signal, the pre-processing procedure applied on a sample signal is illustrated in Fig. 2.

1. *Remove the signal offset.* The electric field offset is removed by subtracting the raw signal with the median of a heavily filtered version of the raw data. A sliding median filter over 21 time steps was selected by visual inspection of the noise characteristics. The removal of the electric field offset centers the signal around zero and reduces bias effects from offset waveforms.

2. *Filter the data.* The signal is filtered using a sliding median filter over seven time steps in order to reduce the high-frequency noise. The seven time-step filter was selected by inspecting the power spectrum of impact signals and by noticing that most information above ($f_{\mathrm{N}} = 35\,\mathrm{kHz}$) is buried in noise, although the TDS sampling frequency is higher ($f_{\mathrm{s}} = 262.1\,\mathrm{kHz}$), thus making a filter length ($< f_{\mathrm{s}}/f_{\mathrm{N}} \approx 7.5$) appropriate without significant loss of information.

3. *Compress the data.* The signal is re-sampled with a compression factor of 4 using linear 1-dimensional interpolation. The compression is done to speed up the training of the classifier, resulting in a re-sampling from 16 384 to 4096 time steps.

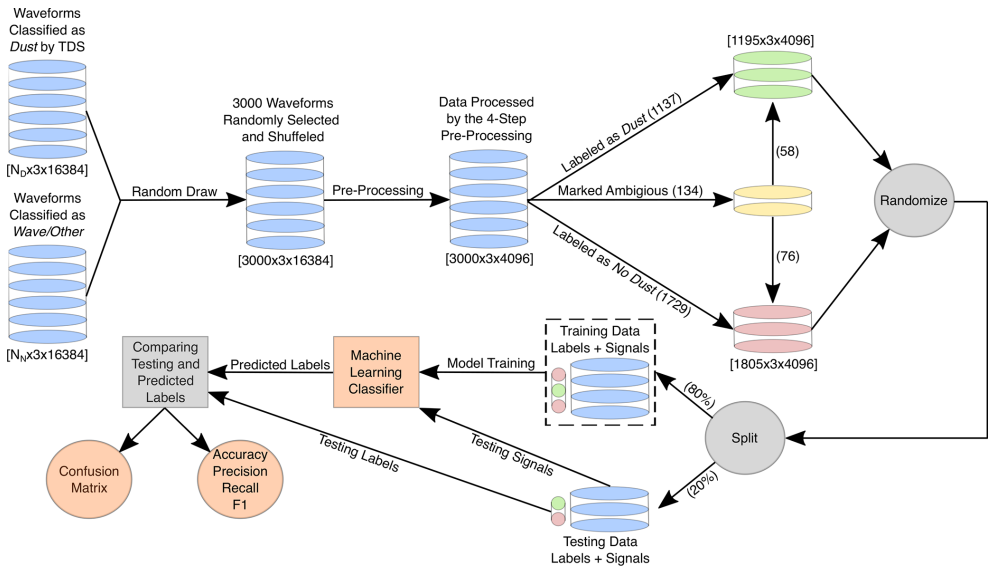

Figure 3. Data flow, from the TDS data sets to the machine learning performance metrics. The diagram illustrates the data flow by the black arrows and the applied process by the arrow label. The cylinders indicate the signal waveforms and the cylinder color indicates the associated label. The gray circles mark data transformation processes. The random draw of the TDS data and the pre-processing is explained in Sect. 3.1, while the manual labeling is described in Sect. 3.2. A description of the randomization and splitting of the manually labeled data into a training and a testing set is included in Sect. 3.3. Sections 3.4 and 3.5 explain the training and testing of the machine learning classifiers. Finally, the performances of the machine learning classifiers are compared and evaluated in Sect. 4.1.

4. *Normalize the signal.* The data are normalized to be between −1 and 1 by dividing all data samples with the maximum absolute value of the signal. The normalization makes the machine learning classifier more robust to variations in the signal strength and eases the parameter optimization during training.

3.2 Manual waveform labeling

Manually labeled data are used both to train the machine learning classifiers and to test the performance of the trained models. Thus, great care is needed in order to construct a high-quality labeled data set, without significant contamination of corrupted data files, biases and mislabeled signals.

We manually labeled the data into either *dust* or *no dust*. Each signal was displayed without indications of the previously assigned label by the TDS classifier in order to reduce bias effects. Furthermore, a zoom function was used to investigate the areas of interest, and options were included both to correct labeling mistakes by the user and to indicate ambiguous signals that do not clearly fit into any label (*dust* or *no dust*). Appendix A presents the graphical user interface (GUI) that was used to label the 3000 observations.

It should be noted that 134 signals (i.e., 4.5 %), out of 3000 manually labeled waveforms, were marked as ambiguous and did not clearly fit into either the *dust* or *no dust* label, see the middle row of Fig. 1 for ambiguous examples. Furthermore, the manual waveform labeling was done by one scientist, although with consultations with other experts. Thus, it is to be expected that different scientists will disagree on a proportion (up to 5 %) of the manual labels. The disagreement level could possibly be reduced if several experts labeled the same data set, and the labeling consensus was used as the effective waveform label.

3.3 Developing the machine learning classifiers

The manually labeled data were split into a training set (containing 80 % of the data) and a testing set (with the remaining 20 %). The training data are used to optimize the free parameters of the machine learning classifiers with respect to the assigned labels, while the testing data are used as an independent set to evaluate the performance of the trained classifiers. The performance of a machine learning classifier is quantified by comparing the outputs of the trained model to the labels of the testing data. Figure 3 illustrates the data flow, from the TDS data sets to the machine learning performance metrics.

There are numerous machine learning techniques that are suitable for time series classification. In this work, we focus

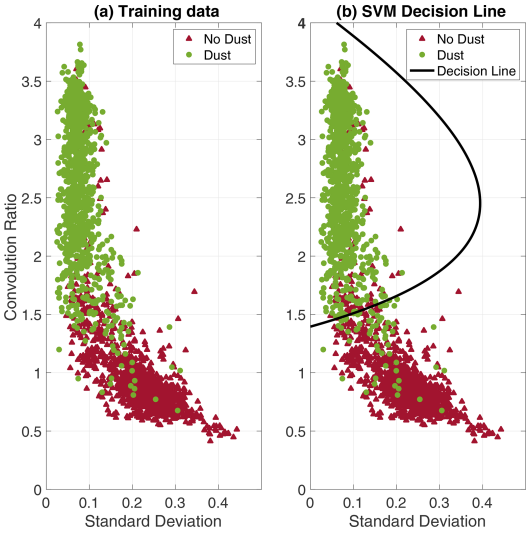

Figure 4. (a) The (1×2) feature vectors extracted from all (2400) observations in the training data, the associated labels are indicated in green (*dust*) and red (*no dust*). **(b)** The SVM decision line is defined as a second-order polynomial, obtained by minimizing the non-separable SVM cost function. The optimized SVM decision line appears to be reasonable, and most observations are separable in the training data.

on two well-known techniques: the support vector machine (SVM), described in Sect. 3.4, and the convolutional neural network (CNN), discussed in Sect. 3.5.

3.4 The support vector machine (SVM)

The support vector machine (Boser et al., 1992; Cortes and Vapnik, 1995) is a robust and versatile classification algorithm, considered to be one of the most influential approaches in supervised learning (Goodfellow et al., 2016). SVMs learn the decision hyperplane that maximizes the discriminative power between the observations categorized into two classes (in this case, *dust* or *no dust*). However, SVMs are highly dependent on the representation of the data and often achieve sub-optimal performance on high-dimensional data (when used directly). In this case, the observations from three antenna measurements, each with 4096 time steps, are both high-dimensional and noisy (each time step contains little information). It is therefore common to extract important characteristics (i.e., features) from the data to provide the SVM with compactly represented information with less noise and redundancies.

3.4.1 Feature extraction

In order to develop a baseline machine learning classifier, comparable to the on-board TDS classification algorithm, a simple 2-dimensional SVM classifier was considered. Thus, every observation with dimension (3×4096) is represented by a 2-dimensional feature vector (1×2). After some initial testing, we selected two features that had a high discriminative power between the *dust* and *no dust* observations.

1. *The standard deviation.* The mean standard deviation is calculated over the three antenna channels, each with 4096 time steps. The standard deviation is an appropriate feature since normalized *dust* signals typically have a lower mean standard deviation than normalized *no dust* signals.

2. *The convolution ratio.* The $\log_{10}$ value of the convolution ratio $(|\text{conv}|_{\max}/|\text{conv}|_{\text{median}})$ is calculated, where $|\text{conv}|$ is the absolute values of the convolution of the antenna signals with a normalized Gaussian of width 0.5 ms. $|\text{conv}|_{\max}$ is the maximum value of $|\text{conv}|$, while $|\text{conv}|_{\text{median}}$ is the median. The convolution ratio was selected as a feature since the *dust* signals typically have a larger convolution ratio than the *no dust* signals. The Gaussian width of 0.5 ms was experimentally found to give high correlations with dust impact signals.

3.4.2 Training the support vector machine

The two features (standard deviation and convolution ratio) were extracted from all observations in the training data. The decision hyperplane, in this 2-dimensional case a decision line, is defined by a polynomial of degree 2 that is optimized by minimizing the non-separable SVM cost function, see e.g., Theodoridis and Koutroumbas (2009) for details. The SVM classifier was trained with a slack variable factor of 1 and equal weighting between the *dust* and *no dust* observations. The 2-dimensional SVM is computationally inexpensive to optimize with a training time of ~ 1 s on a modern laptop. Figure 4 illustrates the training of the SVM classifier.

3.4.3 Testing the support vector machine

The performance of the trained SVM classifier is evaluated using the independent testing data, i.e., the remaining manually labeled data (20 %) that were not used for training the classifier. Figure 5 presents the SVM classification performance on the testing data.

Overall, the SVM classifier achieves a classification accuracy of 94 % on the testing data using the 2-dimensional feature vectors. Note that the inclusion of additional extracted features can possibly enhance the SVM performance. Several additional features can be considered, such as the mean amplitude of the signal, the range between the signal maximum and minimum values and the cross-correlation length (the time lag to the first zero crossing).

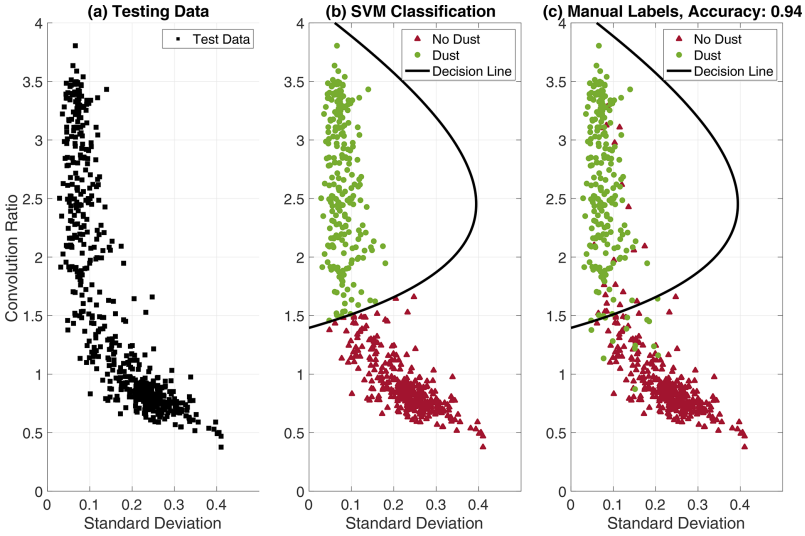

Figure 5. **(a)** The (1×2) feature vectors extracted from the testing data (600 observations with hidden labels). **(b)** The testing data are classified using the trained SVM decision line, where all observations within the polynomial line are classified as *dust*, while all observations outside are classified as *no dust*. **(c)** The "true" labels (from the manual labeling) are revealed. It is clear that some observations are confused, predominantly near the decision line. Still, the SVM classifier achieves an overall classification accuracy of 94 %, calculated by comparing the outputs from the SVM classification **(b)** to the "true" labels **(c)**.

3.4.4 Explainability of the support vector machine

Ideally, we want to develop a machine learning classifier that not only has a high accuracy, but also makes decisions that are understandable for human experts (Holzinger et al., 2019). In other words, we want to be able to explain why the machine learning classifier selected the predicted class for a given observation. In machine learning, this is often referred to as the explainability of the trained classifier. Figure 5 presents the testing data in the 2-D feature vector space, but this plot gives no clear indications of how different signal shapes are distributed and which signatures are confused by the SVM classifier. In order to better understand the decisions made by the SVM classifier, the signal examples in Fig. 1 are studied in detail. The analysis is presented in Fig. 6.

It should be noted that the signal examples in Fig. 6 are not representative for the general distribution of observations in the 2-D feature vector space, since most observations are clustered in distinct *dust* and *no dust* regions, as can be seen in Fig. 5. Figure 6 focuses mostly on signal examples that are challenging to classify. Still, Fig. 6 indicates that the SVM classifier provides mostly comprehensible outputs, but might have difficulties classifying weak dust impact signals and signals with important signatures located at the edge of the snapshot frame.

3.5 The convolutional neural network (CNN)

Convolutional neural networks are algorithms designed for processing grid-like data and have achieved premium performance on a number of different tasks in the recent decade, such as image (He et al., 2016; Kvammen et al., 2020), video (Karpathy et al., 2014) and time series (Wang et al., 2017; Wickstrøm et al., 2021) classification.

3.5.1 Feature extraction

Unlike the SVM, the CNN does not require pre-defined feature extraction routines. Instead, the CNN extracts the features based on a chain of convolution operations and automatically optimizes the convolution filters based on the training data and the associated labels.

For this work, we employed the three-layer fully convolutional network architecture presented in Wang et al. (2017) and suggested for time series classification after extensive testing (Wickstrøm et al., 2022; Fawaz et al., 2020; Karim et al., 2019). The rectified linear unit (ReLU) function (Glorot et al., 2011) was used as the activation function and Batch Normalization (BN) (Ioffe and Szegedy, 2015) was used at each convolutional layer in order to regularize the network and accelerate the training process. Figure 7 presents the employed CNN architecture.

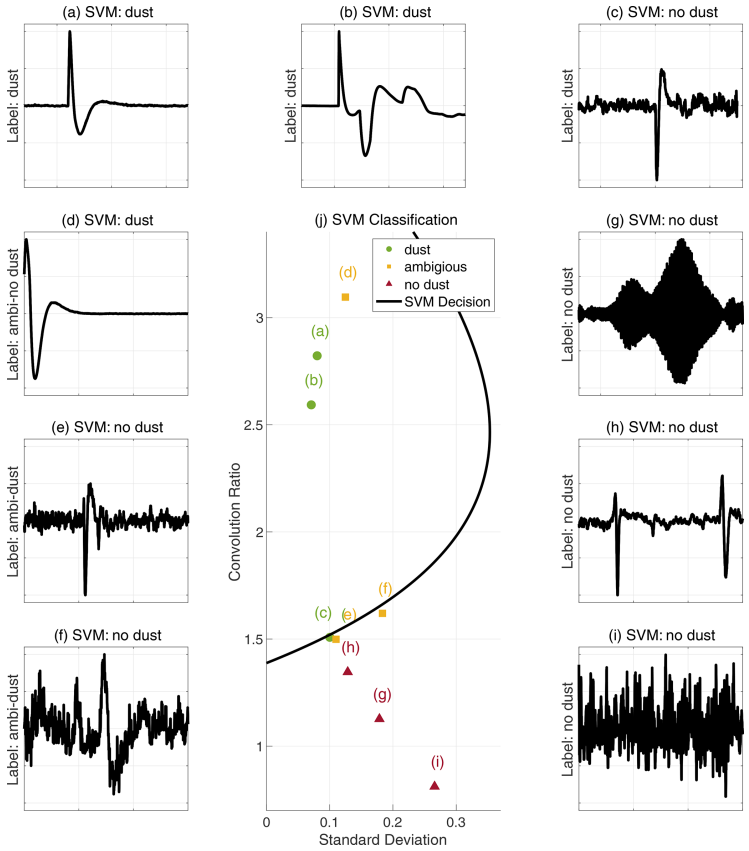

Figure 6. The signal examples are presented in **(a)**–**(i)**, the manual labels are indicated along the y axis and the predicted labels, classified by the SVM decision line, are presented in the subplot titles. Panel **(j)** presents the associated signal examples in the 2-D feature vector space along with the SVM decision line. The *dust* signals are illustrated in green, the *ambiguous* signals are marked in yellow and the *no dust* signals are indicated in red. The SVM classifier provides mostly explainable outputs. The clear dust signals **(a–b)** are located well within the SVM decision line, the *ambiguous* signals **(e–f)** are located near the decision line, while the no dust signals **(g–i)** are clearly located outside. However, *dust* signal **(c)** is erroneously located just outside the decision line, this can possibly be explained by the weak signal-to-noise ratio. In addition, signal **(d)** is located well within the decision line, although this signal is labeled *ambiguous-no dust* due to the signal framing, this indicates that the SVM might have difficulties classifying signatures located at the edge of the snapshot frame. Note that the signals are zoomed to 15 ms intervals around the interesting features, similar to the examples in Fig. 1.

3.5.2 Training the convolutional neural network

The three-layer fully convolutional network consists of 267 010 free parameters (weights and biases) that need to be optimized to solve the dust impact classification task. The free parameters are randomly initialized and thereafter optimized using the ADAM gradient descent optimizer (Kingma and Ba, 2014). The CNN was trained for 225 epochs with a cross-entropy loss function using the 2400 labeled observations in the training data. CNNs are computationally expensive to optimize, as compared to the SVM classifier, and a training time of $\sim$ 20 min was required using TensorFlow on a MacBook Pro with a 32-core M1 Max GPU chip. For more details on neural network training and optimization, see for example (Montavon et al., 2012).

3.5.3 Testing the convolutional neural network

In order to visualize the features extracted by the CNN, we employ the t-distributed Stochastic Neighbor Embedding (t-SNE) method (Van der Maaten and Hinton, 2008). The t-SNE method is used for visualizing high-dimensional data by

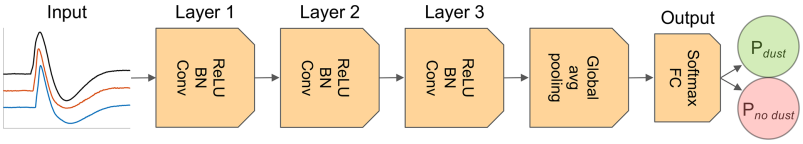

Figure 7. The three-layer fully convolutional network used for the dust impact classification task. The input to the network is the (3×4096) waveform. The feature extraction process is defined by three convolutional layers, consisting of 128, 256 and 128 independent filters with kernel lengths of 8, 5 and 3 weights, respectively. Batch normalization (BN) is used at each convolutional layer to regularize the inputs and the rectified linear unit (ReLU) function was used as the activation function. Finally, the output of the convolutional layers (with dimension 128×4096) is averaged in the global pooling layer to a feature vector with dimension (128×1). The class score is then determined in a fully connected (FC) network layer and the output label probabilities (P_{dust}, $P_{\text{no dust}}$) are calculated using the softmax function. The figure is adopted from Wickstrøm et al. (2021).

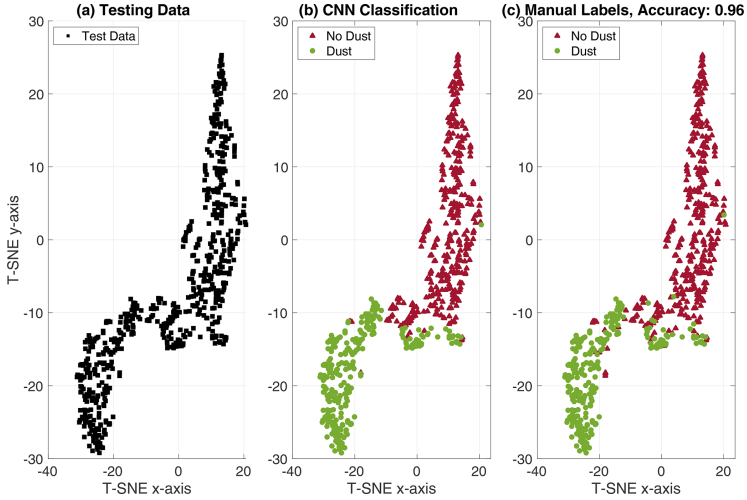

Figure 8. (a) The testing data (600 observations with hidden labels) are visualized by a dimension-reduced t-SNE map, where similar feature vectors are modeled by nearby points, while dissimilar observations are modeled by distant points with high probability. **(b)** The testing data classified by the trained CNN. **(c)** The "true" manual labels are presented. Only a few observations, predominantly in the transition region between the *dust* and *no dust* observations, are confused. An overall classification accuracy of 96 % is calculated by comparing the labels predicted by the CNN to the manual labels. Note that the presented testing data is the same data set that was used to test the SVM classifier, illustrated in Fig. 5.

assigning each observation a location in a 2-D space such that similar observations are modeled by nearby points, while dissimilar observations are modeled by distant points with high probability. The (128×1) testing feature vectors, extracted in the global pooling layer, are presented in a 2-D t-SNE map in Fig. 8, along with a visualization of the CNN classification performance.

Overall, the CNN obtains a high ($\gtrsim 95\,\%$) classification accuracy and might therefore be suitable for automatic processing of electric field signals observed by the RPW instrument on board the Solar Orbiter.

3.5.4 Explainability of the convolutional neural network

Neural networks have traditionally been regarded as black boxes (Shwartz-Ziv and Tishby, 2017; Alain and Bengio, 2016), where the network carries out the desired task, but the network decisions are difficult to interpret. However, progress has been made in recent years for making the neural network decisions more accessible and easier to interpret (i.e., explainable) for human users (Samek et al., 2021). In this section, we analyze the CNN decisions by employing class activation maps and the previously described t-SNE method.

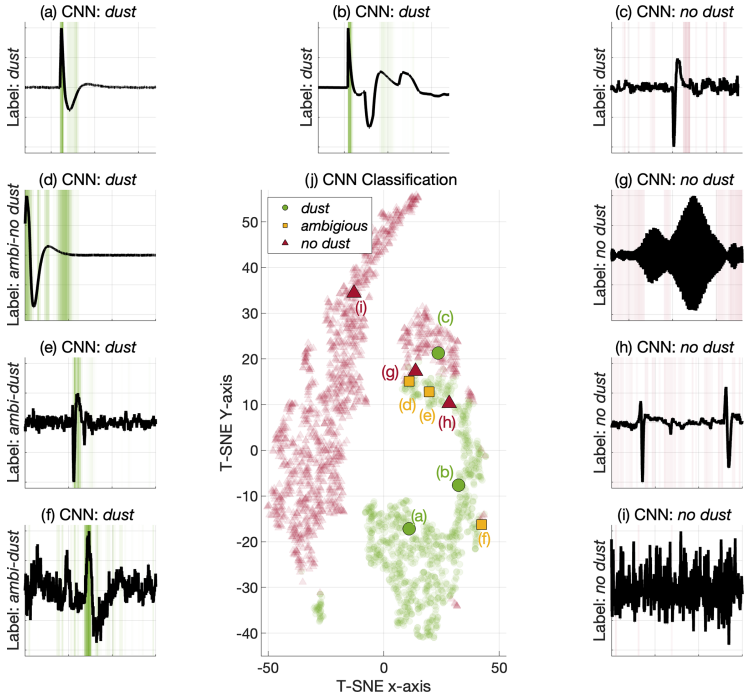

Figure 9. The signal examples and the CAM analysis are presented in **(a)**–**(i)**, the manual labels are indicated along the *y* axis and the predicted label, classified by the CNN, is presented in the subplot titles. The highlighted green color indicates the CAM values associated with the *dust* class, the green regions therefore emphasize the regions that are considered important by the CNN for detecting dust impact signatures. Similarly, the red color indicates the regions that are influential for the *no dust* class. Note that the signals are zoomed to 15 ms intervals around the interesting features, similar to Figs. 1 and 6. Panel **(j)** presents the associated signal examples in the t-SNE space along with the training data signals as transparent points. The *dust* signals are illustrated by the green dots, the *ambiguous* signal examples are marked in yellow and the *no dust* signals are indicated in red. The t-SNE map shows that the clear *dust* signals **(a–b)** are distinctly located in a green (*dust*) region, whereas the clear *no dust* signal **(i)** is distinctly located in a red (*no dust*) region. The remaining signals are located in more mixed regions. It should however be noted that the observations are represented by a 128-dimensional feature vector in the CNN and that the (2-D) t-SNE representation presented in **(j)** diminishes a lot of information, meaning that even the signals located in a mixed region of the t-SNE plot might be separable in the 128-dimensional feature vector space.

Class activation maps (CAMs) (Zhou et al., 2016) highlight the regions of the data that are important for a considered label (l) by analyzing the features extracted in the global pooling layer and the weights in the FC layer that are associated with label (l), see e.g., (Wang et al., 2017) for a detailed description. The outcome of the CAM analysis is that we can visualize the sections of the signal that are influential for the CNN classification decision. Figure 9 presents the CAM analysis of the signal examples in Fig. 1 along with an illustration of the signal features in a dimension-reduced t-SNE space. Note that the t-SNE mapping in Fig. 9 is different from the t-SNE mapping in Fig. 8, since Fig. 9 considers a different CNN where the signal examples are specifically excluded from the training data.

The CAM analysis in Fig. 9 illustrates that the CNN makes classification decisions that are comprehensible (in most cases). It is however interesting to note that signal (c), manually labeled as *dust*, is erroneously classified as *no dust* by the CNN, and that this decision is largely based on the tail (the relaxation period) of the impact signal. It should however be noted that it is more difficult to explain the *no dust* predictions than the *dust* predictions, since the *no dust* CNN decisions are based on the lack of a signature (*dust* impact) rather than on the presence of a signature. In addition, signal (d), manually labeled as *ambiguous-no dust*, is classified as *dust* by the CNN, and this decision is based on a wide region of the signal with emphasis on the tail of the (ambiguous) dust impact signal, this section might not have been highlighted as particularly important by a human expert.

Table 1. The TDS, SVM and CNN classification performance metrics: accuracy, precision, recall and F1-score. The SVM and CNN scores and error values are the mean and the standard deviation across 10 training runs. The bold numbers indicate statistically enhanced performance with a significance level of 0.01, computed using a t-test.

Classifier	Accuracy	Precision	Recall	F1 Score
TDS	0.850	0.746	0.944	0.833
SVM	0.936 ± 0.012	0.903 ± 0.027	0.941 ± 0.017	0.921 ± 0.015
CNN	$\mathbf{0.964 \pm 0.006}$	$\mathbf{0.939 \pm 0.020}$	$\mathbf{0.972 \pm 0.008}$	$\mathbf{0.955 \pm 0.008}$

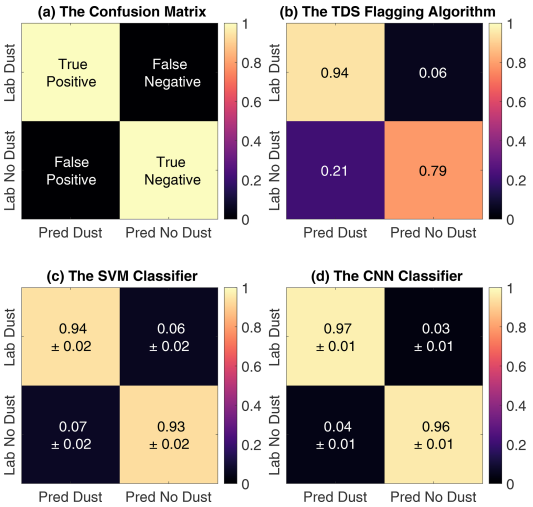

Figure 10. **(a)** The confusion matrix entries are described by the true (correctly classified) and false (erroneously classified) values; compared to the manual labels (Lab), positive indicates *dust* predictions (Pred), and negative indicates *no dust* predictions. **(b)** The TDS classifier confuses *dust* and *no dust* observations, where a significant proportion (> 0.20) of *dust* predictions are manually labeled as *no dust*. **(c)** The SVM classifier predicts both *dust* and *no dust* observations with a high (> 0.90) accuracy. **(d)** The CNN classifier predicts a very large (> 0.95) proportion of both *dust* and *no dust* observations correctly.

In general however, the CNN achieves a high accuracy ($\gtrsim 95\,\%$) and makes decisions that are mostly in line with human interpretation. It is therefore reasonable to infer that the CNN will have a performance comparable to the agreement level between human experts, where disagreement predominantly occurs for ambiguous and noisy signals, while clear *dust* and clear *no dust* signals are classified correctly.

4 Results and discussions

4.1 Analysis of the classification performance

The average classification performance is obtained by training and testing the machine learning classifiers over 10 runs, each run with different training and testing sets. The classifiers are initialized from scratch and the training and testing sets are selected independently 10 times by randomization and splitting of the manually labeled data, as indicated by the gray circles in Fig. 3. The average class-wise performance of the on-board TDS classifier and the machine learning SVM and CNN classifiers are summarized as confusion matrices in Fig. 10. Overall, the CNN has the highest performance for both *dust* and *no dust* classification. In addition, both the SVM and the CNN classifiers obtain stable performances with only small variations for each run.

The classification performance is further evaluated by the accuracy, precision, recall and F1 score. The definitions for the performance metrics are included in Appendix B. The average performance metrics, calculated over 10 runs, are summarized in Table 1. Again, the CNN has the highest performance across all metrics. The CNN obtains a significant improvement in the classification performance with a statistical significance at a level of 0.01, computed using a t-test. The t-test was computed in a pairwise manner between both the CNN and the SVM scores and the CNN and the TDS scores. In all cases, the enhanced performance of the CNN classifier was significant.

The results from both the confusion matrices and the performance metrics strongly suggest that the SVM and CNN classifiers provide binary classification results with higher reliability than the TDS classifier and further that the CNN is the most reliable classifier overall. We therefore propose that the CNN classifier (or similar tools) should be considered for post-processing of the TDS data product in statistical studies of dust impacts observed by the Solar Orbiter RPW instrument.

In addition, it should be noted that 134 signals (i.e., 4.5 %), out of 3000 manually labeled waveforms, were marked as ambiguous, illustrated by the yellow cylinder in Fig. 3, and did not clearly fit into either the *dust* or *no dust* label, see Fig. 1 for label examples. It is therefore improbable to achieve a classification accuracy exceeding $\sim 98\,\%$ for the considered data set, and an accuracy approaching $\sim 99\,\%$

should be considered suspicious and can be an indication of over-fitting.

Both the trained SVM and CNN classifiers are computationally inexpensive to run. One thousand observations are classified in 5 s using the SVM model, while the CNN classifier requires 50 s on a modern laptop, including the needed time for pre-processing and feature extraction. The proposed machine learning classifiers are therefore suitable for processing large data sets with thousands of new observations acquired every month as the Solar Orbiter continues its operation.

4.2 The dust impact rate

In this section, we use the trained classifiers to automatically process a large data set, consisting of 104 032 observations. This data set contains all TSWF observations acquired over a 25-month period, spanning between 15 June 2020 to 14 July 2022, that satisfy the criteria in Sect. 2.1 (sampling rate of 262.1 kHz, 16 384 time steps and XLD1 mode).

Figure 11 presents the TDS, SVM and CNN daily impact rates with included error estimates. The daily impact rate is calculated from the automatically detected daily dust impact number and the time-dependent TDS–RPW duty cycle. The number of dust particles detected by the Solar Orbiter on each day can be modeled as a Poisson process (Kočiščák et al., 2022), where the variance in the daily count is equal to the daily count number, resulting in the standard deviation error bars presented in Fig. 11. The impact rate function curves are obtained by fitting the dust flux model from Zaslavsky et al. (2021) with an included offset as follows:

$$R = F_{1\,\mathrm{AU}} S_{\mathrm{col}} \left(\frac{r}{1\,\mathrm{AU}}\right)^{-2} \frac{v_{\mathrm{impact}}}{v_\beta} \left(\frac{v_{\mathrm{impact}}}{v_{\mathrm{impact}}(1\,\mathrm{AU})}\right)^{\alpha\delta} + C, \quad (7)$$

where $F_{1\,\mathrm{AU}}$ is the unknown cumulative flux of particles above the detection threshold at 1 AU and $S_{\mathrm{col}} = 8\,\mathrm{m}^2$ is the Solar Orbiter collection area, as defined in Zaslavsky et al. (2021). Furthermore, r is the radial distance from the sun, v_{impact} is the relative velocity between the spacecraft and the dust particles, assuming a constant radial and azimuthal velocity vector for the dust particles, $v_\beta = [50\,\mathrm{km\,s^{-1}},\ 0\,\mathrm{km\,s^{-1}}]$, and the product $\alpha\delta = 1.3$, as suggested in Zaslavsky et al. (2021). The assumed constant radial velocity is a good approximation for dust in hyperbolic orbits originating near the Sun that is deflected outward by the radiation pressure force. Finally, we included a constant impact rate offset, C, in order to obtain an improved fit. The description of the dust flux in Eq. (7) is based on the assumption that the dust and spacecraft orbits are in the same orbital plane.

Figure 11 shows that the machine learning classifiers detected significantly more dust particles than the TDS classifier. The SVMs obtained a dust impact detection enhancement of $16\,\% \pm 1\,\%$, while the CNNs had an $18\,\% \pm 8\,\%$ increase. Both the SVM and the CNN classifiers obtain impact rates that are notably higher around the aphelion and distinctly lower in the vicinity of the perihelion, resulting in a lower dynamic range of the impact rates than observed in the TDS data product.

Furthermore, Fig. 11 illustrates that the fitted SVM and CNN impact rate function cures are in very good agreement. It is promising that two entirely different machine learning approaches provide comparable impact rates after classifying a large data set (consisting of 104 032 observations) when trained and tested on a limited data set consisting of 3000 observations. This suggests that both the SVM and CNN classifiers have obtained stable performances and can be used to classify observations outside the domain of the training and testing data.

Still, the shape of the dust impact signal is dependent on the local plasma environment, where influential parameters are as follows: the electron plasma density, the mean electron velocity and the electron temperature (Zaslavsky, 2015; Babic et al., 2022). These parameters will vary throughout the spacecraft orbit. It should therefore be noted that the machine learning classifiers were trained and tested on waveforms acquired over a 1.5-year period, spanning between 15 June 2020 to 16 December 2021. During this period, the Solar Orbiter sampled the interplanetary medium at solar distances ranging from ~ 0.5 to ~ 1.0 AU. The spacecraft will however reach a minimum solar distance of 0.28 AU, and the performance of the machine learning classifiers might suffer if the observed dust impact shapes in the vicinity of ~ 0.3 AU are significantly different from the dust impact shapes at ~ 0.5 to ~ 1.0 AU.

Finally, we note that a dip in the SVM and CNN dust impact rates can be observed in Fig. 11, roughly 0.5–1 month before perihelia 1 and 2 (no data for perihelion 3). This dip is possibly due to a change in the relative velocity between the spacecraft and the interstellar dust particles, which is upstream at 259° in the Ecliptic coordinate system. Still, there is a large natural (Poisson) variation in the dust impact rates at perihelion that make visual analysis difficult with the presented data set. In addition, complicating effects will have an enhanced influence on the daily dust count number towards the Sun, such as an enhancement in false detections due to increased variability in the ambient plasma and validity degradation of the dust flux model assumptions in Eq. (7) close to the formation region of the hyperbolic dust particles.

5 Conclusions

5.1 Summary and scientific implications

We have presented a machine learning-based framework for fully automated detection of dust impacts observed by the Solar Orbiter – Radio and Plasma Waves (RPW) instrument. Two different supervised machine learning approaches were considered: the support vector machine (SVM) and the con-

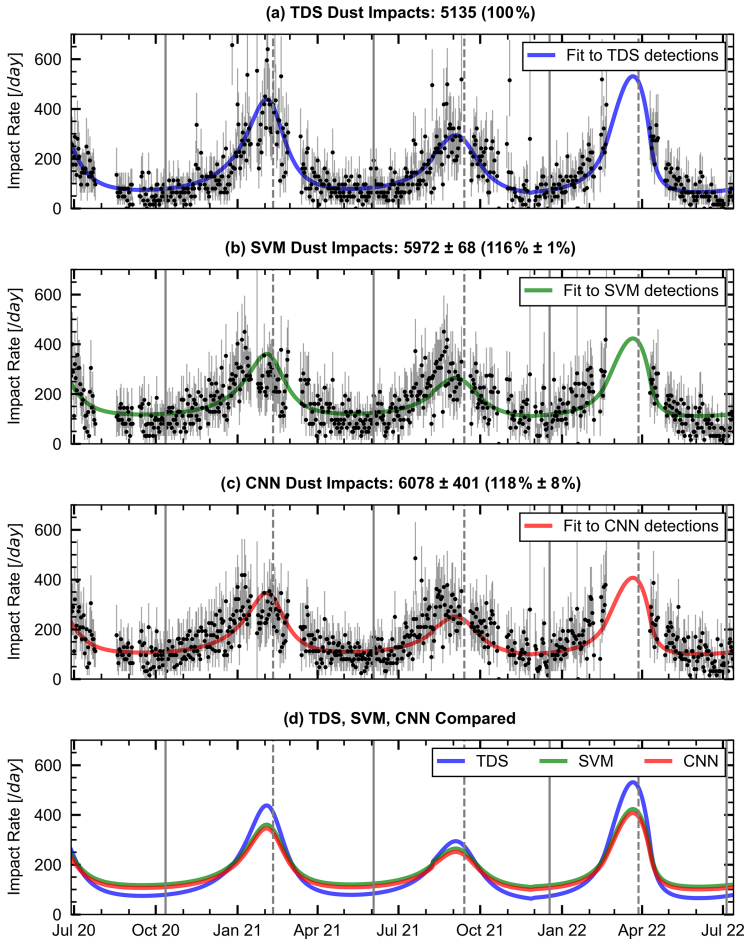

Figure 11. **(a)** The daily dust impact rates according to the TDS classifier. The full vertical lines indicate times when the Solar Orbiter is at aphelion, while the dashed lines indicate times at perihelion. **(b)** The median of the daily impact rates classified by 10 trained SVM classifiers. **(c)** The median of the daily impact rates from the 10 CNN classifiers. The impact rate function curves are obtained by fitting the dust flux model from Zaslavsky et al. (2021), Eq. (7). **(d)** The impact rate function cures are compared. The SVM and CNN dust impact rates are very similar, whereas the TDS provides notably smaller impact rates at aphelion and higher impact rates at perihelion. The accumulated dust impact detections for the TDS classification algorithm and the mean and standard deviation of the dust impact detections for the 10 CNN and SVM classifiers are presented in the subplot titles. Note that the large data gap around April 2022 (perihelion 3) is due to a different observational setup for the Solar Orbiter RPW–TDS system, where the sampling frequency was doubled. These data were excluded since it can not be reliably classified by the SVM/CNN methods without additional data processing and/or training.

volutional neural network (CNN). The CNN classifier obtained the highest performance across all evaluation metrics and achieved 96 % ± 1 % overall classification accuracy and 94 % ± 2 % dust detection precision, a significant improvement to the currently used on-board TDS classification algorithm with 85 % overall classification accuracy and 75 % dust detection precision. We therefore conclude that the CNN classifier (or similar tools) should be considered for post-processing of the TDS data product for statistical studies of dust impacts observed by the Solar Orbiter.

The SVM and CNN classifiers were used to analyze 104 032 observations acquired over a 2-year period, spanning between 15 June 2020 to 14 July 2022. On average, the machine learning classifiers detected more dust parti-

cles than the currently used TDS algorithm, the SVMs had a $16\,\% \pm 1\,\%$ detection enhancement and the CNNs had an $18\,\% \pm 8\,\%$ increase. Furthermore, the SVM and CNN classifiers were in very good agreement and both classifiers obtained a notably higher dust impact rate in the vicinity of aphelion and a distinctly lower impact rate at perihelion, as compared to the dynamic range of the TDS impact rates. This might indicate a higher ambient dust distribution than previously observed. This result is significant since it suggests the presence of dust populations other than the hyperbolic dust particles in the data. Possible other populations are interstellar dust and interplanetary dust in bound orbits.

The labeled data and the trained SVM and CNN classifiers are available online with included user instructions. The proposed method and the presented classifiers can thus provide the interplanetary dust community with thoroughly tested and more reliable data products than those currently in use. The daily dust count numbers from the CNN classification were employed by Kočiščák et al. (2022) to infer meaningful physical properties of the dust population by modeling the number of dust detections within a day as a Poisson-distributed random variable. Kočiščák et al. (2022) further demonstrated that the same procedure did not provide dust parameters that were in line with prior knowledge when using the daily dust detections from the TDS classification. This result is independent of the manually labeled testing data, which might be prone to biases, and further suggests that the CNN approach provides more reliable data products than the currently used TDS algorithm.

5.2 Outlook and method constraints

The presented machine learning classifiers may be considered for on board processing of the observed electric field signals. However, the trained SVM and CNN classifiers presented in this article are trained on Triggered Snapshot WaveForms (TSWF) data, and should not be used for processing 'untriggered" signals without additional training and testing on 'untriggered" data. Additional training can also be used to further enhance the performance of the machine learning classifiers. In particular, adding labeled data acquired near the Sun (~ 0.3 AU) and during periods of strong solar activity will likely improve the overall accuracy and make the machine learning classifiers more robust to challenging conditions.

It should also be noted that the classifiers presented in this work are trained and tested on data labeled by one scientist, although with consultations with other experts. Labeled data from several experts can provide machine learning classifiers that are more in line with the labeling consensus in the interplanetary dust community. Additional labeling can also be used to extend the machine learning classifiers to include automatic detection of other characteristic signatures, such as ion acoustic, Langmuir and solitary waves (Soucek et al., 2021).

Finally, we would like to highlight that a machine learning-based framework can be developed for automatic post-processing of data acquired by radio and plasma waves instruments on board other spacecrafts, such as the Solar Terrestrial Relations Observatory (STEREO) (Zaslavsky et al., 2012), Wind (Malaspina et al., 2014) and the Parker Solar Probe (Szalay et al., 2020). Automatic and reliable detection of dust impact signals observed by multiple instruments at several locations and over several years will likely facilitate statistical studies that will enhance our understanding of the role of dust in the inner solar system, beyond what is attainable with the data products that are currently in use.

Appendix A: Graphical user interface for manual labeling

Figure A1 presents the graphical user interface (GUI) that was used to manually label all considered (3000) signals into either *dust* or *no dust*. In addition, efforts were made to use a similar setup (with the same monitor and figure resolution) throughout the manual labeling in order to reduce bias effects.

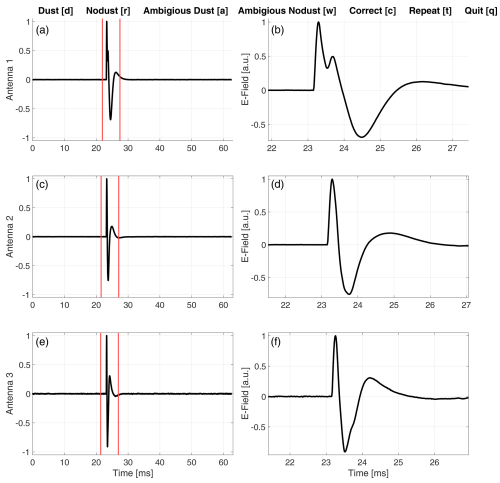

Figure A1. The manual labeling user interface showing a signal observed 28 July 2021. **(a)**, **(c)** and **(e)** display the full snapshot (from 0 to ~ 63 ms) at all antennas. An area of interest is selected by adjusting the red vertical lines. **(b)**, **(d)** and **(f)** display the signal within the area of interest. The signal can be labeled as *dust* by pressing the $[d]$ key on the keyboard and *no dust* by pressing the $[r]$ key. The signal is indicated to be ambiguous if the waveform does not fit clearly into either of the two labels; note however that signals indicated to be ambiguous were also labeled into either *dust* or *no dust* using the $[a]$ and $[w]$ keys. There is also an option to correct $[c]$ the previously labeled signal (in case of an error), repeat $[t]$ the area of interest selection and quit $[q]$ the manual labeling user interface.

Appendix B: The classification performance metrics

The classification performance metrics are calculated using the true positive (TP), true negative (TN), false positive (FP) and false negative (FN) values, defined by comparing the predicted classes and the manually labeled classes, illustrated in Fig. 10.

The overall accuracy of the classifier is the proportion of observations that were correctly predicted by the classifier. The accuracy is mathematically defined as

$$\text{Accuracy} = \frac{\text{TP} + \text{TN}}{\text{TP} + \text{TN} + \text{FP} + \text{FN}}. \tag{B1}$$

Precision (in this case) is defined as the proportion of data points predicted by the classifier as *dust*, whose "true" label is indeed *dust*. Precision is therefore calculated as

$$\text{Precision} = \frac{\text{TP}}{\text{TP} + \text{FP}}. \tag{B2}$$

Recall (in this case) is the proportion of observations manually labeled as *dust*, that were correctly predicted as *dust* by the classifier. Recall is defined as

$$\text{Recall} = \frac{\text{TP}}{\text{TP} + \text{FN}}. \tag{B3}$$

The F1 score acts as a weighted average of precision and recall and is calculated as

$$\text{F1} = 2\left(\frac{\text{Precision} \cdot \text{Recall}}{\text{Precision} + \text{Recall}}\right). \tag{B4}$$

Code and data availability. The code used for this work, the trained classifiers, and the training and testing data sets can be accessed via the following link: https://doi.org/10.5281/zenodo.7404457 (Kvammen, 2022). The Triggered Snapshot WaveForms (TSWF) data files can be accessed at the Solar Orbiter/RPW data archive: https://rpw.lesia.obspm.fr/roc/data/pub/solo/rpw/data/L2/tds_wf_e/ (last access: 26 Ocotber 2022; made available by the Solar Orbiter/RPW Investigation team – M. Maksimovic, PI).

Author contributions. AK wrote the article text, trained and tested the machine learning classifiers and manually labeled the waveforms. KW aided the development of the machine learning classifiers, analyzed the machine learning performance metrics and commented/edited the article. SK performed the dust impact rate analysis, aided with the theoretical background and commented/edited the article. JV and LN contributed to the analysis of the TDS waveforms and the theoretical background. AZ and KRB contributed with the theoretical background and helpful discussions. AG contributed with knowledge of the Solar Orbiter data availability and discussions on the dust waveform shapes. DP and JS provided the data used for this work and explained the data content. IM is the main contributor to the theoretical background, aided the article with numerous comments/suggestions/discussions and shared knowledge that was crucial for this work.

Competing interests. The contact author has declared that none of the authors has any competing interests.

Disclaimer. Publisher's note: Copernicus Publications remains neutral with regard to jurisdictional claims in published maps and institutional affiliations.

Acknowledgements. Andreas Kvammen thanks Audun Theodorsen for aiding the motivation and objective of the article. In addition, Andreas Kvammen thanks Juha Vierienen, Björn Gustavsson and Patrick Guio for helpful discussions. The authors would like to thank the reviewers for their valuable suggestions and appropriate comments.

Financial support. Andreas Kvammen received support from the Research Council of Norway (grant nos. 262941 and 326039). Samuel Kociscak is supported by the Tromsø Research Foundation (grant no. 19_SG_AT). Jakub Vaverka, David Pisa and Jan Soucek received support from the Czech Science Foundation (grant no. 22-10775S). Kristina Rackovic Babic received support from the Ministry of Education, Science and Technological Development of the Republic of Serbia through contract no. 451-03-9/2021-14/200104.

Review statement. This paper was edited by Gunter Stober and reviewed by two anonymous referees.

References

Alain, G. and Bengio, Y.: Understanding intermediate layers using linear classifier probes, ArXiv, https://doi.org/10.48550/arXiv.1610.01644, 2016.

Aubier, M., Meyer-Vernet, N., and Pedersen, B.: Shot noise from grain and particle impacts in Saturn's ring plane, Geophys. Res. Lett., 10, 5–8, 1983.

Babic, K. R., Zaslavsky, A., Issautier, K., Meyer-Vernet, N., and Onic, D.: An analytical model for dust impact voltage signals and its application to STEREO/WAVES data, Astron. Astrophys., 659, A15, https://doi.org/10.1051/0004-6361/202142508, 2022.

Boser, B. E., Guyon, I. M., and Vapnik, V. N.: A training algorithm for optimal margin classifiers, in: Proceedings of the fifth annual workshop on Computational learning theory, Association for Computing Machinery, 144–152, https://doi.org/10.1145/130385.130401, 1992.

Bougeret, J.-L., Kaiser, M. L., Kellogg, P. J., Manning, R., Goetz, K., Monson, S., Monge, N., Friel, L., Meetre, C., Perche, C., Sitruk, L., and Hoang, S.: Waves: The radio and plasma wave investigation on the Wind spacecraft, Space Sci. Rev., 71, 231–263, 1995.

Collette, A., Grün, E., Malaspina, D., and Sternovsky, Z.: Micrometeoroid impact charge yield for common spacecraft materials, J. Geophys. Res.-Space, 119, 6019–6026, 2014.

Cortes, C. and Vapnik, V.: Support-vector networks, Mach. Learn., 20, 273–297, 1995.

Fawaz, H. I., Lucas, B., Forestier, G., Pelletier, C., Schmidt, D. F., Weber, J., Webb, G. I., Idoumghar, L., Muller, P.-A., and Petitjean, F.: InceptionTime: Finding AlexNet for time series classification, Data Min. Knowl. Disc., 34, 1936–1962, https://doi.org/10.1007/s10618-020-00710-y, 2020.

Glorot, X., Bordes, A., and Bengio, Y.: Deep Sparse Rectifier Neural Networks, in: Proceedings of the Fourteenth International Conference on Artificial Intelligence and Statistics, edited by: Gordon, G., Dunson, D., and Dudík, M., Proc. Mach. Learn. Res., 15, 315–323, 2011.

Goodfellow, I., Bengio, Y., and Courville, A.: Deep learning, MIT press, ISBN: 9780262035613, 2016.

Grün, E., Zook, H. A., Fechtig, H., and Giese, R.: Collisional balance of the meteoritic complex, Icarus, 62, 244–272, 1985.

Gurnett, D. A., Grün, E., Gallagher, D., Kurth, W., and Scarf, F.: Micron-sized particles detected near Saturn by the Voyager plasma wave instrument, Icarus, 53, 236–254, 1983.

He, K., Zhang, X., Ren, S., and Sun, J.: Deep Residual Learning for Image Recognition, in: IEEE Conference on Computer Vision and Pattern Recognition, IEEE Comput. Soc., 770–778, https://doi.org/10.1109/CVPR.2016.90, 2016.

Holzinger, A., Langs, G., Denk, H., Zatloukal, K., and Müller, H.: Causability and explainability of artificial intelligence in medicine, Wiley Interdisciplinary Reviews, Data Min. Knowl. Disc., 9, e1312, https://doi.org/10.1002/widm.1312, 2019.

Hornung, K., Malama, Y. G., and Kestenboim, K. S.: Impact vaporization and ionization of cosmic dust particles, Astrophys. Space Sci., 274, 355–363, 2000.

Ioffe, S. and Szegedy, C.: Batch Normalization: Accelerating Deep Network Training by Reducing Internal Covariate Shift, in: nternational Conference on Machine Learning, edited by: Bach, F. and Blei, D., Vol. 37, Proc. Mach. Learn. Res., 37, 448–456, 2015.

Ishimoto, H.: Modeling the number density distribution of interplanetary dust on the ecliptic plane within 5 AU of the Sun, Astron. Astrophys., 362, 1158–1173, 2000.

Karim, F., Majumdar, S., Darabi, H., and Harford, S.: Multivariate LSTM-FCNs for time series classification, Neural Networks, 116, 237–245, https://doi.org/10.1016/j.neunet.2019.04.014, 2019.

Karpathy, A., Toderici, G., Shetty, S., Leung, T., Sukthankar, R., and Fei-Fei, L.: Large-Scale Video Classification with Convolutional Neural Networks, in: 2014 IEEE Conference on Computer Vision and Pattern Recognition, 24–27 June 2014, Columbus, Ohio, USA, 1725–1732, https://doi.org/10.1109/CVPR.2014.223, 2014.

Kingma, D. and Ba, J.: Adam: A Method for Stochastic Optimization, in: International Conference on Learning Representations, 7–9 May 2015, San Diego, California, USA, arXiv, https://doi.org/10.48550/arxiv.1412.6980, 2014.

Kočiščák, S., Kvammen, A., Mann, I., Sørbye, S. H., Theodorsen, A., and Zaslavsky, A.: Modelling Solar Orbiter Dust Detection Rates in Inner Heliosphere as a Poisson Process, arXiv preprint arXiv:2210.03562, https://doi.org/10.48550/arxiv.2210.03562, 2022.

Kvammen, A.: AndreasKvammen/ML_dust_detection: v1.0.0 (v1.0.0), Zenodo [code and data set], https://doi.org/10.5281/zenodo.7404457, 2022.

Kvammen, A., Wickstrøm, K., McKay, D., and Partamies, N.: Auroral image classification with deep neural networks, J. Geophys. Res.-Space, 125, e2020JA027808, https://doi.org/10.1029/2020JA027808, 2020.

Maksimovic, M., Bale, S., Chust, T., et al.: The solar orbiter radio and plasma waves (rpw) instrument, Astron. Astrophys., 642, A12, https://doi.org/10.1051/0004-6361/201936214, 2020.

Malaspina, D. M., Newman, D. L., Willson III, L. B., Goetz, K., Kellogg, P. J., and Kerstin, K.: Electrostatic solitary waves in the solar wind: Evidence for instability at solar wind current sheets, J. Geophys. Res.-Space, 118, 591–599, 2013.

Malaspina, D. M., Horányi, M., Zaslavsky, A., Goetz, K., Wilson III, L., and Kersten, K.: Interplanetary and interstellar dust observed by the Wind/WAVES electric field instrument, Geophys. Res. Lett., 41, 266–272, 2014.

Malaspina, D. M., Szalay, J. R., Pokorný, P., Page, B., Bale, S. D., Bonnell, J. W., de Wit, T. D., Goetz, K., Goodrich, K., Harvey, P. R., MacDowall, R. J., and Pulupa, M.: In situ observations of interplanetary dust variability in the inner heliosphere, Astrophys. J., 892, 115, https://doi.org/10.3847/1538-4357/ab799b, 2020.

Mann, I. and Czechowski, A.: Dust destruction and ion formation in the inner solar system, Astrophys. J., 621, L73, https://doi.org/10.1086/429129, 2005.

Mann, I. and Czechowski, A.: Dust observations from Parker Solar Probe: dust ejection from the inner Solar System, Astron. Astrophys., 650, A29, https://doi.org/10.1051/0004-6361/202039362, 2021.

Mann, I., Kimura, H., Biesecker, D. A., Tsurutani, B. T., Grün, E., McKibben, R. B., Liou, J.-C., MacQueen, R. M., Mukai, T., Guhathakurta, M., and Lamy, P.: Dust near the Sun, Space Sci. Rev., 110, 269–305, 2004.

Mann, I., Nouzák, L., Vaverka, J., Antonsen, T., Fredriksen, Å., Issautier, K., Malaspina, D., Meyer-Vernet, N., Pavlů, J., Sternovsky, Z., Stude, J., Ye, S., and Zaslavsky, A.: Dust observations with antenna measurements and its prospects for observations with Parker Solar Probe and Solar Orbiter, Ann. Geophys., 37, 1121–1140, https://doi.org/10.5194/angeo-37-1121-2019, 2019.

Montavon, G., Orr, G. B., and Müller, K.-R. (Eds.): Neural Networks: Tricks of the Trade, Springer Berlin Heidelberg, https://doi.org/10.1007/978-3-642-35289-8, 2012.

Müller, D., Cyr, O. S., Zouganelis, I., Gilbert, H. R., Marsden, R., Nieves-Chinchilla, T., Antonucci, E., Auchère, F., Berghmans, D., Horbury, T. S., Howard, R. A., Krucker, S., Maksimovic, M., Owen, C. J., Rochus, P., Rodriguez-Pacheco, J., Romoli, M., Solanki, S. K., Bruno, R., Carlsson, M., Fludra, A., Harra, L., Hassler, D. M., Livi, S., Louarn, P., Peter, H., Schühle, U., Teriaca, L., del Toro Iniesta, J. C., Wimmer-Schweingruber, R. F., Marsch, E., Velli, M., De Groof, A., Walsh, A., and Williams, D.: The solar orbiter mission-science overview, Astron. Astrophys., 642, A1, https://doi.org/10.1051/0004-6361/202038467, 2020.

Samek, W., Montavon, G., Lapuschkin, S., Anders, C. J., and Müller, K.-R.: Explaining Deep Neural Networks and Beyond: A Review of Methods and Applications, Proceedings of the IEEE, 247–278, https://doi.org/10.1109/JPROC.2021.3060483, 2021.

Shwartz-Ziv, R. and Tishby, N.: Opening the Black Box of Deep Neural Networks via Information, ArXiv, abs/1703.00810, https://doi.org/10.48550/arxiv.1703.00810, 2017.

Soucek, J., Píša, D., Kolmasova, I., Uhlir, L., Lan, R., Santolík, O., Krupar, V., Kruparova, O., Baše, J., Maksimovic, M., Bale, S. D., Chust, T., Khotyaintsev, Yu. V., Krasnoselskikh, V., Kretzschmar, M., Lorfèvre, E., Plettemeier, D., Steller, M., Štverák, Š., Vaivads, A., Vecchio, A., Bérard, D., and Bonnin, X.: Solar Orbiter Radio and Plasma Waves–Time Domain Sampler: In-flight performance and first results, Astron. Astrophys., 656, A26, https://doi.org/10.1051/0004-6361/202140948, 2021.

Szalay, J., Pokornỳ, P., Bale, S., Christian, E., Goetz, K., Goodrich, K., Hill, M., Kuchner, M., Larsen, R., Malaspina, D., McComas, D. J., Mitchell, D., Page, B., and Schwadron, N.: The near-sun dust environment: initial observations from parker solar probe, Astrophys. J. Suppl. Ser., 246, 27, https://doi.org/10.3847/1538-4365/ab50c1, 2020.

Theodoridis, S. and Koutroumbas, K.: Chap. 3 – Linear Classifiers, in: Pattern Recognition (Fourth Edition), edited by: Theodoridis, S. and Koutroumbas, K., 91–150, Academic Press, Boston, 4th Edn., https://doi.org/10.1016/B978-1-59749-272-0.50004-9, 2009.

Trosten, D. J., Strauman, A. S., Kampffmeyer, M., and Jenssen, R.: Recurrent Deep Divergence-based Clustering for Simultaneous Feature Learning and Clustering of Variable Length Time Series, in: ICASSP 2019–2019 IEEE International Conference on Acoustics, Speech and Signal Processing (ICASSP), 3257–3261, https://doi.org/10.1109/ICASSP.2019.8682365, 2019.

Van der Maaten, L. and Hinton, G.: Visualizing data using t-SNE, J. Mach. Learn. Res., 9, 2579–2605, http://jmlr.org/papers/v9/vandermaaten08a.html (last access: 12 January 2023), 2008.

Vaverka, J., Pellinen-Wannberg, A., Kero, J., Mann, I., De Spiegeleer, A., Hamrin, M., Norberg, C., and Pitkänen, T.: Potential of earth orbiting spacecraft influenced by meteoroid hypervelocity impacts, IEEE Trans. Plasma Sci., 45, 2048–2055, 2017.

Vech, D. and Malaspina, D. M.: A novel machine learning technique to identify and categorize plasma waves in spacecraft measurements, J. Geophys. Res.-Space, 126, e2021JA029567, https://doi.org/10.1029/2021JA029567, 2021.

Villar, J. R., Vergara, P., Menéndez, M., de la Cal, E., González, V. M., and Sedano, J.: Generalized Models for the Classification of Abnormal Movements in Daily Life and its Applicability to Epilepsy Convulsion Recognition, International J. Neural Syst., 26, 1650037, https://doi.org/10.1142/s0129065716500374, 2016.

Wang, Z., Yan, W., and Oates, T.: Time series classification from scratch with deep neural networks: A strong baseline, in: 2017 International joint conference on neural networks (IJCNN), 1578–1585, IEEE, https://doi.org/10.1109/IJCNN.2017.7966039, 2017.

Wickstrøm, K., Mikalsen, K. Ø., Kampffmeyer, M., Revhaug, A., and Jenssen, R.: Uncertainty-Aware Deep Ensembles for Reliable and Explainable Predictions of Clinical Time Series, IEEE J. Biomed. Health, 25, 2435–2444, https://doi.org/10.1109/jbhi.2020.3042637, 2021.

Wickstrøm, K., Kampffmeyer, M., Mikalsen, K. Ø., and Jenssen, R.: Mixing up contrastive learning: Self-supervised representation learning for time series, Pattern Recogn. Lett., 155, 54–61, https://doi.org/10.1016/j.patrec.2022.02.007, 2022.

Zaslavsky, A.: Floating potential perturbations due to micrometeoroid impacts: Theory and application to S/WAVES data, J. Geophys. Res.-Space, 120, 855–867, 2015.

Zaslavsky, A., Meyer-Vernet, N., Mann, I., Czechowski, A., Issautier, K., Le Chat, G., Pantellini, F., Goetz, K., Maksimovic, M., Bale, S. D., and Kasper, J. C.: Interplanetary dust detection by radio antennas: Mass calibration and fluxes measured by STEREO/WAVES, J. Geophys. Res.-Space, 117, A5, https://doi.org/10.1029/2011JA017480, 2012.

Zaslavsky, A., Mann, I., Soucek, J., Czechowski, A., Píša, D., Vaverka, J., Meyer-Vernet, N., Maksimovic, M., Lorfèvre, E., Issautier, K., Rackovic Babic, K., Bale, S. D., Morooka, M., Vecchio, A., Chust, T., Khotyaintsev, Y., Krasnoselskikh, V., Kretzschmar, M., Plettemeier, D., Steller, M., Štverák, Š., Trávníček, P., and Vaivads, A.: First dust measurements with the Solar Orbiter Radio and Plasma Wave instrument, Astron. Astrophys., 656, A30, https://doi.org/10.1051/0004-6361/202140969, 2021.

Zhou, B., Khosla, A., Lapedriza, A., Oliva, A., and Torralba, A.: Learning deep features for discriminative localization, in: Proceedings of the IEEE conference on computer vision and pattern recognition, 2921–2929, arXiv, https://doi.org/10.48550/arxiv.1512.04150, 2016.

Paper II: Modeling Solar Orbiter dust detection rates in the inner heliosphere as a Poisson process

S. Kočiščák, A. Kvammen, I. Mann, S. Holbek Sørbye,
A. Theodorsen, and A. Zaslavsky
Astronomy and Astrophysics 670, A140 (2023)
doi: 10.1051/0004-6361/202245165
GitHub: SamuelKo1607/solo_dust_2022

A&A 670, A140 (2023)
https://doi.org/10.1051/0004-6361/202245165

Astronomy & Astrophysics
Special issue

Solar Orbiter First Results (Nominal Mission Phase)

Modeling Solar Orbiter dust detection rates in the inner heliosphere as a Poisson process

S. Kočiščák[1], A. Kvammen[1], I. Mann[1], S. H. Sørbye[2], A. Theodorsen[1], and A. Zaslavsky[3]

[1] Department of Physics and Technology, UiT The Arctic University of Norway, 9037 Tromsø, Norway
e-mail: samuel.kociscak@uit.no
[2] Department of Mathematics and Statistics, UiT The Arctic University of Norway, 9037, Tromsø, Norway
[3] LESIA, Observatoire de Paris, Université PSL, CNRS, Sorbonne Université, Université de Paris, Paris, France

Received 7 October 2022 / Accepted 3 January 2023

ABSTRACT

Context. Solar Orbiter provides dust detection capability in the inner heliosphere, but estimating physical properties of detected dust from the collected data is far from straightforward.
Aims. First, a physical model for dust collection considering a Poisson process is formulated. Second, it is shown that dust on hyperbolic orbits is responsible for the majority of dust detections with Solar Orbiter's Radio and Plasma Waves (RPW). Third, the model for dust counts is fitted to Solar Orbiter RPW data and parameters of the dust are inferred, namely radial velocity, hyperbolic meteoroids predominance, and the solar radiation pressure to gravity ratio as well as the uncertainties of these.
Methods. Nonparametric model fitting was used to get the difference between the inbound and outbound detection rate and dust radial velocity was thus estimated. A hierarchical Bayesian model was formulated and applied to available Solar Orbiter RPW data. The model uses the methodology of integrated nested Laplace approximation, estimating parameters of dust and their uncertainties.
Results. Solar Orbiter RPW dust observations can be modeled as a Poisson process in a Bayesian framework and observations up to this date are consistent with the hyperbolic dust model with an additional background component. Analysis suggests a radial velocity of the hyperbolic component around $(63 \pm 7)\,\mathrm{km\,s^{-1}}$ with the predominance of hyperbolic dust being about $(78 \pm 4)\%$. The results are consistent with hyperbolic meteoroids originating between 0.02 AU and 0.1 AU and showing substantial deceleration, which implies effective solar radiation pressure to a gravity ratio $\gtrsim$0.5. The flux of the hyperbolic component at 1 AU is found to be $(1.1 \pm 0.2) \times 10^{-4}\,\mathrm{m^{-2}s^{-1}}$ and the flux of the background component at 1 AU is found to be $(5.4 \pm 1.5) \times 10^{-5}\,\mathrm{m^{-2}s^{-1}}$.

Key words. zodiacal dust – methods: statistical

1. Introduction

Among dust detected with in situ measurements within 1 AU, particles on unbound hyperbolic trajectories originating in the relative vicinity of the Sun play a major role, as has already been shown in the case of measurements of Solar Orbiter (Zaslavsky et al. 2021). Most of these hyperbolic particles of a submicron size are believed to be so-called β meteoroids, which are generated by a high radiation pressure to gravity ratio, denoted as β:

$$\beta = \frac{F_{\mathrm{radiation}}}{F_{\mathrm{gravity}}}. \tag{1}$$

It is clear that in the region of dust sizes $s \gg \lambda \approx 500\,\mathrm{nm}$, where s denotes the dimension of a dust particle and λ denotes the wavelength of incident light, $F_{\mathrm{radiation}}$ depends on a dust particle's cross section, while F_{gravity} depends on a dust grain's volume. Hence, the smaller the particle, the higher the β value. A maximum of β is therefore reached when $s \approx \lambda$ and usually $\beta_{\mathrm{max}} \approx 1$. Notably, both $F_{\mathrm{radiation}}$ and F_{gravity} depend on the inverse square of heliocentric distance, hence β remains constant for a given particle throughout its trajectory. We note that $F_{\mathrm{radiation}}$ and F_{gravity} are the predominant forces for the β meteoroids, as electromagnetic forces become relevant for dust grains of size $s < 100\,\mathrm{nm}$ (Mann et al. 2014). Dust of size $s < 100\,\mathrm{nm}$ can also be on an unbound trajectory due to electromagnetic forces (Czechowski & Mann 2021; Mann & Czechowski 2021).

For $\beta = 1$, the grain neither accelerates nor decelerates due to Solar influence. For $\beta = 0.5$, the grain feels solar attraction, but effective Solar attraction is reduced to one-half, which means that a sudden change in β from 0 to 0.5, for example due to a change in the size of the grain, causes an originally circular orbit to become an unbound, parabolic orbit. Particles with $\beta \geq 0.5$ are created mostly in collisions of larger dust (Dohnanyi 1972, Zook & Berg 1975, and Grün et al. 1985). Larger particles have very low $\beta \ll 1$ and are therefore originally on Keplerian orbits (referred to as initial orbits hereafter), hence $\beta = 0.5$ could be considered the minimal value needed for dust to become unbound.

The population of bound ($\beta \ll 0.5$) dust particles inside 1 AU is notably responsible for visual observations of zodiacal light. Their spatial density has been observed to depend on heliocentric distance approximately as $\sim r^{-1.3}$ (Leinert et al. 1981), which holds well down to 20 $R_\odot$, or 0.1 AU. Inward of that distance, they show shallower dependence, suggesting a maximum in density somewhere inward of 0.05 AU, or 10 $R_\odot$ (Stenborg et al. 2021). Regions with high density of bound dust is very likely the region of origin of β meteoroids, as the collision rate of bound dust depends on the square of its spatial density (Mann & Czechowski 2005).

As β meteoroids likely make up most of the submicron hyperbolic dust where the particles considered have sizes $s > 100\,\mathrm{nm}$, the two terms are almost interchangeable for the purpose of the present discussion (Zaslavsky et al. 2021). The

term β meteoroids is used where radiation pressure ejection is important and the term hyperbolic dust is used where only trajectories of the grains are relevant.

The detection of bound dust particles is usually done remotely, both historically (Van de Hulst 1947 and Leinert et al. 1981) and currently (Howard et al. 2019 and Stenborg et al. 2021), taking advantage of light scattering properties of these particles. The detection of submicron particles is done mostly in situ (at an encounter with a particle), due to their insignificant light scattering properties and low spatial density, often taking advantage of the so-called impact ionization effect (Friichtenicht 1962 and Alexander & Bohn 1968). Impact ionization dust detection is a passive data-gathering process carried out by either a specialized instrument (Dietzel et al. 1973 and Srama et al. 2004) or often as a byproduct of electric (Gurnett et al. 1997; Meyer-Vernet et al. 1986; Kurth et al. 2006; Wang et al. 2006; Zaslavsky et al. 2012, 2021; Vaverka et al. 2018; Malaspina et al. 2020; Mozer et al. 2020; and Nouzk et al. 2021) or magnetic (Malaspina et al. 2022 and Gasque et al. 2022) measurements. Due to high energy density present at the impact site, free charge is generated upon a hypervelocity dust impact. The charge generated is partially picked up by the spacecraft body and/or antennas, which results in specific signatures in fast electric measurements (Zaslavsky 2015; Meyer-Vernet et al. 2017; Vaverka et al. 2017; Mann et al. 2019; Shen et al. 2021; Rackovic Babic et al. 2022). The amount of generated charge Q has been empirically found to approximately follow the equation

$$Q = Am^{\gamma}v^{\alpha}, \tag{2}$$

where in the range of impact velocities $20\,\mathrm{km\,s^{-1}} < \mathbf{v} < 50\,\mathrm{km\,s^{-1}}$ achieved in laboratory (Friichtenicht 1962; Dietzel et al. 1972; and Shu et al. 2012) $\gamma \approx 1$ and $3 \lesssim \alpha \lesssim 5$. All three parameters A, γ, and α are dependent on both the material of the grain and the target (Grün 1984; Grün et al. 2007; and Collette et al. 2014).

For many decades now, it has been standard to express cumulative mass distribution of dust near 1 AU in terms of a power-law distribution over about 20 decades of masses, from nanodust to comets and asteroids and above. Clearly, the distribution is an approximation and the distribution is described with a different exponent in different intervals. However, it is often the case that a single experiment is sensitive over several orders of magnitude and finds that the mass distribution (number of particles with a mass of at least m) follows a power-law

$$F(m) = F(m_0)\left(\frac{m}{m_0}\right)^{-\delta} \tag{3}$$

over the observed range. For example, the work of Whipple (1967) reported $\delta \approx 1.34$ for the mass range 10^{-8}–10^{-1} kg and $\delta \approx 0.51$ for the mass range 10^{-13}–10^{-8} kg. Compiling previous estimates and relying on the stationarity of a dust cloud, Dohnanyi (1970) reported $\delta \approx 7/6$ for sporadic meteoroids of masses from macroscopic down to 10^{-11} kg and $\delta \approx 1/2$ between 10^{-14} kg and 10^{-11} kg. Grün et al. (1985) suggested $\delta \approx 0.8$ in the range 10^{-21}–10^{-17} kg, that is β meteoroids and smaller. Recently, Zaslavsky et al. (2021) inferred $\delta \approx 0.34$ for Solar Orbiter's Radio and Plasma Waves (RPW) dust detections of dust of $m \gtrsim 10^{-17}$ kg. It is not clear whether Eq. (3) represents a good approximation for β meteoroids.

A Poisson point process is a stochastic process defined by the following properties: (1) a Poisson distribution of counts within an arbitrarily chosen bounded region (for example a temporal interval); (2) statistical independence of counts within disjoint regions (temporal intervals); and (3) no two events can happen at the exact same location (time).

It is reasonable to assume that the third condition is met, especially near 1 AU. For Solar Orbiter specifically, the detection of two subsequent impacts is possible unless they happened in the same 62 ms window, which is unlikely given the mean waiting time ≈200 s on the most hit intensive days (see Fig. 4). The first two conditions demand that a detection of a dust particle does not influence the probability of detection of a particle at any other point in time, for example particles do not interact, and their reservoir cannot be depleted. In the case of β meteoroids, all of these can be assumed, as particles are likely formed far away from the spacecraft, they are sparsely distributed, and their trajectories are uncorrelated. We are aware that the Solar System's dust cloud is not homogeneous on small scales and that a large stream (Szalay et al. 2021) or a coronal mass ejection (Ragot & Kahler 2003) could alter the rate on short timescales, but we see no evidence for that with Solar Orbiter. Therefore, a Poisson process is the simplest conceivable model and it is natural to consider dust counts as an inhomogeneous Poisson point process, that is a Poisson process with a nonconstant rate. This means that the rate depends on other parameters, in our case the distance from the Sun and spacecraft velocity. In fact, the observed number of detections within a naturally considered temporal interval, for example an hour or a day, is usually a low number. This implies a considerable probability of zero detections, which makes the random variable of detections per temporal interval a poor fit to a frequently considered normal distribution, which allows for negative numbers. Hence, a Poisson distribution of counts should be considered.

Inferring the variable detection rate could be done by least squares fitting a model onto a time series of detections per unit time, as is often done. A least squares fit produces the maximum likelihood estimate when the error of the data (residuals) are normally distributed. However, detections per unit time have a Poisson distribution, as discussed above. It is possible to obtain a maximum likelihood estimate with more careful analysis, but uncertainty is not directly accessible and must be estimated by other means (for example using the bootstrap method). Adapting a procedure designed specifically to fit a Poisson process to Poisson observations grants the resolution needed to fit a complicated model precisely. Moreover, given we meet model assumptions, we can make more meaningful error estimates and potentially compare competing models in a meaningful way.

In the present work, we take advantage of the Bayesian inference, which is a general procedure that works with models for observations with unknown parameters and meets both of the above-mentioned criteria: it handles the Poisson distribution and provides an uncertainty estimate. In this approach, unknown parameters are regarded as random variables coming from an unknown distribution, about which some prior information is available (in the form of a prior belief, or prior distribution). The procedure infers the posterior (improved) distribution of unknown parameters based on the prior distribution and observed data. This distribution automatically carries information about uncertainty.

Integrated nested Laplace approximation (Rue et al. 2009, 2017; INLA for short) implements an approximate Bayesian inference for a wide class of three-stage hierarchical models. This class of models contains multilevel (nested) models, spatio-temporal models, survival models, and others (Gómez-Rubio 2020). A decisive advantage of INLA as opposed to other Bayesian methods (for example sampling-based methods) is its computational efficiency allowing for one to fit more

complicated models to more observations within available time, making it the method of choice for the course of this work. The inference is carried out using the R-INLA package (Martins et al. 2013 and Rue et al. 2017) for the Bayesian inference.

In Sect. 2, we briefly introduce the Solar Orbiter mission, its dust measurement results, and the data product that we use throughout the work. Section 3 is a discussion and analysis of observed hyperbolic dust velocity. The fitting of the dust detection rate using INLA is presented in Sect. 4 and we conclude our findings in Sect. 5. Finally, an outlook for Solar Orbiter and other missions is briefly discussed in Sect. 6.

2. Solar Orbiter's dust observations and data products

Solar Orbiter is a spacecraft that orbits the Sun on an elliptical trajectory. Solar Orbiter underwent several gravity assists and its orbital parameters have therefore changed several times since its launch in early 2020. As of the summer of 2022, Solar Orbiter has had a low inclination, effectively making measurements in the ecliptic plane. Its aphelion is close to 1 AU and perihelion 0.3 AU; however, for the majority of its mission so far, its perihelion has been close to 0.5 AU.

Radio and Plasma Waves (RPW) is an experiment onboard Solar Orbiter designed to measure both the electric and the magnetic field in three components in a wide frequency band, from near-DC to 16 MHz in the case of the electric field (Maksimovic et al. 2020). The measurements of electric fields, and as is crucial for the present work, allow for the detection of cosmic dust impacts, which is one of the auxiliary scientific objectives of Solar Orbiter. A part of the data analyzed here was accessed at Solar Orbiter/RPW Investigation (2022)[1], specifically time domain sampler (TDS) waveform electrical data (Level 2).

In their recent work, Zaslavsky et al. (2021) describe properties of Solar Orbiter's RPW as a dust detector. It has the capacity of $C \approx 250\,\mathrm{pF}$, a sensitivity to pulses of $V \gtrsim 5\,\mathrm{mV}$, a collection area of $S_{\mathrm{col}} \approx 8\,\mathrm{m}^2$, and a duty cycle of $D \approx 6.2\%$. They show that Solar Orbiter's RPW instrument is indeed capable of dust detections and that these could be modeled as hyperbolic dust. The authors mostly discuss β meteoroids, as they are likely the observed population, but in principle the model fits to any hyperbolic dust population. The model for the detection rate R presented in the aforementioned work,

$$R = F_{1\,\mathrm{AU}} S_{\mathrm{col}} \left(\frac{r}{1\,\mathrm{AU}}\right)^{-2} \frac{v_{\mathrm{impact}}}{v_{\mathrm{dust}}} \left(\frac{v_{\mathrm{impact}}}{v_{\mathrm{impact}}(1\,\mathrm{AU})}\right)^{\alpha\delta}, \tag{4a}$$

$$v_{\mathrm{impact}} = |\boldsymbol{v}_{\mathbf{dust}} - \boldsymbol{v}_{\mathbf{sc}}|, \\ = \sqrt{\left(v_{\mathrm{dust}}^{\mathrm{radial}} - v_{\mathrm{sc}}^{\mathrm{radial}}\right)^2 + \left(v_{\mathrm{dust}}^{\mathrm{azimuthal}} - v_{\mathrm{sc}}^{\mathrm{azimuthal}}\right)^2} \tag{4b}$$

has three parameters: $\alpha\delta$, $F_{1\,\mathrm{AU}} S_{\mathrm{col}}$, and v_{dust}. We note that, both $\alpha\delta$ and $F_{1\,\mathrm{AU}} S_{\mathrm{col}}$ are products of two quantities. All three parameters could have a spatio-temporal dependence.

The model shows a good fit to the data with the parameters that are considered constant: the outward radial heliocentric speed of $v_{\mathrm{dust}} \approx 50\,\mathrm{km/s}$ and exponent $\alpha\delta \approx 1.3$. The value for v_β was inferred by relating the difference in the detection rate in the inbound and the outbound leg of an orbit (Zaslavsky et al. 2021) and it was used directly, not as a free parameter of Eq. (4a). A value of $\delta \approx 0.34$, which is a dimensionless parameter in mass distribution of detected dust grains (see Eq. (3)), was inferred from the distribution of impact pulse amplitudes. The value of α, which stands for the power of velocity in charge-yield Eq. (2) is deduced from the knowledge of $\alpha\delta$ and δ. It is important to note that α is often measured in a laboratory setup and its inferred value is compatible with ground-based measurements (Collette et al. 2014). The exponent of $\alpha\delta$ accounts for the change in sensitivity due to higher velocity, hence the flux is to be hereafter understood as the flux of detectable grains or the flux of grains that are large and fast enough. The parameter $F_{1\,\mathrm{AU}}$ stands for the flux at 1 AU, $F_{1\,\mathrm{AU}} \approx 8 \times 10^{-5}\,\mathrm{m}^{-2}\,\mathrm{s}^{-1}$ (see Zaslavsky et al. 2021 for details).

In addition to L2 Solar Orbiter RPW data, this work makes use of the data product provided by Kvammen et al. (2023), which is a result of a convolutional neural-network-classified time-domain-sampled data. It builds on a supervised classification algorithm trained using a randomly chosen subsample of manually labeled data. Its main advantage over visual inspection of all data on-board classified as dust (which is a time-consuming task) is that it is fully automatic and reasonably time-consuming. Therefore, it allows for not only type 1 error correction (detection confirmation), but also for type 2 error correction, implying a search for dust in the vast data that has not been classified as dust by an on-board algorithm a priori. Building upon the analysis of TDS snapshots, it is worth mentioning that the classifier distinguishes impacts happening in distinct snapshots, but it is not reliable with the detection of two impacts within the same snapshot, which is an unlikely situation. There is also a necessary amplitude filter, as only transmitted TDS snapshots could be classified, while only snapshots containing phenomena of a sufficient amplitude are transmitted. This however does not spoil the assumption of Poisson distribution and it is accounted for in the analysis. Although no supervised classifier could get rid of human bias and error completely, these data provide the most reliable Solar Orbiter dust detection data available to date, as has been shown in Kvammen et al. (2023). The data set consists of 4606 dust detections acquired over approximately 669 h within 457 days between 29 June 2020 and 16 December 2021. There are several intervals of unavailable data lasting longer than a week in July and August of 2020 (23 days) and September of 2021 (9 days). We make use of the data that were publicly available on 01 September 2022. We refer to these data as TDS/TSWF-E/CNN and it is publicly accessible (see Kvammen et al. 2023).

3. Impact rates and velocities of hyperbolic dust

3.1. Single-particle velocities

We note that β meteoroids are moving mostly radially outward from their region of origin, which is located well within 0.5 AU. Figures 1, 2 display possible single-particle velocity profiles (see Appendix A for underlying equations). As $\beta < 0.5$ leads to finite aphelion, $\beta \approx 1$ requires a rather specific set of parameters, and values of $\beta \gtrsim 0.5$ are shown. We note that this choice is inconsequential and was made for illustration purposes only, as we do not presuppose a β value in a further analysis. In fact, we do not presuppose that the observed population includes β meteoroids, though that is likely the case. The effective initial orbit of β grain's parent body must lie outside of the near-solar dust-free zone, but in the region with a high bound dust concentration, which restrains the r_0 values shown. As shown in Fig. 1, radial β meteoroid velocities expected between 0.5 AU and 1 AU

[1] Solar Orbiter / Radio and Plasma Waves Data, data retrieved from Observatoire de Paris, LESIA, https://rpw.lesia.obspm.fr/roc/data/pub/solo/rpw/data/L2/

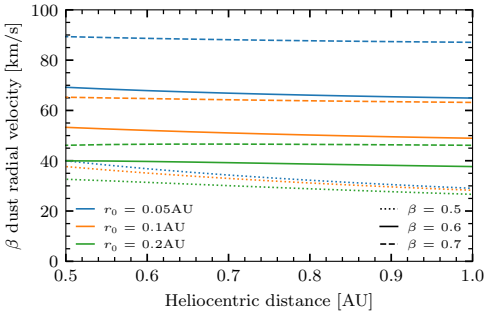

Fig. 1. Radial velocity profiles of β meteoroids released by a sudden parameter change (for example due to a collision) from an initially circular orbit. A selection of β values and origins (r_0) is shown.

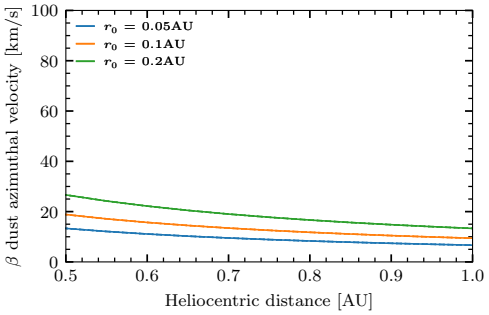

Fig. 2. Azimuthal velocity profiles of β meteoroids released by a sudden parameter change (for example, due to a collision) from an initially circular orbit. A selection of origins (r_0) is shown, with the β value not being relevant.

are between 30 km s^{-1} and 90 km s^{-1} for the given combinations of parameters and they are nearly independent of heliocentric distance (nearly constant). Solar gravity and radiation pressure forces are central forces; therefore, the β value does not influence azimuthal velocity as a function of heliocentric distance, which is governed by angular momentum conservation and the initial orbit only. Azimuthal velocities of β meteoroids of chosen parameters between 0.5 AU and 1 AU are therefore between 7 km s^{-1} and 30 km s^{-1} and decreasing $\propto r^{-1}$, as shown in Fig. 2.

If dust detections on Solar Orbiter's RPW correspond to hyperbolic dust, a difference in detection rate $R_{\rm in}$ versus $R_{\rm out}$ due to spacecraft radial velocity should be present, as is indeed the case. It is shown by Zaslavsky et al. (2021) that this approach allows for an order of magnitude estimation of the radial component of dust velocity $v_{\rm dust;rad} \approx 50\,{\rm km\,s^{-1}}$, which is in line with expectations. In the present work, we extend the approach to estimate continuous heliocentric-distance-dependent dust radial velocities, using the data product of Kvammen et al. (2023) and taking into account more unknown variables that influence our estimates.

3.2. Velocity estimation

A first estimate of $v_{\rm dust;rad}$ is obtained if a model for the dust collection rate with linear dependence on relative Solar Orbiter and dust velocity $v_{\rm impact}$ is assumed ($R \propto v_{\rm impact}$). This corresponds to linear dependence on the volume of space scanned per unit of time only:

$$v_{\rm dust;rad} \approx \frac{R_{\rm in}+R_{\rm out}}{R_{\rm in}-R_{\rm out}}|v_{\rm sc;rad}|, \tag{5}$$

where $|v_{\rm sc;rad}|$ is the absolute value of the spacecraft's radial velocity at a given heliocentric distance. We note that $R_{\rm in}$ and $R_{\rm out}$ are obtained at the same heliocentric distance, but in inbound and outbound legs of the orbit, respectively. If, however, a different dependence of $R(v_{\rm impact})$ is assumed, Eq. (5) changes. Assuming $R \propto v_{\rm impact}^{q}$, a second estimate of $v_{\rm dust;rad}$ is obtained by

$$v_{\rm dust;rad} = |v_{\rm sc;rad}|\frac{\left(R_{\rm in}^{2/q}+R_{\rm out}^{2/q}\right)}{\left(R_{\rm in}^{2/q}-R_{\rm out}^{2/q}\right)} + \frac{\sqrt{\tilde{D}}}{\left(R_{\rm in}^{2/q}-R_{\rm out}^{2/q}\right)}, \tag{6a}$$

$$\tilde{D} = v_{\rm sc;rad}^2\left(R_{\rm in}^{2/q}+R_{\rm out}^{2/q}\right)^2 - v_{\rm sc}^2\left(R_{\rm in}^{2/q}-R_{\rm out}^{2/q}\right)^2, \tag{6b}$$

where q is equivalent to $1+\alpha\delta$ in Eq. (4a) and $\tilde{D}$ has no direct physical interpretation. We took the spacecraft's azimuthal velocity into account, but not the dust's azimuthal velocity, as that would be a second unknown component for which we do not have enough information. It is nonetheless possible to correct for assumed dust azimuthal velocity by subtracting it from $v_{\rm sc}$ (see Appendix B for the derivation of Eqs. (5)–(6b)).

It follows from Eq. (6a) that with $R_{\rm in}$ and $R_{\rm out}$ being observed, the value of $q > 1$ leads to a higher velocity estimate than in the case of $q = 1$, an estimate that is higher by a factor of q in first order approximation. Zaslavsky et al. (2021) reported inferred velocities $v_{\rm dust;rad} \approx 50\,{\rm km/s}$ assuming $q = 1$ and they show compatibility of detection rates with the model assuming $q = 1+\alpha\delta \approx 2.3$ according to Eq. (4a). With assumptions being met, $v_{\rm dust;rad} \approx 50\,{\rm km/s}$ is likely an underestimate. The most important assumption here is that the dust does indeed come from a hyperbolic population.

We note that the assumption that all detected dust grains are hyperbolic is difficult to verify or falsify. The most prominent trend in detections is that the counts diminish with increasing heliocentric distance, which could easily hide a plethora of other components, such as bound dust or interstellar dust. The first correction to the assumption that all detections come from a hyperbolic dust stream is the assumption of having a two-component field: hyperbolic dust and sporadic (background) detections, with the latter having no dependence on the spacecraft location or velocity. This is not to say that the nonhyperbolic component has no temporal dependence, this is just the simplest conceivable correction. For further discussion, readers can refer to Sect. 4.4.

3.3. Velocity inference

Assuming that the dust flux is not explicitly dependent on time, the dust detection rate is a function of orbital phase as long as the orbital parameters do not change. Conversely, gravity assists change orbital parameters, such as perihelion, aphelion, and eccentricity. For the present analysis, we therefore treated sets of orbits, delimited by gravity assists, as separate data sets. In this way, data were aggregated for several orbits with the same orbital parameters, but we did not aggregate incompatible measurements. For instance, dust detection counts recorded near 0.6 AU on branches 2 and 3 are expected to be very different due to a vastly different Solar Orbiter radial velocity (see Solar Orbiter's radial velocity and its heliocentric location throughout its trajectory in Fig. 3). Minor orbital alterations between gravity assists have been neglected.

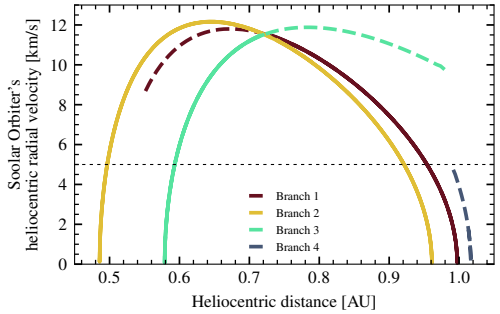

Fig. 3. Solar Orbiter's heliocentric distance and absolute value of its radial velocity. Colors separate individual branches of the orbit that come with changes in orbital parameters at gravity assists. Dashed lines correspond to all the combinations of radial velocity and location, while solid lines denote that Solar Orbiter passed through both inbound and outbound arms for the combination. The horizontal dashed line denotes Solar Orbiter's radial velocity of 5 km s^{-1}.

Since 29 June 2020, Solar Orbiter has undergone three gravity assists, producing four distinct sets of data. The last of these chronologically so far did not accumulate data sufficient for analysis, and crucially did not produce any detections in the inbound part of the orbit at the time of analysis, hence the first three branches were used. The difference between a detection rate in the inbound and outbound leg of an orbit could be used for dust radial velocity inference, provided that radial spacecraft velocity is not negligible, compared to dust radial speed. Hence data represented by dashed lines in Fig. 3 are not used for this analysis. Data with radial spacecraft velocity $< 5\,\mathrm{km\,s^{-1}}$ are not used as they carry little information (see horizontal dashed line in Fig. 3).

In order to estimate radially dependent velocity, we produced smooth estimates of radially dependent detection rates, as defined in the TDS/TSWF-E/CNN data set. The fitting was done separately for inbound and outbound legs for each gravity assist delimited data set. In order to not rely on assumptions, we decided to use nonparametric fitting, specifically Nadaraya–Watson kernel regression (Watson 1964 and Nadaraya 1964) with a Gaussian kernel ($FWHM \approx 2.355\sigma = 0.15$ AU). This is a simple and robust local-averaging fitting procedure, producing C^∞ estimates. Dust detection counts are Poisson random variables; therefore, they have a variance equal to their mean value. To evaluate the uncertainty, we constructed confidence intervals for the nonparametric fit by bootstrapping on daily dust counts: new samples were generated with original counts as rates for new Poisson-distributed random variables. For an illustration of all three data sets and fitted rates, readers can refer to Fig. 4. It is important to keep in mind that the detection rates hereafter have been normalized to the observation time. For every branch, we only used the heliocentric distance interval where both inbound and outbound legs are available, bounded by the innermost and the outermost detection on the leg (see the grayed areas in Fig. 4). We did not use the $r < 0.62$ AU of branch 2, as there are no outbound detections near 0.6 AU and the detections near 0.5 AU show little difference between the inbound and the outbound leg. This may be due to a spatial limitation of the given model, an unlikely combination due to scarce data, a truly higher radial velocity, or a combination of more effects.

Having smooth detection rate estimates, we produced velocity estimates using Eq. (6a) (see Fig. 5). Bootstrap samples

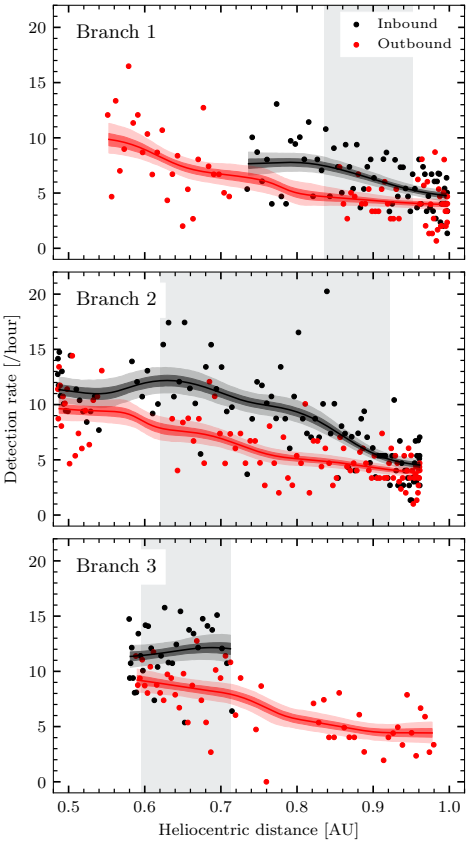

Fig. 4. Nonparametric fitting of the detection rate observed between 29 June 2020 and 27 November 2021 in th inbound and outbound part of the trajectory, with branches being separated by gravity assists on 26 December 2020 and 8 August 2021. The lines are the results of nonparametric fitting and only grayed intervals are used for further analysis; readers can compare this with Fig. 3.

of detection rates were used to calculate the shown percentile confidence intervals. Notably, not all the bootstrap samples for $\lambda_{\mathrm{bg}} = 4\,\mathrm{h^{-1}}$ allowed for a solution, which is apparent from the jitters of the blue curve at $r > 0.75$ AU. Confidence intervals were constructed from the solutions that were obtained. This issue is to be expected, as $\lambda_{\mathrm{bg}} = 4\,\mathrm{h^{-1}}$ implies very little hyperbolic dust at $r > 0.8$ AU (see Fig. 4) and therefore uncertainty in the inferred velocity. The estimate shown in Fig. 5 assumes $\alpha\delta = 1.3$ and an initial heliocentric distance of 0.1 AU, with the latter in the form of correction for dust azimuthal velocity.

To further estimate the uncertainty, we included three relevant parameters (in total): (1) a background (nonhyperbolic) rate λ_{bg}, corrected for by subtraction from the estimated detection rate; (2) the product $\alpha\delta$ included in Eq. (6a); and (3) azimuthal dust velocity corresponding to different initial circular orbits, as shown in Fig. 2, giving a straightforward generalization of Eq. (6a).

We have an estimate of the region of likely velocities (see Fig. 6), given a reasonable variation of free parameters. The analysis shows the velocity to be mostly between 40 km s^{-1} and

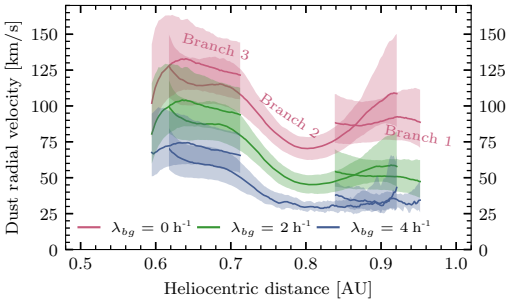

Fig. 5. Velocity estimated from TDS/TSWF-E/CNN. Different colors correspond to different assumed background rates. Shaded areas correspond to 50% confidence intervals and the solid lines correspond to median values for a given heliocentric distance. Different branches of $\lambda_{bg} = 0\,h^{-1}$ are labeled. Only parts of the branches where $v_{sc} > 5\,km\,s^{-1}$ are shown.

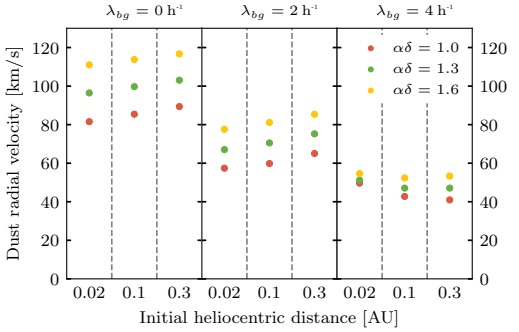

Fig. 6. Velocity estimated from TDS/TSWF-E/CNN. Single velocities were obtained from profiles for better readability. The points were constructed as averages of velocities at 0.65, 0.75, and 0.85AU for all the branches, where a velocity is the median solution for all the bootstrap replications. For full profiles, readers can refer to Appendix C.

$100\,km\,s^{-1}$, according to Fig. 6. We know that the rate λ_{bg} of constant, nonhyperbolic dust could clearly not be lower than 0 and could not be much higher than $\approx 4\,h^{-1}$ either, because the total detection rate is about $\approx 4\,h^{-1}$ at a heliocentric distance ≈ 1 AU, which would imply 100% contribution of background dust in this region (see Fig. 4). This explains why no solutions of Eq. (6a) are found near 1 AU in that case, as Fig. 5 shows. The reason being that the difference between inbound and outbound rates are observed to be too high, such that they cannot be explained in the case of $\lambda_{bg} = 4\,h^{-1}$. A rather low amount ($\lesssim 1\,h^{-1}$) of nonhyperbolic dust would imply a higher velocity in the range of $\approx 100\,km\,s^{-1}$. The conclusion is that the higher the background detection rate λ_{bg} is, the lower the underlying dust velocity. Similarly, a higher $\alpha\delta$ product implies a higher velocity, and a larger initial radius (in the case of β meteoroids) implies higher underlying radial velocity. Furthermore, assuming β meteoroids, low velocities $\gtrsim 50$ $km\,s^{-1}$ imply a low β factor (see Fig. 1). While bearing many uncertainties in mind, this inference is very robust as it does not depend on a specific model for dust, in particular it is independent of dust spatial density as a function of heliocentric distance, because we only compare observations on the same heliocentric distance. The background component is among the biggest unknowns (see Appendix C for full velocity profiles that produce the data in Fig. 6).

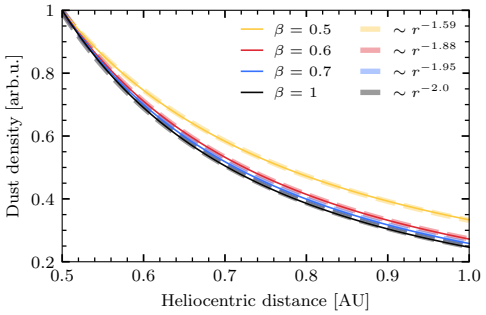

Fig. 7. Modeled dust spatial densities for different β values assuming a circular initial orbit of 0.1 AU. Solid lines show the spatial density and they were normalized to the density at 0.5 AU. Dashed lines are approximations to the solid lines, assuming a power dependence on r.

3.4. Spatial density

If the hyperbolic grains do not accelerate (for example β meteoroids with $\beta \approx 1$ are assumed), a radial dependence of spatial density of $\sim r^{-2}$ is the result. This is not the case if acceleration or deceleration is present. Particularly, it makes sense to assume slowing dust ($\beta < 1$), as Fig. 5 suggests slowing rather than accelerating dust. Also, $\beta \approx 1$ or even $\beta > 1$ needs a rather specific set of conditions (a combination of material and specific size, see Mann 2010), while $0.5 < \beta < 1$ is possible for a broad range of dust parameters. The observed effective β is then determined by aggregation of all components. The equation for detection rate (4a) contains r^{-2}, but it remains the correct expression for dust flux even if v_{dust} is not constant. In that case, r^{-2} should not be interpreted as a spatial density of dust, but as a geometric factor. The spatial density is then expressed through the nonconstant v_{dust}. However, this makes it very difficult to fit model (Eq. (4a)) to the data, as v_{dust} is no longer a numeric parameter, but a function of r.

We shall continue to explore the spatial density view and examine the effective exponent of r given β meteoroids with some $0.5 \leq \beta < 1$. Figure 7 shows an example of how the β value influences the spatial dust density (for a spatial dust density calculation, see Appendix A). The analysis of spatial density as a result of deceleration does not require the dust to be β meteoroids, but the relation to the β value clearly does. In Fig. 7, an initial orbit of 0.1 AU is assumed; readers can refer to Appendix E for plots of the dust spatial density variation similar to Fig. 7 for different initial orbits. The particular exponents depend on the initial orbit, but the general trend of a lower β value implying deceleration remains.

4. Daily count inference

4.1. Model formulation

We decided to model the number of dust detections within a day as a Poisson-distributed random variable, as dust detection itself is a prime example of a Poisson point process in time, as discussed in Sect. 1. The rate λ of the process is considered dependent on multiple parameters $\boldsymbol{\theta}$. Notably, we consider λ to

not be explicitly dependent on time, but to be temporarily dependent indirectly, through the orbital parameters and the orbital phase of the spacecraft. Importantly, the rate is also considered dependent on the parameters of the dust cloud. Therefore, we formulated a hierarchical Bayesian model with five parameters, $\epsilon_v, \epsilon_r, \lambda_\beta, \lambda_{\rm bg}$, and v_r, which, for simplicity, we denote as $\boldsymbol{\theta} = (\epsilon_v, \epsilon_r, \lambda_\beta, \lambda_{\rm bg}, v_r)$. These parameters were used to model the rate λ and by extension detected counts (see Eqs. (7a) to (7d)). We note that the rate λ (see Eq. (7b)) is a generalization of Eq. (4a) with an additional constant (background) term and a variable exponent of heliocentric distance.

In order to keep the present model simple and yet allow for nonconstant velocity, we used the parameters v_r and ϵ_r as the mean radial dust velocity and density exponent, respectively (see Appendix D for a further interpretation). This combination allows for one to fit a single constant mean velocity and effective acceleration (through the exponent ϵ_r) at the same time with just two constant scalar parameters. It is important to keep in mind though that the parameter v_r is the effective mean radial velocity of the dust grains. The velocity of an individual dust grain changes as it moves through the Solar System. The exact meaning of this effective mean is therefore opaque, as the measurement was done at a variable heliocentric distance. However, the radial velocity between 0.5 AU and 1 AU changes gradually and, in the extreme case of $\beta = 0.5$ and $r_0 = 0.05$ AU, it changes by about 30 % (see Fig. 1), which is a smaller difference than the difference due to either different β or r_0. Therefore, it is of lesser importance whether the inferred mean is the temporal mean, the spatial mean, or anything in between.

The Poisson likelihood (Eq. (7a)) includes the exposure time E (in hours) and the rate λ (in detections per hour). Then Eq. (7c) is a straightforward definition of relative velocity between the spacecraft and the dust particle, while Eq. (7d) describes the decomposition of dust velocity into radial and azimuthal components. In practice, the model defines the parameter v_r as the radial velocity of a dust particle and the variable v_a as the azimuthal velocity of the same particle, but only v_r is regarded as a random variable. The variable v_a is directly related to heliocentric distance $|\boldsymbol{r}|$ according to Eq. (7e), which is approximately equivalent to the $r_0 = 0.1$ AU line in Fig. 2. This is due to the simpler and less important dependence of $v_{\rm impact}$ on v_a and as a compromise in order to keep the number of free parameters reasonable with respect to the available data (the attempts to fit six parameters were not fruitful). The main goal of the fitting procedure is to determine the marginal posterior distributions of each of the parameters $\boldsymbol{\theta}$ of the model

$$N|\lambda, \boldsymbol{\theta} \sim Poiss(E \cdot \lambda(\boldsymbol{\theta})), \tag{7a}$$

$$\lambda(\boldsymbol{\theta}) = \lambda_\beta \cdot v_{\rm impact}^{\epsilon_v} \cdot r^{\epsilon_r} + \lambda_{\rm bg}, \tag{7b}$$

$$v_{\rm impact} = \frac{|\boldsymbol{v}_{\rm sc} - \boldsymbol{v}_{\rm dust}|}{50\,{\rm km\,s^{-1}}}, \tag{7c}$$

$$\boldsymbol{v}_{\rm dust} = v_r \cdot \boldsymbol{e_r} + v_a \cdot \boldsymbol{e_\phi}, \tag{7d}$$

$$v_a = 12\,{\rm km\,s^{-1}}\,\frac{0.75\,{\rm AU}}{|\boldsymbol{r}|}. \tag{7e}$$

There are N detections observed in a given day, the exposure E is the total time when the instrument was collecting data in a mode that allows for dust detection, hence it is known precisely. The location and velocity of Solar Orbiter are also known precisely. In Eq. (7c), a dimensionless parameter is constructed – it has computational advantages if $v_{\rm impact} \approx 1$, as a rather high power of the variable was computed in the process. Equations (7c)–(7e) explain the role of the parameter v_r in Eq. (7b) and they have only been separated from Eq. (7b) for better readability. We note that purely 2D motion of dust particles, within the ecliptic plane, is assumed in Eq. (7d).

The parameter ϵ_v is the exponent of $v_{\rm impact}$ in the mean rate formula and it incorporates the dependence on the rate of volume scanning ($V/t \propto S \cdot v_{\rm impact}$), hence $v_{\rm impact}^1$, and the dependence on charge yield α and dust mass power-law exponent δ in the form of $v^{\alpha\delta}$. The dependence is then $v_{\rm impact}^{1+\alpha\delta} = v_{\rm impact}^{\epsilon_v}$. The parameter ϵ_r is the exponent of heliocentric distance r, which is notably influenced by acceleration and deceleration of dust, as discussed in Sect. 3.4. Readers can refer to Appendix D for a further interpretation. The parameter λ_β plays the role of a normalization constant, accounting for an absolute dust spatial density and spacecraft detection area and holds the physical unit of $\rm h^{-1}$. It is uninteresting to study this parameter in itself, in the sense that it merely normalizes the model so that the detection rate corresponds to the observed mean rate and has no consequence on the physical characteristics of any given particle. The parameter $\lambda_{\rm bg}$ has the meaning of detections per hour as well, but it is clearly interpreted as the background detection rate, that is to say the rate of detections that are not attributable to hyperbolic dust. The parameter v_r also has a very direct meaning, which is the mean outward radial velocity of the hyperbolic dust in our experimental range. We note that variation of impact velocity is still allowed by variation in spacecraft velocity $\boldsymbol{v}_{\rm sc}$. Acceleration is accounted for in ϵ_r.

4.2. Prior distributions of parameters

For Bayesian inference, choosing reasonable priors is important. Ideally, priors should be informative (narrow) enough to capture the prior knowledge about parameters, but vague (wide) enough so that they still allow for additional information to play a role. It is physically infeasible for the parameters λ_β and $\lambda_{\rm bg}$ to be negative, as they have a meaning of detection rate. Furthermore, positive radial velocity is also required by the model to work. Therefore, we opted for gamma priors for these three parameters. Although we are quite sure about the sign of the parameters ϵ_v and ϵ_r, neither the model nor the physical unit actually rules out the possibility of ϵ_v or ϵ_r having any sign. We therefore opted for normal priors for ϵ_v and ϵ_r. The choice of prior family for ϵ_v, ϵ_r, and v_r is of little importance. Generally speaking, prior choice makes less of a difference the more data are analyzed.

In order to incorporate our actual prior belief about the model, we chose what we believe are moderately informative priors for the parameters. The following paragraphs discuss our choice. For a graphical representation of the prior distributions of the parameters, readers can refer to Fig. 8.

The parameter ϵ_v stands for $1 + \alpha\delta$. Since we have indications from Zaslavsky et al. (2021) that $\delta \approx 0.3$ and most laboratory experiments show (Collette et al. 2014) that $3 \lesssim \alpha \lesssim 5$, we expect $1.9 \lesssim \epsilon_v = 1 + \alpha\delta \lesssim 2.5$. We therefore chose the prior $\epsilon_v \sim Norm(mean = 2.2, stdev = 0.2)$, which places emphasis on the range $2.0 < \epsilon_v < 2.4$ and yet does not prohibit any real ϵ_v. We note that δ and α are the only pieces of information used for prior construction taken from outside of this work. For more discussion, readers can refer to Appendix I.

Provided that there are no major sources of dust between 0.5 AU and 1 AU and provided that dust neither accelerates nor decelerates, $\epsilon_r = -2$, which follows easily from mass conservation. If we relax the latter assumption, then $\epsilon_r \neq -2$. In fact, the dependence no longer follows r^{ϵ_r} exactly, but as is shown in Fig. 7, for β meteoroids of $0.5 \lesssim \beta \lesssim 1$ the dependence is

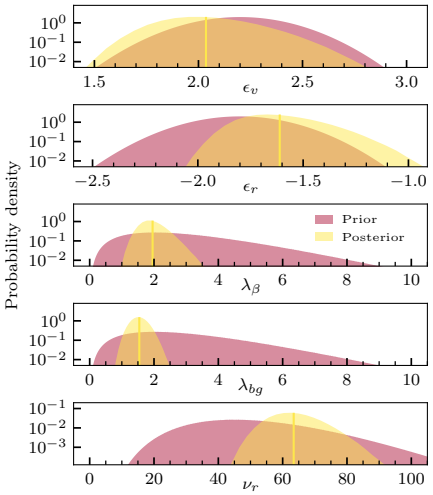

Fig. 8. Prior and posterior distributions for the parameters $\boldsymbol{\theta}$. The prior distributions are described in the main text. Summary statistics for posterior distributions are described in Table 1.

Table 1. Marginal posterior mean and the standard deviation for all the parameters.

	Mean	St. dev.
ϵ_v	2.04	0.20
ϵ_r	−1.61	0.16
λ_β	1.96	0.38
λ_{bg}	1.54	0.25
ν_r	63.4	6.7

Notes. Readers can refer to Fig. 8 for a visual representation of the posterior distributions.

very similar to r^{ϵ_r} with $-2 \lesssim \epsilon_r \lesssim -1.59$. We therefore chose a prior $\epsilon_r \sim Norm(mean = -1.8, stdev = 0.2)$, which emphasizes the range $-2.0 < \epsilon_r < -1.6$ but in principle allows for any real ϵ_r. As for the parameter λ_β, we know it is on the order of the total rate, which is $6.9\,\text{h}^{-1}$ on average. The interpretation of the parameter is made less clear by the normalization in Eq. (7c). However, the factor of $v_{\text{impact}}^{\epsilon_v}$ is on the order of 1 and the factor of r^{ϵ_r} is > 1, hence we expect $1 \lesssim \lambda_\beta \lesssim 10$. We chose a less informative prior of $\lambda_\beta \sim Gamma(shape = 3, scale = 1)$.

Figure 5 shows that for background detections, $\lambda_{\text{bg}} < 4\,\text{h}^{-1}$ is feasible. We chose a less informative prior $\lambda_{\text{bg}} \sim Gamma(shape = 3, scale = 1)$, which is wide and allows for any positive λ_{bg}.

Based on Fig. 6, we believe that values $40\,\text{km s}^{-1} \lesssim \nu_r \lesssim 80\,\text{km/s}$ are mostly expected. We chose the prior $\nu_r \sim Gamma(shape = 10, scale = 5)$ that emphasizes that range, with the mean of $50\,\text{km s}^{-1}$, which is the value that Zaslavsky et al. (2021) reported. This prior still allows for any positive value of ν_r.

4.3. Posterior distributions

The analysis was performed using TDS/TSWF-E/CNN data. For an analogous analysis performed on Solar Orbiter on board identified dust impacts, readers can refer to Appendix H. Posteriors

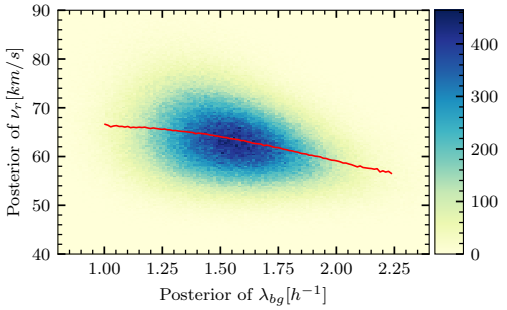

Fig. 9. Covariance between ν_r (radial dust velocity) and λ_{bg} (background detection rate); correlation is −0.3. The red line is the mean ν_r conditioned on λ_{bg} and it was produced by sampling from the joint posterior distribution of $\boldsymbol{\theta}$.

were inferred using R-INLA. The model (7b) was complicated by the steep dependence of the rate λ, especially the dependence on exponential parameters ϵ_v and ϵ_r. We note that a radial velocity $\gtrsim$60 km/s is consistent with detection rate $\lambda_{\text{bg}} \approx 1.5$ and $\alpha\delta \approx 1.0$, according to Fig. 6. It is important to note that the exact choice of priors and other parameters, such as the reference azimuthal velocity in Eq. (7c) and the procedure starting point (as INLA works on a grid largely defined by the initial point), influences the exact result; although, no major difference is encountered when parameters or priors are reasonably varied (see Appendix I). As for the initial point, the mode of the joint prior was used: $\boldsymbol{\theta} = (2.2, -1.8, 2, 2, 45)$.

Several measures can be used to evaluate the appropriateness of a model to a data set. We inspected the conditional predictive ordinates (CPO) and the predictive integral transform (PIT), which indicated no issues (see Appendix F for details).

4.4. Discussion of the posterior distribution

The inferred posterior distribution of velocities shown in Fig. 8 is not to be interpreted as a distribution of velocities within the dust cloud directly, but rather as a distribution of the effective mean velocities encountered on each day, or even better – the uncertainty in effective velocity. There could indeed be dust grains with velocity well off the effective support of the posterior distribution, as long as the mean of all velocities does not exceed the region indicated by the posterior distribution.

The $\boldsymbol{\theta}$ parameters are not independent. Figure 9 shows the covariance between the ν_r (radial velocity) and λ_{bg} (background detection rate) parameters. A negative correlation suggests that higher ν_r is likely to occur in the case of lower λ_{bg}. This offers a sanity check: a higher velocity would mean a lower difference between an inbound and outbound flux, which has a similar effect to the higher background component scenario – a negative correlation between ν_r and λ_{bg} is thus expected. For covariances between all parameters, readers can refer to Appendix G.

The TDS/TSWF-E/CNN data set contains $6.9\,\text{h}^{-1}$ detections on average. The inferred value of $\lambda_{\text{bg}} = (1.54 \pm 0.25)\,\text{h}^{-1}$ implies that, in total, (78 ± 4) % of dust is attributed to hyperbolic dust within the model. The constant background λ_{bg} is the simplest available generalization and is therefore likely an oversimplification. The hyperbolic dust detection rate shows a strong negative correlation with heliocentric distance. If, for instance, nonhyperbolic dust shows a similar anticorrelation, the actual nonhyperbolic component is higher than inferred. Conversely, if

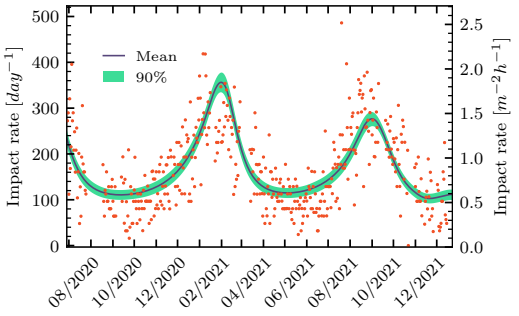

Fig. 10. Estimated posterior mean of the dust impact with 90 % HPD credible intervals. The credible intervals are not supposed to cover the data scatter (see text for an interpretation of the credible intervals that are shown).

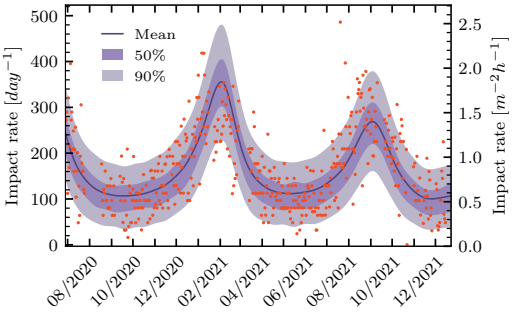

Fig. 11. Estimated posterior mean of the hyperbolic dust detections and HPD prediction intervals. The prediction intervals are supposed to cover the data scatter (see text for an interpretation of the prediction intervals that are shown).

nonhyperbolic prevalence shows a correlation with the heliocentric distance, the actual nonhyperbolic component is lower than inferred. Both cases would also imply changes to the inferred parameters of hyperbolic dust (see Appendix J for a visual explanation). If the nonhyperbolic component is mostly nondust (for example, misattributed electrical phenomena), independence on the heliocentric distance is reasonable. However, if most of the nonhyperbolic contribution is due to bound (Keplerian) dust particles, then anticorrelation is expected. If interstellar dust (ISD) streaming predominantly from one direction approximately within the ecliptic plane is present, a positive correlation is also feasible due to the velocity vector orientation.

Indeed, ISD was observed (Baguhl et al. 1996; Zaslavsky et al. 2012; and Malaspina et al. 2014) to arrive mainly from a 258 ° ecliptic longitude. The highest flux is observed when a spacecraft has an antiparallel velocity, which vaguely coincides with a higher heliocentric distance phase of Solar Orbiter's orbit so far. If ISD is an important contribution to λ_{bg}, the actual background flux may be lower than the suggested $\lambda_{\mathrm{bg}} \approx 1.5\,\mathrm{h}^{-1}$. For now, ISD is not apparent in Solar Orbiter data and the fact that models fit well without ISD suggests it is not an important component of Solar Orbiter detections. Near the solar minimum of 2020, the solar magnetic field had a defocusing configuration with the Lorentz force acting on the interstellar dust in the outer heliosphere pointing away from the heliospheric current sheet (Mann 2010), hence depleting the ISD flux in the near-ecliptic region and inside 1 AU. Identifying ISD with Solar Orbiter is, however, beyond the scope of the present work, but it remains worthy of future investigation, especially since ISD may become more important during the current solar cycle (Mann 2010). For now, no bound dust particles are apparent either, nor are the retrograde dust particles. If the constant background is a crude oversimplification and the nonhyperbolic component has a prominent dependence on heliocentric distance, the present interpretation of the $\boldsymbol{\theta}$ parameters is not correct, as the model is not on point. Inclusion of more parameters in the model (for example a more sophisticated nonhyperbolic term) may be feasible with more data in the coming months.

The posterior mean of the detection rate is shown in Fig. 10 in units of: $\mathrm{m}^{-2}\mathrm{h}^{-1}$, assuming a detection area of $8\,\mathrm{m}^2$ (Solar Orbiter thermal shield approximate area); and day^{-1}, taking into account the detection time per day and extrapolating to 24 h. We note that the credible intervals reflect the uncertainty of the inferred mean detection rate (the uncertainty of our knowledge, given the data), which is the same uncertainty as visualized in Fig. 8. The spread of data points in Fig. 10 is much wider and mostly defined by the variance of the Poisson random variable, given the mean rate, rather than the uncertainty in the mean rate. The prediction intervals of the Poisson random variable are shown in Fig. 11 and, there, data points seem to be appropriately covered by the credible intervals.

The inferred value of the parameter $\epsilon_r \approx -1.6$ suggests that dust grains are slowing distinctly on their way out of the inner heliosphere between 0.5 AU and 1 AU, resulting in a spatial distribution different from the trivial $\lambda \propto r^{-2}$ case. Readers can refer to Fig. 7 for a comparison. With an inferred velocity of $(63 \pm 7)\ \mathrm{km\,s}^{-1}$ between 0.5 AU and 1 AU, significant deceleration suggests a much higher velocity closer to the Sun. Assuming β meteoroids with a circular initial orbit, the ϵ_r value implies a specific β value needed for just the right level of deceleration. Deceleration is a result of energy transfer from kinetic to potential, and therefore, given the initial heliocentric distance, the deceleration rate depends on the initial velocity. This makes the assumption of a circular initial orbit crucial when we are to infer the β parameter. For example, a β value needed to explain an observed ϵ_r is different if the β meteoroid parent object has an eccentricity of 0.3, rather than 0. For an analysis of the implied β values in the case of the circular parent orbit, readers can refer to Fig. 12. Various initial parent body orbit radii are shown in Fig. 12 to demonstrate that the model is not very sensitive to that parameter. For comparison, we note that velocities $\gtrsim 60\ \mathrm{km\,s}^{-1}$ are consistent with $\beta \approx 0.6$ and the origin between 0.05 AU and 0.1 AU, according to Fig. 1. We note that 0.05 AU $\approx 10\,R_\odot$, where $R_\odot$ is the Solar radius.

However, it is feasible to expect a parent body with an eccentricity of 0.3, as the mean eccentricity in the inner asteroid belt is $e \approx 0.15$ (Malhotra & Wang 2016). If a dust grain is ejected from a given heliocentric distance r, the eccentricity $e = 0.3$ implies a +14% ejection speed if r is the perihelion and a −16% ejection speed if r is the aphelion, compared to ejection from a circular orbit of radius r. In the case of $e \neq 0$, $\beta > 0.5$ is not the right condition for the unbound β meteoroid. In fact, for $e = 0.3$ the condition is approximately $\beta > 0.35$ for perihelion, and $\beta > 0.65$ for aphelion ejection. It is important to keep in mind that the +14% could also be Δv transferred at collision, as collisions between larger dust objects are likely a major source of β meteoroids. Then the 14% relative speed would, for instance, correspond to the collision of two asteroids on

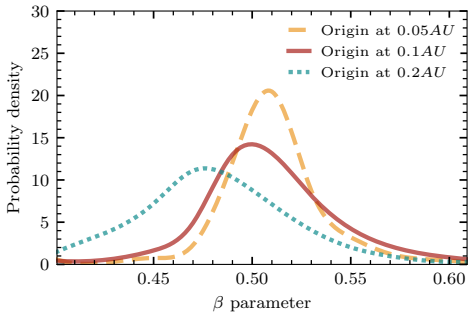

Fig. 12. β parameter resulting from ϵ_v posterior distribution under the assumption of a circular parent body orbit (see text for a discussion).

circular orbits with a relative inclination of 8 °, which is also a very feasible scenario. For instance, if the example of +14% of Δv (or an eccentricity of 0.3) is a good representative of the process, the resulting implied β would be not $\beta \gtrsim 0.5$, but rather $\beta \gtrsim 0.35$. Eccentricities and relative velocities in the zodiacal cloud remain uncertain. We note that even in the described case, we are still considering a dust grain with a purely azimuthal velocity at liberation, which is yet another simplification.

4.5. Comparison with previous results

As Solar Orbiter has been operated only since 2020 and will be operated at least until 2027, the results presented in this paper are one of the earlier ones for the mission. Based on similar data, though collected over a shorter time period, Zaslavsky et al. (2021) have reported several physical parameters of the β-meteoroid population. Interestingly, they have reported radial velocity to be about 50 km s^{-1}, which is within two standard deviations from (63 ± 7) km s^{-1} reported here, but it is important to bear in mind that the number was inferred under substantially different assumptions. The velocity is crucial to infer the β-meteoroid flux at 1 AU for example, which Zaslavsky et al. (2021) have reported to be 8×10^{-5} m^{-2}s^{-1}. Under our model assumptions (constant radial dust velocity) and taking the joint posterior distribution of the parameters, we report $(1.6 \pm 0.1) \times 10^{-4}$ m^{-2}s^{-1} for hyperbolic dust and the residual component ($\lambda_{\rm bg}$) together (measured on a stationary spherical object, per m^2 of the cross section), a value higher by a factor of ≈2. For the component consistent with hyperbolic dust only, we report the flux of $(1.1 \pm 0.2) \times 10^{-4}$ m^{-2}s^{-1} and for the component attributed to the residual, background component $(5.4 \pm 1.5) \times 10^{-5}$ m^{-2}s^{-1}. As for $\alpha\delta$ (keeping in mind that $\alpha\delta = \epsilon_v - 1$ here), Zaslavsky et al. (2021) have reported consistency with $\alpha\delta = 1.3$, while we report $\epsilon_v - 1 = (1.04 \pm 0.20)$.

As for a comparison of the present results with the β-meteoroid flux near 1 AU, Wehry & Mann (1999) reported the flux of β meteoroids in the ecliptic plane detected by Ulysses between 1.0–1.6AU to be $(1.5 \pm 0.3) \times 10^{-4}$ m^{-2}s^{-1}. Zaslavsky et al. (2012) reported a flux of β meteoroids at 1 AU of size 100–300 nm on STEREO/Waves in the range of 1–6 $\times 10^{-5}$ m^{-2}s^{-1}, which is a somewhat lower value than reported here. Solar Orbiter detections are likely of 100 nm and larger dust, but the upper limit is somewhat higher for Solar Orbiter due to a wider dynamic range (3–150 mV for STEREO and 3–700 mV for Solar Orbiter), which may account for some of the difference. Malaspina et al. (2015), however, reported the value for STEREO/Waves by about a factor of 2.5 higher than Zaslavsky et al. (2012), which is on its upper bound virtually identical to the value reported here. For the Wind/WAVES experiment, Malaspina et al. (2014) reported $(2.7 \pm 1.4) \times 10^{-5}$ m^{-2}s^{-1} for the sum of β meteoroids and interstellar dust of 0.1–11 μm size. It has yet to be determined if and how much interstellar dust contributes to the measurements of Solar Orbiter's RPW analyzed in the present work. Recently, Szalay et al. (2021) have reported 4–8×10^{-5} m^{-2}s^{-1} for the β-meteoroid flux at 1 AU measured with Parker Solar Probe. The upper bound of this estimate is similar to the value reported in the present work.

5. Conclusions

We have presented the analysis of the velocity of hyperbolic dust grains between 0.5 AU and 1 AU based on the highest-quality available data on daily dust detections by Solar Orbiter's RPW, including a discussion of implications for the velocity in the case of nonhyperbolic (be it another dust population or false detections) component to the counts. Velocities in the range 30–110 km s^{-1} are compatible with the data. We have presented a Bayesian hierarchical model and demonstrated how it is used to infer physical parameters of the hyperbolic dust population in the studied region. It is likely that (1.5 ± 0.3) h^{-1} are in fact not caused by hyperbolic dust. Then observations are consistent with a mean radial velocity of the hyperbolic component (63 ± 7) km s^{-1} between 0.5 AU and 1 AU. Spatial dependence of the detection rate suggests substantial deceleration of the observed hyperbolic dust particles. If they are β meteoroids, the value of β is likely just above the liberation threshold, specifically $\beta \gtrsim 0.5$ under the assumption of circular orbits of parent bodies. Hence closer to their origin, they likely have velocities higher than the inferred (63 ± 7) km s^{-1}. As a result of our modeling, we provide estimates of hyperbolic dust flux at 1 AU of $(1.1 \pm 0.2) \times 10^{-4}$ m^{-2}s^{-1}, which is a value compatible with the results of other relevant measurements.

6. Outlook

Solar Orbiter will be significantly inclined, starting in 2025, which will require further generalization of the model to account for the dust distribution out of the ecliptic plane. The parameters of hyperbolic dust out of ecliptic will likely provide more information on in-ecliptic hyperbolic dust, such as its parent bodies' mean eccentricity. Due to independence on β, knowledge of the azimuthal velocity would be a good indicator of the origin of β meteoroids, but it is hard to infer as the azimuthal component is much smaller than the radial component. The ecliptic detections may help in this regard as well.

As mentioned earlier, the de-focusing solar magnetic field configuration near the 2020 solar minimum does not favor the detection of ISD. With solar cycle 25, the focusing field configuration will return at some time before the solar minimum of 2031. It is possible that a significant ISD component will be observed in the years following the solar maximum of 2025, which will, if observed, provide new opportunities for dust population discrimination and a more comprehensive dust cloud description thanks to Solar Orbiter RPW data.

Acknowledgements. Author contributions: Concept: S.K., A.T., I.M. Data analysis: S.K., S.H.S., A.K. Interpretation: S.K., I.M., A.T., S.H.S., A.K., A.Z. Manuscript preparation: S.K. The code and the data used in present work are publicly available at https://github.com/SamuelKo1607/solo_dust_2022. This work made use of publicly available data provided by A. Kvammen:

https://github.com/AndreasKvammen/ML_dust_detection. S.K. and A.T. are supported by the Tromsø Research Foundation under the grant 19-SG-AT. This work on dust observations in the inner heliosphere is supported by the Research Council of Norway (grant number 262941). In addition, A.K. acknowledges the support from the Research Council of Norway (grant number 326039). Authors sincerely appreciate the support of Solar Orbiter/RPW Investigation team and thank the anonymous reviewer for constructive comments. This work was made possible by R-INLA package, authors thank to R-INLA team, see https://www.r-inla.org.

References

Alexander, W., & Bohn, J. 1968, in COSPAR Plenary Meeting, No. NSSDC-ID-66-049A-21-PM (North-Holland Publishing Co.)
Baguhl, M., Grün, E., & Landgraf, M. 1996, Space Sci. Rev., 78, 165
Collette, A., Grün, E., Malaspina, D., & Sternovsky, Z. 2014, J. Geophys. Res.: Space Phys., 119, 6019
Czechowski, A., & Mann, I. 2021, A&A, 652, A131
Dietzel, H., Neukum, G., & Rauser, P. 1972, J. Geophys. Res., 77, 1375
Dietzel, H., Eichhorn, G., Fechtig, H., et al. 1973, J. Phys. E: Sci. Instrum., 6, 209
Dohnanyi, J. 1970, J. Geophys. Res., 75, 3468
Dohnanyi, J. 1972, Icarus, 17, 1
Friichtenicht, J. 1962, Rev. Sci. Instrum., 33, 209
Gasque, C., Bale, S., Bowen, T., et al. 2022, AGU Fall Meeting 2021
Gómez-Rubio, V. 2020, Bayesian Inference with INLA (CRC Press)
Grün, E. 1984, in The Giotto Spacecraft Impact-induced Plasma Environment (ESA SP), 224, 39
Grün, E., Zook, H. A., Fechtig, H., & Giese, R. 1985, Icarus, 62, 244
Grün, E., Pawlinka, S., & Srama, R. 2007, Dust accelerator tests with Cassini RPWS samples (Max-Planck-Institut für Kernphysik), Tech. Rep.
Gurnett, D., Ansher, J., Kurth, W., & Granroth, L. 1997, Geophys. Res. Lett., 24, 3125
Howard, R. A., Vourlidas, A., Bothmer, V., et al. 2019, Nature, 576, 232
Kurth, W., Averkamp, T., Gurnett, D., & Wang, Z. 2006, Planet. Space Sci., 54, 988
Kvammen, A., Wickstrøm, K., Kociscak, S., et al. 2023, Ann. Geophys., 41, 69
Leinert, C., Richter, I., Pitz, E., & Planck, B. 1981, A&A, 103, 177
Maksimovic, M., Bale, S., Chust, T., et al. 2020, A&A, 642, A12
Malaspina, D., Horányi, M., Zaslavsky, A., et al. 2014, Geophys. Res. Lett., 41, 266
Malaspina, D. M., O'Brien, L. E., Thayer, F., Sternovsky, Z., & Collette, A. 2015, J. Geophys. Res.: Space Phys., 120, 6085
Malaspina, D. M., Szalay, J. R., Pokornỳ, P., et al. 2020, ApJ, 892, 115
Malaspina, D. M., Stenborg, G., Mehoke, D., et al. 2022, ApJ, 925, 27
Malhotra, R., & Wang, X. 2016, MNRAS, 465, 4381
Mann, I. 2010, Annu. Rev. Astron. Astrophys., 48, 173
Mann, I., & Czechowski, A. 2005, ApJ, 621, L73
Mann, I., & Czechowski, A. 2021, A&A, 650, A29
Mann, I., Meyer-Vernet, N., & Czechowski, A. 2014, Phys. Rep., 536, 1
Mann, I., Nouzak, L., Vaverka, J., et al. 2019, Ann. Geophys., 37, 1121
Marshall, E., & Spiegelhalter, D. 2003, Stat. Med., 22, 1649
Martins, T. G., Simpson, D., Lindgren, F., & Rue, H. 2013, Comput. Stat. Data Anal., 67, 68
McBride, N., & McDonnell, J. 1999, Planet. Space Sci., 47, 1005
Meyer-Vernet, N., Aubier, M., & Pedersen, B. 1986, Geophys. Res. Lett., 13, 617
Meyer-Vernet, N., Moncuquet, M., Issautier, K., & Schippers, P. 2017, J. Geophys. Res.: Space Phys., 122, 8
Mozer, F., Agapitov, O., Bale, S., et al. 2020, ApJS, 246, 50
Nadaraya, E. A. 1964, Theory Probab. Applic., 9, 141
Nouzk, L., James, D., Nemecek, Z., et al. 2021, ApJ, 909, 132
Pettit, L. 1990, J. Roy. Stat. Soc. B (Stat. Methodol.), 52, 175
Rackovic Babic, K., Zaslavsky, A., Issautier, K., Meyer-Vernet, N., & Onic, D. 2022, A&A, 659, A15
Ragot, B., & Kahler, S. 2003, ApJ, 594, 1049
Rue, H., Martino, S., & Chopin, N. 2009, J. Roy. Stat. Soc. B (Stat. Methodol.), 71, 319
Rue, H., Riebler, A., Sørbye, S. H., et al. 2017, Annu. Rev. Stat. Applic., 4, 395
Shen, M. M., Sternovsky, Z., Garzelli, A., & Malaspina, D. M. 2021, J. Geophys. Res.: Space Phys., 126, e2021JA029645
Shu, A., Collette, A., Drake, K., et al. 2012, Rev. Sci. Instrum., 83, 075108
Srama, R., Ahrens, T. J., Altobelli, N., et al. 2004, in The Cassini-Huygens Mission (Springer), ed. C. T. Russell, 465
Stenborg, G., Howard, R., Hess, P., & Gallagher, B. 2021, A&A, 650, A28
Szalay, J., Pokornỳ, P., Malaspina, D., et al. 2021, Planet. Sci. J., 2, 185
Van de Hulst, H. 1947, ApJ, 105
Vaverka, J., Pellinen-Wannberg, A., Kero, J., et al. 2017, IEEE Trans. Plasma Sci., 45, 2048
Vaverka, J., Nakamura, T., Kero, J., et al. 2018, J. Geophys. Res.: Space Phys., 123, 6119
Wang, Z., Gurnett, D., Averkamp, T., Persoon, A., & Kurth, W. 2006, Planet. Space Sci., 54, 957
Watson, G. S. 1964, Sankhyā: Indian J. Stat. A, 359
Wehry, A., & Mann, I. 1999, A&A, 341, 296
Whipple, F. L. 1967, The Zodiacal Light and the Interplanetary Medium (National Aeronautics and Space Administration), ed. J. L. Weinberg, 409
Zaslavsky, A. 2015, J. Geophys. Res.: Space Phys., 120, 855
Zaslavsky, A., Meyer-Vernet, N., Mann, I., et al. 2012, J. Geophys. Res.: Space Phys., 117
Zaslavsky, A., Mann, I., Soucek, J., et al. 2021, A&A, 656, A30
Zook, H. A., & Berg, O. E. 1975, Planet. Space Sci., 23, 183

Appendix A: Single-particle velocity and spatial density

For the purposes of Figs. 2 and 1, dust grains were assumed to move within the ecliptics, liberated from an initially circular orbit and with their motion governed by the gravity and solar radiation pressure only; therefore,

$$|v| = \sqrt{v_0^2 + 2GM(1-\beta)\left(\frac{1}{r} - \frac{1}{r_0}\right)}, \tag{A.1}$$

$$v_{tan} = v_0 \frac{r_0}{r}, \tag{A.2}$$

$$v_{rad} = \sqrt{v^2 - v_{tan}^2}, \tag{A.3}$$

where v_0 is the initial (purely radial) velocity and r_0 is the initial heliocentric distance (radius of the circular orbit). Furthermore, given a radial velocity profile of a radially escaping dust grain $v_{rad}(r)$, the dust spatial density ρ at a heliocentric distance r is

$$\rho(r) = \rho(r_0)\left(\frac{r_0}{r}\right)^2 \frac{v_{rad}(r_0)}{v_{rad}(r)}, \tag{A.4}$$

where r_0 is a reference heliocentric distance.

Appendix B: Dust radial velocity estimation

If we suppose that the detection rate is proportional to $v_{relative}^q$, then

$$R = R_0 \cdot v_{relative}^q = R_0 \left(\boldsymbol{v_{dust}} - \boldsymbol{v_{sc}}\right)^q \tag{B.1}$$

$$= R_0 \left[\sqrt{(v_{dust;rad} - v_{sc;rad})^2 + v_{sc;azim}^2}\right]^q, \tag{B.2}$$

where we assumed $v_{dust;azim} = 0$. Then, at any given heliocentric distance r,

$$R_{in}^{2/q} = R_0^{2/q}\left((v_{dust;rad} + |v_{sc;rad}|)^2 + v_{sc;azim}^2\right), \tag{B.3}$$

$$R_{out}^{2/q} = R_0^{2/q}\left((v_{dust;rad} - |v_{sc;rad}|)^2 + v_{sc;azim}^2\right), \tag{B.4}$$

and therefore

$$\frac{R_{in}^{2/q}}{R_{out}^{2/q}} = \frac{(v_{dust;rad} + |v_{sc;rad}|)^2 + v_{sc;azim}^2}{(v_{dust;rad} - |v_{sc;rad}|)^2 + v_{sc;azim}^2}, \tag{B.5}$$

from which

$$0 = v_{dust;rad}^2 \cdot \left(R_{in}^{2/q} - R_{out}^{2/q}\right) \tag{B.6}$$

$$+ v_{dust;rad} \cdot \left(-2v_{sc;rad}\left(R_{in}^{2/q} + R_{out}^{2/q}\right)\right) \tag{B.7}$$

$$+ \left(R_{in}^{2/q} - R_{out}^{2/q}\right) \cdot \left(v_{sc;rad}^2 + v_{sc;azim}^2\right), \tag{B.8}$$

which leads to a quadratic root of

$$v_{dust;rad} = \frac{2|v_{sc;rad}|\left(R_{in}^{2/q} + R_{out}^{2/q}\right) \pm \sqrt{D}}{2\left(R_{in}^{2/q} - R_{out}^{2/q}\right)}, \tag{B.9}$$

$$D = 4v_{sc;rad}^2\left(R_{in}^{2/q} + R_{out}^{2/q}\right)^2 - 4v_{\rm sc}^2\left(R_{in}^{2/q} - R_{out}^{2/q}\right)^2, \tag{B.10}$$

where (+) in Eq. (B.9) leads to positive velocity $v_{sc;rad}$. It is easy to see that in the special case of $q = 1$; $v_{sc;azim} = 0$ that

$$D = 4v_{sc;rad}^2\left[\left(R_{in}^2 + R_{out}^2\right)^2 - \left(R_{in}^2 - R_{out}^2\right)^2\right], \tag{B.11}$$

$$= 16v_{sc;rad}^2 R_{in}^2 R_{out}^2, \tag{B.12}$$

and, by extension,

$$v_{dust;rad} = \frac{|v_{sc;rad}|\left[\left(R_{in}^2 + R_{out}^2\right) \pm 2R_{in}R_{out}\right]}{\left(R_{in}^2 - R_{out}^2\right)}, \tag{B.13}$$

which is

$$v_{dust;rad} = \frac{|v_{sc;rad}|\left(R_{in} + R_{out}\right)}{\left(R_{in} - R_{out}\right)} \tag{B.14}$$

for (+) in the numerator.

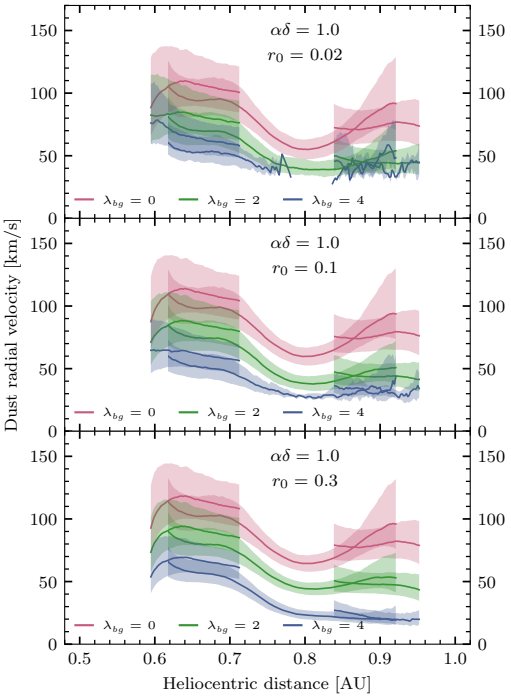

Fig. C.1. Velocity estimated from TDS/TSWF-E/CNN under the assumption of $\alpha\delta = 1.0$. The panels correspond to different initial heliocentric distances. The colors correspond to different assumptions as to the background detection rate.

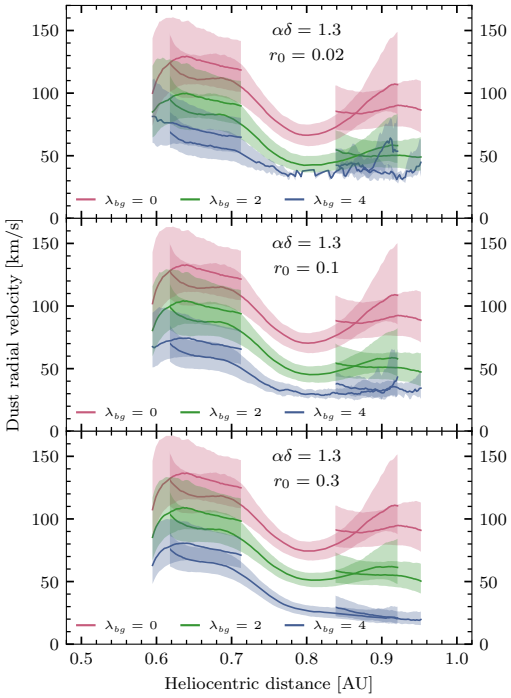

Fig. C.2. Velocity estimated from TDS/TSWF-E/CNN under the assumption of $\alpha\delta = 1.3$. The panels correspond to different initial heliocentric distances. The colors correspond to different assumptions as to the background detection rate.

Appendix C: Velocity inference — Full velocity profiles

The velocity profiles inferred in Section 3.2 are shown in Figs. C.1 to C.3 (readers can compare them to Figs. 5 and 6). We note that the missing solutions (jittery line) for heliocentric distance > 0.7 AU and $\lambda_{bg} = 4$ cause incomplete data shown in Fig. 6. These solutions only exist for some combinations of the free parameters, in particular for $\lambda_{bg} = 4$.

Appendix D: Interpretation of the parameter ϵ_r

An intuitive explanation of the parameter ν_r as the mean dust velocity and of the factor r^{ϵ_r} as the spatial density can be clarified, assuming $\nu_r \propto r^{\xi}$. With the model (7b), the nonconstant component $\tilde{R}$ of the rate R is proportional to

$$\tilde{R} \propto r^{\epsilon_r} \cdot v_{impact}^{\epsilon_v}, \tag{D.1}$$

where $\epsilon_r = -2$ in the case of no acceleration of the dust. Furthermore, ϵ_v is explained as $\epsilon_v = 1 + \alpha\delta$, and therefore

$$\tilde{R} \propto r^{-2} \cdot v_{impact}^{1} \cdot v_{impact}^{\alpha\delta}. \tag{D.2}$$

The factor of v_{impact}^{1} actually comes from the proportionality

$$\tilde{R} \propto \frac{v_{impact}}{\nu_r} \tag{D.3}$$

if we assume only radial motion for simplicity; readers can compare this with Eq. (4a). It is also apparent from the following: Assuming a stationary spacecraft ($v_{impact} = \nu_r$), the detection rate (in s^{-1}) is a product of the flux $F(r)$ (in s^{-1}) and the detection area S (in m^2), independently of ν_r. We therefore have, for nonaccelerating dust,

$$\tilde{R} \propto r^{-2} \cdot \frac{v_{impact}}{\nu_r} \cdot v_{impact}^{\alpha\delta}, \tag{D.4}$$

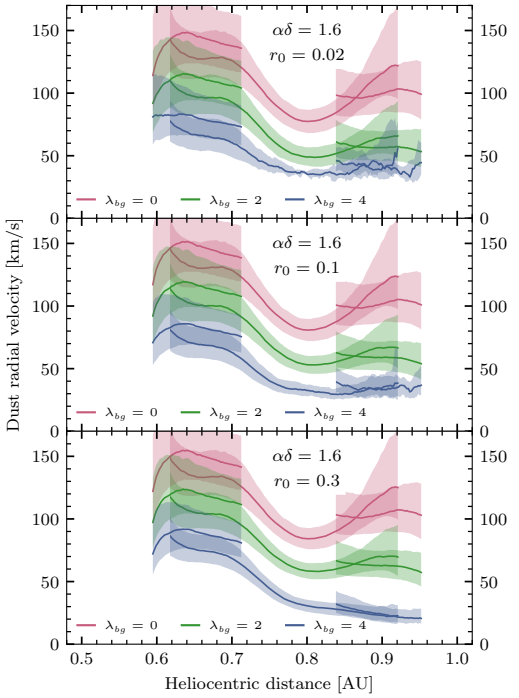

Fig. C.3. Velocity estimated from TDS/TSWF-E/CNN under the assumption of $\alpha\delta = 1.6$. The panels correspond to different initial heliocentric distances. The colors correspond to different assumptions as to the background detection rate.

and finally assuming $v_r \propto r^{\xi}$, we get

$$\tilde{R} \propto r^{-2} \cdot r^{-\xi} \cdot v_{impact} \cdot v_{impact}^{\alpha\delta} = r^{-2-\xi} \cdot v_{impact}^{\epsilon_v}, \tag{D.5}$$

and therefore

$$\epsilon_r = -2 - \xi. \tag{D.6}$$

There is a dichotomy in Eq. (D.5) in that the assumption of $v_{\rm dust} \propto r^{\xi}$ was used to expand the v_{dust} but not the v_{impact}. This is one way of interpreting the approximation described in Section 4.1; we assumed a nonconstant dust velocity in the factor for the spatial dust density, but a constant radial dust velocity in the expression for v_{impact} (see Eq. (7c)). This was done because of a clear relation of $\epsilon_r \lesssim -2$ to acceleration and deceleration of the dust, which in our case ($\epsilon_r \approx -1.6 \implies \xi \approx -0.4$) reveals that the dust is decidedly decelerating.

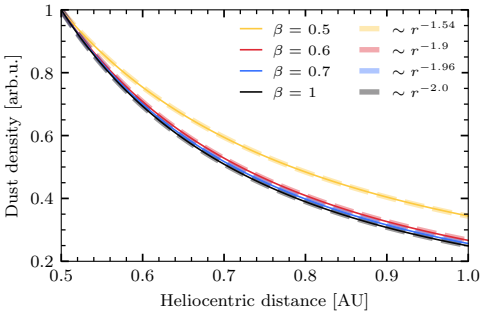

Fig. E.1. Modeled dust spatial densities for different β values assuming a circular initial orbit of 0.05 AU. The solid lines show the spatial density and are normalized to the density at 0.5 AU. The dashed lines are approximations to the solid lines, assuming a power dependence on r.

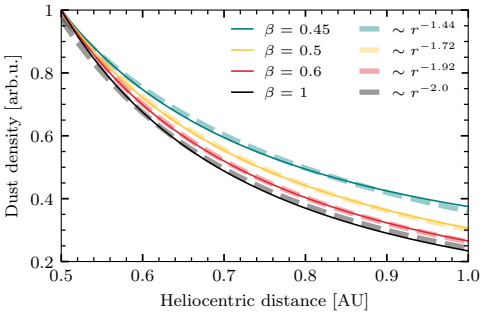

Fig. E.2. Modeled dust spatial densities for different β values assuming a circular initial orbit of 0.2 AU. The solid lines show the spatial density and are normalized to the density at 0.5 AU. The dashed lines are approximations to the solid lines, assuming a power dependence on r.

Appendix E: Spatial density profiles

We assumed that the initial orbital distance influences the relationship between β values and the spatial dust density profiles. In Fig. 7, the initial orbit of 0.1 AU was assumed. Readers can refer to plots E.1 and E.2 for similar plots with different assumptions as to the initial orbit., and Fig. E.3 for a similar plot if the eccentricity of $e = 0.2$ and the perihelion ejection with a perihelion of $r = 0.1$ AU is assumed. Although the estimates of the exponents vary, the general conclusion of a lower β implying a lower exponent holds. We note that the profile gets significantly influenced when β is close to the threshold, and that it depends on the initial orbit and eccentricity. Therefore, $\beta < 0.5$ is shown where 0.5 is much higher than the liberation threshold.

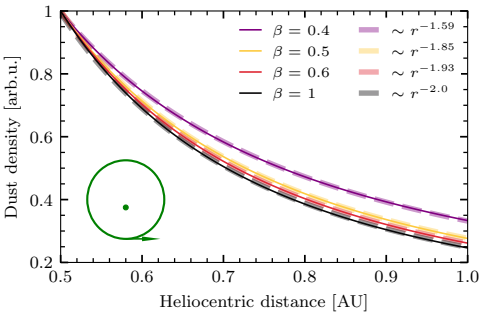

Fig. E.3. Modeled dust spatial densities for different β values assuming an elliptical initial orbit with an eccentricity of $e = 0.2$ and perihelion ejection. A perihelion of 0.1 AU was assumed. The solid lines show the spatial density and are normalized to the density at 0.5 AU. The dashed lines are approximations to the solid lines, assuming a power dependence on r.

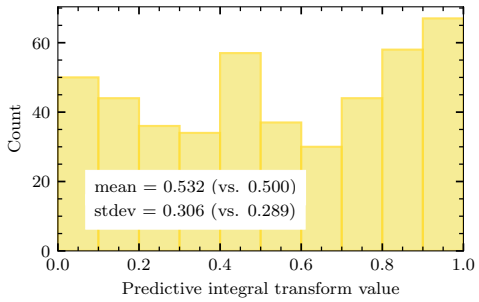

Fig. F.1. Histogram of PIT values for the model described in Section 4.3. Mean and standard deviation were compared to the values for uniform distribution.

Appendix F: Model assessment

There are several options for model evaluation implemented in R-INLA (Gómez-Rubio 2020, Chapter 2.4). We briefly describe two measures of choice.

The conditional predictive ordinates (CPO, see Pettit (1990)) for a given observation point gives the posterior probability of each observation when this observation is omitted in the model fitting. CPO is used to detect surprising observations or outliers. We examined the fit for failure flags for all the points, which would suggest a contradiction between the model and a data point. No failures were encountered.

The predictive integral transform (PIT, see Marshall & Spiegelhalter (2003)) measures the probability that a new observation will be lower than the observed value for each observation point individually. The histogram of the PIT values should therefore be similar to the uniform distribution between 0 and 1 when the model explains the data well (see Fig. F.1).

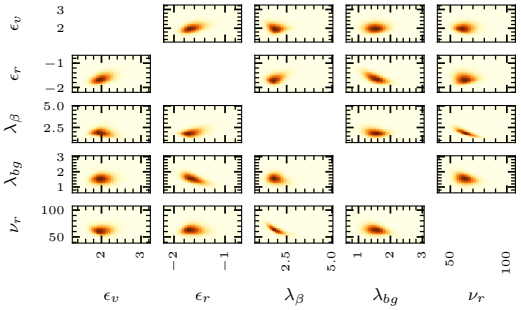

Fig. G.1. Illustration of the covariance between all parameter pairs, constructed using sampling from the joint posterior distribution of all parameters.

Table G.1. Covariance between all parameter pairs, constructed using sampling from the joint posterior distribution of all parameters.

	ϵ_v	ϵ_r	λ_β	λ_{bg}	ν_r
ϵ_v		0.451	-0.109	0.068	-0.015
ϵ_r	0.451		0.392	-0.621	0.027
λ_β	-0.109	0.392		-0.244	-0.799
λ_{bg}	0.068	-0.621	-0.244		-0.303
ν_r	-0.015	-0.027	-0.799	-0.303	

Appendix G: Covariance plots of posteriors

As is shown in figure G.1, basically all parameter pairs show a substantial correlation. The pairs hold useful information, but this is hardly surprising and they are easy to interpret, with the Eq. (7b) model in mind. The correlation is unimportant in the case of λ_β, which has a role of a normalization constant.

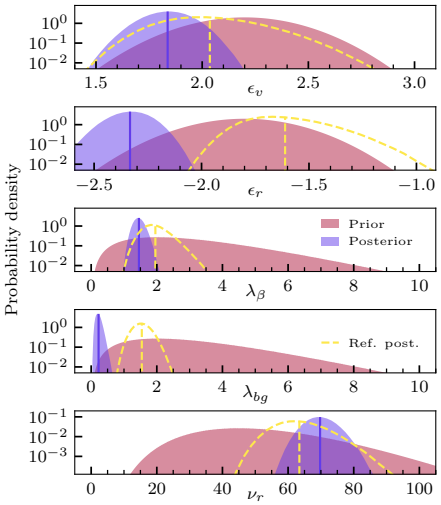

Fig. H.1. Prior and posterior distributions of parameters, making use of the original TDS (onboard processed) data. Prior distributions are described in the main text in sec. 4. Posterior distributions are described in Tab. H.1. Posteriors from Fig. 8 are shown as a reference in dashed lines for comparison.

Appendix H: Model fitting to original data

The procedure described in sec. 4 was also applied to the original TDS data, meaning impacts were identified onboard Solar Orbiter, described by Maksimovic et al. (2020), which are different from TDS/TSWF-E/CNN data (Kvammen et al. 2023) used otherwise in sec. 4. The CNN-refined data used in sec. 4 have fewer type 1 and type 2 errors, as well as better correspondence with visual inspection by experts than the original data (see discussion in Kvammen et al. (2023)). However, the original data were used previously (Zaslavsky et al. 2021) and the inspection of the result of the procedure is instructive nonetheless. The results are presented in Fig. H.1.

The most important and intuitive difference is that a much lower λ_{bg} is inferred in this case (readers can compare this with Fig. 8). As described in Kvammen et al. (2023), the CNN procedure identifies substantially more impacts near-aphelion, which suggests more background dust, with everything else being equal. It is important to keep in mind that, as evaluated by Kvammen et al., the prevalence of impacts erroneously labeled as dust impacts among TDS data is close to 20 %, which is much higher than λ_{bg} infered here.

Importantly, the inferred velocity ν_r does not change substantially, even though ϵ_v and especially ϵ_r do change consequentially. Importantly, $\epsilon_r < -2$ implies accelerating dust, which implies $\beta > 1$ and requires specific material and a particular size of the grains, hence this is unlikely — at least for β meteoroids. We note that ϵ_r is effectively far from our prior expectations, providing a poor fit to our prior knowledge. These results lend additional credence to the improvement of the CNN data.

Table H.1. Summary statistics for the parameters, making use of the original TDS (onboard processed) data. For a visual representation, readers can refer to Fig. H.1.

	Mean	St. dev.
ϵ_v	1.84	0.10
ϵ_r	-2.33	0.09
λ_β	1.45	0.16
λ_{bg}	0.23	0.08
ν_r	69.8	4.06

Appendix I: Variation of priors and model parameters

In this appendix, we investigate the dependence of the results in sec. 4 on the model parameters and priors. To contextualize this variation, we review how the priors and model parameters depend on previous work, in particular Zaslavsky et al. (2021).

The velocity ν_r has been inferred independently in this work and the fact that it is found to be compatible with the findings of Zaslavsky et al. is only reassuring. The velocity ν_a was assumed based on first principles (see Section 4.1) and is of lesser importance compared to ν_r. The background detection rare λ_{bg} is discussed in the present work, independent of any previous findings and the rate λ_β merely serves the role of a normalization constant. Both rates are closely tied to the observed counts and are therefore constrained by the data. The exponent ϵ_r is discussed and assessed from first principles in the present work, while the exponent ϵ_v is inspired by Zaslavsky et al. (2021). The designated prior mean of 2.2 decomposes to the sum of 1 (from first principles) and $1.2 = \alpha\delta$, where only $\delta \approx 0.34 \pm 0.07$ is taken from Zaslavsky et al. (2021) and where the uncertainty of 0.07 corresponds to a 95% confidence. Moreover, δ there is not yielded by Zaslavsky et al. from the fit to the flux, but rather from the analysis of the charge distribution presented therein, which adds another piece of information, independent from the flux itself. For simplicity, we used the value of Zaslavsky et al. for δ and the same analysis of TDS/TSWF-E/CNN data yields very similar results. Then α is known from laboratory measurements, for example from McBride & McDonnell (1999) and Collette et al. (2014). Collette et al. found $\alpha \approx 4$ for most materials. For consistency, however, we continued to use the findings of McBride & McDonnell, who reported $\alpha \approx 3.5$. Assuming 95 % confidence of $\alpha \approx 3.5 \pm 1$, we arrived at $\alpha\delta \approx 1.2 \pm 0.4$ in terms of 95 % confidence. We therefore believe that the standard deviation of the ϵ_v prior of 0.2 represents the uncertainty well. Further analysis shows that ϵ_v is not inferred substantially differently in the case of wider priors for the parameters (see Fig. I.1 for an example). The figure shows that in the case in which all parameter priors are considered to be broader, the result mean stays within the reference posterior credible range. Also a practically flat prior for ϵ_v leads to a similar posterior, given the remaining priors are taken as in Fig. 8.

It is true that the priors themselves express the uncertainty in prior knowledge; however, to demonstrate the robustness of the analysis, we here show perturbed priors and the resulting posterior combinations (Figs. I.1 and I.2) to show that the result – though somewhat dependent on the prior selection – does not change dramatically if priors are chosen arbitrarily slightly differently. Also the choice of the value of parameter v_a (which is not a free parameter in our modeling, see Eq. (7e)) is examined here (see Figs. I.3 and I.4). Last but not least, we show the posteriors in the case of change of the initialization of the

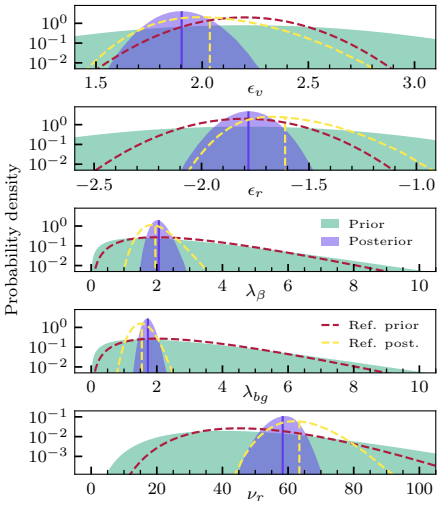

Fig. I.1. Prior and posterior distributions of the parameters, with the priors being substantially wider (less informative). The priors and posteriors from Fig. 8 are shown with dashed lines for comparison.

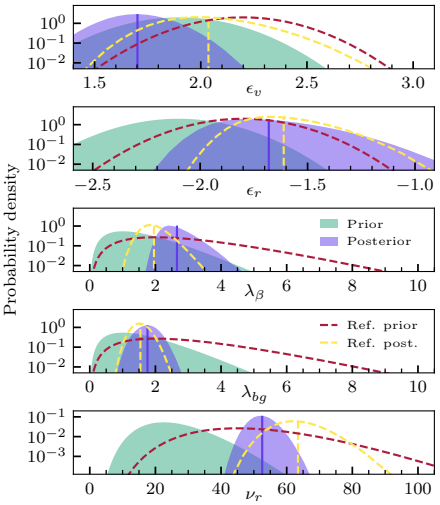

Fig. I.2. Prior and posterior distributions of parameters, with priors shifted toward lower values. The priors and posteriors from Fig. 8 are shown with dashed lines for comparison.

iterative procedure to estimate the parameters (Fig. I.5). We do not claim that any of these results is as trustworthy as the main result shown in Fig. 8; we had reasoning behind choosing the priors and parameters that we chose. We note that the mean of the marginal posteriors shown in Figs. I.1 to I.5 lie within high credibility regions of posteriors shown in Fig. 8 and vice versa, which supports the claim that the analysis presented here is robust. It is important to observe that parameter values inferred with a lower precision (wider posterior distributions) are more susceptible to change due to a change in parameters, which is in line with expectations and with the meaning of precision here. A good choice of priors is still important to get the highest quality estimate, but the result is not critically sensitive.

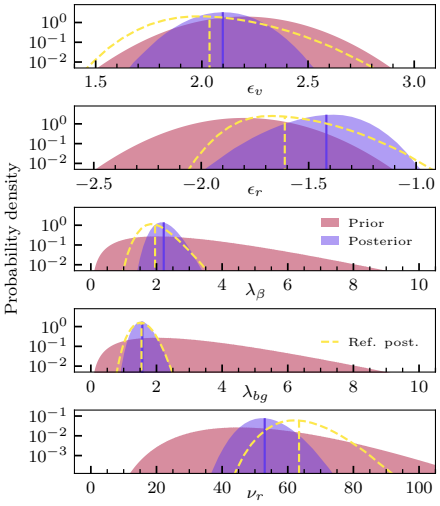

Fig. I.3. Prior and posterior distributions of parameters, with the fixed parameter of azimuthal velocity having been changed from 12 km/s at 0.75 AU to constant 0 km/s. The posteriors from Fig. 8 are shown with dashed lines for comparison.

Appendix J: Possible background profiles

In the present analysis, the nonhyperbolic component was assumed to be present and constant. Readers can refer to Fig. J.1 for examples of possible nonhyperbolic component profiles, as discussed in Section 4.4. In the plot, the mean rate of the nonhyperbolic component is the same in all three panels. We note that despite that, the dynamic range (that is ratios of maximum over minimum values) changes significantly as a result of the

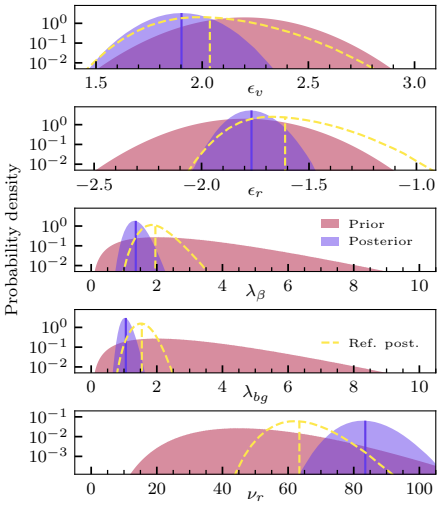

Fig. I.4. Prior and posterior distributions of parameters, with the fixed parameter of azimuthal velocity at 0.75 AU having been changed from 12 km/s to 24 km/s, which is a value higher by 100 %. The posteriors from Fig. 8 are shown with dashed lines for comparison.

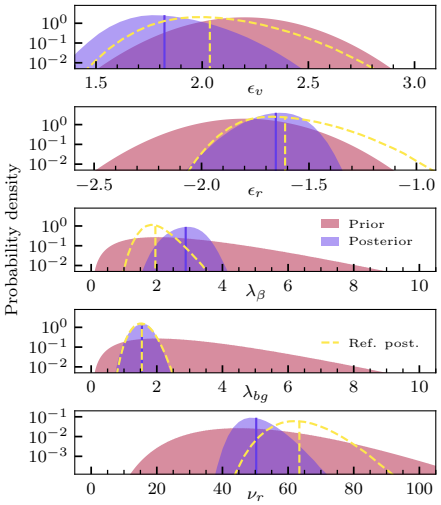

Fig. I.5. Prior and posterior distributions of parameters, with a starting point of $\epsilon_v = 3; \epsilon_r = -3; \lambda_\beta = 3; \lambda_{\rm bg} = 3; \nu_r = 30$. The posteriors from Fig. 8 are shown with dashed lines for comparison.

change in the temporal profile of the nonhyperbolic component. A significant deviation from the constant case would therefore likely change both the inferred prevalence of the nonhyperbolic component and the parameters of the hyperbolic grains.

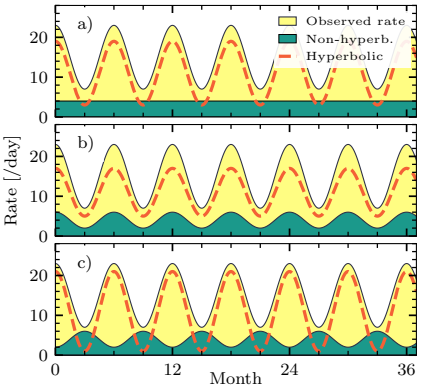

Fig. J.1. Detection rate: selection of different combinations of hyperbolic and nonhyperbolic rates compounding to the same observed detection rate. In panel a), the background component is independent of the heliocentric distance. In panel b), the nonhyperbolic component is negatively correlated with the heliocentric distance. In panel c), the nonhyperbolic component is positively correlated with the heliocentric distance.

Paper III: Impact ionization double peaks analyzed in high temporal resolution on Solar Orbiter

S. Kočiščák, A. Kvammen, I. Mann, N. Meyer-Vernet, D. Píša, J. Souček, A. Theodorsen, J. Vaverka, and A. Zaslavsky
Annales Geophysicae 42, No. 1 (2024)
doi: 10.5194/angeo-42-191-2024
GitHub: SamuelKo1607/solo_dust_2023

Ann. Geophys., 42, 191–212, 2024
https://doi.org/10.5194/angeo-42-191-2024

Annales Geophysicae
Open Access
EGU

Impact ionization double peaks analyzed in high temporal resolution on Solar Orbiter

Samuel Kočiščák[1], Andreas Kvammen[1], Ingrid Mann[1], Nicole Meyer-Vernet[2], David Píša[3], Jan Souček[3], Audun Theodorsen[1], Jakub Vaverka[4], and Arnaud Zaslavsky[2]

[1]Department of Physics and Technology, UiT The Arctic University of Norway, 9037 Tromsø, Norway
[2]LESIA, Observatoire de Paris, Université PSL, CNRS, Sorbonne Université, Université de Paris, Paris, France
[3]Department of Space Physics, Institute of Atmospheric Physics of the Czech Academy of Sciences, Prague, Czechia
[4]Faculty of Mathematics and Physics, Charles University, Prague, Czechia

Correspondence: Samuel Kočiščák (samuel.kociscak@uit.no)

Received: 8 September 2023 – Discussion started: 12 September 2023
Revised: 3 April 2024 – Accepted: 5 April 2024 – Published: 29 May 2024

Abstract. Solar Orbiter is equipped with electrical antennas performing fast measurements of the surrounding electric field. The antennas register high-velocity dust impacts through the electrical signatures of impact ionization. Although the basic principle of the detection has been known for decades, the understanding of the underlying process is not complete, due to the unique mechanical and electrical design of each spacecraft and the variability of the process.

We present a study of electrical signatures of dust impacts on Solar Orbiter's body, as measured with the Radio and Plasma Waves electrical suite. A large proportion of the signatures present double-peak electrical waveforms in addition to the fast pre-spike due to electron motion, which are systematically observed for the first time. We believe this is due to Solar Orbiter's unique antenna design and a high temporal resolution of the measurements. The double peaks are explained as being due to two distinct processes. Qualitative and quantitative features of both peaks are described. The process for producing the primary peak has been studied extensively before, and the process for producing the secondary peak has been proposed before (Pantellini et al., 2012a) for Solar Terrestrial Relations Observatory (STEREO), although the corresponding delay of 100–300 µs between the primary and the secondary peak has not been observed until now.

Based on this study, we conclude that the primary peak's amplitude is the better measure of the impact-produced charge, for which we find a typical value of around 8 pC. Therefore, the primary peak should be used to derive the impact-generated charge rather than the maximum. The observed asymmetry between the primary peaks measured with individual antennas is quantitatively explained as electrostatic induction. A relationship between the amplitude of the primary and the secondary peak is found to be non-linear, and the relation is partially explained with a model for electrical interaction through the antennas' photoelectron sheath.

1 Introduction

Since their first in situ observation, interplanetary dust grains were observed not only with specialized instruments but also as byproducts of other measurements, making dust detections much more abundant. One promising and actively discussed option for auxiliary dust detection of recent years is impact ionization detection with electrical antennas (Meyer-Vernet, 2001; Mann et al., 2014, and references therein). When a spacecraft collides with a dust grain at a relative velocity exceeding a few kilometers per second, the impact releases free charge due to the high energy density present on the impact site (Friichtenicht, 1964). The released charge is quasi-neutral, yet the present fields often act to separate positive and negative constituents quickly, allowing for its effective detection through the signature in the electric field measurement, once separated. How exactly the detection is done depends greatly on the spacecraft's properties, surrounding environment, impact site, and detecting apparatus. In any case, the perturbation of the electric field stays present for less than 1 ms, while the process of charge separation takes

even less time. Therefore, fast electrical measurements are needed in order to observe the process closely.

Solar Orbiter is one of the first (Bale et al., 2016; Maksimovic et al., 2020; Mann et al., 2019) missions to include a wave analyzer suite designed with dust detection in mind. Dust impact events are readily recognized based on a characteristic peak (Zaslavsky et al., 2021; Kvammen et al., 2023), yet the analysis and the interpretation of the recorded signals are made difficult by unclear dependence of the process on spacecraft properties, which is also an issue with other spacecraft conducting similar detection (Zaslavsky et al., 2012; Malaspina et al., 2014; Vaverka et al., 2017; Ye et al., 2019; Page et al., 2020; Ye et al., 2020; Zaslavsky et al., 2021; Kellogg et al., 2021; Racković Babić et al., 2022). In the present paper we report the first observation of a double-peak structure (in addition to the fast electron pre-spike) associated with dust impacts recorded with electrical antennas. The double-peak structure is explained as being caused by two charge collection processes happening simultaneously or in a quick succession and analyzed as such.

We structure the article as follows: in this section, we present Solar Orbiter as a dust detector. We inspect the data and describe our findings in Sect. 2. In Sect. 3, we describe the electrical process theoretically and with quantitative estimates as due to two processes. In Sects. 4 and 5, we focus on primary and secondary peaks respectively. We show that the primary peaks are understood with current knowledge, and we discuss potential explanations for the secondary peaks. We summarize in Sect. 6.

1.1 Solar Orbiter as a dust detector

Solar Orbiter is a three-axis stabilized spacecraft, launched on 10 February 2020, orbiting the Sun, with an aphelion near 1 AU and a perihelion shrinking from 0.5 AU to currently 0.28 AU. Solar Orbiter has remained close to the ecliptic plane so far but will be gaining orbital inclination gradually, starting in 2023 and reaching the maximum inclination of 24 ° and possibly 33 ° in the late 2020s.

The area of the Solar Orbiter's body and shield combined is $\approx 28.4\,\mathrm{m}^2$. In addition, the backside of the solar panels is conductive and coupled to the body, which adds another $15.1\,\mathrm{m}^2$ (Zaslavsky et al., 2021). The spacecraft therefore provides $\approx 43.5\,\mathrm{m}^2$ of surface sensitive to dust impacts, where, importantly, $\approx 7.4\,\mathrm{m}^2$ is taken by the heat shield front side, which is the effective cross section as seen from the Sun. The effective cross section in the ram direction is $\approx 4\,\mathrm{m}^2$ (ESA, 2023). We note that the areas are based on a simplified description of the spacecraft as a cuboid with a heat shield, while a portion of the area is covered by insensitive surfaces. Other sensitive surfaces may contribute to the area besides the cuboid. The heat shield is made of calcium-phosphate-coated titanium, while the body is covered with various metallic and non-metallic materials. Which materials are exposed definitely plays a role in the distribution of impact amplitudes, and this is worthy of future investigation.

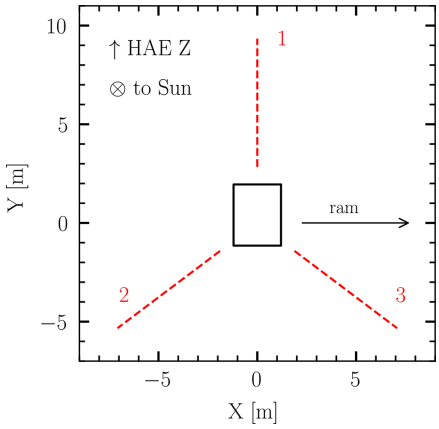

Figure 1. The Solar Orbiter's heat shield (black rectangle) and the RPW antennas (dashed red) viewed in the spacecraft reference frame (from behind).

1.1.1 Radio and Plasma Waves instrument

The Radio and Plasma Waves instrument (RPW) is a combined electric and magnetic suite for an in situ study of fields and waves (Maksimovic et al., 2020). It provides fast electrical measurements with its three rigid conical nickel cobalt alloy antennas, which enable detection of dust impact events. Each of the antennas is 6.5 m long with a near-base diameter of 38 mm and lies in one plane recessed approximately 1 m behind the heat shield; see the diagram in Fig. 1. Though dust impact events might be identifiable in the electrical spectra, the Time Domain Sampler subsystem (TDS) of RPW is the key to a robust analysis (Zaslavsky et al., 2021), since the dust impacts are solitary pulse events which provide little information on spectra.

1.1.2 Radio and Plasma Waves data

The three RPW electrical antennas measure in various configuration modes: monopole, dipole, and mixed. In the monopole configuration, abbreviated SE1, antennas measure voltage against the spacecraft body – this configuration is in principle best suited for dust detection, as the dust impacts' influence on the body potential is of interest. In the dipole mode (DIFF1), antennas measure the electric potential against each other, which has the benefit of the largest effective length for the electrical fields study, but the measurement is nearly insensitive to the changes of the potential of the body. Nonetheless, dust impacts were identified in dipole measurements before and can be identified in DIFF1 measurements of Solar Orbiter, given that the impact influ-

ences the potential of an antenna. DIFF1 measurement also provides redundant information on electric fields, as the three antennas lie in a plane; hence only two components could be measured. In the mixed mode (XLD1), the three channels are occupied by two dipoles and a monopole, which in principle retains benefits of both of the aforementioned configurations, as both monopole and dipole signals could be reconstructed. For a more detailed description, see Appendix A. The XLD1 mode is the one that the instrument spends the most time in ($\approx 95.4\,\%$).

The RPW records electrical waveforms with a 6.25 % duty cycle, that is the first 62.5 ms of every second. In trigger mode, the onboard algorithm decides whether to keep each of the recordings, based on the maximum amplitude observed within the window. Up to several hundreds out of approx. 86 400 windows a day are stored and transmitted. The onboard algorithm also classifies the stored waveforms into three different phenomena categories, one of which is the dust impact (more details in Souček et al., 2021). The onboard algorithm, however, does not achieve the precision and accuracy of ground based classifications. In a recent paper, Kvammen et al. (2023) re-did the classification with machine-learning techniques, and this dataset (Kvammen, 2022) is used in the present paper.

Due to technical limitations of the amplifiers, the recorded waveforms can only be trusted within a limited bandwidth. For the purpose of waveform analysis and plotting in the present work, the raw data are altered by a sequence of digital filters to expand this range as much as possible. As a result, the waveforms are trusted in the bandwidth of $500\,\mathrm{Hz} < f < 70\,\mathrm{kHz}$. For a comprehensive description, consult Appendix B.

2 Observation of impact ionization on Solar Orbiter

Solar Orbiter's RPW electrical antennas (Maksimovic et al., 2020) are similar in terms of construction and the sampling rate to the Solar Terrestrial Observatory (STEREO)/Waves electrical suite (Bale et al., 2008). The antennas are rigid thick poles, with the difference that in the case of STEREO/Waves, the bases of the three orthogonal antennas are physically close to one another, while in the case of Solar Orbiter/RPW, the three antennas lie in one plane, and their bases are physically distant, with the spacecraft's body between them. Nevertheless, the systems' semblance suggests comparable capabilities for dust detection. Therefore, in this section we will present and examine the dust data acquired with Solar Orbiter/RPW, building on the results of and comparing to STEREO/Waves.

2.1 Single and triple hits

STEREO had observed two kinds of dust impact events, so-called single hits and triple hits. The difference is that the

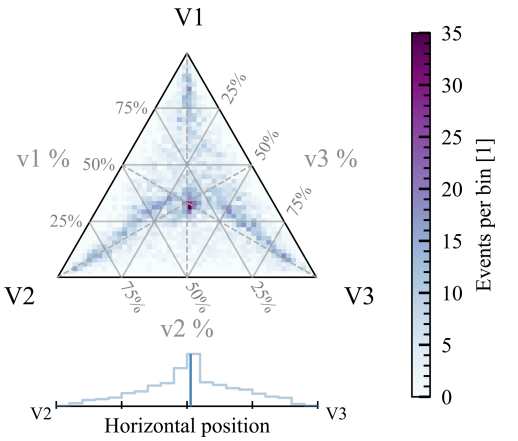

Figure 2. Heat map in the ternary plot for the channel maxima ($VX = \mathrm{ant}_X - \mathrm{body}$) for all the events identified as dust impacts. 4534 data points contribute to the heat map.

triple hits are observed similarly strong on all three channels, which suggests that most of the process takes place on the common ground the channels measure against, rather than on each of the antennas (Zaslavsky et al., 2012). The single hits were reportedly produced by nanodust impacts, which were observed on both STEREO and Cassini with similar fluxes (Schippers et al., 2014, 2015; Meyer-Vernet et al., 2017) when the solar wind electric field focused them towards the ecliptic (Juhász and Horányi, 2013) – a condition that stopped after 2012 (Le Chat et al., 2015). Since they produce small voltages, they were only observed on the antenna lying within the impact cloud, whose voltages could be amplified (Pantellini et al., 2012a; Zaslavsky et al., 2012), and their flux was several orders of magnitude larger than that of beta particles and much more variable, as predicted by Mann et al. (2007). Although STEREO-like single hits are not expected to return until after 2024 (Poppe and Lee, 2020, 2022), it is useful to compare the channels' amplitudes to one another, and we will keep using the terms single and triple hits for Solar Orbiter events, where appropriate. We compare the amplitudes using the ternary plot of channels' maxima, that is the highest amplitude of the voltage between the antenna and the body. The ternary plot is the plot in an equilateral triangle, in which the position in the triangle corresponds to the relative contribution of the three contributors to the sum. In our case, ternary plots are normalized to the sum of three channel maxima for an impact, showing a relative amplitude of the three channel maxima; see Fig. 2.

We see that many events lie near the center, which corresponds to a similar response on all three antennas. However, many events lie towards the corners as well, especially near the triangle's medians, which implies an amplitude in one

channel higher than in the other two channels, which are in turn nearly equal to one another. This suggests that a process concerning antenna might be present – similar to the conclusion made for STEREO's single hits (Zaslavsky et al., 2012; Pantellini et al., 2012a). The spacecraft has a rough lateral mirror symmetry between antennas 2 and 3, while antenna 1 lies in the plane of symmetry. We see a small preference of antenna 3 against antenna 2, which is to be expected, since antenna 3 is closest to the ram direction, while antenna 2 is close to the anti-ram. The schematic view of the three antennas with respect to the spacecraft body is shown in Fig. 1. We also see that double hits (strong in two and weak in one channel) are not very frequent, but clearly the pair of antenna 3 and antenna 1 is the most prevalent for such hits. This is also to be expected given the direction of the ram. Note that this is a crude representation as it only accounts for the global positive maxima and is therefore an imperfect measure of impact location. Overall, the preference for ram direction is apparent, and a process concerning antennas is hinted at through the presence of single hits.

2.2 Waveform inspection

Upon inspection of the corrected signals (see Appendix B) recorded in monopole (SE1) mode (see Fig. 3), we see that many of the waveforms show the following structure: a simultaneous peak of similar amplitude in all three of the channels (Fig. 3a; let us denote the peak a *primary* peak), often followed by a *secondary* peak of a different amplitude and delay in each channel, not always present in all of the channels (Fig. 3b, c, d). Sometimes one of the channels shows a more prominent peak instead of the primary peak (Fig. 3d). It seems reasonable to explain these cases as the secondary peak following shortly after the primary peak and hence overshadowing the primary peak. Since it is often the case that just one of the channels shows a secondary peak much stronger than the primary peak (Fig. 3b, c, d), we identify the often-seen single hits as being due to the secondary peak (see Fig. 2 and the corresponding discussion). The two-peak structure is clearly present in many of the impacts ($\approx 50\,\%$), and even more are consistent with the pattern. To the best of our knowledge, this is the first time when such clear double-peak structures in the impact signals were observed. For separate ternary plots for the impacts that do and that do not show double-peak structure, see Appendix C.

Signals recorded in mixed (XLD1) mode, decomposed to the monopole channels (see Appendix A) and corrected the same way as monopole signals (see Appendix B), fit the description outlined in the previous paragraph as well (see Fig. 4). This is not surprising, given that the information retained in XLD1 data is virtually the same, except for saturation levels and, to a minor extent, bandwidth. This however confirms that we are justified to treat decomposed XLD1 data the same way as one would treat the monopole signals.

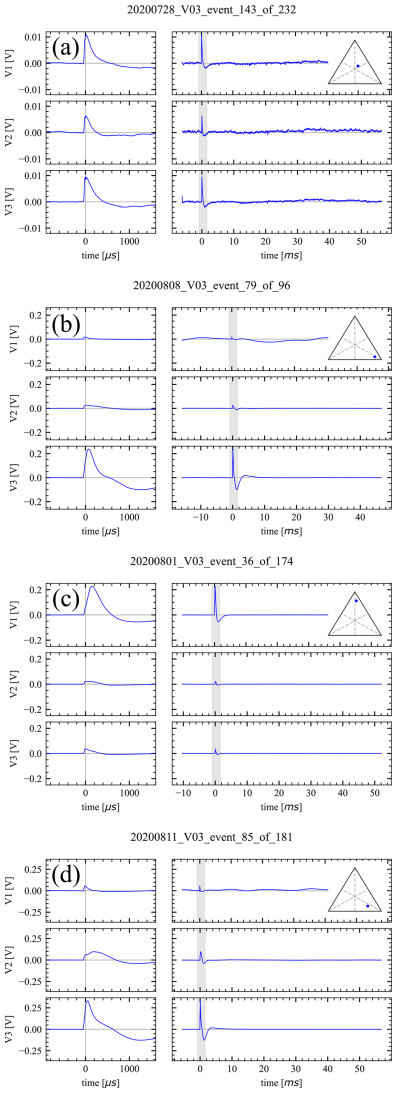

Figure 3. Dust impact events, recorded in true monopole (SE1) mode, corrected (see Appendix B). The voltages are shown as $VX = \mathrm{ant}_X - \mathrm{body}$. The triangular insets show the corresponding location of the event on the amplitude ternary plot; consult Fig. 2. The left-hand side shows detail of the shaded portion of the right-hand side, which in turn shows the whole recording of 62 ms. **(a)** A clear triple hit: simultaneous and with similar amplitude in all three channels. **(b)** Channel V3 shows larger amplitude, compared to channels V1 and V2. A relative delay of $\approx 50\,\mu$s is present. **(c)** Channel V1 shows larger amplitude, compared to channels V2 and V3. A relative delay of $\approx 150\,\mu$s is present. **(d)** A common primary peak is visible in channels V1 and V2, a secondary peak is present in V2, and a larger amplitude and a delay are present in V3.

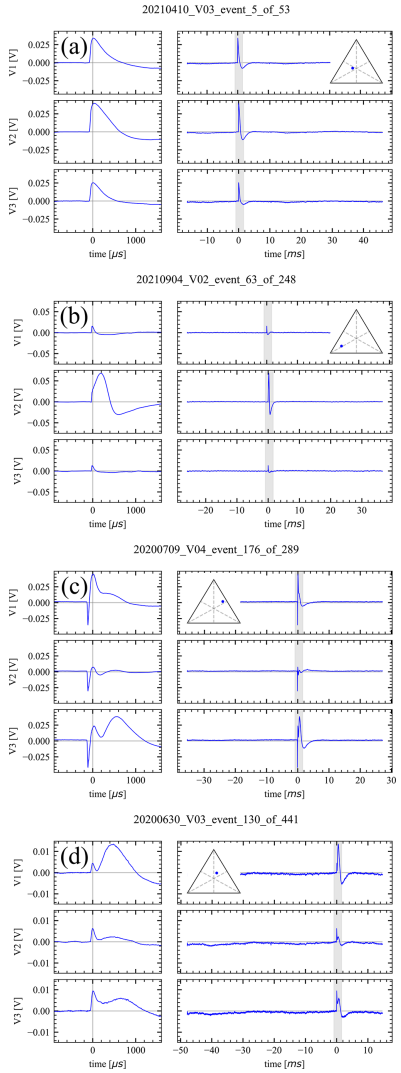

Figure 4. Dust impact events, monopoles reconstructed from signals recorded in hybrid monopole/dipole (XLD1) mode, corrected (see Appendix B). The voltages are shown as $VX = \text{ant}_X - \text{body}$. The triangular insets show the corresponding location of the event on the amplitude ternary plot; consult Fig. 2. The left-hand side shows detail of the shaded portion of the right-hand side, which in turn shows the whole recording of 62 ms. **(a)** A clear triple hit: simultaneous and with similar amplitude in all three channels. **(b)** Channel V2 shows larger amplitude, compared to channels V1 and V3. A relative delay of $\approx 200\,\mu$s is present. **(c)** A common primary peak is visible all the channels, a secondary peak is present in V3, with hints of it in V1 and V2. A negative pre-spike is clearly present. **(d)** A common primary peak is visible in all three channels, and a larger amplitude and delay peak are present in V1. Hints of secondary peaks are present in V2 and V3 with different delays.

In addition to the primary and the secondary peak, there is often a negative pre-spike present in the waveforms, immediately preceding the main signal. We believe this to be due to electron dynamics, and we will address it in Sects. 3.2 and 4.3.

There is a post-impact negative overshoot present in many of the recordings shown in plots in Figs. 3 and 4. One possible explanation for this behavior was developed and described in Zaslavsky (2015) as being due to a partial collection of the electrons by antennas, that have a longer discharge time constant τ_{RC} compared to the spacecraft's body. More generally, the behavior is the same, even if the antenna is charged by a different process than the one described by Zaslavsky (2015); that is, the charge does not have to originate directly in the impact plasma. We will not pursue the explanation now, as the tails of the impacts are generally on the edge or outside of the trusted bandwidth, that is, $f < 500$ Hz or $\tau > 2$ ms. Let us only note that even though the overshoots are likely distorted and out of scope of this paper, they are likely at least partially physical, as similar overshoots were observed on STEREO (Zaslavsky, 2015) and Parker Solar Probe (Kellogg et al., 2021).

2.3 Features' extraction

For the present analysis, we used the convolutional neural network (CNN)-refined data described in Kvammen et al. (2023), decomposed into monopole signals. In order to describe the events of interest only, that is the body impacts sunlit metallic parts conductively coupled to the spacecraft's body, we employ the following filtering criteria: only the impacts of a maximum amplitude below 0.3 V that are predominantly positive in all the monopole channels were analyzed. The upper limit of 0.3 V is employed in order to avoid reaching the saturation level. We note that predominantly negative pulses produced by antenna hits are also present in the data yet out of scope of the present work, as the electrical process is different for these. Besides, for the sake of data quality, we disregarded the signals captured very near the beginning or the end of the recording window that is within the first or the last 100 samples, or 0.38 ms, since these often do not show the full peaks of interest. After applying these criteria, we are left with $\gtrsim 50\,\%$ of the waveforms in the CNN dataset.

We are interested in the following parameters: amplitude of the primary peak, electron pre-spike presence and amplitude, secondary peaks' presence and amplitudes, and the primary peak's rise and decay times, where the former two peaks (electron and primary peaks) are assumed to be common in all three channels, and the latter (secondary) is analyzed channel-wise. For a comprehensive description of how these are extracted, the reader is referred to Appendix D.

3 Dust impact pulse and process description

Given the previous literature (Friichtenicht, 1964; Auer and Sitte, 1968; Gurnett et al., 1983; Zaslavsky et al., 2012; Pantellini et al., 2012a; Meyer-Vernet et al., 2014; Collette et al., 2015; Meyer-Vernet et al., 2017; Vaverka et al., 2017; Nouzák et al., 2018; Mann et al., 2019; Ye et al., 2019; Kočiščák et al., 2020; Kellogg et al., 2021; Shen et al., 2021b, a; Racković Babić et al., 2022; Shen et al., 2023) and what we observe in the case of Solar Orbiter's RPW data, we formulate a following simplified outlook on the process.

Since the spacecraft is practically always in the sunlight, photoelectrons are released from its body, leading to a positive charge of the most of the spacecraft's body. Upon a hypervelocity dust impact on the spacecraft body, quasi-neutral charge is released. In the case of a spacecraft's body hit, measurement of the spacecraft's antennas potential against its body ($\Phi_{\mathrm{ant}} - \Phi_{\mathrm{body}}$) shows an evolution of the voltage difference, summarized on different timescales as follows. The phases numbered (1)–(5) are also visualized in Fig. 5.

1. *The impact.* A quasi-neutral cloud is born in the near vicinity of the spacecraft. Neglecting a usually small charge possibly carried by the incident dust grain, no change is induced in the spacecraft's potential due to the impact, as the newborn cloud is quasi-neutral, and all the charged particles remain in the near vicinity of each other and therefore have no net influence on the potential. Due to the high density and low mean free path in the newborn cloud, the cloud is at least partially thermalized (Ye et al., 2019; Kočiščák et al., 2020).

2. *The electron motion timescale.* A portion of the electrons is collected by the spacecraft's body. Simultaneously, a fraction of released electrons with energies high enough to surpass the spacecraft's potential well escapes from the vicinity of the spacecraft. The much slower, net positive ion cloud remains in the vicinity of the impact site. There are two effects going on simultaneously: (a) body potential rises, since the electrons that escaped no longer influence its potential, and (b) antenna potential rises, since neither the escaped electrons nor the electrons collected by the body influence its potential any longer. The latter effect is asymmetric with respect to the three channels, since each antenna is influenced differently, owing to the location of the impact site. The escaping electrons are, however, visible in the form of a symmetric negative spike, owing to the influence of the body potential, possibly forming the aforementioned negative pre-spike. These two (asymmetric positive and symmetric negative) influences counteract each other, and therefore the result is ambiguous, depending on the spacecraft's potential, as well as the instrument geometry and impact site, besides other factors.

3. *The timescale of the impact cloud retreating from the vicinity of the spacecraft's surface.* As the spacecraft body is positively charged, the net positive impact cloud is repelled. When the impact cloud's electrostatic induction on the body ceases, the electrons previously collected by the body show in the form of a positive peak in the voltage difference, which we denoted as the primary peak. The rise time of the primary peak is therefore the time that ions need to escape far enough from the spacecraft body's vicinity or, alternatively, time until the ion cloud is sparse and far enough so that it is shielded by the photoelectron sheath. The peak is in principle the same on all the channels, since it happens on the body, rather than on the individual antennas. An asymmetry might still be visible due to the electrostatic induction of the ion cloud on the antennas that may not have halted yet, discussed in the previous paragraph. This asymmetry halts on a timescale similar to the rise time of the primary peak, as they both depend on ion motion and shielding.

4. *The timescale of the impact cloud reaching the antennas.* There is a spike due to ions getting so close to the antennas, that they influence their potential locally. The peak is delayed behind the primary peak due to a finite drift and diffusion velocity of the ions. In fact, the delay of $\gtrsim 100\,\mu\mathrm{s}$ provides a clear distinction from the induction effect of the ion cloud on the antennas that is observed on a much faster timescale, discussed in phase 2. The antenna charging process is not obvious. Several possibilities for the charging process were previously proposed, observed, and debated.

5. *The timescale of potential equalization.* Neglecting other influence, the spacecraft's potential is positive and in equilibrium due to balance between the photoelectron current with negative dependence on the spacecraft's potential and the ambient (solar wind) electron collection current with positive dependence on spacecraft's potential. This balance is perturbed by the net negative charge collection from the dust impact, and it is restored on a timescale much more slowly than the impact cloud motion timescale.

Each phase corresponds to one process being dominant; therefore the phases may or may not begin and end with peaks, which depends on amplitudes and timing for the given event. We note that certain phases may or may not be pronounced in individual waveforms, due to a specific voltage balance or phase timing or an insufficient temporal resolution of the waveform sampler. Different behavior may be observed in the case of a less likely impact on a scientific instrument, a non-metallic surface, or a non-illuminated back side of the body. We note that even though the solar panels have a large area compared to the spacecraft's body, they are nonconductive on the front side, which makes them less sensitive

to dust impacts. Much is not understood about the panels' response to the impacts, and this is out of scope presently, though it is worthy of future investigation.

3.1 Charge production equation

The charge is released from the impact site shortly after the dust impact. The amount of charge was found (Auer and Sitte, 1968) to depend on the mass and velocity and is often assumed to follow this empirical equation:

$$\frac{Q}{\mathrm{C}} = A\left(\frac{m}{\mathrm{kg}}\right)^{\alpha}\left(\frac{v}{\mathrm{km\,s^{-1}}}\right)^{\beta}, \tag{1}$$

where m and v are the grain's mass and velocity respectively, and A, α, and β are material constants. We note that the process is stochastic and depends on other parameters, such as the angle of incidence of the impact velocity, so the exact charge can not be reliably predicted, even if these parameters are known, but Eq. (1) was found to work for the mean charge obtained in a repeated experiment. For experimental results and discussion, the reader is referred to Collette et al. (2014) and references therein.

3.2 Electron pre-spike

The negative, electron pre-spike forms due to electrons escaping from the potential well of the positively charged spacecraft. One of the extreme cases is that the potential of the spacecraft is so high compared to the energies of the electrons that virtually no electrons escape, and, hence, no electron peak is observed. In the other extreme case, the potential of the spacecraft is so low that all the electrons moving initially outward (that is, one half of all the electrons) escape. Since the Solar Orbiter operates in the solar wind and in sunlight, its potential does not usually get below +5 V, which means that the latter scenario is unlikely. In reality, values between the two extremes are obtained, leaning towards the former scenario.

3.3 Primary peak

As the Solar Orbiter is typically positively charged to ≈ 7 V, the positive ions released at the impact are repelled from the spacecraft's body and leave behind the negative charge. It was explained and evaluated before (Zaslavsky et al., 2021) that if the peak is due to a sudden deposition of free charge Q onto the body of the spacecraft, and the antenna's potential ϕ_{ant} remains roughly constant throughout the process, the peak's amplitude V is linked to the amount of deposited charge as follows:

$$V \approx \frac{Q\Gamma}{C_{\mathrm{sc}}}, \tag{2}$$

where C_{sc} is the electrical capacity of the spacecraft's body ($C_{\mathrm{sc}} \approx 355$ pF), while Γ is the capacitive transfer function

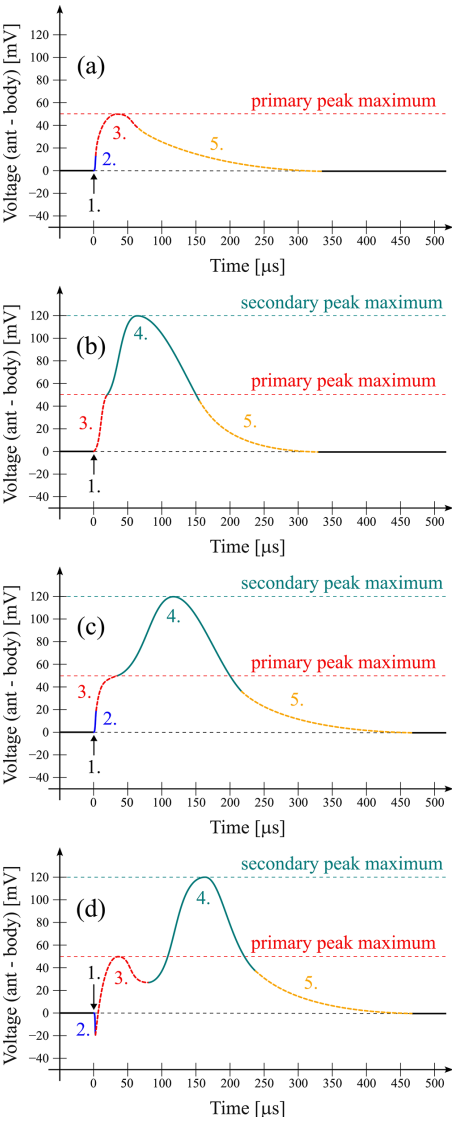

Figure 5. The phases of impact ionization process, as described in Sect. 3. Different eventualities are shown to demonstrate the variability of the pulses that fit the proposed framework. The curves are fictitious, with reasonable primary and secondary peak amplitudes of 50 and 120 mV, as well as a reasonable timescales. The second phase provides an ambiguous step function and is not otherwise related to a specific shape of the curve. Compare to the individual channels in the panels of Fig. 4. **(a)** No secondary peak is visible; **(b)** the peaks are discerned by an inflection point; **(c)** all the phases are clearly visible, although only one local maximum is reached; and **(d)** all the phases are visible, and two local maxima are reached. The amplitude of the primary peak is 70 mV, rather than 50 mV.

between the body and the antenna:

$$\Gamma = \frac{C_{\text{ant}}}{C_{\text{ant}} + C_{\text{stray}}}, \tag{3}$$

where C_{ant} is the antenna's self-capacitance ($C_{\text{ant}} \approx 55$–$70$ pF, depending on the variable local plasma conditions), and C_{stray} is the capacitive coupling between the antenna and the body, including the preamplifier capacitance ($C_{\text{stray}} \approx 108$ pF). It should be noted that Eqs. (2) and (3) present a simplified outlook, sufficient for our current endeavor. More precise approaches have been taken recently (Shen et al., 2021b; Racković Babić et al., 2022). The approximation requires that the rise of the signal is much faster than the relaxation, which is, as we will see, well met. Then we have $\Gamma \approx 0.34$–0.39. Numbers considered, for the primary peak, we calculate

$$\frac{V}{Q} \approx 10^9\, V/C. \tag{4}$$

In their recent modeling effort, Racković Babić et al. (2022) concluded that, in the case of STEREO spacecraft with a similar antenna system, Eq. (2) underestimates the total charge released by about 30 % due to finite rise and finite decay timescales but is a reliable linear measure of the charge released.

We also note that in the case of the presence of the electron peak, we evaluate the amplitude V of the primary peak in reference to the low point of the electron peak, that is to the high point of the spacecraft's potential.

3.3.1 Antenna-induced primary peak asymmetry

In this section, an order-of-magnitude estimate of impact cloud influence on antennas is presented. As explained in Sect. 3, shortly after the impact, electrons are collected by the spacecraft or escape from the cloud of impact-generated plasma. Therefore, the leftover is a net positive charge cloud near the impact site. As the cloud moves away from the impact site, its influence on the body potential gradually ceases, and the primary peak appears, which is the scope of point 3 in Sect. 3. The cloud however influences not only the spacecraft body but also each of the three antennas via induction, as debated in Meyer-Vernet et al. (2014) and Shen et al. (2021a). This influence also ceases once the ion cloud is far away from the spacecraft, but before that happens, this influence is the source of an asymmetry of the primary peak as measured with individual channels, as demonstrated by Shen et al. (2021a). This influence does not require that the ions have moved far from the impact site and is the scope of point 2 in Sect. 3. As an order-of-magnitude estimate, let us study the influence on the antennas' potential if a point charge is located near the heat shield.

Assume a point charge Q at the location $\boldsymbol{x_q}$ and the Debye length of λ_{D}. The electric potential at the point of space $\boldsymbol{x}$ is

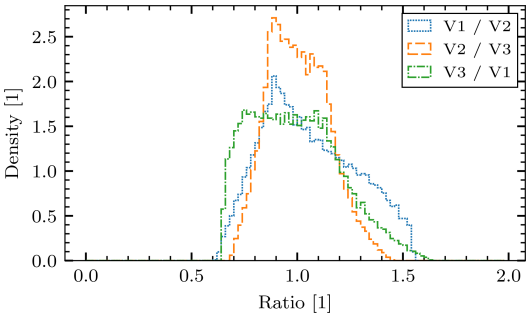

Figure 6. The ratio of primary peak amplitudes as predicted by the model for detection in different channels.

then coulombic with Debye shielding:

$$\Phi = \frac{Q}{4\pi\epsilon} \frac{e^{-\frac{|\boldsymbol{x}-\boldsymbol{x_q}|}{\lambda_{\text{D}}}}}{|\boldsymbol{x}-\boldsymbol{x_q}|}. \tag{5}$$

The Debye length in solar wind plasma is typically between 3 and 8 m (Guillemant et al., 2013) and hence greater than or similar to the linear dimension of the spacecraft, and the shielding by photoelectron cloud is neglected for simplicity; hence the exponential factor in Eq. (5) is assumed to be equal to unity. A thin antenna (defined by a path $\boldsymbol{l}$) measures a potential of

$$\Phi_{\text{ant}} = \frac{1}{|l|} \int_{\boldsymbol{l}} \Phi \mathrm{d}\boldsymbol{l}. \tag{6}$$

Each antenna responds to the point charge differently, depending on their relative location. The response of the spacecraft's body is assumed as in Eq. (4). Employing a Monte Carlo model for the charge location on the heat shield, we find that the ratio R of primary peak amplitude detected with different channels is up to $R \approx 1.5$; see Fig. 6. Similar conclusion can be arrived to based on the results of Shen et al. (2021a), albeit for a different configuration of antennas. For a more detailed description of the model, refer to Appendix F.

3.4 Secondary peak

Should the antenna get charged, the corresponding voltage would be given by an equation equivalent to the one for the charging of the body but with a different value of the capacitance,

$$V \approx \frac{Q\Gamma}{C_{\text{ant}}}, \tag{7}$$

and is hence different by a factor of $C_{\text{sc}}/C_{\text{ant}}$. By substitution for the difference, we find that

$$\frac{V}{Q} \approx 6 \cdot 10^9\, V/C. \tag{8}$$

It is unlikely that the antenna will get charged by collection of free charges (O'Shea et al., 2017); however the secondary peak might be caused by various mechanisms. Should the antenna only detect the approaching charge remotely (via induction), its response would depend on the geometry of the encounter: the closer the charge gets to the antenna, the stronger the response, with the maximum equal to the charge collection in case of a very close approach. Should the antenna charge due to photoemission (Pantellini et al., 2012a; Kellogg, 2017), the above-mentioned equation holds, and the Q would be the charge due to photoemission. Finally, we note that since the secondary peak is noticeably retarded by $\gtrsim 100\,\mu s$ with respect to the primary peak (see Figs. 3, 4), it can not be explained as an electrostatic response to the impact plasma cloud located near the impact site – the motion towards the antenna must be important, and the charging process must be local, requiring proximity of the ion cloud to the antenna. Besides, we observe the electrostatic response as well, on a different timescale, in the form of the primary peak asymmetry.

3.5 Timescales

The electron peak rises when the electrons no longer induce charge on the spacecraft body. It happens no later than when the electrons are displaced from the spacecraft's body by a displacement comparable to the size of the spacecraft body (≈ 1 m). Consider that the energy of the electrons has to be high enough to overcome the positive potential of the spacecraft's body. The temperature of the impact cloud was estimated before (Friichtenicht et al., 1971; Eichhorn, 1976; Collette et al., 2016; Kočiščák et al., 2020) to be $\gtrsim 1\,\mathrm{eV}\,k_B^{-1}$, which implies an electron velocity of $v_e \gtrsim 500\,\mathrm{km\,s^{-1}}$, leading to a rise time of $\tau_e \lesssim 2\,\mu s$, which is well below the 262 ksps resolution of the sampler; hence it appears to be instantaneous. If an electron pre-spike appears to be stronger on certain antennas, it might indicate that it is partially due to electron collection by the antenna.

Similar to the electron peak, the primary peak appears as soon as the released ions no longer induce charge on the spacecraft's body. Two processes cause this: physical displacement of the ions and the shielding of the ions by the electrons (ambient electrons and photoelectrons). Adopting a moderate ion temperature of $5\,\mathrm{eV}\,k_B^{-1}$ (Collette et al., 2016; Kočiščák et al., 2020) and assuming carbon nuclei, we find the ion speed to be $v_i \approx 9\,\mathrm{km\,s^{-1}}$. By applying a general electrostatic model for collected and induced charging of all the relevant elements, that is both the antennas and the body of a simplified physical model of a spacecraft, Shen et al. (2021a) measured the speed of ions expanding from a dust impact in laboratory. They found the expansion speed to be $v_i = 11.3 \pm 0.7\,\mathrm{km\,s^{-1}}$. This value is compatible with the laboratory results of Shen et al. (2021b), who found $v_i = 9 \pm 1\,\mathrm{km\,s^{-1}}$ using a scaled-down model of Cassini spacecraft. Based on in situ dust impact measurements on Magnetospheric Multiscale (MMS) spacecraft and making use of its tip-sensitive antennas, Vaverka et al. (2021) reported $v_i = 27 \pm 5\,\mathrm{km\,s^{-1}}$. Recently, Racković Babić et al. (2022) reported $13\,\mathrm{km\,s^{-1}}$ using a multi-element model applied to STEREO spacecraft's data. Assuming the expansion speed of 10–20 $\mathrm{km\,s^{-1}}$ we find that the displacement of 1 m occurs in $\approx$ 50–100 µs – a time well resolved by the RPW sampler. Should the impact happen within the photoelectron sheath, the photoelectrons are easily the dominant electron population. Assuming typical plasma conditions at 1 AU and an ion speed of $v_i = 10\,\mathrm{km\,s^{-1}}$, Meyer-Vernet et al. (2017) estimated the timescale for the shielding of $Q = 1.6$ pC charge to

$$\tau_{ph} \approx 12\,\mu s;\ \tau_{ph} \propto Q^{1/3} d^{2/3} v_i^{-2/3}, \tag{9}$$

which is on the edge of the resolution of the RPW sampler.

The potential altered by the net charge left deposited on the spacecraft's body will decay towards the original spacecraft potential, that is, until the equilibrium is reached again. Under the assumption that the potential perturbation is small compared to the equilibrium potential, the time constant τ_{RC} of the decay is

$$\tau_{RC} \approx \frac{C_{sc} k_B T_{ph}}{e|I_e|} \approx \frac{C_{sc} k_B T_{ph}}{e^2 n_e v_e S_{sc}}, \tag{10}$$

where $k_B T_{ph}$ is the photoelectron temperature (in eV), and $|I_e|$ is the magnitude of the ambient electron current on the body of the spacecraft, expanded into the product of the charge, density, velocity, and surface $e n_e v_e S_{sc}$. For details, the reader is referred to Henri et al. (2011). Assuming $C_{sc} = 355$ pF, $k_B T_{ph} = 3$ eV, $n_e = 5 \times 10^6\,\mathrm{m^{-3}}$, $v_e = 500\,\mathrm{km\,s^{-1}}$, and $S_{sc} = 28.4\,\mathrm{m^2}$, we get an order-of-magnitude estimate of

$$\tau_{RC} \approx 93\,\mu s \tag{11}$$

for a typical $r = 1$ AU solar wind environment. It is often reasonable to assume $n_e \propto r^{-2}$.

4 Statistical analysis of the primary peak

The primary peaks are found synchronous and with similar amplitude in all three channels; therefore we believe that the primary peak is the result of the net charge deposition to the spacecraft's body due to impact. In this section, we examine the statistical properties for the primary peaks, such as the distribution of their amplitudes and their rise and decay times. We also compare these to theoretical predictions.

4.1 Amplitude distribution

We analyzed the primary peak amplitudes (as described in Sect. 2.3 and Appendix D) as these are the better measure of the total released charge, compared to the channel global maxima reported previously (Zaslavsky et al., 2021), since

the dataset now excludes secondary peaks' amplitudes. The smallest consistently resolved peaks are $\gtrsim 0.5$ mV, and the largest included peaks are amplitudes of ≤ 0.3 V. Assuming the relation between the primary peak amplitude V and the charge Q in the form of Eq. (4), we find the mean charge to be $Q_{\mathrm{mean}} \approx 21$ pC and the median to be $Q_{\mathrm{median}} \approx 8.1$ pC. Further discussion is available in Appendix E.

The charge production equation (see Eq. 1) for Solar Orbiter is unknown. We assume a production relation as in McBride and McDonnell (1999), that is $\frac{Q}{C} = 0.7\left(\frac{m}{\mathrm{kg}}\right)^{1.02}\left(\frac{v}{\mathrm{km\,s^{-1}}}\right)^{3.48}$, and a mean incident velocity as in Kočiščák et al. (2023), $v_{\mathrm{mean}} = 63\,\mathrm{km\,s^{-1}}$. We find the mean incident dust mass $m_{\mathrm{mean}} \approx 1.5 \times 10^{-17}$ kg, which corresponds to a spherical dust grain with the diameter of 0.24 µm, assuming the density of $\rho = 2\,\mathrm{g\,cm^{-3}}$.

4.2 Rise time

We analyzed the rise time of the primary peak and compared it with the estimates presented in Meyer-Vernet et al. (2017) for the case of the sunlit impact surface and for the case of the shaded impact surface (see Sect. 3.5). We adapted the estimates to the median charge of 8.1 pC, as well as the ion speeds of $v_{\mathrm{i}} = 10$ and $20\,\mathrm{km\,s^{-1}}$, obtained as described in Sect. 3.5. The estimates were done assuming only one (photoelectron shielding or ambient plasma shielding) process, while the other one plays a role as well, as described in Meyer-Vernet et al. (2017) Therefore, even sunlit estimates are overestimates. On the experimental side, the exact definition of the rise time is important, as the rise profile is usually not exponential. In order to exclude a potential fast contribution of the induced charge (as in Sect. 3.3.1), we define the rise time as the time needed to get from $1/e$ of the maximum to the maximum value of the peak.

Figure 7 shows the dependence of the rise time on the heliocentric distance. Inferred means are close to the theoretical estimate for sunlit surface impact. Figure 8 shows the dependence of the rise time on the primary peak amplitude, assuming heliocentric distance of 0.75 AU. The data show significantly less variation than predicted; however the sunlit estimate is clearly better than the shade estimate. There might be several reasons for the disagreement of the data with the theory. Either the process understanding as in Meyer-Vernet et al. (2017) is incomplete, or there are correlations present between the variables in Eq. (9). We note that several papers (for example, Collette et al., 2016; Nouzák et al., 2020) suggested that the higher impact velocity might lead to a higher ion velocity v_{i} in addition to a higher charge yield Q, although recent measurements did not observe this (Shen et al., 2021a). If a higher impact speed is correlated with a higher ion expansion speed, then these effects partially counteract each other, and the scaling of the rise time τ_{ph} is not as in Eq. 9. The theoretical predictions made in Meyer-Vernet et al. (2017) and the ion escape velocity between 10 and $20\,\mathrm{km\,s^{-1}}$ are compatible with the data with respect to the timescale of the rise time. The theory is also compatible with the variation with the heliocentric distance, though the dependence of the rise time on the impact charge was not observed as predicted, with sunlit estimates providing a better fit to the data, compared to shade estimates.

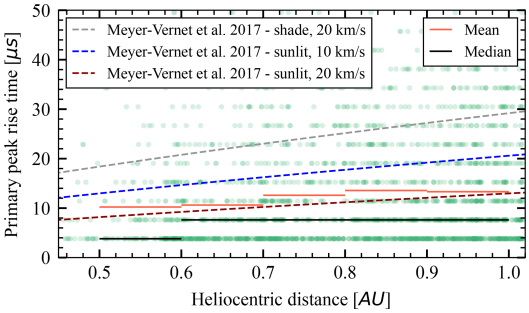

Figure 7. Rise times of the primary peaks as a function of the heliocentric distance. Predictions from Meyer-Vernet et al. (2017) are shown in the case that impact cloud shielding is dominated by photoelectrons (sunlit) or solar wind plasma (shade). The predictions are for the median primary peak's charge of 8.1 pC and for an ion escape velocity of 10 and $20\,\mathrm{km\,s^{-1}}$.

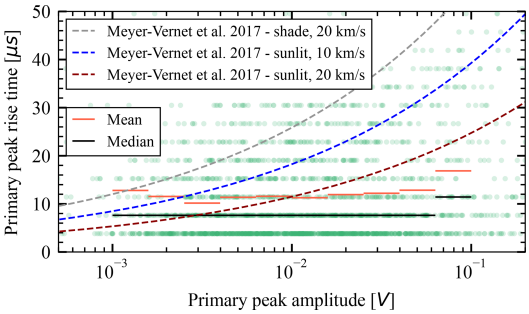

Figure 8. Rise times of the primary peaks as a function of the body's peak amplitude. Predictions from Meyer-Vernet et al. (2017) are shown in the case that impact cloud shielding is dominated by photoelectrons (sunlit) or solar wind plasma (shade). The predictions are for the heliocentric distance of 0.75 AU and for an ion escape velocity of 10 and $20\,\mathrm{km\,s^{-1}}$.

4.3 Negative pre-spike

The negative pre-spike is present intermittently, for example in Fig. 4c. The presence indicates that a portion of free electrons was able to escape the spacecraft's potential well. We note that the induced charge on the antennas due to the positive impact cloud appears nearly as quickly as the electron pre-spike, and these two effects therefore counteract each

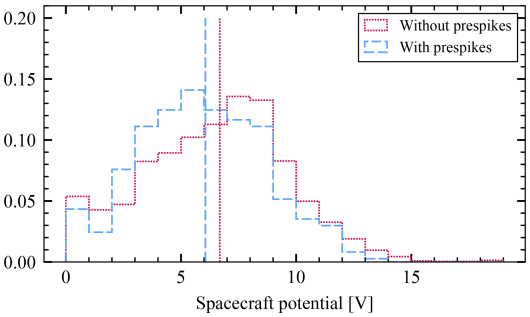

Figure 9. The histogram of spacecraft potential at each dust impact for impact with and without pre-spikes. Averages are shown for the two populations as vertical lines.

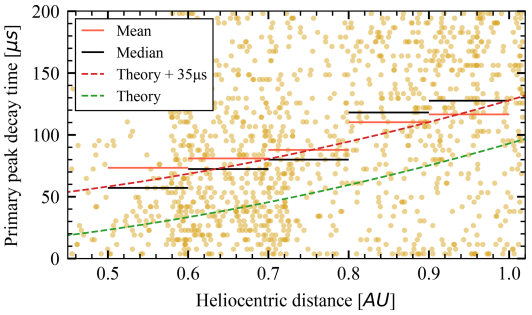

Figure 10. Decay times of the primary peaks as a function of the heliocentric distance.

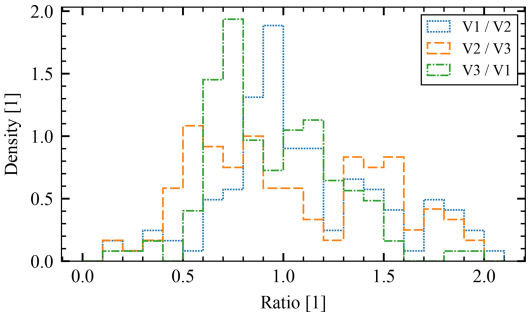

Figure 11. Antenna-induced asymmetry to the primary peak's amplitude.

other, differently in each channel. The induction on the antennas may be fast and ample enough so that the electron pre-spike is obscured. Concerning the presence and the amplitude of the pre-spike, the exact impact location certainly plays a role, since spacecraft's surface potential is not uniform. On top of that, the spacecraft's potential must play a role as a lower potential implies a shallower potential that electrons need to overcome in order to escape. To see this dependence, we examine the spacecraft potential data product, based on low-frequency receiver measurements of RPW (Maksimovic et al., 2020). We note that this a result of an indirect measurement and therefore the reliability is limited, especially in the case of very high or very low values. A correlation between the pre-spike presence and a relatively lower potential is expected, which is why we show a separate normalized histogram of spacecraft potentials at the times of impacts with pre-spikes and without; see Fig. 9. Pre-spikes are present for nearly any spacecraft potential, but the correlation is apparent, as expected.

4.4 Decay time

We established the decay time for the primary peaks as the time to get from 100 % to $1/e$, always for the channel that showed the lowest primary peak amplitude, as that is the one least affected by a possible secondary peak. Furthermore, we disregarded any value over 200 µs for the same reason – if the decay time is very long, it is likely due to the secondary peak. We note that only impact shapes such as in panels (a) and (d) in Fig. 5 allow for this analysis. We compare the result to the theoretical values presented in Sect. 3.5; see Fig. 10. The decay time shows a clear variation, albeit different from the model (Eq. 10). The data show a significant scatter and are compatible with the model with an additional constant offset of around 35 µs. We note that there are uncertainties, for example, in the spacecraft capacitance C_{sc} and in the spacecraft surface S_{sc}. The shallower dependence might be a result of electron temperature being higher at lower heliocentric distance, which we do not take into account in the theoretical calculation. We also can not exclude an artifact of the secondary peaks that are present, though not apparent, as these may introduce error that is hard to estimate. The definition of the decay time might play a role, as the decay profile is often non-exponential.

4.5 Antenna-induced asymmetry

We studied the amplitudes of individual primary peaks in order to compare them to the theoretical predictions of Sect. 3.3.1. We only analyzed the events that show no secondary peak in any channel. In parallel to Fig. 6, ratios of channel pairs are shown in the histogram in Fig. 11. The histogram does not show data with the ratio > 2.2, and as a result, 5 of 327 values are not shown. Similarly to the results of the numerical model shown in Fig. 6, values < 0.5 are rare, as are the values $\gtrsim 2$, which implies that the process as described in Sect. 3.3.1 is a good model for the situation, as it explains the magnitude of observed asymmetry.

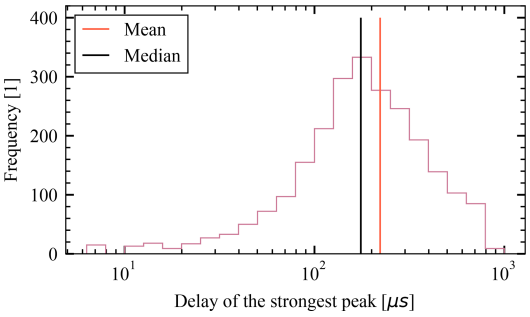

Figure 12. Histogram of the strongest secondary peak's delay against the primary peak.

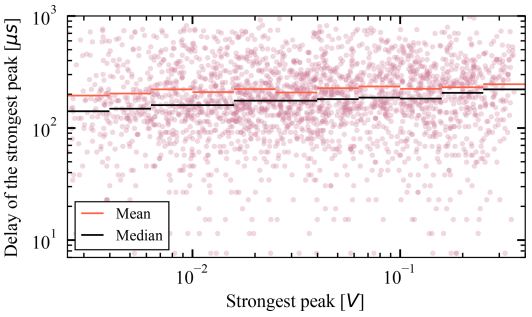

Figure 13. Strongest secondary peak's delay against the primary peak as a function of its amplitude.

5 Statistical analysis of the secondary peak

An important proportion of the impacts (≈ 50 %) shows a clear double-peak structure, while even more are compatible with the double-peak structure. The secondary peaks' prominent features include the following:

- strong asymmetry in the three channels,
- intermittent presence,
- variable but pronounced delay with respect to the primary peak.

The first point leads to the conclusion that the process causing secondary peaks mainly takes place on the antennas, rather than on the spacecraft body. This implies that, in the process, the affected antenna is charged more positively. The latter two points imply that the effect relies on a drift of the cations. In this section, we describe statistical properties of the identified secondary peaks.

5.1 Delays

The typical delay lies in the range of 100 µs to 300 µs; see the histogram in Fig 12. The secondary peak's delay varies, nearly uncorrelated with the peak's amplitude or the spacecraft's heliocentric distance; see Figs. 13 and 14. This time is too long to correspond to charge generation, collection, or even equalization due to ambient plasma currents, as we described all of these earlier, and they happen within $\lesssim 150$ µs.

Assuming the ion velocity of 10–20 km s^{-1} as before, the time delay of 100 to 300 µs translates to 1–6 m of displacement. We note that the Solar Orbiter's heat shield's size is approximately 2.4×3.1 m^2, and the antennas are 6.5 m long. We therefore conclude that this delay is due to ion motion, since it is the only electric process that happens on this timescale. The fact that no important variation is observed in Fig. 14 suggests that the ion velocity does not vary with the heliocentric distance.

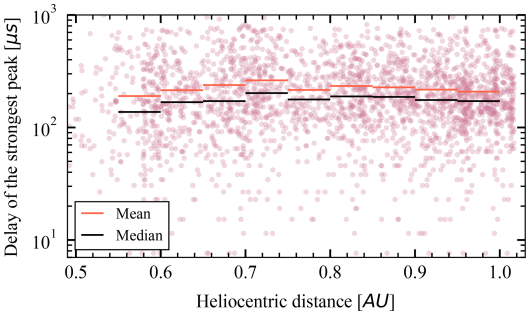

Figure 14. Strongest secondary peak's delay against the primary peak as a function of the spacecraft's heliocentric distance.

We note that the delay of 100 to 300 µs is far enough for the cloud to get shielded by the photosheath, due to its high electron number density (compare with values shown in Figs. 7 and 8). However, the photosheath decays with the distance from the illuminated surface rather quickly, with the typical Debye length of 0.25 m close to Solar Orbiter's perihelia and 1 m close to 1 AU (Guillemant et al., 2013). We therefore come to a conclusion that at least a part of the impact cloud passes through the photosheath (consult Appendix G), and this cloud later influences the antennas. We also note that the photosheath is not uniform and weaker at places that are less illuminated, such as spacecraft sides.

The delay does not show variation with the peak absolute amplitude (Fig. 13), but it shows a weak correlation with the amplitude relative to the primary peak amplitude, as is shown in Fig. 15. The primary peak's amplitude is a good measure of the total charge released on the impact, and since we study the secondary peak as a random process, normalization to the impact magnitude is natural.

We also note that the secondary peak is not only delayed; it also evolves and decays on a $\gtrsim 100$ µm timescale, as is apparent from waveforms shown in Figs.3 and 4. This hints that

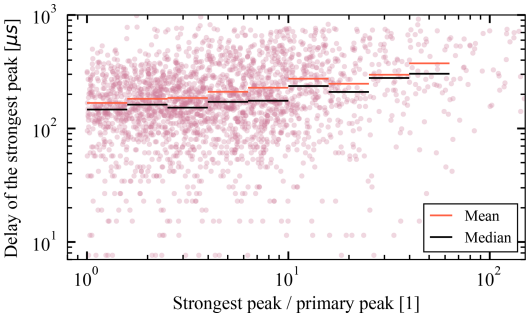

Figure 15. Strongest secondary peak's delay against the primary peak as a function of the strongest secondary peak's amplitude relative to the primary peak.

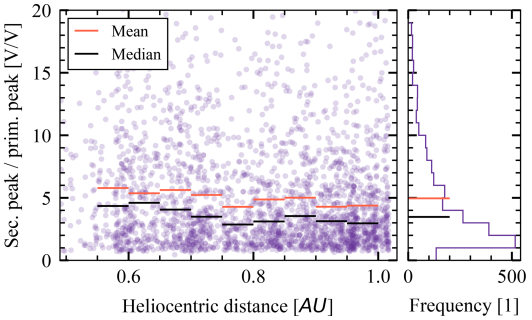

Figure 16. The secondary peak relative to the primary peak as a function of heliocentric distance for the events that show a secondary peak. If the secondary peak is present in multiple channels, the strongest one is shown. The absence of values < 1 is due to the secondary peak being obscured by the primary peak. We do not intend to imply there are no small secondary peaks, but we can not identify them reliably.

the evolution of the secondary peak is also dependent on the dynamics of the ion cloud's motion. This is also consistent with the positive correlation between the secondary peak's relative amplitude and the delay with respect to the primary peak (Fig. 15).

5.2 Amplitudes

The secondary peak's amplitude varies, and the peak is not always present. We do not claim that small secondary peaks are non-existent; however for the purpose of our analysis, the secondary peaks are considered absent in cases when their amplitudes are much smaller than the primary peak's amplitudes, as then we can not identify them reliably. If the secondary peak is present in a channel, we study its amplitude relative to the amplitude of the primary peak, as the primary peak's amplitude is a good measure of the total charge released on the impact. See Fig. 16 for the plot of relative amplitude of the secondary peak over the primary peak vs. the heliocentric distance in cases where the secondary peak is present. We observe that the typical relative amplitude is between 3 and 5 but often is over 10. There is not a strong correlation between the relative amplitude of the secondary peak and the heliocentric distance.

Given the time delay that corresponds to the ion motion along Solar Orbiter and what was suggested and observed previously with different spacecraft, one may try to explain the secondary peak as the antenna's response to the ion cloud's electric field. This field may be due to the charge separation electric field of the cloud (Oberc, 1996) or due to the different plasma potential within the impact cloud (Zaslavsky et al., 2012). Alternatively, this peak may be due to collection of ions from the impact cloud (Meyer-Vernet et al., 2014; Zaslavsky, 2015; Vaverka et al., 2021; Kellogg et al., 2021). In the extreme case of the collection of all the created ions by a single antenna, the amplitude would be approximately proportional to the amplitude of the primary peak by a factor of $C_{sc}/C_{ant} \approx 5$. That is ignoring the fact that the ion cloud is exposed to the solar wind plasma for 100 to 300 μs. The response to the charge collection is also an upper estimate of the response to the induced fields. We also note that a complete collection of the ions by an antenna is unlikely. The reason is that the antennas present a small cross-section for the ions, since they occupy a small solid angle as seen from usual impact site and are metallic and therefore positively charged (O'Shea et al., 2017). Moreover, we often find the secondary peak in multiple channels, which clearly rules out the option that one antenna collects all the ions. Therefore the factor of ≈ 5 is understood as a very safe overestimate of the secondary peak amplitude, if it is due to the antenna's response to the ion cloud's electric field. As is shown in Fig. 16, the limit of 5 is breached very often, which rules out the linear response of the antenna to the electric field of the escaping ions. The conclusion is that an additional antenna charging process must be present. A similar conclusion was arrived at by Pantellini et al. (2012b) for STEREO spacecraft's single hits.

The capacitance of the antennas and of the spacecraft increase with decreasing heliocentric distance due to photoelectron sheath's presence, but since a greater portion of the antennas is sunlit compared to the spacecraft body, one would expect a positive correlation in the Fig. 16, should the variable capacitance be important, which is not observed.

5.3 A possible process

In Sect. 5.2 we concluded that an additional effect must be present near the antennas, allowing none, one, or more of them to be charged beyond the linear electrostatic response to the ion cloud that is present post-impact.

A mechanism providing a strong response to a relatively small positive charge near the thick cylindrical antennas of STEREO/WAVES was proposed by Pantellini et al. (2012a) and revised by Pantellini et al. (2013). The idea is that although the ions do not induce enough response on the antennas, the provided electric field is strong enough to perturb the photoelectron sheath around the antennas, which manifests as a strong transient charging. Pantellini et al. (2012a) concluded that the strength of the effect is proportional to the cylindrical antenna's radius, as that is proportional to the photoelectron current. We note that the STEREO/WAVES electrical antennas have the diameter of 32 mm near the base (Bale et al., 2008), similar to the ones on Solar Orbiter that have the near-base diameter of 38 mm.

The photoelectron sheath perturbation process as proposed by Pantellini et al. (2012a) is effective once an antenna is partially enveloped by the impact ejecta cloud. Hence, a time delay is expected with respect to the impact on the order of d/v_{ion}, where d is the distance from the antenna to the impact site, and v_{ion} is the ejecta velocity. We note that this was not observed in the case of STEREO single hits (Zaslavsky et al., 2012) but is observed with present results; see Sect. 5.1.

We perform an order-of-magnitude estimate of the maximum secondary peak amplitude, assuming that due to envelopment of a portion of an antenna, the photoelectron return current is fully suppressed for a time. A similar estimate was done before by Pantellini et al. (2012a). The secondary peak's amplitude V_{sec} depends on the total charge the antenna accumulates Q_{ant} due to the effect,

$$V_{\mathrm{sec}} = \frac{\Gamma}{C_{\mathrm{ant}}} Q_{\mathrm{ant}}, \tag{12}$$

while the accumulated charge depends on the photocurrent density j_{ph}, the submerged antenna length $L(t)$, the width w, and the time τ during which the return current is suppressed:

$$Q_{\mathrm{ant}} = \int_0^{\tau} j_{\mathrm{ph}} w L(t)\,\mathrm{d}t. \tag{13}$$

Assuming a constant photon flux ($j_{\mathrm{ph}} = \mathrm{const.}$) and a cylindrical antenna ($w = \mathrm{const.}$), zero initial expansion ($L(0) = 0$) and a constant expansion speed of the cloud until the maximum expansion $L_{\mathrm{max}} = L(\tau)$ are reached in time τ when the suppression is no longer effective, by integrating Eq. (13), we get

$$Q_{\mathrm{ant}} = \frac{1}{2} j_{\mathrm{ph}} w L_{\mathrm{max}} \tau. \tag{14}$$

The maximum submerged length L_{max} is related to the total positive charge Q released at the impact but also to the impact cloud motion geometry and how much photoelectrons and ambient solar wind electrons are bonded by the post-impact cloud before it reaches the antenna. Again, for the order-of-magnitude estimate we assume spherical expansion of the impact cloud and neglect the neutralization of the cloud by ambient electrons; therefore the number density n_{cloud} within the cloud of the charge Q and the radius L_{max} is

$$n_{\mathrm{cloud}} = \frac{Q}{e} \frac{3}{4\pi L_{\mathrm{max}}^3}, \tag{15}$$

where e is the elementary charge. We note that the fact that the cloud ions are screened by the photoelectrons does not imply that the photoelectrons remain bonded to the cloud after the cloud has passed the photoelectron sheath – see discussion in Appendix G. Then assuming that the cloud is effective at suppressing the return current until its number density n_{cloud} reaches the solar wind number density n_{sw}, we get the radius of the maximum extent of

$$L_{\mathrm{max}} = \left(\frac{3Q}{4\pi e n_{\mathrm{sw}}} \right)^{\frac{1}{3}}. \tag{16}$$

Then the time τ to reach this maximum extent, assuming the expansion speed of v_{ion} is

$$\tau = \frac{L_{\mathrm{max}}}{v_{\mathrm{ion}}}. \tag{17}$$

Considering Eq. (2) for relating Q and the primary peak amplitude V_{pr}, we get the relation between the primary and the secondary peak amplitudes

$$V_{\mathrm{sec}} = \frac{\Gamma j_{\mathrm{ph}} w}{2 C_{\mathrm{ant}} v_{\mathrm{ion}}} \left(\frac{3 V_{\mathrm{pr}} C_{\mathrm{sc}}}{4\pi e n_{\mathrm{sw}} \Gamma} \right)^{\frac{2}{3}}. \tag{18}$$

We note that this is a clear overestimate due to the unknown magnitude of the photoelectron screening, besides other uncertainties. Assuming $j_{\mathrm{ph}} \approx 6 \times 10^{-5}\,\mathrm{Am}^{-2}$, $\Gamma \approx 0.37$, $C_{\mathrm{ant}} \approx 60\,\mathrm{pF}$, $n_{\mathrm{sw}} \approx 10^7\,\mathrm{m}^{-3}$, $w \approx 3.8\,\mathrm{cm}$, and the rest as previously, we get

$$\frac{V_{\mathrm{sec}}}{\mathrm{V}} \approx 10 \left(\frac{V_{\mathrm{pr}}}{\mathrm{V}} \right)^{\frac{2}{3}}, \tag{19}$$

which translates to a relative amplitude ($V_{\mathrm{sec}}/V_{\mathrm{pr}}$) of a 100 in the case of $V_{\mathrm{pr}} = 1\,\mathrm{mV}$ and a relative amplitude of 21 in the case of $V_{\mathrm{pr}} = 0.1\,\mathrm{V}$. This is a far higher relative amplitude than observed, which is mostly due to the neglect of the charge screening in this estimate, as well as the ineffectiveness in liberating the photoelectrons from their suborbital trajectories around the antenna. However, a least-squares fit of the ratio $V_{\mathrm{sec}}/V_{\mathrm{pr}}$ for the strongest channel (for only the impacts that show a secondary peak) shows a slope of ≈ 0.74, which is close to the theoretical value of $2/3$; see Fig. 17. Compared to the theoretical estimate, the fit of the ratio is consistent with an additional factor of $\approx 1/10$, which would be roughly the product of the portion of impact ions that influence the antennas and the portion of photoelectrons that are liberated, once immersed in the impact cloud. We also note that the fit is influenced by the lower amplitude limit for

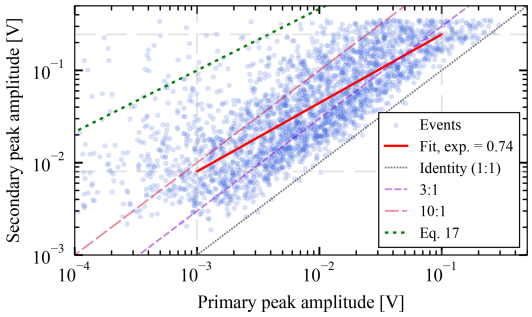

Figure 17. The estimate of the ratio V_{sec}/V_{pr} for the process responsible for the secondary peaks. Each point corresponds to one impact in which a secondary peak was observed. The least-squares fit is shown, alongside 1 : 1, 3 : 1, and 10 : 1 ratio lines and Eq. (19).

detection as well as the cutoff at 0.3V. We conclude that the Pantellini et al. (2012a) effect, as described in present work, is strong enough to explain the observed secondary amplitudes.

The ion motion provides a good explanation for the delay of the secondary peak (see discussion in Sect. 5.1), yet the Pantellini et al. process in the present form does not explain the timescale of $\gtrsim 100\,\mu s$ over which the effect lasts. This is obviously too long for electron motion dynamics but in agreement with the ion motion timescales. In the original paper of Pantellini et al. (2012a), the authors describe how the photoelectron trajectories are temporarily altered due to the presence of a relatively weak electric field of the expanding plasma cloud. This alteration suppresses the photoelectron return current for a time, so that the affected electrons orbit around the influenced antenna's axis. In order to have a longer-lasting secondary peak, as we do, a sink for the excess photoelectrons is required, so that the photoelectrons are not recollected by the antenna on the electron motion timescale, which is what is suggested by Kellogg (2017). The claim that the electrons do not return to the antenna they were emitted from is supported by Zaslavsky et al. (2012), who reported the exponential decay profile of the pulses that were believed to be caused by the Pantellini et al. process. Since the ion cloud does not provide a field strong enough to liberate a significant portion of the bounded photoelectrons to reach infinity, the sink for the photoelectrons has to be present at around the antenna potential. The only suitable sink here is provided by the spacecraft body. Since the body potential is similar to the antenna potential, the affected electrons orbiting around the antenna axis are free to migrate along the antenna axis and can reach it rather easily. Moreover, due to the BIAS subsystem of RPW, the spacecraft body is usually on a somewhat higher potential, compared to the antenna potential (Maksimovic et al., 2020). Given all this, we believe that an important portion of the affected electrons is recollected by the spacecraft's body, so the secondary peak is therefore a result of a temporarily amplified current between the affected antenna and the body. A consequence of this is that each such antenna-emitted body-collected electron is counted twice in the affected monopole channel; hence the peak is enhanced further. Also, the body potential is changed, albeit by a difference smaller by the ratio of the antenna's and the body's capacitance, which then shows synchronously in all the channels – a phenomenon that is observed reasonably often.

6 Conclusions

We studied the charge generation electrical process upon the impact of a dust particle on the surface of Solar Orbiter, as recorded with RPW electrical antennas. We found double-peak dust impact signals in about 50 % the electrical waveforms containing dust impact signatures. To the best of our knowledge, this is the first time such double-peak impact signatures were systematically observed and analyzed.

Upon inspection of the primary peak, we conclude consistence with the state-of-the-art theory for body potential influence by the impact charge. Our analysis indicates a mean impact charge magnitude of 21 pC and a median impact charge magnitude of 8 mV. We find that the rise time of the primary peak is variable and consistent with the timescale of the photoelectron sheath shielding of the impact cloud. We find the decay time consistent with the timescale of the potential equalization due to ambient charge collection. We were able to explain the small observed asymmetry between the primary peaks recorded in individual channels with electrostatic influence of antennas, on top of an otherwise symmetric peak caused by the change in body potential.

The secondary peak is found to be highly variable and very asymmetric with respect to the three channels. A relatively long delay of $\approx$ 100–300 µs with respect to the primary peak suggests that the secondary peak's presence is linked to the impact cloud moving much closer to the antennas. This delay is consistent with an ion escape velocity of 10–20 km s^{-1}. We concluded that the observed amplitudes of the secondary peak are too strong for either impact charge collection by antennas or antennas being immersed in impact cloud potential, which clearly suggests the presence of an additional effect.

We found that the assumption that the channel maxima correspond to the impact charge leads to a systematic error. We believe that the primary peak is the better measure of the impact charge, compared to the global maximum of the channel, which is more likely influenced by the often-present secondary peak. It is therefore advisable to disregard the channel which shows the highest amplitude and to study the amplitudes of the primary peaks instead – the exact procedure used in present work is described in Appendix D.

Our semi-quantitative explanation of the secondary peak's appearance uses the photoelectron sheath perturbation effect, first described in Pantellini et al. (2012a). Furthermore, we hypothesize that the Pantellini et al. (2012a) effect might temporarily enhance the current between the antenna and the spacecraft body, as this would explain the longer-lasting nature of the secondary peaks. Importantly, the amplitudes of the secondary peaks are likely related to the impact location on the spacecraft and the delay between the primary and the secondary peak provides a measure of the location and of the ion expansion speed. This is worthy of future investigation and may prove useful for identification of the dust population, which the incident dust grain came from.

Appendix A: RPW measurement modes

Table A1. The relations between the channels in different measurement modes of RPW. For compactness, $V1$; $V2$; $V3$ denote the voltages between the antenna 1; 2; 3 and the spacecraft body, respectively.

channel	SE1	DIFF1	XLD1
CH1	$V1$	$V1-V3$	$V1-V3$
CH2	$V2$	$V2-V1$	$V2-V1$
CH3	$V3$	$V3-V2$	$V2$

The Radio and Plasma Waves (RPW)electrical suite consists of three cylindrical antennas. There are three measurement modes: monopole (SE1), dipole (DIFF1), and mixed (XLD1). Whichever the mode RPW is in, it produces three channels of electrical data. See Table A1 for the modes' description and Souček et al. (2021) for much more comprehensive explanation.

Since the device spends by far the most time in XLD1 mode, it was chosen as the only mode of interest. Since the monopole data (SE1) are symmetric and the easiest to interpret, the XLD1 data are decomposed to SE1-like data for the analysis and visualization. The decomposition is performed as follows:

$$\mathrm{V1} = \mathrm{CH3} - \mathrm{CH2} \tag{A1}$$

$$\mathrm{V2} = \mathrm{CH3} \tag{A2}$$

$$\mathrm{V3} = \mathrm{CH3} - \mathrm{CH2} - \mathrm{CH1}. \tag{A3}$$

Though such decomposition provides the data user with the three reconstructed monopole channels, the user should be careful for two reasons: first, the saturation level is not clearly defined, as a difference between two saturated signals might not have been saturated otherwise, and second, the transfer function of a dipole is different to the transfer function of a monopole; hence the signal might be distorted, especially the components near the threshold frequencies. These limitations do not prohibit the analysis as described in the present publication.

Appendix B: Raw data filtering

The voltage data `WAVEFORM_DATA_VOLTAGE` of `_rpw-tds-surv-tswf-e_` are used and are only calibrated by a constant, rather than the full empirical transfer function. Since the data show a high-frequency artificial modulation at ≈ 80 and ≈ 110 kHz, the data are filtered with the Butterworth low-pass filter of 32nd order at $f_{\mathrm{lo}} = 70$ kHz, which leaves us with the temporal resolution of $\tau_{\mathrm{min}} \approx 14\,\mu$s.

According to the system's response function as measured by the RPW's engineering team, there is a significant low-frequency distortion in the < 2 kHz region. There is also a minor high-frequency distortion in the $f > 50$ kHz region, which we decided to not correct for, as its impact is very limited. The low-frequency part is corrected using Laplace-domain correction, as the very limited window length of 62 ms introduces other artifacts should the Fourier-domain correction be used. The first-order filter with the critical frequency of $f_{\mathrm{hi}} = 370$ Hz (see Eq. B1) was found to be the best fit according to the response spectrum; see Fig. B1.

$$v_{\mathrm{corr}}(t) = v_{\mathrm{orig}}(t) + 2\pi f_{\mathrm{hi}} \int_0^t v(\tau)\mathrm{d}\tau \tag{B1}$$

As a result, the corrected signal stays well corrected in the range of 500 Hz $< f <$ 70 kHz. We note that higher-order effects might be present as well, which, along with the error we introduce when dividing a small value by another, place a limit on the reliability of the low frequencies below 500 Hz. For the spectra before and after the corrections, see Fig. B2. For the signal before and after the corrections applied, see Fig. B3; pay attention to the overshoot attenuated and the secondary overshoot eliminated.

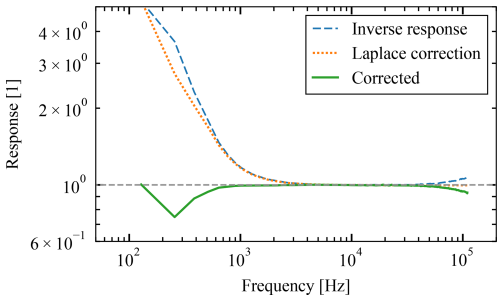

Figure B1. The RPW's response function and the Laplace-domain correction.

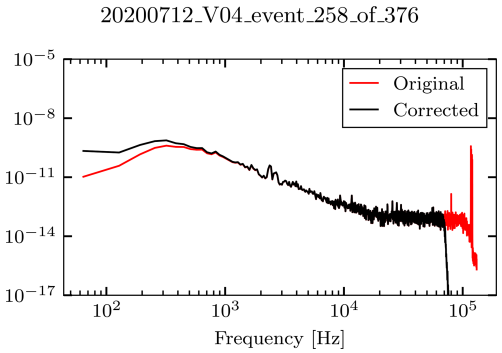

Figure B2. The spectrum of an electrical signal, before the low-pass and the Laplace corrections as well as after. We note that Laplace correction changes the signal on the low-frequency end only, while low-pass filter changes the high-frequency end.

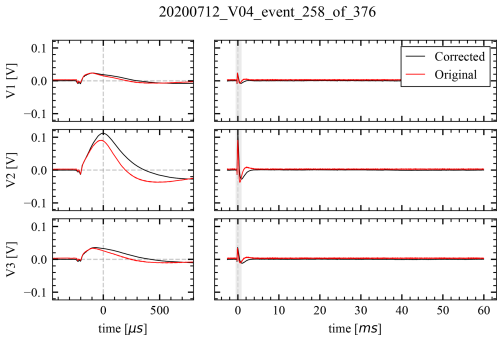

Figure B3. The waveform time series of an electrical signal, where the red line shows voltage time series before the low pass and the Laplace corrections, while the black line shows the same after the two corrections. The left-hand side shows detail of the shaded portion of the right-hand side, which in turn shows the whole recording of 62 ms.

Appendix C: Ternary plot for primary and secondary peaks

The ternary plot in Fig. 2 shows a data point for every event, with the amplitudes based on the channel global maximum. In sections starting with Sect. 2 we treat the waveforms as containing two major peaks (called primary and secondary), while the latter is not always present. Since we argue that the ternary plot (Fig. 2) shows this indirectly, it makes sense to redo the ternary plot for the XLD1 events that do and do not contain secondary peaks respectively; see Fig. C1. It is clear that the primary peaks are much more consistent across the channels, compared to the cases when secondary peaks are added.

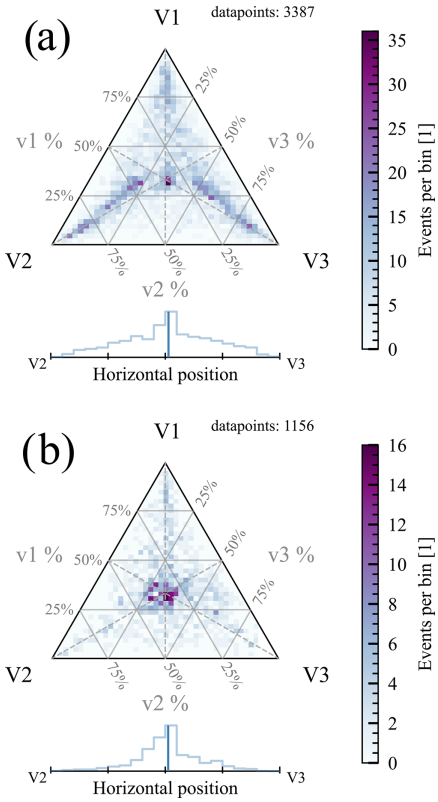

Figure C1. Ternary plot for the global maxima of the three monopole channels, one point for each XLD1 event. **(a)** The impacts that do show at a secondary peak in at least one channel and **(b)** the impacts that do not show any secondary peak in either channel.

Appendix D: Feature extraction

The signals of interest (as defined in Sect. 2.3) were analyzed as follows:

1. A positive primary peak is assumed to be present in each channel, and it is assumed to be of the same amplitude V_{body} in all the channels. The reason is that it is a rather typical case that the primary peak is obscured by a much larger peak in a close succession in at least one of the channels. Therefore, the amplitude of the primary peak is established as the mean of the amplitude of the weaker two, with the reference zero as the mean of the non-affected background signal shortly preceding the impact. The temporal location of the peak is first found approximately, using a minimum of the second derivative near the global signal maximum, and then precisely,

using a local maximum in the correlation of the signal and a one-sided parabola, which works for both distinct peaks and inflection points. The pre-spike and body locations are identified as demonstrated in Fig. D1.

2. The rise time of the primary peak is evaluated as the time to get from 43 % to 80 % of the maximum amplitude, assuming zero on the preceding background level. This range (37 %) corresponds to $1/e$ of the maximum and is chosen so that neither the flat nature of the primary peaks nor the background noise influences the estimate.

3. A secondary positive peak may or may not be present in each of the channels separately. First, primary peak is subtracted from the data in the form of asymmetric Gaussian peak with the rise time $\tau_{\text{rise}}^{\text{body}}$ given by the data and the decay time $\tau_{\text{decay}}^{\text{body}}$ assumed to be equal to $3\tau_{\text{rise}}^{\text{body}}$, as that is found to be a good approximation in cases where no secondary peak is present. Second, the secondary peak is considered present if the signal after the subtraction of the primary peak shows a maximum of amplitude of at least 75 % of the primary peak. Then amplitudes of the present secondary peaks (after primary peak subtraction) are measured. See this step shown in Fig. D2.

4. The decay time of the primary peak is only evaluated on the channel with the lowest global maximum and is done so as the time in takes the signal to decay from 100 % to 63 %, that is $1/e$. Here we evaluate the decay time closer to the maximum as the undershoot effects and the possible secondary peak influence the result much more than the flat nature of the primary peak or the noise.

5. A negative pre-peak may or may not be present and is assumed to be of the same amplitude in all three channels. The presence is decided by a 3σ criterion with regard to the noise. If the peak is found present, the amplitude of the primary peak is corrected by this value in the last step.

Given that in most cases the primary peak is not the channel maximum, careful analysis is advised, as opposed to the assumption that the channel maximum is proportional to the amount of generated charge. However, the secondary peak is only present in one of the channels, therefore assuming that the lowest of the three maxima to be proportional to the amount of generated charge leads to a systematic error that is a lot lower and is advised if a more careful approach is not an option.

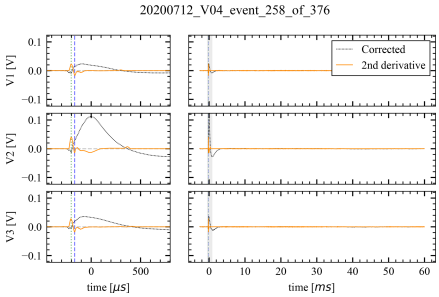

Figure D1. The waveform time series of an electrical signal. The dotted black line shows the voltage signal after the spectral corrections, while the yellow line shows the second derivative. The vertical dashed green and blue lines show the locations of the negative pre-spike and the primary peak, respectively. The left-hand side shows detail of the shaded portion of the right-hand side, which in turn shows the whole recording of 62 ms.

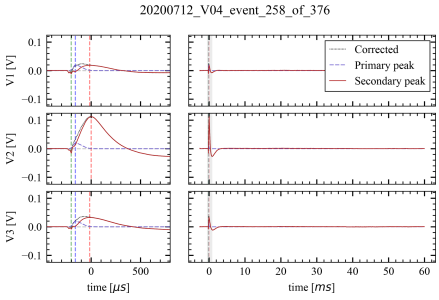

Figure D2. The waveform time series of an electrical signal. The dotted black line shows the voltage signal after the spectral corrections, while the dashed blue line shows the approximated primary peak. The primary peak is subtracted from the measured signal, and the residual is plotted as the red line. The vertical dashed green, blue, and red lines show the locations of the negative pre-spike, the primary peak, and the secondary peaks respectively. The left-hand side shows detail of the shaded portion of the right-hand side, which in turn shows the whole recording of 62 ms.

Appendix E: Primary peaks' amplitude distribution

In Sect. 4.1 we report on the amplitudes of the primary peaks that are connected to the amount of charge liberated at dust impacts. See Fig. E1 for the normalized histogram of the amplitudes. We note that no signals with global maxima over 300 mV are included, which also disqualifies the signals with $V_{\text{body}} < 300$ mV provided that the secondary peak is over the threshold – leading to underestimation of high amplitude ($\gtrsim 100$ mV) counts. Also, given the secondary peak is often of the highest amplitude present, recognition of low-amplitude primary peaks is conditioned by the presence of a secondary peak. Therefore, the presence of small primary

peaks ($\lesssim 10$ mV) is underestimated by a factor that is hard to evaluate. The former bias is more apparent in the black line of Fig. E1, while the latter is more apparent in the light-blue line of the same figure.

We note that, contrary to the distribution of global maxima of the signal on an arbitrary monopole (Zaslavsky et al., 2021), the distribution of the primary peaks' amplitudes does not resemble a power law. This is not a basis to claim that the power law is not present in the distribution of amplitudes, or by extension masses, as there is selection bias present, as was mentioned previously.

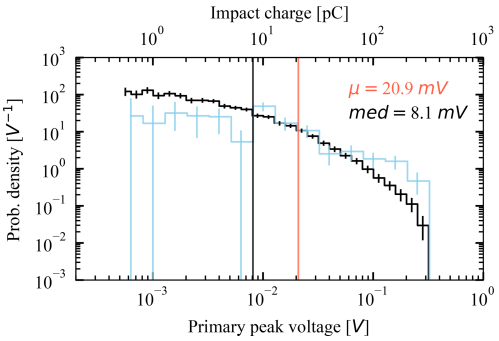

Figure E1. Histogram (normalized) of the primary peak amplitudes of all the signals in black; the mean and median are also shown. A separate normalized histogram of only those hits that do not show a secondary peak in any channel is shown in light blue. The vertical error bars represent the 90 % confidence intervals obtained by bootstrapping. The conversion from the peak voltage to the impact charge is $V/Q = 10^9\, V/C$.

Appendix F: Primary peak asymmetry – the model for antennas' response to a point charge

The model assumes antennas in a plane that are made of thin wire and are 6.5 m long. A response of these antennas to a test charge is calculated, alongside the calculation of the spacecraft's body response to the same charge as by Eq. (2). In order to produce samples of signal responses, the model samples charge locations (impact spots) from a plane parallel with the antenna plane and 1 m in front of the antenna plane, in the rectangle of 2.4 m by 3.1 m, which approximately coincides with the size and the relative location of the Solar Orbiter's heat shield; see Fig. F1. The potential of an antenna is integrated numerically as the average field along the antenna, according to equations in Sect. 3.3.1. The value of λ_D is assumed infinite; hence Eq. (5) is simplified to

$$\Phi = \frac{Q}{4\pi\epsilon}\frac{1}{|\boldsymbol{x}-\boldsymbol{x}_q|}. \tag{F1}$$

The `ch1`, `ch2`, and `ch3` are calculated as the sum of the respective antenna's response with the spacecraft body's response, since the body detects negative, while antennas detect positive charge. We note that a simplification is present: the maxima of the peak of the body response and the peak of the antenna response are typically not synchronous, yet we treat them as such in order to evaluate the ratios of the channel maxima shown in Fig. 6.

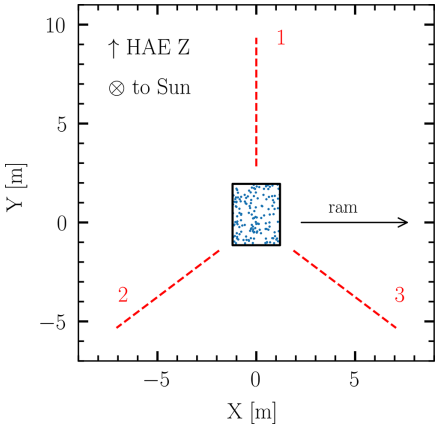

Figure F1. The Solar Orbiter's heat shield (black rectangle) and the RPW antennas (dashed red) viewed from behind, as used for the purpose of the antennas' response to a point charge modeling – sampling illustrated.

Appendix G: Impact cloud potential and photoelectron temperature

The photoelectrons near the illuminated areas of the spacecraft provide a relatively dense ($\approx 10^8\,\mathrm{m}^{-3} = 100\,\mathrm{cm}^{-3}$) region of free negative charges (Meyer-Vernet et al., 2017), with the corresponding photoelectron Debye length of $\lambda_{ph} \approx 0.29-0.98$ m at the heliocentric distance of $R = 0.25-1$ AU (Guillemant et al., 2013). The photoelectron sheath is therefore effective at screening the escaping positive impact cloud from the spacecraft body after it has passed sufficiently far from the body, which is indeed the process that seems to control the rise time of the primary peak; see Sect. 4.2 and Meyer-Vernet et al. (2017). However, the cloud escapes the vicinity of the spacecraft, and it is not straightforward to determine whether it will do so neutralized by the photoelectrons it was exposed to or not. A possible estimate is done by comparing the typical photoelectron energy with the potential barrier the predominantly positive ion cloud poses for them. Should the photoelectrons be relatively cold, compared to the depth of the potential hole of the cloud, they are likely to be captured and hence to neutralize the cloud. Should the

photoelectrons be much more energetic than the ion cloud potential hole, they are likely to screen only and to not be bounded by the cloud, therefore not neutralizing it.

An order-of-magnitude photoelectron energy may be done by comparing the incident UV photon energy ($\approx 10\,\mathrm{eV}$) and the spacecraft's surface material work function ($\approx 4\,\mathrm{eV}$), yielding the typical photoelectron energy of 6 eV near the surface. Guillemant et al. (2013) used the mean photoelectron energy at emission of 3 eV and 10 eV in their numerical estimates of the spacecraft charging. The kinetic energy of an electron at its maximum extent from the antenna is very low. Let our order-of-magnitude estimate be $T_{\mathrm{ph}} = 3\,\mathrm{eV}$.

For an order-of-magnitude estimate of the ion cloud's potential, let us assume spherical expansion of the cloud and a uniform distribution of the charge within the cloud. Assuming the most extreme case, that is the cloud made of cations only, the mean charge of the cloud is $Q \approx 21\,\mathrm{pC}$ (see Sect. 4.1). Then, the potential Φ within the cloud of radius R at the distance from the center of r is readily obtained as

$$\Phi = \frac{1}{4\pi\epsilon_0}\frac{r^2 Q}{R^3}. \tag{G1}$$

The maximum potential is present at the edge of the cloud ($r = R$); that is

$$\Phi_{\max} = \frac{1}{4\pi\epsilon_0}\frac{Q}{R}, \tag{G2}$$

which numerically is

$$\Phi_{\max} \approx \frac{0.2\,\mathrm{Vm}}{R}, \tag{G3}$$

or

$$\Phi_{\max}(R = 10\,\mathrm{cm}) \approx 2\,\mathrm{V}; \tag{G4}$$

$$\Phi_{\max}(R = 1\,\mathrm{m}) \approx 0.2\,\mathrm{V}. \tag{G5}$$

We see that the simple order-of-magnitude estimate shows that the potential within the impact cloud drops below the photoelectron energy well within 10 cm of expansion, suggesting that one may neglect it in calculating the photoelectron current collected by the cloud.

Code and data availability. The code and the data, including the waveforms for all the identified dust impacts, are available at (Kočiščák, 2023). The underlying CNN data are accessible at (Kvammen, 2022). The underlying RPW electrical waveform data files can be accessed at the Solar Orbiter/RPW data archive: https://rpw.lesia.obspm.fr/roc/data/pub/solo/rpw/data/L2/tds_wf_e/ (last access: 8 September 2023; made available by the Solar Orbiter/RPW Investigation team – M. Maksimovic, PI).

Author contributions. Concept: SK, AZ, JV, AT. Data providers: JS, DP, AK. Data analysis: SK, AZ. Interpretation: SK, AZ, NMV, JV, AT, IM. Manuscript preparation: SK.

Competing interests. At least one of the (co-)authors is a member of the editorial board of *Annales Geophysicae*. The peer-review process was guided by an independent editor, and the authors also have no other competing interests to declare.

Disclaimer. Publisher's note: Copernicus Publications remains neutral with regard to jurisdictional claims made in the text, published maps, institutional affiliations, or any other geographical representation in this paper. While Copernicus Publications makes every effort to include appropriate place names, the final responsibility lies with the authors.

Acknowledgements. The work was partially done during Samuel Kočiščák's stay with LESIA, OBSPM, and Samuel Kočiščák is thankful for the hospitality. Authors sincerely appreciate the support of the Solar Orbiter/RPW Investigation team. This work made use of publicly available data provided by Andreas Kvammen at Kvammen (2022). Andreas Kvammen and Samuel Kočiščák were supported by the Tromsø Research Foundation under grant 19-SG-AT. Ingrid Mann was supported by the Research Council of Norway under grants 262941 and 275503. Andreas Kvammen was supported by the Research Council of Norway under grant 326039. Jan Souček, David Píša, and Jakub Vaverka were supported by the Czech Science Foundation under grant 22-10775S. The publication charges for this article have been partially funded by a grant from the publication fund of UiT The Arctic University of Norway. The authors appreciate the constructive feedback provided by Zoltan Sternovsky and an anonymous referee.

Financial support. This research has been supported by the Tromsø Forskningsstiftelse (grant no. 19-SG-AT), the Norges Forskningsråd (grant nos. 262941 and 275503), and the Grantová Agentura České Republiky (grant no. 22-10775S).

Review statement. This paper was edited by Peter Wurz and reviewed by Zoltan Sternovsky and one anonymous referee.

References

Auer, A. and Sitte, K.: Detection technique for micrometeoroids using impact ionization, Earth Planet. Sc. Lett., 4, 178–183, 1968.

Bale, S., Goetz, K., Harvey, P., et al.: The FIELDS instrument suite for Solar Probe Plus: measuring the coronal plasma and magnetic field, plasma waves and turbulence, and radio signatures of solar transients, Space Sci. Rev., 204, 49–82, 2016.

Bale, S. D., Ullrich, R., Goetz, K., Alster, N., Cecconi, B., Dekkali, M., Lingner, N., Macher, W., Manning, R. E., McCauley, J., Monson, S. J., Oswald, T. H., and Pulupa, M.: The electric antennas for the STEREO/WAVES experiment, in: STEREO Mission, Springer New York, 529–547, https://doi.org/10.1007/978-0-387-09649-0_17, 2008.

Collette, A., Grün, E., Malaspina, D., and Sternovsky, Z.: Micrometeoroid impact charge yield for common spacecraft materials, J. Geophys. Res.-Space, 119, 6019–6026, 2014.

Collette, A., Meyer, G., Malaspina, D., and Sternovsky, Z.: Laboratory investigation of antenna signals from dust impacts on spacecraft, J. Geophys. Res.-Space, 120, 5298–5305, 2015.

Collette, A., Malaspina, D., and Sternovsky, Z.: Characteristic temperatures of hypervelocity dust impact plasmas, J. Geophys. Res.-Space, 121, 8182–8187, 2016.

Eichhorn, G.: Analysis of the hypervelocity impact process from impact flash measurements, Planet. Space Sci., 24, 771–781, 1976.

ESA: ESA Science Satellite Fleet – Solar Orbiter 3D model, https://scifleet.esa.int/model/solar_orbiter (last access: 19 March 2023), 2023.

Friichtenicht, J.: Micrometeroid simulation using nuclear accelerator techniques, Nucl. Instrum. Methods, 28, 70–78, 1964.

Friichtenicht, J., Roy, N., and Becker, D.: The Cosmic Dust Analyzer: experimental evaluation of an impact ionization model, in: International Astronomical Union Colloquium, Vol. 13, 299–310, Cambridge University Press, https://doi.org/10.1017/S0252921100049216, 1971.

Guillemant, S., Génot, V., Velez, J.-C. M., Sarrailh, P., Hilgers, A., and Louarn, P.: Simulation study of spacecraft electrostatic sheath changes with the heliocentric distances from 0.044 to 1 AU, IEEE T. Plasma Sci., 41, 3338–3348, 2013.

Gurnett, D. A., Grün, E., Gallagher, D., Kurth, W., and Scarf, F.: Micron-sized particles detected near Saturn by the Voyager plasma wave instrument, Icarus, 53, 236–254, 1983.

Henri, P., Meyer-Vernet, N., Briand, C., and Donato, S.: Observations of Langmuir ponderomotive effects using the Solar TErrestrial RElations Observatory spacecraft as a density probe, Phys. Plasmas, 18, 082308, https://doi.org/10.1063/1.3622667, 2011.

Juhász, A. and Horányi, M.: Dynamics and distribution of nanodust particles in the inner solar system, Geophys. Res. Lett., 40, 2500–2504, 2013.

Kellogg, P. J.: Note on the Pantellini et al. process for dust impact signals on spacecraft, J. Geophys. Res.-Space, 122, 63–70, 2017.

Kellogg, P. J., Bale, S., Goetz, K., and Monson, S. J.: Toward a physics based model of hypervelocity dust impacts, J. Geophys. Res.-Space, 126, e2020JA028415, https://doi.org/10.1029/2020JA028415, 2021.

Kočiščák, S.: SamuelKo1607/solo_dust_2023: first public, Zenodo [data set and code], https://doi.org/10.5281/zenodo.8325050, 2023.

Kočiščák, S., Fredriksen, Å., DeLuca, M., Pavlů, J., and Sternovsky, Z.: Effective temperatures of olivine dust impact plasmas, IEEE T. Plasma Sci., 48, 4298–4304, 2020.

Kočiščák, S., Kvammen, A., Mann, I., Sørbye, S. H., Theodorsen, A., and Zaslavsky, A.: Modeling Solar Orbiter dust detection rates in the inner heliosphere as a Poisson process, Astron. Astrophys., 670, A140, https://doi.org/10.1051/0004-6361/202245165, 2023.

Kvammen, A.: AndreasKvammen/ML_dust_detection: v1.0.0, Zenodo [data set and code], https://doi.org/10.5281/zenodo.7404457, 2022.

Kvammen, A., Wickstrøm, K., Kociscak, S., Vaverka, J., Nouzak, L., Zaslavsky, A., Rackovic Babic, K., Gjelsvik, A., Pisa, D., Soucek, J., and Mann, I.: Machine learning detection of dust impact signals observed by the Solar Orbiter, Ann. Geophys., 41, 69–86, https://doi.org/10.5194/angeo-41-69-2023, 2023.

Le Chat, G., Issautier, K., Zaslavsky, A., Pantellini, F., Meyer-Vernet, N., Belheouane, S., and Maksimovic, M.: Effect of the interplanetary medium on nanodust observations by the solar terrestrial relations observatory, Sol. Phys., 290, 933–942, 2015.

Maksimovic, M., Bale, S., Chust, T., et al.: The solar orbiter radio and plasma waves (RPW) instrument, Astron. Astrophys., 642, A12, https://doi.org/10.1051/0004-6361/201936214, 2020.

Malaspina, D., Horányi, M., Zaslavsky, A., Goetz, K., Wilson III, L., and Kersten, K.: Interplanetary and interstellar dust observed by the Wind/WAVES electric field instrument, Geophys. Res. Lett., 41, 266–272, 2014.

Mann, I., Murad, E., and Czechowski, A.: Nanoparticles in the inner solar system, Planet. Space Sci., 55, 1000–1009, 2007.

Mann, I., Meyer-Vernet, N., and Czechowski, A.: Dust in the planetary system: Dust interactions in space plasmas of the solar system, Phys. Rep., 536, 1–39, 2014.

Mann, I., Nouzák, L., Vaverka, J., Antonsen, T., Fredriksen, Å., Issautier, K., Malaspina, D., Meyer-Vernet, N., Pavlů, J., Sternovsky, Z., Stude, J., Ye, S., and Zaslavsky, A.: Dust observations with antenna measurements and its prospects for observations with Parker Solar Probe and Solar Orbiter, Ann. Geophys., 37, 1121–1140, https://doi.org/10.5194/angeo-37-1121-2019, 2019.

McBride, N. and McDonnell, J.: Meteoroid impacts on spacecraft:: sporadics, streams, and the 1999 Leonids, Planet. Space Sci., 47, 1005–1013, 1999.

Meyer-Vernet, N.: Detecting dust with electric sensors in planetary rings, comets and interplanetary space, in: Spacecraft Charging Technology, edited by: Harris, R. A., 476, 635–643, https://ui.adsabs.harvard.edu/abs/2001ESASP.476..635M (last access: 1 January 2023), 2001.

Meyer-Vernet, N., Moncuquet, M., Issautier, K., and Lecacheux, A.: The importance of monopole antennas for dust observations: Why Wind/WAVES does not detect nanodust, Geophys. Res. Lett., 41, 2716–2720, 2014.

Meyer-Vernet, N., Moncuquet, M., Issautier, K., and Schippers, P.: Frequency range of dust detection in space with radio and plasma wave receivers: Theory and application to interplanetary nanodust impacts on Cassini, J. Geophys. Res.-Space, 122, 8–22, 2017.

Nouzák, L., Hsu, S., Malaspina, D., Thayer, F., Ye, S.-Y., Pavlů, J., Němeček, Z., Šafránková, J., and Sternovsky, Z.: Laboratory modeling of dust impact detection by the Cassini spacecraft, Planet. Space Sci., 156, 85–91, 2018.

Nouzák, L., Sternovsky, Z., Horányi, M., Hsu, S., Pavlů, J., Shen, M.-H., and Ye, S.-Y.: Magnetic field effect on antenna signals induced by dust particle impacts, J. Geophys. Res.-Space, 125, e2019JA027245, https://doi.org/10.1029/2019JA027245, 2020.

Oberc, P.: Electric antenna as a dust detector, Adv. Space Res., 17, 105–110, 1996.

O'Shea, E., Sternovsky, Z., and Malaspina, D.: Interpreting dust impact signals detected by the STEREO spacecraft, J. Geophys. Res.-Space, 122, 11–864, 2017.

Page, B., Bale, S. D., Bonnell, J., Goetz, K., Goodrich, K., Harvey, P. R., Larsen, R., MacDowall, R. J., Malaspina, D. M., Pokorný, P., Pulupa, M., and Szalay, J. R.: Examining dust directionality with the Parker solar probe FIELDS instrument, Astro-

phys. J. Suppl. Ser., 246, 13 pp., https://doi.org/10.3847/1538-4365/ab5f6a, 2020.

Pantellini, F., Belheouane, S., Meyer-Vernet, N., and Zaslavsky, A.: Nano dust impacts on spacecraft and boom antenna charging, Astrophys. Space Sci., 341, 309–314, 2012a.

Pantellini, F., Landi, S., Zaslavsky, A., and Meyer-Vernet, N.: On the unconstrained expansion of a spherical plasma cloud turning collisionless: Case of a cloud generated by a nanometre dust grain impact on an uncharged target in space, Plasma Phys.Contr. F., 54, 045005, https://doi.org/10.1088/0741-3335/54/4/045005, 2012b.

Pantellini, F., Le Chat, G., Belheouane, S., Meyer-Vernet, N., and Zaslavsky, A.: On the detection of nano dust using spacecraft based boom antennas, in: AIP Conference Proceedings, Vol. 1539, 414–417, American Institute of Physics, https://doi.org/10.1063/1.4811073, 2013.

Poppe, A. and Lee, C.: The effects of solar wind structure on nanodust dynamics in the inner heliosphere, J. Geophys. Res.-Space, 125, e2020JA028463, https://doi.org/10.1029/2020JA028463, 2020.

Poppe, A. and Lee, C.: The effects of solar cycle variability on nanodust dynamics in the inner heliosphere: Predictions for future STEREO A/WAVES measurements, J. Geophys. Res.-Space, 127, e2022JA030317, https://doi.org/10.1029/2022JA030317, 2022.

Racković Babić, K., Zaslavsky, A., Issautier, K., Meyer-Vernet, N., and Onić, D.: An analytical model for dust impact voltage signals and its application to STEREO/WAVES data, Astron. Astrophys., 659, 10 pp., https://doi.org/10.1051/0004-6361/202142508, 2022.

Schippers, P., Meyer-Vernet, N., Lecacheux, A., Kurth, W. S., Mitchell, D. G., and André, N.: Nanodust detection near 1 AU from spectral analysis of Cassini/Radio and Plasma Wave Science data, Geophys. Res. Lett., 41, 5382–5388, 2014.

Schippers, P., Meyer-Vernet, N., Lecacheux, A., Belheouane, S., Moncuquet, M., Kurth, W., Mann, I., Mitchell, D., and André, N.: Nanodust detection between 1 and 5 AU using Cassini wave measurements, Astrophys. J., 806, 77, https://doi.org/10.1088/0004-637X/806/1/77, 2015.

Shen, M. M., Sternovsky, Z., Garzelli, A., and Malaspina, D. M.: Electrostatic model for antenna signal generation from dust impacts, J. Geophys. Res.-Space, 126, e2021JA029645, https://doi.org/10.1029/2021JA029645, 2021a.

Shen, M. M., Sternovsky, Z., Horányi, M., Hsu, H.-W., and Malaspina, D. M.: Laboratory study of antenna signals generated by dust impacts on spacecraft, J. Geophys. Res.-Space, 126, e2020JA028965, https://doi.org/10.1029/2020JA028965, 2021b.

Shen, M. M., Sternovsky, Z., and Malaspina, D. M.: Variability of Antenna Signals From Dust Impacts, J. Geophys. Res.-Space, 128, e2022JA030981, https://doi.org/10.1029/2022JA030981, 2023.

Souček, J., Píša, D., Kolmašová, I., Uhlíř, L., Lan, R., Santolík, O., Krupar, V., Kruparova, O., Baše, J., Maksimovic, M., et al.: Solar orbiter radio and plasma waves–time domain sampler: In-flight performance and first results, Astron. Astrophys., 656, 9 pp., https://doi.org/10.1051/0004-6361/202140948, 2021.

Vaverka, J., Pellinen-Wannberg, A., Kero, J., Mann, I., De Spiegeleer, A., Hamrin, M., Norberg, C., and Pitkänen, T.: Potential of earth orbiting spacecraft influenced by meteoroid hypervelocity impacts, IEEE T. Plasma Sci., 45, 2048–2055, 2017.

Vaverka, J., Pavlů, J., Nouzák, L., Šafránková, J., Němeček, Z., Antonsen, T., Mann, I., and Lindqvist, P.-A.: Ion Cloud Expansion after Hyper-velocity Dust Impacts Detected by the Magnetospheric Multiscale Mission Electric Probes in the Dipole Configuration, Astrophys. J., 921, 127, https://doi.org/10.3847/1538-4357/ac1944, 2021.

Ye, S.-Y., Vaverka, J., Nouzák, L., Sternovsky, Z., Zaslavsky, A., Pavlů, J., Mann, I., Hsu, H.-W., Averkamp, T. F., Sulaiman, A. H., Pisa, D., Hospodarsky, G. B., Kurth, W. S., and Horanyi, M.: Understanding Cassini RPWS antenna signals triggered by dust impacts, Geophys. Res. Lett., 46, 10941–10950, https://doi.org/10.1029/2019GL084150, 2019.

Ye, S.-Y., Averkamp, T., Kurth, W., Brennan, M., Bolton, S., Connerney, J., and Joergensen, J.: Juno Waves detection of dust impacts near Jupiter, J. Geophys. Res.-Planet., 125, e06367, https://doi.org/10.1029/2019JE006367, 2020.

Zaslavsky, A.: Floating potential perturbations due to micrometeoroid impacts: Theory and application to S/WAVES data, J. Geophys. Res.-Space, 120, 855–867, 2015.

Zaslavsky, A., Meyer-Vernet, N., Mann, I., Czechowski, A., Issautier, K., Le Chat, G., Pantellini, F., Goetz, K., Maksimovic, M., Bale, S., and Kaspe, J. C.: Interplanetary dust detection by radio antennas: Mass calibration and fluxes measured by STEREO/WAVES, J. Geophys. Res.-Space, 117, A05102, https://doi.org/10.1029/2011JA017480, 2012.

Zaslavsky, A., Mann, I., Souček, J., Czechowski, A., Píša, D., Vaverka, J., Meyer-Vernet, N., Maksimovic, M., Lorfèvre, E., Issautier, K., Rackovic Babic, K., Bale, S. D., Morooka, M., Vecchio, A., Chust, T., Khotyaintsev, Y., Krasnoselskikh, V., Kretzschmar, M., Plettemeier, D., Steller, M., Štverák, Š., Trávníček, P., and Vaivads, A.: First dust measurements with the Solar Orbiter Radio and Plasma Wave instrument, Astron. Astrophys., 656, 13 pp., https://doi.org/10.1051/0004-6361/202140969, 2021.

Paper IV: On the distribution of the near-solar bound dust grains detected with Parker Solar Probe

S. Kočiščák, A. Theodorsen, and I. Mann
submitted to Astronomy and Astrophysics on 9.8.2024
GitHub: SamuelKo1607/psp_dust_2024

Astronomy & Astrophysics manuscript no. output
August 9, 2024

On the distribution of the the near-solar bound dust grains detected with Parker Solar Probe

S. Kočiščák[1,⋆], A. Theodorsen[1], and I. Mann[1]

Department of Physics and Technology, UiT The Arctic University of Norway, 9037, Tromsø, Norway

Received Month DD, YYYY; accepted Month DD, YYYY

ABSTRACT

Context. Parker Solar Probe (PSP) counts dust impacts in the near-solar region, but modelling effort is needed to understand the dust population's properties.
Aims. We aim to constrain the dust cloud's properties based on the flux observed by PSP.
Methods. We develop a forward-model for the bound dust detection rates using the formalism of 6D phase space distribution of the dust. We apply the model to the location table of different PSP's solar encounter groups. We explain some of the near-perihelion features observed in the data as well as the broader characteristic of the dust flux between 0.15 AU and 0.5 AU. We compare the measurements of PSP to the measurements of Solar Orbiter (SolO) near 1 AU to expose the differences between the two spacecraft.
Results. We found that the dust flux observed by PSP between 0.15 AU and 0.5 AU in post-perihelia can be explained by dust on bound orbits and is consistent with a broad range of orbital parameters, including dust on circular orbits. However, the dust number density as a function of the heliocentric distance and the scaling of detection efficiency with the relative speed are important to explain the observed flux variation. The data suggest that the slope of differential mass distribution δ is between 0.14 and 0.49. The near-perihelion observations, however, show the flux maxima, which are inconsistent with the circular dust model, and additional effects may play a role. We found indication that the sunward side of PSP is less sensitive to the dust impacts, compared to the other PSP's surfaces.
Conclusions. We show that the dust flux on PSP can be explained by non-circular bound dust and the detection capabilities of PSP. The scaling of flux with the impact speed is especially important, and shallower than previously assumed.

Key words. cosmic dust – Parker Solar Probe – Solar Orbiter – phase-space distribution

1. Introduction

The Parker Solar Probe (*PSP*) (Fox et al. 2016) and Solar Orbiter (*SolO*) (Müller et al. 2020) space missions are currently exploring the inner Solar System, conducting in-situ measurements on an unprecedented scale and traversing regions never before reached by space probes. Through remote and in-situ detections, they among others also enable unprecedented observations of the innermost region of the interplanetary dust cloud. Most of the interplanetary dust cloud originates from the asteroids and the comets of the solar system and it is observed in the Zodiacal light and its inner extension into the solar corona, called F-corona (see Koschny et al. (2019) for a recent review). While there were only a few in-situ measurements of dust within 1 AU, this changed with SolO and PSP because their experiments investigating plasma waves with antenna measurements: FIELDS (Bale et al. 2016) on PSP and RPW (Maksimovic et al. 2020) on SolO are also sensitive to dust impacts. Earlier analyses of impact measurements of PSP (Szalay et al. 2020, 2021; Malaspina et al. 2020) and SolO (Zaslavsky et al. 2012; Kočiščák et al. 2023) showed that the observation included mainly dust in hyperbolic trajectories, which were carried away from the Sun due to the effect of the radiation pressure force, and dust in bound orbits determined by gravity. The hyperbolic grains, which are pushed outward as a result of the radiation pressure force are often denoted as β-meteoroids, since for those particles the ratio β of the radiation pressure force F_{rp} and the gravity force F_g is roughly 0.5 or larger. Their motion is the typical central force problem, while the effective gravity force the grains are subjected to is reduced by a factor of $(1 - \beta)$. Electromagnetic forces seem to have little influence in comparison, or affect only a small fraction of the dust (Mann & Czechowski 2021). It is assumed that the observed dust is created by dust-dust collisions near the Sun. This would imply that the relative amount of β-meteoroids compared to dust in bound orbits decreases with increasing proximity to the Sun. We therefore investigate whether the observed dust fluxes in the close vicinity of the Sun can be due to dust in bound orbits. We also compare the dust fluxes that are observed with SolO and PSP.

The work is structured as follows: in Sec. 2, we present Parker Solar Probe and Solar Orbiter and the previous results of other authors. We present the principle and the limitations of dust detection with electrical antennas in Sec. 3 along with the the data from the two spacecraft, which we use in later analysis. In Sec. 4, we compare the dust measurements of the two spacecraft near 1 AU. In Sec. 5 we introduce the parametric forward model, which we use to explain the features observed in the dust flux measured by Parker Solar Probe in Sec. 6. We discuss the implications of the results in Sec. 7 and in Sec. 8 we summarize.

⋆ samuel.kociscak@uit.no

2. Parker Solar Probe and Solar Orbiter

2.1. Dust detection with Parker Solar Probe

PSP orbits the Sun on highly eccentric orbits between 0.05 AU and 1 AU. The orbital parameters change significantly during gravity assists, but remain nearly identical between the assists, forming several distinct orbital groups of nearly identical orbits. PSP has made 20 orbits around the Sun so far. PSP was found to be sensitive to impacts of dust grains on the spacecraft body (Szalay et al. 2020; Malaspina et al. 2020; Page et al. 2020) thought the measurements of its FIELDS antenna suite (Bale et al. 2016). In addition to the electrical antennas, dust phenomena were observed with the Wide-Field Imager for Parker Solar Probe (*WISPR*) (Stenborg et al. 2021; Malaspina et al. 2022) and dust possibly damaged the Integrated Science Investigation of the Sun (*IS⊙IS*) instrument (Szalay et al. 2020).

It was found that the dust detection can be successfully modelled as a combination of bound dust and β-meteoroids (Szalay et al. 2021). During the initial orbits, most impacts were attributed to β-meteoroids. However, during the later orbits, in post-perihelia, where the relative speed between β-meteoroids and the PSP is low, the dust counts are sometimes likely to be dominated by bound dust. The β value depends greatly on the grain's size and β-meteoroids have the typical size of $100\,\mathrm{nm} \lesssim d \lesssim 1\,\mu\mathrm{m}$, since this is where β has its maximum (Kimura et al. 2003). The Lorentz force is negligible for β-meteoroids and boud dust, due to the low $Q/m < 1 \times 10^{-7}\,\mathrm{e/m_p}$ (Czechowski & Mann 2010).

The size of the grains detected with antennas is estimated only indirectly. Based on the impact charge yields measured in laboratory hypervelocity experiments, and in combination with estimates of dust impact speed for individual dust populations based on first principles modelling, Szalay et al. (2021) estimated the lower size radius limit for detections as a function of time. They found that during the orbits $8-16$ of PSP, the bound dust grains were detected as small as $r \gtrsim 300\,\mathrm{nm}$ near perihelia and $r \gtrsim 2\,\mu\mathrm{m}$ near aphelia, while the β-meteoroids were detected as small as $r \gtrsim 100\,\mathrm{nm}$ during most of the orbit, except for post-perihelia, where the threshold was close to $r \gtrsim 1\,\mu\mathrm{m}$. We note that while $r = 100\,\mathrm{nm}$ is close to the lower size limit of β-meteoroids, $r = 1\,\mu\mathrm{m}$ is close to the upper size limit.

Szalay et al. (2021) observed a clear double peak structure with a minimum in perihelion during the orbits 4, 5, and 6 of PSP. The minimum was anticipated and at least partially explained by Szalay et al. (2020) as being due to alignment between the nearly-circular speed of bound dust and purely azimuthal speed of PSP in the perihelion. Szalay et al. (2021) also explained the post-perihelion maximum as being potentially due to the encounter between PSP and the hypothesized Geminids β-stream produced by the collisions between the bound dust cloud and the Gemminids meteoroid stream.

2.2. Dust detection with Solar Orbiter

PSP's observations of the inner zodiacal cloud are unique, and the closest available comparable observations are those of Solar Orbiter (Mann et al. 2019). Similarly to PSP, SolO is equipped with electrical antennas of its Radio and Plasma Waves (*RPW*) instrument (Maksimovic et al. 2020), which registers dust impact on the body of the spacecraft through their electrical signatures (Soucek et al. 2021). Compared to PSP, Solo experiences much lower radial speed, and with its perihelia of about 0.3 AU, it doesn't go nearly as close to the Sun. Unlike PSP, the dust flux SolO measures is always dominated by β-meteoroids (Zaslavsky et al. 2021; Kočiščák et al. 2023). Those were concluded to have the radius of $r \gtrsim 100\,\mathrm{nm}$ (Zaslavsky et al. 2021) and $\beta \gtrsim 0.5$ (Kočiščák et al. 2023).

2.3. Components of the observed dust flux

One of the difficulties in explaining the observed flux is that several populations contribute to the detections (Mann et al. 2019; Szalay et al. 2020, 2021; Kočiščák et al. 2023), and therefore one must assume several components of the impact rate, which greatly decreases the fidelity of parameter estimation. As was debated by Szalay et al. (2020), bound dust and β-meteoroids are the main contributors to the dust flux on PSP. Interstellar dust grains (Mann 2010) were not yet reported by either of the spacecraft, but their presence in data is likely, even if they are a minor contributor to the overall detection counts.

A model for the β-meteoroid flux observed by both spacecraft must be currently built on many assumptions, as there are many unknowns to the population of β-meteoroids. Any differences between the fluxes might be attributed to the properties of the population, or to the differences between the two spacecraft, which are numerous. The β-meteoroids population was studied extensively by these (Szalay et al. 2021; Zaslavsky et al. 2021; Kočiščák et al. 2023) and by other spacecraft (Zaslavsky et al. 2012; Malaspina et al. 2014). Although we focus on the bound dust component, constraining this will implicitly provide information on β-meteoroids, since they together make up the detected flux.

Bound dust grains are in bound orbits, and therefore have both positive and negative heliocentric speeds. In the special case of a circular orbit, the dust grain has zero heliocentric component of speed. β-meteoroids are on outbound trajectories, with each of them having a positive heliocentric speed. The proportion of β-meteoroids is the highest, when the spacecraft has negative heliocentric speed. Conversely, the proportion of impacts of bound dust to all impacts is the highest when PSP's radial speed is positive. The relative speed between PSP and bound dust is approximated well by PSP's radial speed (Szalay et al. 2020), which was between $32\,\mathrm{kms^{-1}}$ and $72\,\mathrm{kms^{-1}}$ during the orbital groups $1-5$ between 0.15 AU and 0.5 AU. The relative speed between PSP and β-meteoroids depends on their outward speed and the creation region, and was in tens of km/s in the outbound legs of the studied orbits.

Szalay et al. assumed perfectly circular bound dust trajectories with $\beta = 0$ and β-meteoroids originating at $R_0 = 5R_{sun}$ and having $\beta = 0.5$. Under these assumptions, they found the relative speed between PSP and bound dust to be higher at $0.15\,\mathrm{AU} < R < 0.5\,\mathrm{AU}$ for the 6th and subsequent orbits, compared to β-meteoroids. A two-component fit to the data performed by (Szalay et al. 2021) is consistent with the flux of bound dust being higher than the flux of β for $0.15\,\mathrm{AU} < R < 0.5\,\mathrm{AU}$ during the 6th orbit. In fact, the fit suggests that bound dust flux is more than a decade higher than in β-meteoroid flux for the 6th perihelion's outbound leg at $R = 0.2$ AU. Although the exact numbers and distances are model specific, the general trend is clear: the bound dust flux is higher than β-meteoroid flux for a good portion of the post-perihelion passage, especially for the orbit six and the later orbits.

3. Measurement technique

3.1. Antenna dust detection

When a dust grain collides with a spacecraft at a speed, which exceeds a few km/s, the impact is followed by a release of a plume of quasi-neutral charge cloud (Friichtenicht 1962). The amount of this charge depends on many factors, most importantly the grain's material and mass, and the impact speed. Depending on the spacecraft and the surrounding environment, a portion of the charge is collected by the spacecraft and the rest escapes from its vicinity. This process, which usually happens in μs, may be detected with fast measurements of electrical antennas, if such measurement is present. In this way, electrical antennas performing fast measurements act as dust detectors, while the whole surface of the spacecraft's body is potentially sensitive to the impacts.

The configuration of the antennas, their location with respect to the impact site, and the material of the spacecraft surface are among the factors, which influence the detection efficiency the most (Shen et al. 2023; Collette et al. 2014). Both the FIELDS instrument of PSP and the RPW instrument SolO are equipped with multiple thick cylindrical antennas close to their respective sun-facing heat shields (Bale et al. 2016; Maksimovic et al. 2020). Some of these antennas operate in the monopole configuration for both spacecraft, in which the voltage is measured between the antenna and the spacecraft body. This is the preferable configuration for dust detection, since it makes the body a more sensitive target (Meyer-Vernet et al. 2014), in comparison to dipole antennas. In dipole configuration, voltage is measured between two antennas, and such measurement is not directly sensitive to the potential of the body.

Since detections are recorded on the body of the spacecraft, the effective cross section of the body is important to establish. One of the differences between PSP and SolO is the shape. The body of SolO, excluding the solar panels, has a rough cuboid shape (ESA 2023). The body of PSP, excluding the solar panels, has more cylindrical shape (Garcia 2018). The difference between a cuboid and a cylinder is of no consequence to dust modelling within the plane of ecliptics, but is a factor if there is an inclination between the spacecraft's trajectory and that of the dust.

3.2. PSP's potential

The potential of the spacecraft has influence on the amplitude of the generated signal, which was studied in laboratory previously (Collette et al. 2016; Shen et al. 2023), and this affects the detection efficiency. In the absence of a direct measurement, the floating potential of PSP can be approximated by the average of the DC voltages V_i between the antenna i and the spacecraft (Bale et al. 2020). If the antennas are on the local plasma potential, then the antennas measure voltage between the spacecraft body and the ambient plasma. The dependence of the spacecraft potential on the heliocentric distance is shown in Fig. 1. To reduce the amount of data to show, points were drawn uniformly randomly from the first 30 months of the mission and the potential was inferred this way, using `DFB_WF_DC` data product of FIELDS (Malaspina et al. 2016). There are many factors beyond the heliocentric distance, which influence the final potential (Guillemant et al. 2012, 2013). Even still, one can see that the potential is mostly positive outside of 0.3 AU, close to zero at around 0.2 AU, and changing suddenly inward of 0.15 AU. The potential of the TPS heat shield is presumably different again, since its sunward side is not conductively coupled to the spacecraft, as is discussed in Sec. 3.3. Nevertheless, this data suggests that the dust detection process does not change significantly with the heliocentric distance, if the spacecraft is outside of 0.15 AU. This distance coincides with the distance of $\approx$ 0.16 AU, inside which the heat shield was estimated to become conductively coupled to the spacecraft body (Diaz-Aguado et al. 2021). These two distances are possibly related.

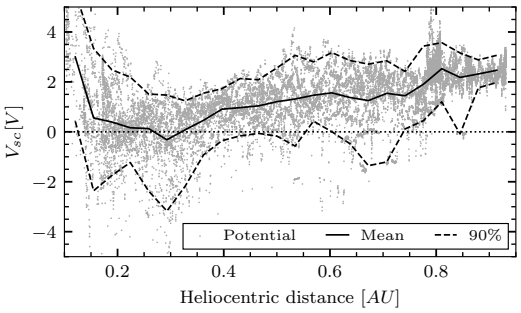

Fig. 1: Spacecraft potential estimated as the average of four *DC* antenna measurements.

3.3. Influence of the heat shield

Both PSP and SolO are protected against the extreme near-solar conditions by heat shields. The heat shields have different surface materials than the rest of the spacecraft. The sunward side of PSP's heat shield (Thermal Protection System — *TPS*) is, in addition, on a different potential to the rest of the body. These both influence dust detection. The sunward side of PSP's heat shield is made of alumina, which is non-conductive nor is it conductively connected to the spacecraft body (Reynolds et al. 2013; Diaz-Aguado et al. 2021). The shield only becomes conductively coupled to the spacecraft body through plasma currents, once the spacecraft is inside of $\approx$ 0.16 AU (Diaz-Aguado et al. 2021). The sunward side of SolO's heat shield is made of titanium and is conductively coupled to the rest of the spacecraft body (Damasio et al. 2015). The heat shields are exposed to dust impacts and even impacts on the non-conductive heat shield of PSP generate impact plasma (Shen 2021), which is potentially identified in the antenna measurements. Unlike impacts in the spacecraft parts connected conductively with the body ground, impacts on the heat shield only produce dipole response, which is more directionally dependent (Shen et al. 2023) and generally weaker (Mann et al. 2019). Moreover, the amount of charge generated by impacts on the PSP's heat shield is comparably lower, with respect to other common spacecraft materials, see Fig. 2.

3.4. Data

In the present work, we use the data of FIELDS-detected dust counts along the trajectory of PSP, made available by Malaspina et al. (2023). The data are built on the `TDSmax` data product of the FIELDS instrument (Bale et al. 2016), and assume that all the fast electrical phenomena strong enough in the monopole measurement detected over quiet enough periods of time contain dust impacts. This was demonstrated to be a good approximation of

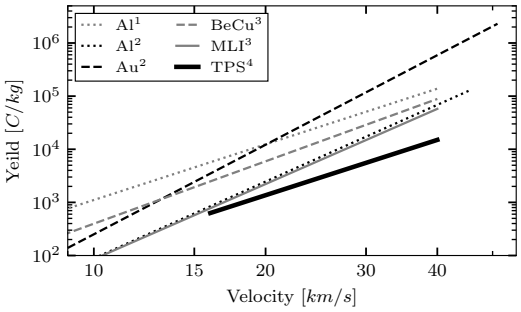

Fig. 2: Mass-normalized impact charge yield for several common spacecraft materials, assuming 10^{-14} kg dust. TPS stands for PSP's Thermal Protection System and MLI stands for the multilayer insulation of Solar Terretrial Relations Observatory (STEREO). References: 1 – McBride & McDonnell (1999), 2 – Grün (1984), 3 – Collette et al. (2014), 4 – Shen (2021). All experiments were done with iron grains.

the actual dust count, with about 10.5 % false positive rate and about 7 % miss rate (Malaspina et al. 2023). The data are structured in intervals of 8 h, and contain the impact count in the time interval corrected for under-counting. The data also contain the total effective observation time in the 8 h interval, corrected for the time then wave activity made dust detection ineffective. The data product is described in detail by Malaspina et al. (2023). The data from the orbits 1 – 16, and, therefore from the first five orbital groups are examined.

In addition to the PSP data, we also use SolO dust data. SolO detects dust with the electrical antennas of RPW instrument, and we use the convolutional neural network (*CNN*) data product provided by (Kvammen 2022). The data product builds on the data set of time-domain sampled triggered electrical waveform data and was shown to have a low false positive error rate of about 4 % and about 3 % of miss rate (Kvammen et al. 2022).

4. PSP and SolO dust flux comparison

Although SolO and PSP have very different orbits at any given time, a direct comparison of dust fluxes can be done for several points near 1 AU, where the two spacecraft had a similar heliocentric distance and speed — albeit at different times and different helio-ecliptic latitudes. Six such time intervals were found and are listed in Tab. 1. Three of these are in pre-perihelion, with negative heliocentric radial speed ($v_r < 0$) and three are in post-perihelion ($v_r > 0$). In pre-perihelion, the ram direction of the spacecraft lies between azimuthal and sunward. The proportion of impacts on the heat shield is likely higher, than in post-perihelion, when the ram-direction lies between azimuthal and anti-sunward.

We compare the 14-day average flux F during the six alignments (7 days before and 7 days after the alignment), and the comparison is shown in Fig. 3. The flux implied by SolO is by a factor of two to three higher than the flux implied by PSP. Since the flux per unit area and time are compared, the ratio depends on the cross sections, which are here assumed 6.11 m^2 and 10.34 m^2 for PSP and SolO respectively. A part of the difference might be due to the difference between instruments and detection algorithms, leading to a different size sensitivity. The detection algorithm on PSP's FIELDS for example applies a signal threshold of 50 mV (Malaspina et al. 2023), which has to be surpassed, in order for detection to count. This threshold, in combination with the dust speed and mass distribution, influences the total detected counts.

One can see from Fig. 3 that the relative detection rate of PSP with respect to SolO is higher in post-perihelia than in pre-perihelia. Unlike PSP, SolO's body is covered with conductive materials on all sides. If SolO is assumed to be equally sensitive to dust impacts from all sides, this implies that the sunward side of PSP is less sensitive than the rest of the spacecraft. This is possibly related to the non-conductive nature of the PSP's heat shield. A less sensitive heat-shield would also contribute to the lower overall flux through reducing the effective cross section of PSP.

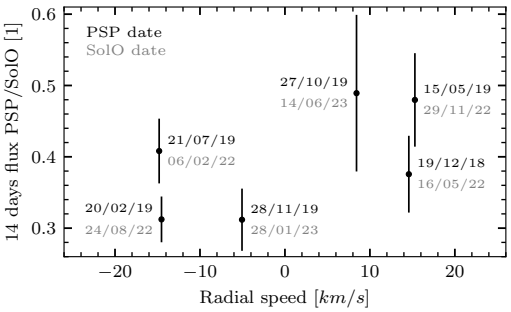

Fig. 3: Comparison of the 14 days cumulative flux (centered at the indicated day) observed with PSP and with SolO during their near alignments. The error bars are $\pm\sigma$, bootstrapped assuming Poisson distribution. See Tab. 1 for the heliocentric locations, velocity components and fluxes corresponding to the individual points.

5. Description of the model

In this section, we present a parametric model for bound dust detection rate on a spacecraft, which we will use to explain some of the observed features of the impact rate recorded on PSP. The model is built using the formalism of 6D distribution function over space $\boldsymbol{r} = (x, y, z)$ and velocity $\boldsymbol{v} = (v_x, v_y, v_z)$: $f(\boldsymbol{r}, \boldsymbol{v}) = f(x, y, z, v_x, v_y, v_z)$, similarly to how this is done in plasma theory. A single population of bound dust is assumed. The dust number density $n(\boldsymbol{r})$ is evaluated as

$$n(\boldsymbol{r}) = \iiint_{\mathbb{R}^3} f(x, y, z, v_x, v_y, v_z)\, dv_x\, dv_y\, dv_z, \tag{1}$$

where the unit of n is $[n] = m^{-3}$. The flux $j(\boldsymbol{r})$ as measured by the spacecraft is evaluated as the first moment of relative speed between the spacecraft and the dust. For example, the flux through a stationary test loop oriented perpendicular to the x-axis is

$$j_x(\boldsymbol{r}) = \iiint_{\mathbb{R}^3} |v_x| f(x, y, z, v_x, v_y, v_z)\, dv_x\, dv_y\, dv_z, \tag{2}$$

where the unit of j_x is $[n] = m^{-3}s^{-1}$. The model in this form does not include the distribution of masses, and merely assumes all the dust grains are detected on contact with the spacecraft,

Table 1: Near alignments of speed and heliocentric distance between PSP and SolO.

PSP date	R [AU]	λ [°]	v_r [km s^{-1}]	v_ϕ [km s^{-1}]	F [m^{-2} h^{-1}]	SolO date	R [AU]	λ [°]	v_r [km s^{-1}]	v_ϕ [km s^{-1}]	F [m^{-2} h^{-1}]
27/10/19	0.886	316	7.9	17.7	0.13	14/06/23	0.878	66	8.9	22.5	0.27
28/11/19	0.911	335	−5.1	17.3	0.12	28/01/23	0.928	99	−5.0	21.6	0.38
19/12/18	0.785	306	15.4	19.9	0.16	16/05/22	0.821	41	13.8	25.1	0.43
20/02/19	0.785	348	−15.5	20.2	0.28	24/08/22	0.822	118	−13.7	25.7	0.89
21/07/19	0.779	348	−15.8	20.4	0.34	06/02/22	0.818	118	−13.9	25.9	0.83
15/05/19	0.760	304	16.9	20.6	0.23	29/11/22	0.785	51	13.8	25.1	0.48

regardless of the impact speed v_{impact} or grain's mass m. The focus of the model is not to explain the absolute amount of the detected dust, the model works with a multiplicative prefactor.

The spatial scaling of density $n(\boldsymbol{r})$ is assumed spherically symmetric:

$$n(\boldsymbol{r}) \propto r^{\gamma}, \tag{3}$$

where r is the distance from the Sun. This allows for the presented study of the exponent γ.

An important component of the model is the $6D$ distribution function f, which describes the dust cloud and is derived in Appendix A to be in the shape

$$f(x, y, z, v_x, v_y, v_z) = C \cdot (r v_\phi)^{\gamma} \delta(z) \delta(v_z) \delta\left(v_r \pm \tilde{v}\right), \tag{4}$$

where $\tilde{v}$ is the radial speed of dust given by

$$\tilde{v} = \frac{\sqrt{(e^2-1)\mu^2 + 2\mu v_\phi^2 r - v_\phi^4 r^2}}{v_\phi r}, \tag{5}$$

which is Eq. A.30 of Appendix A. The independent integration variable for the moments of f (such as Eq. 2) is chosen to be the dust azimuthal speed v_ϕ. The integration boundaries are then the lower-most and the higher-most speeds the dust grains might have, given their eccentricity e and the effective gravity $\mu(\beta)$. Therefore,

$$\sqrt{\frac{(1-e)\mu}{r}} < v_\phi < \sqrt{\frac{(1+e)\mu}{r}}, \tag{6}$$

which is Eq. A.33 of Appendix A.

The model captures dust's eccentricity e, inclination θ, radiation pressure to gravity ratio β, and the fraction of retrograde dust grains in the population rp. The tilt of the dust cloud is not included, as it is not higher than a few degrees (Mann et al. 2006) and therefore inconsequential for the current effort. The model can be generalized to out of ecliptics case by assuming dependence on the distance from the plane of ecliptics z. Yet, the spacecraft of interest operate very close to the ecliptic plane and the current assumption is deemed sufficient for the present study. The model is capable of capturing dependence of the flux through the surface i, denoted j_i on impact speed by evaluating a moment different from $|v_{impact}|$. In this work, we assume the dependence

$$j_i \propto v_{impact}^{\epsilon}, \tag{7}$$

where ϵ is the relative speed exponent, equivalent to $1 + \alpha\delta$ as used in several publications (Szalay et al. 2021; Zaslavsky et al. 2021; Kočiščák et al. 2023), where α is the proportionality exponent in the charge generation equation

$$q \propto m v^{\alpha}, \tag{8}$$

and δ is the slope of the mass distribution

$$n(m) \propto m^{-\delta}. \tag{9}$$

The model treats all the parameters $e; \theta; \beta; rp; \gamma; \epsilon$ as single values (degenerate distributions). This can be, owing to the linearity, generalized to a sum of terms approximating an arbitrary distribution of these parameters, if desired. The model might in principle deal with an arbitrary shape of the spacecraft, but since the spacecraft of interest is PSP, a cylindrical shape with the axis pointing towards the Sun is assumed.

Practically, the model evaluates the flux on the spacecraft, given the position and the speed of the spacecraft, and is therefore straight-forward to use the model to generate flux profiles starting with a position table of the spacecraft of interest, which is presently PSP.

The derivation of the equations and a detailed discussion of the model is in Appendix A. Namely: in Sec. A.1, the assumptions on the distribution function f are explained, and in Sec. A.2, the orbital dynamics equations are laid out, which are needed to integrate the flux. The integration is done in Sec. A.3 and normalization of the flux to a known number density at 1 AU is explained in Sec. A.4. Sec. A.5 examines the assumption of power-law scaling of perihelia dust density, which is an important assumption for the derivation. The model from Sec. A.1 – A.5 includes the free parameters $e; \beta; \gamma$, and in Sec. A.6 we generalize the model to account for the remaining parameters $\theta; rp; \epsilon$.

6. Observed flux and model results

In this section, we compare the post-perihelion data of each orbit with the results of the model for orbital parameters representing each of the encounter groups. These are described in Appendix B. We choose the post-perihelion region for two reasons. First, the bound dust impacts are more frequent than those of β-meteoroids in this region. Second, if the sunward side of PSP is less sensitive to dust impacts, this matters the least in post-perihelia, since the sunward side is less exposed. We study post-perihelia outward of 0.15 AU, since inward the dust detection process might change, as the properties of PSP change close to the Sun, as well as to avoid the possible dust depletion zone. In the next step, we also study the near-perihelion minimum of flux observed in the data to see, which features of the dust cloud included in the model might cause the dip.

6.1. Scaling of the flux with distance

One of the features which the model should reproduce is the scaling of the observed flux with the heliocentric distance. In this section, we compare the model results to the data in the region between 0.15 AU and 0.5 AU, where the flux is dominated by bound dust impacts.

Inspection of the data shows that, with the exception of the first orbital group, which has its perihelion outside of 0.15 AU, the flux scales approximately as $j \propto R^{-2.5}$ over the outbound leg of each orbit. This is shown in Fig. 4. A variation is observed between individual orbits within the same orbital group, which was previously attributed to the stochastic nature of the dust cloud (Malaspina et al. 2020).

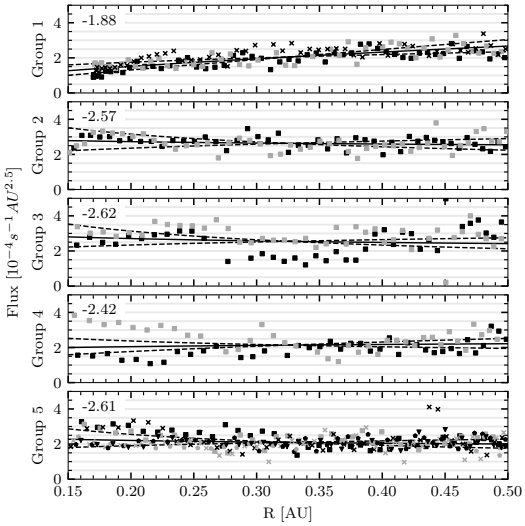

Fig. 4: The flux as detected by PSP in the outbound part of each orbit, compensated by $R^{-2.5}$, grouped by orbital groups. Individual encounters within a group are distinguished by markers of different shape or color. The solid lines are the power-law least squares fits to the observed flux, exponent of which is shown in the top left corner of each panel. To demonstrate the approximate accuracy of the $R^{-2.5}$ scaling, the dashed lines are the power-law fits of the data, with the exponent offset by ±0.3 from the least squares fit.

The base model is considered: $e = 0; \theta = 0; rp = 0; \beta = 0; \gamma = -1.3; \epsilon = 1$. This is in line with the assumption of particles on circular orbits, with no inclination, no radiation pressure, without retrograde grains, and with spatial number density scaling as $n \propto R^{-1.3}$ and the assumption that every grain is always detected, if impact happened: $j \propto v_{impact}$. It is found that this assumption in not compatible (Fig. 5) with the slope observed in the data (Fig. 4), since the dependence produced by the model is appreciably shallower than $\propto R^{-2.5}$.

We study, what combination of parameters changes the slope to the desired $\propto R^{-2.5}$. It is found that the parameters $e; \theta; \beta; rp$ all influence the slope in the desired direction (see Appendix C), yet even in the most favorable case, they do not suffice to explain the slope observed in the data, as is shown in Fig. 5. It is also seen from Fig. 5 that especially the flux during the later orbits is very little influenced by these four parameters. The explanation, therefore, lies at least partially in the scaling of density with the two parameters not yet varied: the heliocentric distance exponent γ and the relative speed exponent ϵ. These both influence the slope appreciably, as is seen in Figs. 7 and 8. We see that in the case of all the other parameters being equal to the base value, $\gamma \approx 3$, resp. $\epsilon \approx -3$ show nearly flat plots, and, therefore,

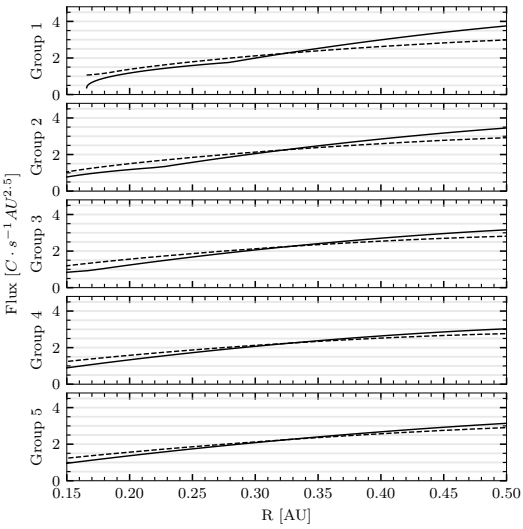

Fig. 5: The base model-predicted flux is shown in the solid line, compensated by $R^{-2.5}$. The slope is considerably shallower than $\propto R^{-2.5}$, hence the inclining trend after the compensation. The model-predicted flux in the case of $e = 0.5; \theta = 45°; rp = 10\%; \beta = 0.5; \gamma = -1.3; \epsilon = 1$ is shown in the dashed line. Even these, rather extreme, assumptions don't suffice to explain the slope observed in the data.

serve as upper estimates of the values. Many combinations of the six parameters are capable of reproducing the right slope. We therefore study the range of combinations, which reconstructs the slope acceptably well. A viable combination of parameters is shown in Fig. 9, but we note that the slope is not very sensitive to changes in $e; \theta; \beta; rp$. Viable combinations of the most influential parameters: γ and ϵ are shown in Fig. 6, where the other four parameters are included together in two cases: the base case, and the upper estimate: the dashed case from Fig. 5. Fig. 6 shows $-2 < \gamma < -1$, which is the range of expected values of γ for bound dust (Ishimoto & Mann 1998). We find our results compatible with previously reported $\gamma \approx 1.3$ (Leinert et al. 1981; Stenborg et al. 2021), in which case $2 < \epsilon < 2.5$

6.2. Near-sun profile

The model is capable of reproducing features observed in the data close to perihelia. Notably, there is a distinct minimum in the measured flux in the perihelion. This minimum was attributed to the velocity alignment between PSP and bound dust (Szalay et al. 2021), which is implicitly included in the present model as well. In this section, the near-solar flux is studied as a function of the free parameters of the model.

The observational data are shown in Fig. 10 and the near-perihelion minimum is apparent. We note that the flux is not symmetric around perihelia due to the presence of β-meteoroids in pre-perihelia, where the relative speed between them and the spacecraft is high. We focus on the post-perihelia, as we will seek the consistence between these and the model predictions. We also note that the PSP perihelia lie well inside the β-meteoroid creation region (Szalay et al. 2021), where the β-

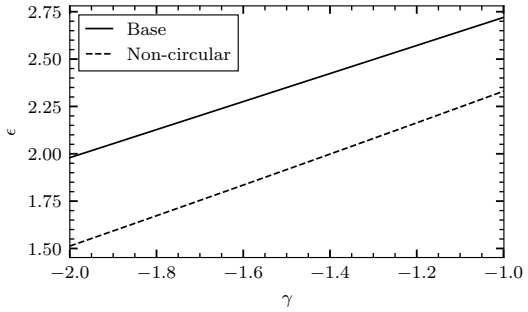

Fig. 6: The combinations of γ and ϵ which produce a profile approximately matching the slope of -2.5 in the region of $0.15\,\mathrm{AU} < R < 0.5\,\mathrm{AU}$. The base model assumes $e = 0; \theta = 0; rp = 0; \beta = 0$ and the non-circular model assumes rather extreme $e = 0.5; \theta = 45°; rp = 0.1; \beta = 0.5$.

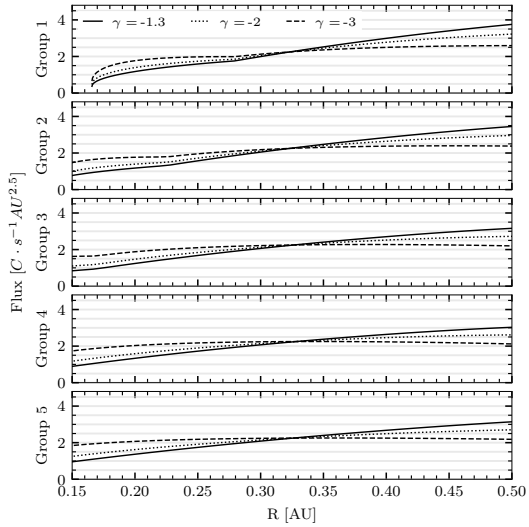

Fig. 7: The base model-predicted flux is shown in the solid line. In addition, the influence of the heliocentric distance exponent γ on the slope is demonstrated.

meteoroid grains still have an important angular momentum and their trajectories are therefore similar to the trajectories of bound dust grains, making the distinction less clear.

The base model predicted flux is shown in Fig. 11 and we note it is symmetric around the perihelia: since only the bound dust population is assumed, and the heat shield is assumed as sensitive as the rest of the spacecraft, there is nothing to cause the asymmetry. The same set of vertical lines, approximately corresponding to the heliocentric locations of the maxima are shown symmetric around the perihelia in Figs. 10 and 11. There is no post-perihelion maximum in orbital group 1, the vertical line is based solely on the pre-perihelion maximum. In case of the base model (as before, $e = 0; \theta = 0; rp = 0; \beta = 0; \gamma = -1.3; \epsilon = 1$),

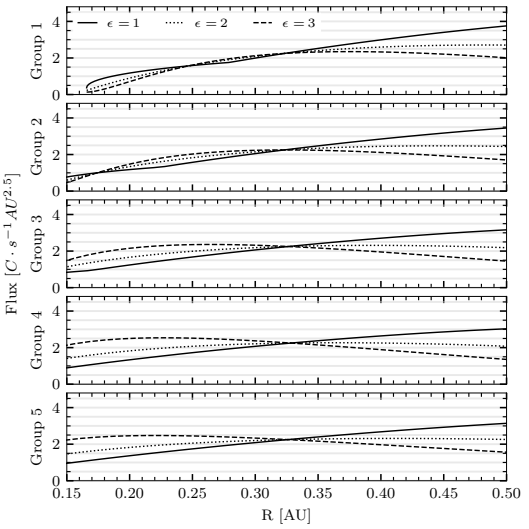

Fig. 8: The base model-predicted flux is shown in the solid line. In addition, the influence of the velocity exponent ϵ on the slope is demonstrated.

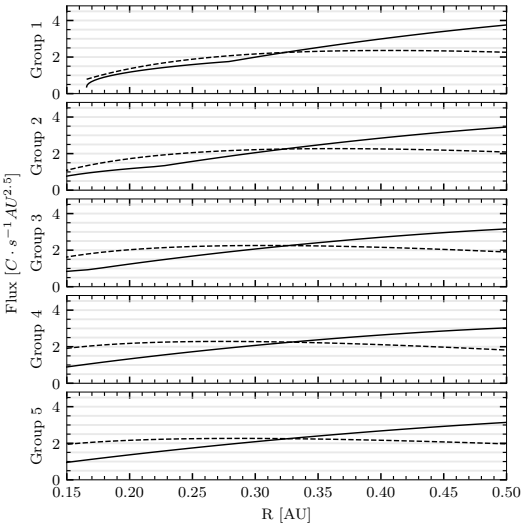

Fig. 9: The base model-predicted flux is shown in the solid line. In addition, the model with parameters: $e = 0.1; \theta = 10°; rp = 0.03; \beta = 0.05; \gamma = -1.9; \epsilon = 2$ is shown as a representative of a viable option.

the maxima in the flux are predicted decidedly closer to the perihelia than observed. It is observed in the same figure that by varying the velocity exponent ϵ the location of the expected maxima is moved, possibly to the extent that it is consistent with the data. None of the other parameters influences the location of the maxima of the flux appreciably and they are shown and dis-

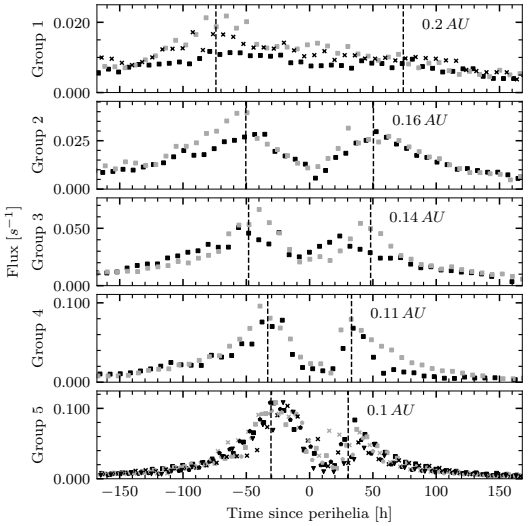

Fig. 10: The detection rate of dust impacts near the perihelia. The data from individual solar encounters are grouped according to the orbital groups. Individual encounters within a group are distinguished by markers of different shape or color.

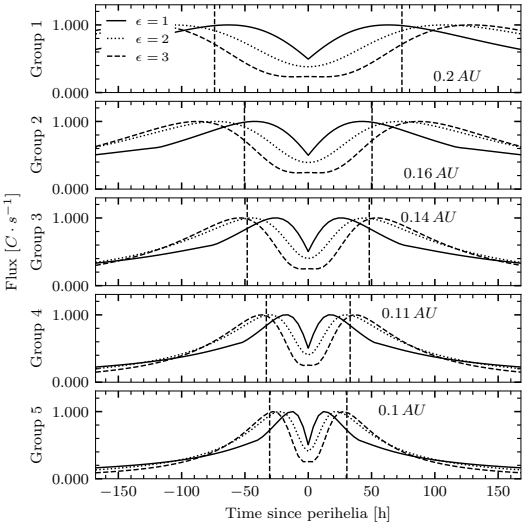

Fig. 11: The base model-predicted flux near the perihelia is shown in solid line. Different values of ϵ are shown for comparison. The same vertical dashed lines as in Fig. 10 are shown for reference.

cussed in App. D. They however do influence the relative depth of the near-perihelion flux minimum. Increasing any value except for the velocity exponent ϵ would result in a shallower perihelion dip, see the comparison on the influence of each individual parameter in App. D. We note that the dip is predicted shallower (approx. 50 % of the maximum) than observed (less than 25 % of the maximum) even in the base case.

Fig. 12 shows the same combination of parameters as Fig. 9 does, which was found reasonable and viable to explain the observed post-perihelion slope. Even with this reasonably conservative parameter choice, the perihelion dip is a lot less pronounced, due to a less sharp alignment between the spacecraft's and the dust's speed. It is also observed that ϵ is less effective at changing the position of the maxima, if other parameters are higher than in the base model. Therefore, we find it unlikely that the near perihelion dip is solely due to the velocity alignment between the dust cloud and the spacecraft.

7. Discussion

To extract physical information from the dust counts data of PSP and SolO, we performed different analyses in different heliospheric regions. In this section, we discuss our results with respect to the heliocentric distance.

7.1. *Near* 1 AU

Near 1 AU, the comparison between PSP and SolO is possible and shows that PSP detects fewer dust impacts compared to SolO (see Fig. 3), especially in pre-perihelia. This is possibly an instrumental effect of a smaller sized dust being detected more effectively with SolO. As PSP's sunward side, where the heat shield is, has a different surface material to the rest of the spacecraft, it is possibly less sensitive to dust impacts, compared to the rest of the spacecraft (see Fig. 2). This implies that β-meteoroid impacts might be underrepresented in the data, as these are more likely to impact on the heat shield side, compared to the bound dust grains. Other instrumental effects might play a role, such as the position of antennas, and/or the presence of solar panels.

Beyond the likely instrumental cause of the difference of the flux on PSP and SolO, physical explanations are possible. Small sub-micron dust with $r < 100$ nm might be influenced by electromagnetic force. It was shown for dust of radius $r \leq 30$ nm that the flux might change both with solar cycle, that is on the order of years (Poppe & Lee 2022), and with solar rotation, that is on the order of days Poppe & Lee (2020); Mann & Czechowski (2021) even in the case of a symmetric source. A similar, albeit weaker effect might play a role for $r \approx 100$ nm dust as well. The individual points in space where we compared PSP and SolO (Fig. 3) are separated by months or weeks for a given spacecraft, and pre-perihelion and post-perihelion data points alternate in time. Therefore, a possible long-term change from 2019 to 2022 does not strongly affect the result. Due to the low number of data points, we can not dismiss the possible influence of a well-timed short-term variation, which needs to be on the order of 25 % to explain the observed difference. With the low number of points, a stochastic counting error is not negligible, but the points are based on tens and hundreds of detections over 14 days each, leading to error bars smaller than the observed variance.

We note that the points of similar heliocentric distance and speed between PSP and SolO lie on different heliocentric longitudes. Localized sources of β-meteoroids (Szalay et al. 2021) or the interstellar dust (Mann 2010) might contribute to the difference observed between the spacecraft, although there are no indications of localized β-meteoroid sources at 1 AU. The perihelia of SolO in 2022 and 2023 are oriented close to the upstream direction of the interstellar dust, which means that more interstellar dust is likely present in the pre-perihelion data than in the

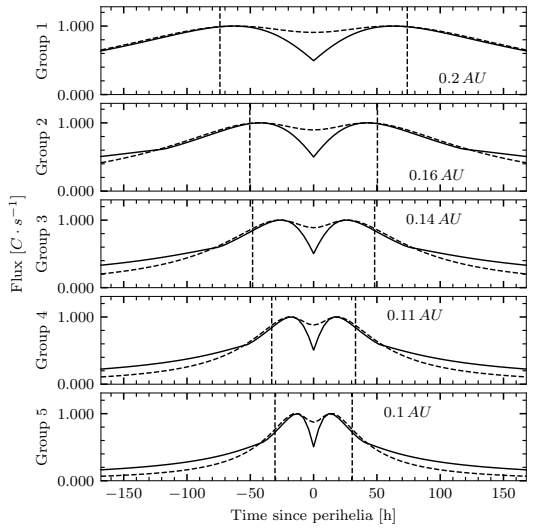

Fig. 12: The base model-predicted flux near the perihelia is shown in solid line. In addition, the model with parameters: $e = 0.1; \theta = 10°; rp = 0.03; \beta = 0.05; \gamma = -1.9; \epsilon = 2$ is shown as a representative of a viable option.

post-perihelion data. The interstellar dust flux f_{ISD} was reported to be coming from the heliocentric longitude of approximately $\lambda \approx 250°$ with the flux of $f_{ISD} < 0.036\,\mathrm{m^{-2}s^{-1}}$ between 2016 and 2020 (Racković Babić 2022). This is an order of magnitude lower than the pre-perihelia SolO fluxes reported here (Tab. B.1). Although the interstellar dust might contribute to the difference, its flux is too low to explain the whole difference.

7.2. Between 0.15 AU and 0.5 AU

Between 0.15 AU and 0.5 AU, we were looking for the solutions of a parametric bound dust model, which would explain the observed slope of the detected flux. The two lines of $\epsilon(\gamma)$ in Fig. 6 may be regarded as an upper and a lower estimate of the velocity exponent ϵ. We find that ϵ lies between 1.5 and 2.7, assuming the value of the exponent γ between -2 and -1. This is much lower then previously assumed 4.15 (Szalay et al. 2021). We note that the bound dust which contributes to the results is mostly of the μm and sub-μm size. For a reasonably conservative $\alpha \approx 3.5$ (Collette et al. 2014) in $\epsilon = 1 + \alpha\delta$, it is implied that $0.14 < \delta < 0.49$, which is a much lower value than $\delta \approx 0.9$ observed for larger dust (Grün et al. 1985; Pokorný et al. 2024). The value of α is better constrained than the value of δ. This is therefore an indication that the mass distribution may not be a single power-law in the mass range of interest and at all heliocentric distances. However, this makes sense, because of the narrow mass interval: the power-law distribution of masses was described over 20 decades of magnitude in mass (Grün et al. 1985), while PSP detects grains wihch span less than two orders of magnitude (Malaspina et al. 2023). Since the dust in question is bound, there is a necessary depletion in the small size region, as small dust ($r \lesssim 100\,\mathrm{nm}$) is not bound, due to high β. Interestingly, our value is compatible with $\delta \approx 0.34$, which was reported by Zaslavsky et al. (2021) for β-meteoroids, which are also limited in mass, and the power-law distribution of masses is therefore also problematic.

7.3. Near perihelia

We studied the compatibility between the bound dust model and the observed perihelion dip. A similar dip is formed due to the velocity alignment between the spacecraft and the bound dust, but the dip is too shallow and readily smeared out by non-zero eccentricity, inclination, or other parameters. If the near perihelion dip is not due to the velocity alignment, other factors might contribute to the dip, and we list several of them. First, the dust number density is believed to diminish closer to the Sun. A dust free zone was hypothesised to exist (Russell 1929), since the dust grains do not survive for long in the extreme conditions near the Sun. It was estimated using WISPR that a dust depletion zone enveloping the dust free zone lies inward of $19\,R_{sun} \approx 0.09$ AU and the dust free zone likely lies inward of $5\,R_{sun} \approx 0.023$ AU (Stenborg et al. 2021). Such dust depletion zone may explain the apparent depletion of dust near perihelia. The second possible explanation of the dip is the ineffective detection. The antenna detection process is very much dependent on the spacecraft's charge state and the surrounding environment (Shen et al. 2021; Racković Babić et al. 2022; Shen et al. 2023). An indication that the process changes rapidly inward of 0.15 AU is that the spacecraft's potential seems to be a steep function of the heliocentric distance in this region, potentially disturbing the otherwise effective dust detection. For example, the heat shield becoming conductively coupled to the spacecraft's body inward of ≈ 0.16 AU (Diaz-Aguado et al. 2021) also changes spacecraft's charge state. See Sec. 3.2 for the discussion of the spacecraft potential. The third possible contribution to the dip is that if the relative speed between the dust and the spacecraft is higher than a certain threshold, all the bound dust grains are detected, and therefore the flux plateaus. This would not produce the dip on its own, but would lead to a shallower growth near the Sun, compared to the case, when the proportionality of flux to $\propto v^{\epsilon}$ is assumed all the way. In addition to these three explanations, we note that the minima near the perihelia might be a result of maxima before and after the perihelia, rather then a depletion. Such maxima might result from either crossing the Geminids β-stream (Szalay et al. 2021), or the spacecraft getting more sensitive to dust impacts, possibly due to a higher potential (Fig. 1) and/or better sensitivity of the heat shield.

7.4. Further work

We developed a model to describe bound dust impact rates onto spacecraft, which work with sharp values of the free parameters, but is easily generalized to distributions. Other free parameters are feasible to be included, such as the tilt of the dust cloud with respect to the ecliptic plane, which might be useful for modelling the flux once the orbit of SolO becomes more inclined. It is straight-forward to develop a similar model for dust on hyperbolic trajectories, such as β-meteoroids or interstellar dust. The distribution of inclinations and eccentricities within β-meteoroid cloud is worthy of future investigation.

The masses are presently treated in a crude way, assuming power-law distribution of masses, which translates to the efficiency of detection. As we argue, the assumption of a power-law distributed masses might not be justified. A $7D$ distribution function describing masses, in addition to the phase space, would of-

fer a more nuanced model, but would push the limits of what information is possibly retrieved from the data.

8. Conclusions

The impact rate model, which we developed in this work, takes into account dust cloud parameters: eccentricity e, inclination i, radiation pressure to gravity ratio β, and retrograde dust fraction rp. In addition, the model takes into account semi-empirical parameters: the exponent γ of number density dependence on heliocentric distance and the exponent ϵ of the detection rate dependence on the impact speed. We compared the model results to the dust count data of the first 16 orbits of PSP.

Although the model does produce a dip in flux due to the velocity alignment between the dust and the spacecraft in the circular dust base case, but the dip is not sufficient and is smeared away easily, especially with non-zero eccentricity. The dip observed close to each of the perihelia for the third and subsequent orbits of PSP is reproduced neither as deep nor as wide by the model as is observed in the data. Therefore, other effects contribute to the dip beyond the velocity alignment, namely the dust depletion zone or instrumental effects.

The parameters of the dust cloud: e, i, β, rp all have minor influence on the model profile, while the semi-empirical parameters γ and ϵ are crucial. By varying these, we can reproduce the observed dependence of flux in the post-perihelion region on the heliocentric distance between 0.15 AU and 0.5 AU, where the influence of β dust is expected the lowest. The parameter ϵ, which represents the combined influence of dust mass distribution and impact charge production, is found lower than what was previously used for PSP dust data analysis, and likely between 1.5 and 2.7. This is consistent with the slope δ of differential mass distribution of μm and sub-μm dust between 0.14 and 0.49, which is shallower than what was reported for bigger bound dust further away from the Sun.

A comparison of the dust counts of PSP and SolO shows that PSP observed comparatively less dust in pre-perihelia than in post-perihelia, with the difference of about 25 %. This suggests that PSP's sun-facing side, and therefore the heat shield (TPS), offers a less dust sensitive target, compared to the other surfaces of PSP. Because of this instrumental effect, the observations are not incompatible with a stationary and symmetric dust cloud. However, due to the low number of data points, we can not reject the possibility that the effect is physical, possibly attributed to the short-term temporal or spatial variation of the cloud.

Acknowledgements. Author contributions: Concept: SK, AT, IM. Model development: SK, AT. Data analysis: SK, AT. Interpretation: SK, IM, AT. Manuscript preparation: SK, IM. SK and AT were supported by the Tromsø Research Foundation under the grant 19_SG_AT. This work on dust observations in the inner heliosphere received supported from the Research Council of Norway (grant number 262941 and 275503). SK appreciates the constructive discussions with Jakub Vaverka, Libor Nouzák, Jamey Szalay, Mitchell Shen, and Arnaud Zaslavsky, and the assistance of David Malaspina with interpreting the PSP dust data. The code and the data set used in this work are publicly available at `https://zenodo.org/records/13284890`.

References

Bale, S., Goetz, K., Bonnell, J., et al. 2020, arXiv preprint arXiv:2006.00776
Bale, S., Goetz, K., Harvey, P., et al. 2016, Space science reviews, 204, 49
Collette, A., Grün, E., Malaspina, D., & Sternovsky, Z. 2014, Journal of Geophysical Research: Space Physics, 119, 6019
Collette, A., Malaspina, D., & Sternovsky, Z. 2016, Journal of Geophysical Research: Space Physics, 121, 8182
Czechowski, A. & Mann, I. 2010, The Astrophysical Journal, 714, 89
Damasio, C., Defilippis, P., Draper, C., & Wild, D. 2015, in 45th International Conference on Environmental Systems ICES–2015-7612-1, Vol. 6
Diaz-Aguado, M., Bonnell, J., Bale, S., Wang, J., & Gruntman, M. 2021, Journal of Geophysical Research: Space Physics, 126, e2020JA028688
ESA. 2023, ESA Science Satellite Fleet — Solar Orbiter 3D model, accessed: 19.3.2023
Fox, N., Velli, M., Bale, S., et al. 2016, Space Science Reviews, 204, 7
Friichtenicht, J. 1962, Review of Scientific Instruments, 33, 209
Garcia, M. 2018, NASA-3D-Resources/3D Models/Parker Solar Probe, commit: 39dc094
Giese, R., Kneissel, B., & Rittich, U. 1986, Icarus, 68, 395
Grün, E. 1984, The Giotto Spacecraft Impact-induced Plasma Environment, 39
Grün, E., Zook, H. A., Fechtig, H., & Giese, R. 1985, Icarus, 62, 244
Guillemant, S., Génot, V., Matéo-Vélez, J.-C., Ergun, R., & Louarn, P. 2012, 30, 1075
Guillemant, S., Génot, V., Velez, J.-C. M., et al. 2013, IEEE Transactions on Plasma Science, 41, 3338
Ishimoto, H. & Mann, I. 1998, Planetary and space science, 47, 225
Kimura, H., Mann, I., & Jessberger, E. K. 2003, The Astrophysical Journal, 582, 846
Kočiščák, S., Kvammen, A., Mann, I., et al. 2023, Astronomy & Astrophysics, 670, A140
Koschny, D., Soja, R. H., Engrand, C., et al. 2019, Space science reviews, 215, 1
Kvammen, A. 2022, ML Dust Detection, `https://github.com/AndreasKvammen/ML_dust_detection`
Kvammen, A., Wickstrøm, K., Kociscak, S., et al. 2022, EGUsphere [preprint], 2022
Leinert, C., Richter, I., Pitz, E., & Planck, B. 1981, Astronomy and Astrophysics, 103, 177
Maksimovic, M., Bale, S., Chust, T., et al. 2020, Astronomy & Astrophysics, 642, A12
Malaspina, D., Horányi, M., Zaslavsky, A., et al. 2014, Geophysical Research Letters, 41, 266
Malaspina, D. M., Ergun, R. E., Bolton, M., et al. 2016, Journal of Geophysical Research: Space Physics, 121, 5088
Malaspina, D. M., Stenborg, G., Mehoke, D., et al. 2022, The Astrophysical Journal, 925, 27
Malaspina, D. M., Szalay, J. R., Pokorný, P., et al. 2020, The Astrophysical Journal, 892, 115
Malaspina, D. M., Toma, A., Szalay, J. R., et al. 2023, The Astrophysical Journal Supplement Series, 266, 21
Mann, I. 2010, Annual Review of Astronomy and Astrophysics, 48, 173
Mann, I. & Czechowski, A. 2021, Astronomy & Astrophysics, 650, A29
Mann, I., Köhler, M., Kimura, H., Cechowski, A., & Minato, T. 2006, The Astronomy and Astrophysics Review, 13, 159
Mann, I., Nouzak, L., Vaverka, J., et al. 2019, Annales Geophysicae, 37, 1121
McBride, N. & McDonnell, J. 1999, Planetary and Space Science, 47, 1005
Meyer-Vernet, N., Moncuquet, M., Issautier, K., & Lecacheux, A. 2014, Geophysical Research Letters, 41, 2716
Müller, D., Cyr, O. S., Zouganelis, I., et al. 2020, Astronomy & Astrophysics, 642, A1
Page, B., Bale, S. D., Bonnell, J., et al. 2020, The Astrophysical Journal Supplement Series, 246, 51
Pokorný, P., Moorhead, A. V., Kuchner, M. J., Szalay, J. R., & Malaspina, D. M. 2024, The Planetary Science Journal, 5, 82
Poppe, A. & Lee, C. 2020, Journal of Geophysical Research: Space Physics, 125, e2020JA028463
Poppe, A. & Lee, C. 2022, Journal of Geophysical Research: Space Physics, 127, e2022JA030317
Racković Babić, K., Zaslavsky, A., Issautier, K., Meyer-Vernet, N., & Onic, D. 2022, Astronomy & Astrophysics, 659, A15
Racković Babić, K. 2022, PhD thesis, Université Paris sciences et lettres; Univerzitet u Beogradu
Reynolds, E. L., Driesman, A., Kinnison, J., & Lockwood, M. K. 2013, in AIAA Guidance, Navigation, and Control (GNC) Conference, 4879
Russell, H. N. 1929, Astrophysical Journal, vol. 69, p. 49, 69, 49
Shen, M.-H. 2021, PhD thesis, University of Colorado at Boulder
Shen, M. M., Sternovsky, Z., Garzelli, A., & Malaspina, D. M. 2021, Journal of Geophysical Research: Space Physics, 126, e2021JA029645
Shen, M. M., Sternovsky, Z., & Malaspina, D. M. 2023, Journal of Geophysical Research: Space Physics, 128, e2022JA030981

Soucek, J., Píša, D., Kolmasova, I., et al. 2021, Astronomy & Astrophysics, 656, A26
Stenborg, G., Howard, R., Hess, P., & Gallagher, B. 2021, Astronomy & Astrophysics, 650, A28
Szalay, J., Pokorný, P., Bale, S., et al. 2020, The Astrophysical Journal Supplement Series, 246, 27
Szalay, J., Pokorný, P., Malaspina, D., et al. 2021, The Planetary Science Journal, 2, 185
Zaslavsky, A., Mann, I., Soucek, J., et al. 2021, Astronomy & Astrophysics, 656, A30
Zaslavsky, A., Meyer-Vernet, N., Mann, I., et al. 2012, Journal of Geophysical Research: Space Physics, 117

Appendix A: Integrating the phase-space density

Appendix A.1: Phase-space density

Assume there is a time-invariant dust density f in the usual 6D phase space:

$$f(\boldsymbol{r}, \boldsymbol{v}) = f(x, y, z, v_x, v_y, v_z), \tag{A.1}$$

which is normalized to number density as

$$n(x, y, z) = \iiint_{\mathbb{R}^3} f(x, y, z, v_x, v_y, v_z)\, dv_x\, dv_y\, dv_z, \tag{A.2}$$

which is a very useful way of looking at it, since $n(\boldsymbol{r})$ can be measured remotely for bigger ($\gtrsim 1\,\mu$m) dust grains. We note that we disregarded grain size for now, the density n represents the number density of *suitable* dust grains, whatever the suitability criteria are.

Since the Solar system near the ecliptic is our main goal, we will introduce simplifying assumptions on f:

- We assume that the plane $x \otimes y$ is the ecliptic, with $(0, 0)$ point being the Sun and assume that all the grains within the distribution move within this plane, with no pole-ward component of the speed v_z.
- We assume that the dust cloud has a rotational symmetry around the z axis, and for convenience we are going to use the density $\tilde{f}$ expressed using (r, ϕ) instead of (x, y), where $r = \sqrt{x^2 + y^2}$ and ϕ is the angle of rotation around z-axis, measured from an arbitrary ray in the ecliptic.
- We assume the dust grains don't collide. Then we make use of Liouville's theorem on the space $(\boldsymbol{r}, \boldsymbol{v})$.

The first assumption is translated to f using degenerate distributions $\delta(\cdot)$ as

$$f(x, y, z, v_x, v_y, v_z) = f(x, y, 0, v_x, v_y, 0)\delta_0(z)\delta_0(v_z). \tag{A.3}$$

The second assumption is translated using r, ϕ as

$$\begin{aligned} &f(x, y, 0, v_x, v_y, 0)\delta_0(z)\delta_0(v_z) \\ =&f(r, 0, 0, v_x, v_y, 0)\delta_0(z)\delta_0(v_z) \\ =&\tilde{f}(r, 0, 0, v_x, v_y, 0)\delta_0(z)\delta_0(v_z), \end{aligned} \tag{A.4}$$

where the first three arguments of f are all position arguments, where $\tilde{f}$ has a position, angle, and a position arguments. We also use a more compact 3D distribution f, with the meaning

$$\begin{aligned} &f(x, y, z, v_x, v_y, v_z) \\ &= \tilde{f}(r, \phi, 0, v_r, v_\phi, 0)\delta_0(z)\delta_0(v_z) \\ &\equiv f(r, v_r, v_\phi)\delta_0(z)\delta_0(v_z)\ \forall \phi \in \mathbb{R}, \end{aligned} \tag{A.5}$$

since we assumed rotational symmetry in ϕ. The third assumption has the form of

$$\begin{aligned} f(\boldsymbol{r}_1, \boldsymbol{v}_1) = f(\boldsymbol{r}_2, \boldsymbol{v}_2) \Leftrightarrow \\ f(r_1, v_{r,1}, v_{\phi,1}) = f(r_2, v_{r,2}, v_{\phi,2}) \end{aligned} \tag{A.6}$$

provided that the points $(\boldsymbol{r}_1, \boldsymbol{v}_1), (\boldsymbol{r}_2, \boldsymbol{v}_2)$ (or, alternatively expressed points $(r_1, v_{r,1}, v_{\phi,1}), (r_2, v_{r,2}, v_{\phi,2})$) share the same trajectory of the system in the phase space. We note that we use velocity, not the momentum, which is justified, since we assume the mass conservation $dm/dt = 0$ for each particle. We assume the dust cloud is composed of bound dust grains, each of them on a heliocentric orbit. Then Eq. A.6 holds for any two points of an orbit of a grain. If we assume all the grains follow the same gravity field with the effective gravitational parameter

$$\mu = (1 - \beta)\kappa M_{Sun}, \tag{A.7}$$

where β is the grain's radiation pressure to gravity ratio and κM_{Sun} is the solar gravitational parameter. Then all the grains which acquire the state of $(\boldsymbol{r}_1, \boldsymbol{v}_1)$ will also acquire the state of $(\boldsymbol{r}_2, \boldsymbol{v}_2)$, if this a valid solution for one of them. Therefore, we may study f in a convenient point of the orbit of our choice while being assured, it remains the same throughout the orbit. We are soon going to see that the perihelion of the orbit of a dust grains is a convenient point.

Appendix A.2: Orbital mechanics

To study the density f in a point of the orbit of our choice, we must describe the orbits and be able to translate between the points within the orbit. From Eq. A.6 we know that

$$f(r_{peri}, 0, v_{peri}) = f(r, v_r, v_\phi), \tag{A.8}$$

provided that the spacecraft state in perihelion $(r_{peri}, 0, v_{peri})$ shares the same orbit with a general state (r, v_r, v_ϕ). By applying the laws of orbital motion, we are going to find the relationship between the points $(r_{peri}, 0, v_{peri})$ and (r, v_r, v_ϕ). We know the angular momentum is conserved:

$$r_{peri} v_{peri} = v_\phi r \Leftrightarrow v_{peri} = \frac{v_\phi r}{r_{peri}} \Leftrightarrow r_{peri} = \frac{v_\phi r}{v_{peri}}. \tag{A.9}$$

as well as the energy is:

$$v_{peri}^2 - \frac{2\mu}{r_{peri}} = v_\phi^2 + v_r^2 - \frac{2\mu}{r}. \tag{A.10}$$

Substituting v_{peri} from the angular momentum, we get

$$\left(\frac{v_\phi r}{r_{peri}}\right)^2 - \frac{2\mu}{r_{peri}} = v_\phi^2 + v_r^2 - \frac{2\mu}{r}, \tag{A.11}$$

and multiplying by r^2 we get

$$\begin{aligned} r_{peri}^2\left(v_\phi^2 + v_r^2 - \frac{2\mu}{r}\right) + r_{peri}(2\mu) - (v_\phi^2 r^2) = 0 \\ a r_{peri}^2 + b r_{peri} + c = 0. \end{aligned} \tag{A.12}$$

The two formal solutions of this equation are

$$r_{peri} = \frac{-b \pm \sqrt{b^2 - 4ac}}{2a}, \tag{A.13}$$

where $(+)$ and $(-)$ correspond to the aphelion and perihelion respectively, since we didn't assume anything other than a stationary point yet. Hence, $(-)$ corresponds to the true r_{peri} and substituting back for a, b, c and substituting for v_{peri} from Eq. A.9 we get:

$$\begin{aligned} r_{peri} &= \frac{-b - \sqrt{b^2 - 4ac}}{2a} = \frac{-\mu - \sqrt{\mu^2 + \left(v_\phi^2 + v_r^2 - \frac{2\mu}{r}\right)(v_\phi^2 r^2)}}{\left(v_\phi^2 + v_r^2 - \frac{2\mu}{r}\right)} \\ v_{peri} &= \frac{v_\phi r}{r_{peri}}. \end{aligned} \tag{A.14}$$

These two equations are what was needed to solve Eq. A.8. However, our goal is to study different eccentricities. Since an arbitrary distribution of eccentricities is straight-forward to approximate with a linear combination of sharp-eccentricity terms, we will now focus on a sharp eccentricity e. Assuming that all the grains are not only exposed to the same effective gravity μ, but they also have the same orbital eccentricity e, it is apparent that *only one speed v_{peri} is allowed in the perihelion r_{peri}, which conforms to the eccentricity e* ($\star$). Vis-viva equation in perihelion gives

$$v_{peri} = \sqrt{\mu \frac{1+e}{r_{peri}}}. \tag{A.15}$$

Substituting for v_{peri} from Eq. A.9, we get

$$\left(\frac{v_\phi r}{r_{peri}}\right)^2 = \mu \frac{1+e}{r_{peri}}$$
$$r_{peri} = \frac{v_\phi^2 r^2}{\mu(1+e)}. \tag{A.16}$$

This equation is the bond between an arbitrary r, v_r, v_ϕ and the only corresponding r_{peri}, v_{peri} given the eccentricity e.

As a reasonable simplification (Giese et al. 1986), we assume the number density $n(x, y, z)$ in the ecliptic depends on the heliocentric distance:

$$n(x, y, z) = n(r, 0)\delta_0(z) = A\left(\frac{r}{r_0}\right)^\gamma \delta_0(z) = \delta_0(z)\frac{A}{r_0^\gamma} r^\gamma, \tag{A.17}$$

where γ is a parameter, reasonably constrained by experiment. We normalized the expression by the number density at r_0, which might be for example 1 AU. Assume this dependence ($\propto r^\gamma$) holds for the distribution of dust grains in their perihelia (see section A.5 for the discussion), which is surely an acceptable assumption, at least for low e, since at low e, the difference between r_{peri} and r_{aph} is very small.

Appendix A.3: Velocity moments' integration

The net flux of particles through the x-plane is the first speed moment

$$j_x = \iiint_{\mathbb{R}^3} v_x f(\boldsymbol{r}, \boldsymbol{v})\, dv_x\, dv_y\, dv_z. \tag{A.18}$$

The SI unit is $[j_x] = m^{-2}s^{-1}$. We are however not interested in the net flux j_x but the total flux $j_{tot,x}$ onto the plane x. For the stationary plane x, we have

$$j_{tot,x} = \int_0^\infty \iint_{\mathbb{R}^2} v_x f(\boldsymbol{r}, \boldsymbol{v})\, dv_x\, dv_y\, dv_z + \int_{-\infty}^0 \iint_{\mathbb{R}^2} -v_x f(\boldsymbol{r}, \boldsymbol{v})\, dv_x\, dv_y\, dv_z. \tag{A.19}$$

Should the probe be moving in $+x$-direction with the speed of $v_{p,x}$, the detected net flux is going to be

$$j_{tot,x} = \int_{v_{p,x}}^\infty \iint_{\mathbb{R}^2} (v_x - v_{p,x}) f(\boldsymbol{r}, \boldsymbol{v})\, dv_x\, dv_y\, dv_z - \int_{-\infty}^{v_{p,x}} \iint_{\mathbb{R}^2} (v_x - v_{p,x}) f(\boldsymbol{r}, \boldsymbol{v})\, dv_x\, dv_y\, dv_z. \tag{A.20}$$

Since we assumed all the dust being concentrated around the ecliptic plane (Eqs. A.3, A.5):

$$\begin{aligned} j_{tot,x} &= \int_{v_{p,x}}^\infty \iint_{\mathbb{R}^2} (v_x - v_{p,x}) f(r, v_r, v_\phi)\delta_0(z)\delta_0(v_z)\, dv_x\, dv_y\, dv_z \\ &- \int_{-\infty}^{v_{p,x}} \iint_{\mathbb{R}^2} (v_x - v_{p,x}) f(r, v_r, v_\phi)\delta_0(z)\delta_0(v_z)\, dv_x\, dv_y\, dv_z \\ &= \delta_0(z) \int_{v_{p,x}}^\infty \int_{\mathbb{R}} (v_x - v_{p,x}) f(r, v_r, v_\phi)\, dv_x\, dv_y \\ &- \delta_0(z) \int_{-\infty}^{v_{p,x}} \int_{\mathbb{R}} (v_x - v_{p,x}) f(r, v_r, v_\phi)\, dv_x\, dv_y. \end{aligned} \tag{A.21}$$

And since we align the x-axis with the probe, the speed $v_x = v_r$ is the radial dust speed and $v_y = v_\phi$ is the azimuthal dust speed, both in the unit of translational speed (as not to confuse with the angular speed $\dot{\phi} \neq v_\phi = r\dot{\phi}$). The flux measured on radially oriented surfaces of the probe is

$$\begin{aligned} j_{tot,rad} &= \delta_0(z) \int_{v_{p,rad}}^\infty \int_{\mathbb{R}} (v_r - v_{p,rad}) f(r, v_r, v_\phi)\, dv_r\, dv_\phi \\ &- \delta_0(z) \int_{-\infty}^{v_{p,rad}} \int_{\mathbb{R}} (v_r - v_{p,rad}) f(r, v_r, v_\phi)\, dv_r\, dv_\phi, \end{aligned} \tag{A.22}$$

and, analogically, the flux measured on the azimuthally oriented surfaces as

$$\begin{aligned} j_{tot,azim} &= \delta_0(z) \int_{\mathbb{R}} \int_{v_{p,azim}}^\infty (v_\phi - v_{p,azim}) f(r, v_r, v_\phi)\, dv_r\, dv_\phi \\ &- \delta_0(z) \int_{\mathbb{R}} \int_{-\infty}^{v_{p,azim}} (v_\phi - v_{p,azim}) f(r, v_r, v_\phi)\, dv_r\, dv_\phi, \end{aligned} \tag{A.23}$$

where $v_{p,azim}$ is the azimuthal speed of the probe (prograde, locally in $+y$-direction).

To obtain the most convenient form of f in an easily integrable shape, we use two additional pieces of information: 1. the dependence on the heliocentric distance (Eq. A.17), and 2. the fact, that Eqs. A.16 and A.14 must be demanded consistent, which is the equivalent to the ($\star$) claim. We are shortly going to integrate f over v_r and v_ϕ, as in Eqs. A.22 and A.23. We know that not all combinations of v_r, v_ϕ are possible given r, e. Instead of integrating in two dimensions, we will integrate in $v_r \otimes v_\phi$ space along the path $v_r(v_\phi)$ given by ($\star$). Hence, we relate Eqs. A.16 and A.14 with the goal of obtaining $v_r(v_\phi)$:

$$\frac{-\mu - \sqrt{\mu^2 + \left(v_\phi^2 + v_r^2 - \frac{2\mu}{r}\right)(v_\phi^2 r^2)}}{\left(v_\phi^2 + v_r^2 - \frac{2\mu}{r}\right)} = \frac{v_\phi^2 r^2}{\mu(1+e)} \tag{A.24}$$

This quadratic equation has two solutions for v_r:

$$v_r = \pm \frac{\sqrt{(e^2-1)\mu^2 + 2\mu v_\phi^2 r - v_\phi^4 r^2}}{v_\phi r} = \pm\tilde{v}, \tag{A.25}$$

These solutions correspond to the radial speeds of pre-perihelion (in-going, $v_r < 0$) and post-perihelion (out-going, $v_r > 0$) dust, as at a given r and with a given v_ϕ. Since f of the dust cloud is assumed stationary, the grains don´t collide and are in repetitive orbits, therefore there are exactly as many in-going as out-going.

Now to get a convenient shape of f, assuming separable power-law scaling with distance (consistently with Eq. A.17):

$$\begin{aligned} f(r, v_r, v_\phi) &= f(r, v_\phi)\delta(v_r \pm \tilde{v}) \\ &\propto r^\gamma \hat{f}(v_\phi)\delta(v_r \pm \tilde{v}), \end{aligned} \tag{A.26}$$

where in the first step we expressed the condition A.25 and newly used a 2D distribution f according to $f(r, v_\phi)\delta(v_r \pm \tilde{v}) = f(r, v_r, v_\phi)$ and in the second step we expressed the condition that $n(r) \propto r^\gamma$ using a new 1D $\hat{f}(v_\phi)$ and we lost the normalization. Since Liouville's theorem says that the density is the same along the trajectory of the grain, it is the same in perihelion as well, and its moments are the same, and therefore integrating over z, v_z, v_r in an arbitrary time (LHS) and in perihelion (RHS):

$$\begin{aligned} r^\gamma \hat{f}(v_\phi) &= r_{peri}^\gamma \hat{f}(v_{peri}) \\ r^\gamma \hat{f}(v_\phi) &= \left(\frac{v_\phi^2 r^2}{\mu(1+e)}\right)^\gamma \hat{f}\left(\frac{\mu(1+e)}{v_\phi r}\right) \\ r^\gamma \hat{f}(v_\phi) &= (\mu(1+e))^{-\gamma}\, v_\phi^{2\gamma} r^{2\gamma} \hat{f}\left(\frac{\mu(1+e)}{v_\phi r}\right). \end{aligned} \tag{A.27}$$

Since $\mu(1+e)$ is a plain number, and except for $\hat{f}(\dots)$ we only have r^{c_1} and $v_\phi^{c_2}$ and we demand the equality for arbitrary r, v_ϕ, the only thinkable solution for $\hat{f}$ is of the form

$$\hat{f}(x) = Cx^b, \tag{A.28}$$

therefore:

$$\begin{aligned} r^\gamma C v_\phi^b &= (\mu(1+e))^{-\gamma}\, v_\phi^{2\gamma} r^{2\gamma} C \left(\frac{\mu(1+e)}{v_\phi r}\right)^b \\ 1 &= (\mu(1+e))^{b-\gamma}\, v_\phi^{2\gamma-2b} r^{\gamma-b} \\ 1 &= \left(\frac{v_\phi^2 r}{\mu(1+e)}\right)^{\gamma-b}, \end{aligned} \tag{A.29}$$

Where the only suitable solution is $b = \gamma$. Therefore, $\hat{f}(x) = Cx^\gamma$ Eq. A.26 with Eq. A.25 give:

$$\begin{aligned} &f(r, v_r, v_\phi) = \\ &\quad = C \cdot (r v_\phi)^\gamma \delta(z)\delta(v_z)\delta(v_r \pm \tilde{v}) \\ &\quad = C \cdot (r v_\phi)^\gamma \delta(z)\delta(v_z)\delta\left(v_r \pm \frac{\sqrt{(e^2-1)\mu^2 + 2\mu v_\phi^2 r - v_\phi^4 r^2}}{v_\phi r}\right). \end{aligned} \tag{A.30}$$

The last parenthesis of this equation may be interpreted as the integration trajectory in the $v_r \otimes v_\phi$ space. Since our integration parameter of the contraction from the the $v_r \otimes v_\phi$ space to a 1D space of the path is going to be v_ϕ, we need the integration boundaries for v_ϕ. The integration boundaries are given by the lowermost and the uppermost v_ϕ the probe may encounter, given r,e. The lowest possible v_ϕ corresponds to the probe being in aphelion, whereas the highest corresponds to it being in the perihelion. We use Eq. A.25, and both in the perihelion and in the aphelion, we get $v_r = 0$, hence

$$(e^2-1)\mu^2 + 2\mu v_\phi^2 r - v_\phi^4 r^2 = 0, \tag{A.31}$$

and this quadratic equation in v_ϕ^2 has two solutions:

$$v_\phi^2 = \frac{(1 \pm e)\mu}{r}, \tag{A.32}$$

corresponding to the highest possible v_ϕ (in the case r is the perihelion) and the lowest possible (in the case r is the aphelion). Negative v_ϕ would correspond to the dust grains on retrograde orbits and are disregarded as we only want to include prograde dust grains for now. These are, therefore, our integration boundaries:

$$\sqrt{\frac{(1-e)\mu}{r}} < v_\phi < \sqrt{\frac{(1+e)\mu}{r}}. \tag{A.33}$$

We note that these correspond to the degenerate solutions of Eq. A.25, which makes sense, since Eq. A.25 defines a cyclic trajectory in the $v_r \otimes v_\phi$ space.

Radial flux

$$\begin{aligned} j_{tot,rad} &= \delta(z) \int_{v_{p,rad}}^{\infty} \int_{\mathbb{R}} (v_r - v_{p,rad}) f(r, v_r, v_\phi)\, dv_r\, dv_\phi \\ &\quad - \delta(z) \int_{-\infty}^{v_{p,rad}} \int_{\mathbb{R}} (v_r - v_{p,rad}) f(r, v_r, v_\phi)\, dv_r\, dv_\phi \\ &= \delta(z) C r^\gamma \int_{v_{p,rad}}^{\infty} \int_{\mathbb{R}} (v_r - v_{p,rad}) v_\phi^\gamma \delta(v_r \pm \tilde{v})\, dv_r\, dv_\phi \\ &\quad - \delta(z) C r^\gamma \int_{-\infty}^{v_{p,rad}} \int_{\mathbb{R}} (v_r - v_{p,rad}) v_\phi^\gamma \delta(v_r \pm \tilde{v})\, dv_r\, dv_\phi. \end{aligned} \tag{A.34}$$

The expression contains two terms: $j_{tot,rad} = \delta_0(z) C r^\gamma (j_{rad}^+ - j_{rad}^-)$, which have the boundaries $v_r > v_{p,rad}$ and $v_{p,rad} > v_r$ respectively, which corresponds to flux on the sun-facing (+) and on the anti-sunward (−) respectively. We translate these boundaries from v_r to v_ϕ in order to integrate over the parameter v_ϕ using the Heaviside function. Each of these two has two variants: post-perihelion (*post*, $v_r > 0$) and pre-perihelion (*pre*, $v_r < 0$) dust, as $\pm\tilde{v}$ in Eq. A.25. Thus, we get four integral terms, each with a prefactor of $1/2$:

$$\begin{aligned} j_{rad}^{+,pre} &= \frac{1}{2} \int_{v_{p,rad}}^{\infty} \int_{\mathbb{R}} (v_r - v_{p,rad}) v_\phi^\gamma \delta(v_r + \tilde{v})\, dv_r\, dv_\phi \\ &= \frac{1}{2} \int_{\mathbb{R}} \int_{\mathbb{R}} (v_r - v_{p,rad}) v_\phi^\gamma \delta(v_r + \tilde{v})\, H(v_r - v_{p,rad})\, dv_r\, dv_\phi \\ &= \frac{1}{2} \int_{\mathbb{R}} (-\tilde{v} - v_{p,rad}) v_\phi^\gamma H(-\tilde{v} - v_{p,rad})\, dv_\phi \\ &= \frac{1}{2} \int_{\sqrt{\frac{(1-e)\mu}{r}}}^{\sqrt{\frac{(1+e)\mu}{r}}} (-\tilde{v} - v_{p,rad}) v_\phi^\gamma H(-\tilde{v} - v_{p,rad})\, dv_\phi, \end{aligned} \tag{A.35}$$

$$\begin{aligned} j_{rad}^{+,post} &= \frac{1}{2} \int_{v_{p,rad}}^{\infty} \int_{\mathbb{R}} (v_r - v_{p,rad}) v_\phi^\gamma \delta(v_r - \tilde{v})\, dv_r\, dv_\phi \\ &= \frac{1}{2} \int_{\sqrt{\frac{(1-e)\mu}{r}}}^{\sqrt{\frac{(1+e)\mu}{r}}} (\tilde{v} - v_{p,rad}) v_\phi^\gamma H(\tilde{v} - v_{p,rad})\, dv_\phi, \end{aligned} \tag{A.36}$$

$$\begin{aligned} j_{rad}^{-,pre} &= \frac{1}{2} \int_{-\infty}^{v_{p,rad}} \int_{\mathbb{R}} (v_r - v_{p,rad}) v_\phi^\gamma \delta(v_r + \tilde{v})\, dv_r\, dv_\phi \\ &= \frac{1}{2} \int_{\sqrt{\frac{(1-e)\mu}{r}}}^{\sqrt{\frac{(1+e)\mu}{r}}} (-\tilde{v} - v_{p,rad}) v_\phi^\gamma H(\tilde{v} + v_{p,rad})\, dv_\phi, \end{aligned} \tag{A.37}$$

$$j^{-,post}_{rad} = \frac{1}{2}\int_{-\infty}^{v_{p,rad}}\int_{\mathbb{R}}(v_r - v_{p,rad})v_\phi^\gamma \delta\left(v_r - \tilde{v}\right)\, dv_r\, dv_\phi$$
$$= \frac{1}{2}\int_{\sqrt{\frac{(1-e)\mu}{r}}}^{\sqrt{\frac{(1+e)\mu}{r}}}(\tilde{v} - v_{p,rad})v_\phi^\gamma H(-\tilde{v} + v_{p,rad})\, dv_\phi, \tag{A.38}$$

where

$$\tilde{v} = \frac{\sqrt{(e^2-1)\mu^2 + 2\mu v_\phi^2 r - v_\phi^4 r^2}}{v_\phi r}, \tag{A.39}$$

and altogether:

$$j_{tot,rad} = C\delta_0(z)r^\gamma\left(j^{+,pre}_{rad} + j^{+,post}_{rad} - j^{-,pre}_{rad} - j^{-,post}_{rad}\right). \tag{A.40}$$

We note that even and odd terms are straightforward to join as the only difference is the complementary Heaviside, but in the present shape it is easy to account for different effective areas from front and from the back of the probe in this function, since front and back terms are separated. Eqs. A.35 – A.38 are straight-forward to evaluate numerically, for example with Monte Carlo integration, drawing values of v_{phi} between the boundaries (Eq. A.33).

Azimuthal flux

$$j_{tot,azim} = \delta(z)\int_{\mathbb{R}}\int_{v_{p,azim}}^{\infty}(v_\phi - v_{p,azim})f(r, v_r, v_\phi)\, dv_r\, dv_\phi$$
$$- \delta(z)\int_{\mathbb{R}}\int_{-\infty}^{v_{p,azim}}(v_\phi - v_{p,azim})f(r, v_r, v_\phi)\, dv_r\, dv_\phi,$$
$$= \delta(z)Cr^\gamma\int_{\mathbb{R}}\int_{v_{p,azim}}^{\infty}(v_\phi - v_{p,azim})v_\phi^\gamma\delta\left(v_r \pm \tilde{v}\right)\, dv_r\, dv_\phi$$
$$- \delta(z)Cr^\gamma\int_{\mathbb{R}}\int_{-\infty}^{v_{p,azim}}(v_\phi - v_{p,azim})v_\phi^\gamma\delta\left(v_r \pm \tilde{v}\right)\, dv_r\, dv_\phi \tag{A.41}$$

The expression contains two terms: $j_{tot,azim} = \delta(z)Cr^\gamma(j^+_{azim} - j^-_{azim})$, which have the boundaries $v_\phi > v_{p,azim}$ and $v_{p,azim} > v_\phi$ respectively. Since we assume prograde dust only ($v_\phi > 0$), and pre-perihelion and post-perihelion have the same effect on the azimuthal flux, there is no further multiplication of terms, as in the case of radial flux.

$$j^+_{azim} = \int_{\mathbb{R}}\int_{v_{p,azim}}^{\infty}(v_\phi - v_{p,azim})v_\phi^\gamma\delta\left(v_r \pm \tilde{v}\right)\, dv_r\, dv_\phi$$
$$= \int_{v_{p,azim}}^{\infty}(v_\phi - v_{p,azim})v_\phi^\gamma\, dv_\phi$$
$$= \int_{\max\left[\sqrt{\frac{(1+e)\mu}{r}}, v_{p,azim}\right]}^{\max\left[\sqrt{\frac{(1+e)\mu}{r}}, v_{p,azim}\right]}(v_\phi - v_{p,azim})v_\phi^\gamma\, dv_\phi$$
$$= \left[\frac{v_\phi^{\gamma+2}}{\gamma+2} - \frac{v_\phi^{\gamma+1}v_{p,azim}}{\gamma+1}\right]_{\max\left[\sqrt{\frac{(1-e)\mu}{r}}, v_{p,azim}\right]}^{\max\left[\sqrt{\frac{(1+e)\mu}{r}}, v_{p,azim}\right]}, \tag{A.42}$$

$$j^-_{azim} = \int_{\mathbb{R}}\int_{-\infty}^{v_{p,azim}}(v_\phi - v_{p,azim})v_\phi^\gamma\delta\left(v_r \pm \tilde{v}\right)\, dv_r\, dv_\phi$$
$$= \int_{-\infty}^{v_{p,azim}}(v_\phi - v_{p,azim})v_\phi^\gamma\, dv_\phi$$
$$= \int_{\min\left[\sqrt{\frac{(1+e)\mu}{r}}, v_{p,azim}\right]}^{\min\left[\sqrt{\frac{(1+e)\mu}{r}}, v_{p,azim}\right]}(v_\phi - v_{p,azim})v_\phi^\gamma\, dv_\phi$$
$$= \left[\frac{v_\phi^{\gamma+2}}{\gamma+2} - \frac{v_\phi^{\gamma+1}v_{p,azim}}{\gamma+1}\right]_{\min\left[\sqrt{\frac{(1-e)\mu}{r}}, v_{p,azim}\right]}^{\min\left[\sqrt{\frac{(1+e)\mu}{r}}, v_{p,azim}\right]}, \tag{A.43}$$

where we very liberally ignred $\delta_0(v_r \pm \ldots)$, but since we integrate in v_r over $\mathbb{R}$, it doesn't matter where exactly this mass is accounted for. Altogether we have:

$$j_{tot,azim} = \delta(z)Cr^\gamma(j^+_{azim} - j^-_{azim}), \tag{A.44}$$

which is easy and straightforward to evaluate. Finally,

$$j_{tot} = j_{tot,azim} + j_{tot,rad}. \tag{A.45}$$

Appendix A.4: Normalization

In order to normalize the flux properly to a known value of density at 1 AU in the unit of m^{-3}, we need to evaluate the number density at r_0, which might conveniently be 1 AU. If we don't do that, then Eqs. A.35 - A.38, A.42, A.43 all vary as $\propto 2\sqrt{e}$ for low e. Let's evaluate $n(r = r_0)$ for the parameter e. Analogically to Eqs. A.40 and A.44:

$$n = \delta(z)\int_{\mathbb{R}}\int_{\mathbb{R}} f(r, v_r, v_\phi)\, dv_r\, dv_\phi,$$
$$= \delta(z)Cr_0^\gamma\int_{\mathbb{R}}\int_{\mathbb{R}} v_\phi^\gamma\delta\left(v_r \pm \tilde{v}\right)\, dv_r\, dv_\phi$$
$$= \delta(z)Cr_0^\gamma\int_{\sqrt{\frac{(1-e)\mu}{r_0}}}^{\sqrt{\frac{(1+e)\mu}{r_0}}} v_\phi^\gamma\, dv_\phi$$
$$= \delta(z)Cr_0^\gamma\left[\frac{v_\phi^{\gamma+1}}{\gamma+1}\right]_{\sqrt{\frac{(1-e)\mu}{r_0}}}^{\sqrt{\frac{(1+e)\mu}{r_0}}}$$
$$= \delta(z)Cr_0^\gamma\frac{1}{\gamma+1}\left[v_\phi^{\gamma+1}\right]_{\sqrt{\frac{(1-e)\mu}{r_0}}}^{\sqrt{\frac{(1+e)\mu}{r_0}}}$$
$$= \delta(z)Cr_0^\gamma\frac{1}{\gamma+1}\left(\left(\frac{(1+e)\mu}{r_0}\right)^{\frac{\gamma+1}{2}} - \left(\frac{(1-e)\mu}{r_0}\right)^{\frac{\gamma+1}{2}}\right)$$
$$= \delta(z)Cr_0^\gamma\frac{1}{\gamma+1}\left(\frac{\mu}{r_0}\right)^{\frac{\gamma+1}{2}}\left((1+e)^{\frac{\gamma+1}{2}} - (1-e)^{\frac{\gamma+1}{2}}\right) \tag{A.46}$$

Thus, we get that:

$$\delta_0(z)C = \frac{n}{r_0^\gamma}\left(\frac{r_0}{\mu}\right)^{\frac{\gamma+1}{2}}\frac{(\gamma+1)}{\left((1+e)^{\frac{\gamma+1}{2}} - (1-e)^{\frac{\gamma+1}{2}}\right)}, \tag{A.47}$$

where $[n] = m^{-3}$ at the distance of r_0.

Appendix A.5: Number density assumption

To derive the fluxes following the assumption of number density scaling as $n \propto r^{\gamma}$, we conveniently assumed the equivalence

$$n \propto r^{\gamma} \Leftrightarrow n \propto r_{peri}^{\gamma}. \tag{A.48}$$

Here we demonstrate the validity of this assumption. Assume a dust grain is in orbit with the perihelion r_{peri} and aphelion

$$r_{aph} = \frac{1+e}{1-e} r_{peri}, \tag{A.49}$$

where e is the eccentricity. The grain therefore spends time at the heliocentric distance r:

$$r_{peri} < r < r_{aph}, \tag{A.50}$$

and the time spent, and therefore the probability $g(r)$ the grain will be (in random time) found at r it spends at r is proportional to the inverse of the radial speed $|v_r|$:

$$g(r|r_{peri}) \propto |v_r|^{-1}(r) = \left|\frac{dr}{dt}(r)\right|^{-1} = \left(v^2 - v_{\phi}^2\right)^{-\frac{1}{2}}, \tag{A.51}$$

where v and v_{ϕ} are the total and azimuthal speeds of the grain. Then we have from vis-viva equation:

$$v^2 = \mu\left(\frac{2}{r} - \frac{1}{a}\right) = \mu\left(\frac{2}{r} - \frac{1-e}{r_{peri}}\right), \tag{A.52}$$

and v_{ϕ} is obtained using momentum conservation as

$$v_{\phi} = \frac{v_{peri} r_{peri}}{r}, \tag{A.53}$$

where the perihelion speed v_{peri} is also obtained from vis-viva as

$$v_{peri} = \sqrt{\mu \frac{1+e}{r_{peri}}}, \tag{A.54}$$

which altogether gives:

$$\begin{aligned} g(r|r_{peri}) \propto |v_r|(r) &= \left(\mu\left(\frac{2}{r} - \frac{1-e}{r_{peri}}\right) - \left(\frac{\sqrt{\mu\frac{1+e}{r_{peri}}} r_{peri}}{r}\right)^2\right)^{-\frac{1}{2}} \\ &= \left(\mu\left(\frac{2}{r} - \frac{1-e}{r_{peri}} - \frac{(1+e) r_{peri}}{r^2}\right)\right)^{-\frac{1}{2}} \\ &= \left(\frac{2\mu}{r}\left(1 - \left(\frac{(1-e)}{2}\frac{r}{r_{peri}} + \frac{(1+e)}{2}\frac{r_{peri}}{r}\right)\right)\right)^{-\frac{1}{2}}. \end{aligned} \tag{A.55}$$

Obtaining r from r_{peri} is a random process governed by the probability density function $g(r|r_{peri})$. We can therefore draw a sample of r_{peri} according to $g(r_{peri})$ and transform r_{peri} to r using the density $g(r|r_{peri})$ derived here. Fig. A.1 shows the γ compensated probability density function of $g(r_{peri})$ before the transformation and $g(r)$ after the transformation. A compensated density plot shows a constant, if the slope of the density is the value, for which we compensate, that is γ in our case. As is observed, the dependence $n \propto r^{\gamma}$ is really retained after the transformation, if $n \propto r_{peri}^{\gamma}$ is assumed.

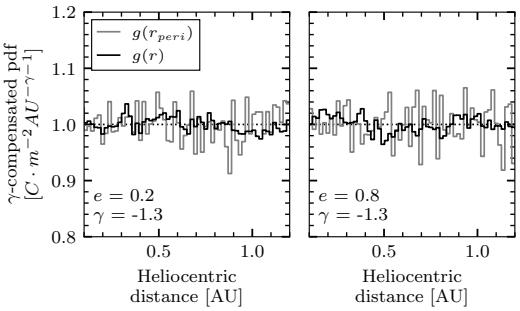

Fig. A.1: A sample of r_{peri} is drawn according to $n \propto r_{peri}^{\gamma}$ and transformed using $g(r|r_{peri})$. The distribution shows $n \propto r^{\gamma}$.

Appendix A.6: Generalization

Already included parameters The integrals for flux $j_{tot,rad}$ and $j_{tot,azim}$ as derived and expressed in Sec. A.3 already allow for evaluation of the flux along a trajectory of a spacecraft, given the eccentricity of the dust's orbits e, radiation pressure to gravity ratio β, distance-scaling parameter γ and cuboid-approximated spacecraft areas, since the flux is evaluated for each of the relevant spacecraft sides independently.

Retrograde grains The simplest addition is the fraction of retrograde grains in the dust cloud. Until, now all the dust grains were considered prograde, but the fraction of retrograde dust is taken into account by weighted summing of the flux encountered along the true spacecraft trajectory, with the flux encountered by mirrored (retrograde) spacecraft trajectory.

Higher exponent of the relative speed If the detection is effective regardless of the impact speed, the flux is proportional to the relative speed between the spacecraft and the dust cloud. If the flux is assumed proportional to an exponent ϵ of velocity, which is higher than unity, such as because of the detection threshold size variation with the impact speed, this is taken into account by evaluating the higher moment of $(v_r - v_{p,rad})$ and $(v_{\phi} - v_{p,azim})$ in the terms of Eqs. A.40 and A.44 respectively, which is straight forward. We note that the normalization needs to be adjusted in this case as well, as a scale relative velocity v_0 has to be introduced, at which the number density is measured.

Inclination A single inclination angle θ different from zero can be introduced, under the assumption that all the grains share the same inclination value, albeit in different (non-parallel) orbital planes, that is with random ascending nodes. Under this assumption, a spacecraft in the plane of ecliptics will only encounter dust grains of this given inclination θ. As discussed in Sec. 2.2, it is reasonable to approximate PSP by a cylinder. This makes no difference compared to a cuboid approximation, until $\theta \neq 0$ is examined.

We note that an arbitrary inclination of the orbital plane of each of the grains does not play a role in $j_{tot,rad}$. For the azimuthal component, we need to evaluate the moment $|\boldsymbol{v}_{\phi} - \boldsymbol{v}_{p,azim}|$ over the f, as a function of inclination θ. We assume the cylin-

Table B.1: The representative orbital parameters for PSP's encounter groups.

Encounter group	Perihelion distance [Gm]	Perihelion distance [AU]	Perihelion speed [km/s]
1	24.8	0.166	95
2	19.4	0.130	109
3	14.2	0.095	127
4	11.1	0.074	147
5	9.2	0.061	163

drical symmetry:

$$v_{cyl}(v_\phi) \equiv |\boldsymbol{v}_\phi - \boldsymbol{v}_{p,azim}| = \sqrt{v_{p,azim}^2 \sin^2\theta + \left(v_\phi - v_{p,azim}\cos\theta\right)^2}, \tag{A.56}$$

which we then need to integrate to

$$j_{tot,azim} = \delta(z) C r^\gamma (j^+_{azim} - j^-_{azim}), \tag{A.57}$$

where

$$j^+_{azim} = \int_{\sqrt{\frac{(1-e)\mu}{r}}}^{\sqrt{\frac{(1+e)\mu}{r}}} v_{cyl}(v_\phi) v_\phi^\gamma H\left(v_{cyl}(v_\phi)\right) dv_\phi, \tag{A.58}$$

$$j^-_{azim} = \int_{\sqrt{\frac{(1-e)\mu}{r}}}^{\sqrt{\frac{(1+e)\mu}{r}}} v_{cyl}(v_\phi) v_\phi^\gamma H\left(-v_{cyl}(v_\phi)\right) dv_\phi. \tag{A.59}$$

Since by definition $|\cdot| > 0$:

$$j^+_{azim} - j^-_{azim} = \int_{\sqrt{\frac{(1-e)\mu}{r}}}^{\sqrt{\frac{(1+e)\mu}{r}}} v_{cyl}(v_\phi) v_\phi^\gamma \, dv_\phi, \tag{A.60}$$

which we evaluate easily, for example with Monte Carlo integration, drawing values of v_{phi} between the integration boundaries (Eq. A.33).

We note that both non-zero eccentricity and non-zero inclination make the assumption of non-interacting grains problematic, but the collisional evolution of the dust cloud is beyond the scope of this work, and taken care of in reality by the micrometer dust cloud being constantly replenished by the product of collision of bigger grains.

Appendix B: Model trajectories of PSP

Every PSP's solar encounter is different from the previous one, even within the same orbital group. This is solely because of the motion of the Sun, which in the first approximation orbits around the common barycenter of the Sun — Jupiter system, which lies outside of the solar photosphere. PSP orbits the Sun on an orbit with perihelion distance sufficiently close the the Sun, so that this effect plays a role when the distance from the Sun is critical. This is however not as consequential as to change the results presented in this work. To get rid of the effect, we study fictitious, simplified solar encounters, which are assumed to lie in the ecliptic plane ($z = 0$) and which represent the actual ones well. The parameters of the encounters which we use for the present study are listen in Tab. B.1.

Appendix C: The flux slope scaling with orbital parameters

In Sec. 6.1, we claimed that the parameters: $e; \theta; \beta; rp$ all act to make the slope of flux steeper, when their values differ from the base case, but in the case of the later orbits, they tend to lead to very little change. Their influence is independently shown in Figs. C.1 – C.4.

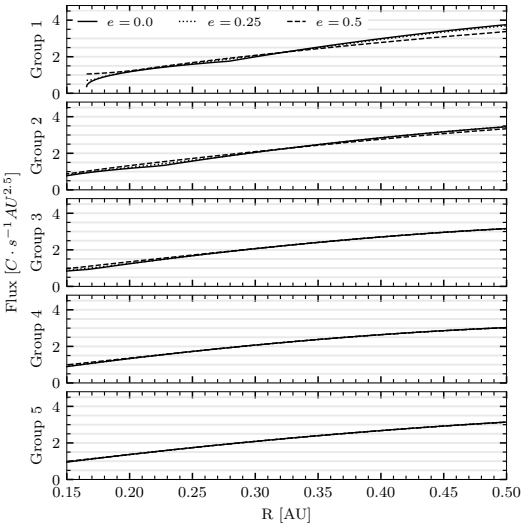

Fig. C.1: The base model-predicted flux is shown in the solid line. In addition, the influence of eccentricity on the slope is demonstrated.

Appendix D: The near-perihelia flux dependence on other parameters

In Sec. 6.2, we claimed that the parameters: $e; \theta; \beta; \gamma, rp$ do not change the location of the flux maxima appreciably. They however make the magnitude of the near-perihelia dip smaller, especially the parameter e does. Their influence is independently shown in Figs. D.1 – D.5.

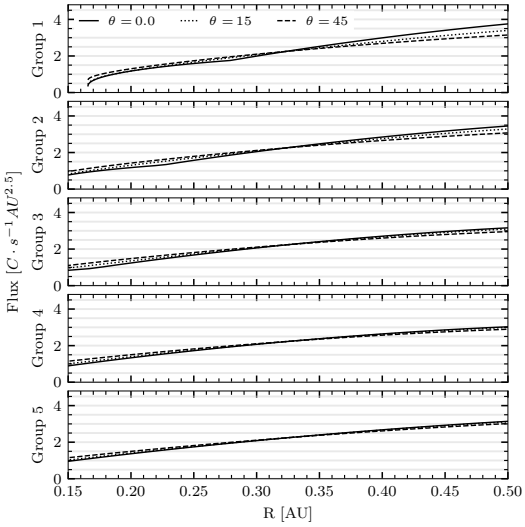

Fig. C.2: The base model-predicted flux is shown in the solid line. In addition, the influence of inclination on the slope is demonstrated.

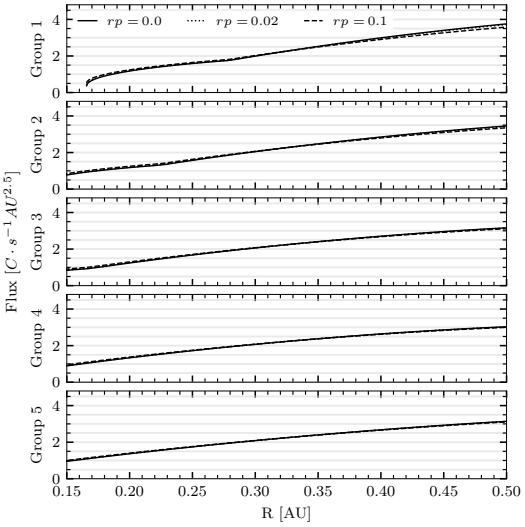

Fig. C.4: The base model-predicted flux is shown in the solid line. In addition, the influence of retrograde fraction on the slope is demonstrated.

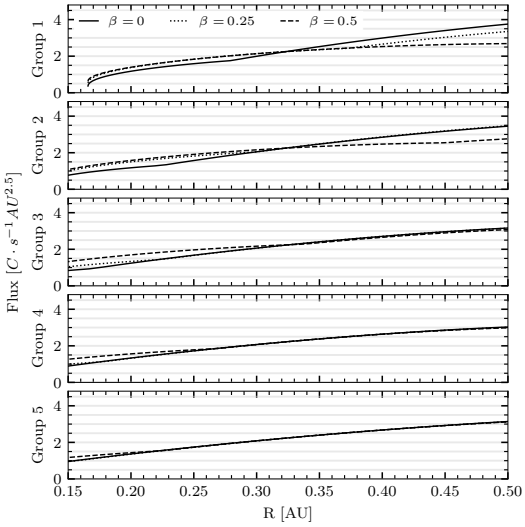

Fig. C.3: The base model-predicted flux is shown in the solid line. In addition, the influence of β value on the slope is demonstrated.

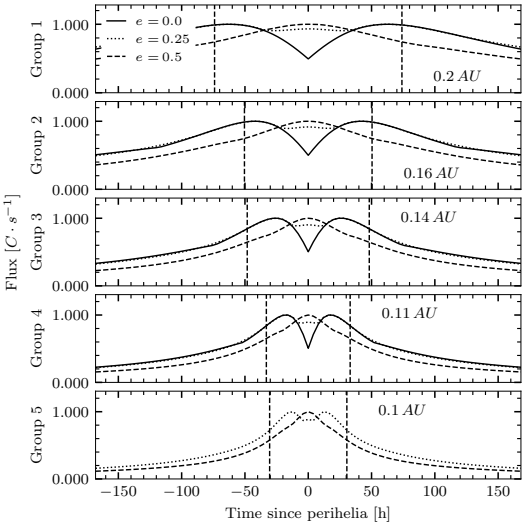

Fig. D.1: The base model-predicted flux is shown in the solid line. In addition, the influence of eccentricity on the slope is demonstrated.

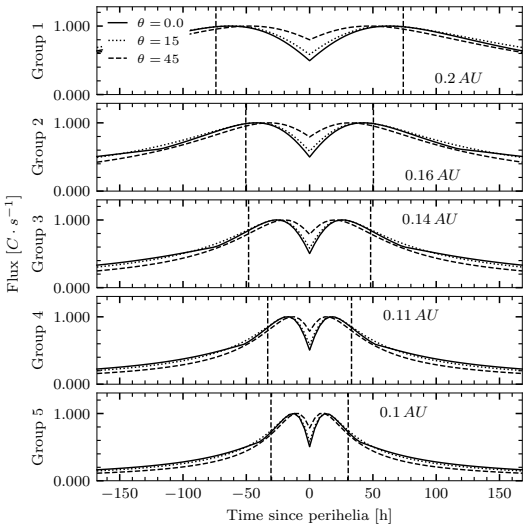

Fig. D.2: The base model-predicted flux is shown in the solid line. In addition, the influence of inclination is shown.

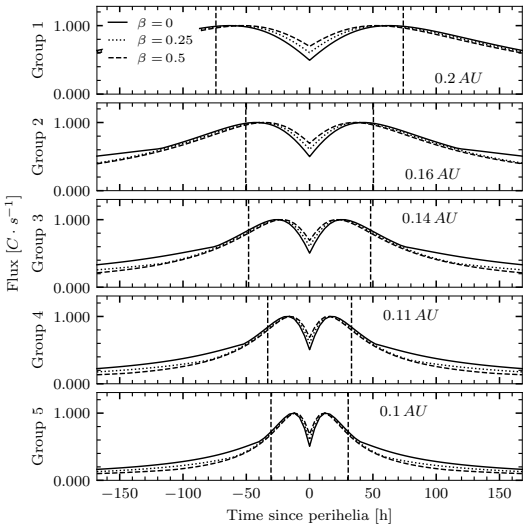

Fig. D.3: The base model-predicted flux is shown in the solid line. In addition, the influence of β value is shown.

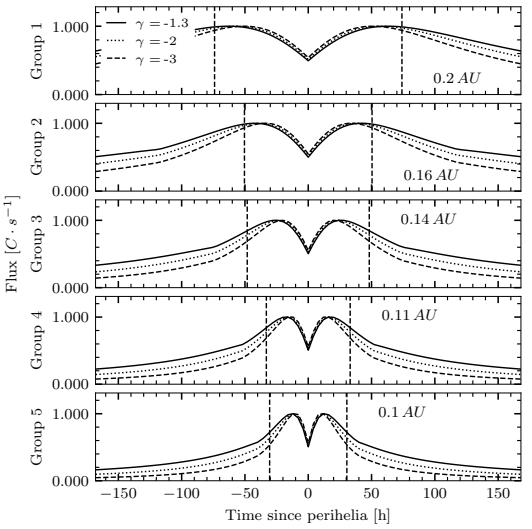

Fig. D.4: The base model-predicted flux is shown in the solid line. In addition, the influence of the spatial density scaling with heliocentric distance γ is shown.

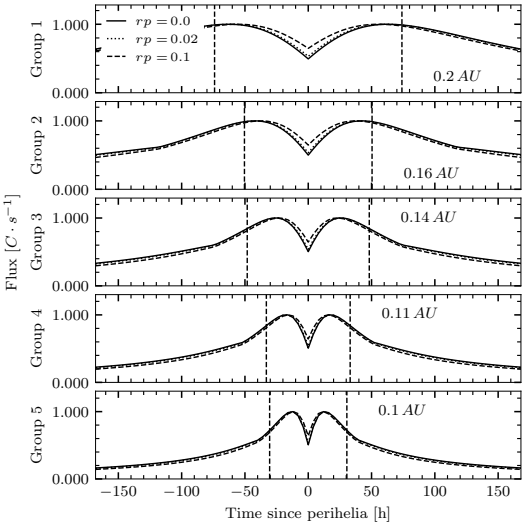

Fig. D.5: The base model-predicted flux is shown in the solid line. In addition, the influence of retrograde fraction is shown.